NANYANG TECHNOLOGICAL UNIVERSITY

PROCESSING-PROPERTIES RELATIONSHIP OF NANOSTRUCTURED NI-FE-MO MAGNETIC MATERIALS

PROCESSING-PROPERTIES RELATIONSHIP OF NANOSTRUCTURED NI-FE-MO MAGNETIC MATERIALS

SHEN YANPING

SHEN YANPING

SCHOOL OF MATERIALS SCIENCE AND ENGINEERING

2006

2006

Processing-Properties Relationship of Nanostructured Ni-Fe-Mo Magnetic Materials

Shen Yanping

School of Materials Science and Engineering

A thesis submitted to the Nanyang Technological University
in fulfilment of the requirement for the degree of
Doctor of Philosophy

2006

PREFACE

This dissertation is submitted to Nanyang Technological University for the degree of Doctor of Philosophy. It is an account of the research I have undertaken in the School of Materials Engineering from September 2001 to March 2005 under the supervision of Dr. Hng Huey Hoon.

To the best of my knowledge the work described in this dissertation is original, except where due reference has been made to the work of others, and nothing is included which is the outcome of work done in collaboration. No part of this dissertation, or any similar to it, has been, or is currently being, submitted for any degree, or other qualification, at any other university.

An account of some of the results described has already appeared in the following papers.

"Synthesis and characterization of high-energy ball milled Ni-15%Fe-5%Mo"
Yanping Shen, Huey Hoon Hng and Joo Tian Oh
J. Alloy. Compd, 379 (2004) 266-271.

"Formation kinetics of Ni-15%Fe-5%Mo during ball milling"
Yanping Shen, Huey Hoon Hng and Joo Tien Oh
Mater. Lett, 58 (2004) 2824-2828.

"High-enery ball milled Ni-15%Fe-5%Mo powders"
Yanping Shen, Huey Hoon Hng and Joo Tien Oh
1st International Conference on Materials Processing for Properties and Performance (MP3) & 10th Annual Conference of Institute of Materials, 1-3 August 2002, Singapore, p488

ACKNOWLEDGEMENTS

I would like to express my most sincere gratitude to my supervisor, Dr. Hng Huey Hoon, for her invaluable guidance and encouragement throughout this study. She has shared numerous interesting discussions and concepts with me. Without her expertise, supervision and constant support, this work would not have been possible.

My special thanks are extended to my senior Mr. Qiu Wei, Research Fellow Dr. Huang Haitao, postgraduate students Miss. Li Huafang and Miss. Cheng Guiping, and all other friends in NTU, for their assistance in my research work and their company in my daily life.

In the course of this project, assistance was given by helpful technicians in many ways. Their supports and sound advices are deeply appreciated. I would like to thank these technicians:
Advanced Materials Characterization lab: Guo Jun, Irene and Lee Chin;
Materials processing lab: Thomas, Patrick and Eric;
Materials Characterization lab: Sharon and Poh Tin;

Last, but not least, the author would like thank all those who have offered me support and assistance during my Ph.D. work but whose name are not mentioned here. I am also grateful to Nanyang Technological University for the financial support that enabled me to pursue my postgraduate study.

Finally, I deeply appreciate my parents. Their care and concern always support me to overcome difficulties in my life.

ABSTRACT

Processing-properties relationship of nanostructured Ni-Fe-Mo soft magnetic materials has been undertaken in this study. Two compositions of Ni-based magnetic materials were studied, namely Ni-15%Fe-5%Mo and Ni-15%Fe-5%Mo-5%B. The samples were prepared by high energy ball milling (HEBM) and melt spinning (MS). Different characterization techniques were employed including X-ray powder diffraction (XRPD), scanning electron microscopy (SEM), transmission electron microscopy (TEM) and differential scanning calorimetry (DSC). Magnetic properties were characterized by coercivity $\mathbf{H_c}$ and saturation magnetization $\mathbf{M_s}$ using vibrating sample magnetometer (VSM).

The investigation of HEBM Ni-Fe-Mo was to study the properties of nanostructured magnetic materials. Materials used in this experiment were elemental Mo powders and pre-alloyed $FeNi_3$ powders. The results showed that even after 100 h of high energy ball milling, the only detected phase was $FeNi_3$. Mo atoms were substituted into the $FeNi_3$ phase, and destroyed the long-range $FeNi_3$ lattice to form short-range order. Saturation magnetization decreased during the substitution process. However, coercivity was mainly affected by the milling process and was independent of the substitution of Mo.

Since no amorphous phase was formed during the milling process of the Ni-Fe-Mo alloy, boron was added to the Ni-Fe-Mo alloy system with the composition Ni-15%Fe-5%Mo-5%B to form the amorphous phase. Partially amorphous powders were obtained by HEBM after 10 h of milling, and further milling time did not produce a totally amorphous powders. Magnetic properties were affected by the amorphization of the powders. DSC results showed that an exothermic peak of 530°C was observed during the heating process After annealing, $(Fe, Ni, Mo)_{23}B_6$ phase was crystallized from the amorphous phase and co-existed with $FeNi_3$ phase. The increase in saturation magnetization was mainly due to the crystallization of the amorphous phase. Coercivity after annealing was mainly affected by the crystallization process and the grain size.

Melt spinning technique was used to obtain amorphous Ni-15%Fe-5%Mo-5%B ribbon. By varying the processing conditions, two types of ribbons were prepared, namely totally amorphous and partially amorphous. Two crystallization stages occurred during the annealing process. They were the primary crystallization and secondary crystallization at about 432°C and 600°C respectively. The phase precipitated from the amorphous matrix at the primary crystallization was $(Fe, Ni, Mo)_{23}B_6$. Ferromagnetic $FeNi_3$ phase was precipitated at the secondary crystallization stage. Microstructure and magnetic properties of the annealed partially amorphous ribbon were better than the annealed totally amorphous ribbon.

Overall, it was found that nanostructured magnetic materials from partially amorphous sample produced by HEBM and MS. Post heat treatment of the as-milled and as-spun samples gave rise to nanostructured materials and better magnetic properties were obtained.

LIST OF TABLES

LIST OF FIGURES

CONTENTS

Chapter 1 Introduction

Magnetic materials undergo tremendous development in the 20th century (Chin, 1992; Boll, 1994; Arrott, 2000; Coey, 1996, 2001a, 2001b; Mchenry and Laughlin, 2000). The study of the relationship between magnetic properties and microstructure is fundamental for the development and application of soft magnetic materials. Magnetic materials encompass a wide variety of materials, which are used in a diverse range of applications (Mchenry and Laughlin, 2000; Coey, 2001a). They are utilized in the creation and distribution of electricity. They are used for the storage of data on audio and video tape as well as on computer disks. In the world of medicine, they are used in body scanners as well as a range of applications where they are attached to or implanted into the body. The home entertainment market relies on magnetic materials in applications such as PCs, CD players, televisions, games consoles and loud speakers.

There are two approaches in the study of magnetic materials. The first approach is the conventional method, which involves making the grain size as large as possible. The conventional processing methods to improve magnetic properties include heat treatment in vacuum, heat treatment in hydrogen and magnetic annealing (Cullity, 1972; Bozorth, 1978; Goldman, 1999). In recent years, the second approach on the study of magnetic materials emerges. Investigations are focused on the nanocrystalline magnetic materials for applications in magnetic devices requiring soft magnetic materials such as transformers and inductive devices (McHenry and Laughlin, 2000). The fact that the magnetic exchange length is typically nanometers or tens of nanometers illustrates the underlying importance of this length scale in magnetic systems. By varying the grain size of a material from micrometer to nanometer scale, its magnetic structure will change from multidomains to a single

domain configuration (Qin et al, 1999a, 1999b). Accordingly, the magnetization process will change from domain wall motion to magnetization rotation mechanism. When the grain size is much smaller than the single domain particle and domain wall sizes, random anisotropy prevails. This leads to pronounced reduction of magnetocrystalline anisotropy, resulting in very low coercivity and very high permeability (Suzuki and Cadogan, 1998; Suzuki, 1999).

Over the past several decades, amorphous and more recently nanostructured materials have been investigated for applications in magnetic devices requiring magnetically soft magnetic materials. Most of the attention has been focused on Fe-based and Fe-Co based materials (McHenry et al, 1999a, 1999b; Willard et al, 1996; McHenry et al, 2003). Very little attention has been focused on Ni-based soft magnetic materials. Ni-based soft magnetic materials containing around 75-82 wt% Ni are usually called Permalloys (Cullity, 1972; Jakubovics, 1987). They have higher permeability and lower coercivity, and are widely used in electrical and electronic industries for the making of audio coils, transformers and magnetic shields. Most of the work on Ni-based soft magnetic materials found in the literature is on bulk materials, and very little has been focused on the nanoscale. Therefore, the main objective of the work is to investigate the processing-properties relationship of nanostructured Ni-Fe-Mo alloys belonging to the Ni-based soft magnetic materials. Two compositions are studied in this project, namely Ni-15%Fe-5%Mo and Ni-15%Fe-5%Mo-5%B. The reason to add Boron is to amorphize the material. The samples are prepared by high energy ball milling (HEBM) and melt spinning (MS).

The literature survey in Chapter 2 covers the general introduction for magnetic materials, including the definition and the microstructure effect on the properties. Emphasis is given to amorphous and nanocrystalline soft magnetic materials, including the fabrication techniques and alloy systems. The addition of Mo element to the magnetic properties is also included in the extensively studied Ni-Fe based soft magnetic materials.

A brief summary of the sample preparation, details of the characterization techniques employed in this project and methods of data evaluation are outlined in Chapter 3.

The characterization of nanostructured Ni-15%Fe-5%Mo powders prepared by high energy ball milling for different milling times is presented in Chapter 4. This study serves as an introduction and a basis for the study of nanostructured Ni-15%Fe-5%Mo-5%B systems prepared by ball milling and melt spinning. Attention is given to the microstructural of these systems including the effect of the grain size and residual strain, and the formation kinetics of the dissolution of Mo atoms. Magnetic properties of the as-milled powders for different milling times are also discussed.

In order to understand the Ni-15%Fe-5%Mo alloy with the addition of Boron, the investigation of Ni-15%Fe-5%Mo-5%B powders prepared by high energy ball milling is described in Chapter 5. There are two parts in this investigation. The first part is to study the feasibility of producing an amorphous phase by adding B into the Ni-Fe-Mo alloy system. The second part is to study the crystallization process of the as-milled powders to produce nanostructured soft magnetic materials. The magnetic properties of the as-milled and annealed samples are evaluated in these two parts respectively.

In order to compare with the HEBM Ni-15%Fe-5%Mo-5%B powders, melt spinning technique is used to produce the amorphous ribbon. This is presented in Chapter 6. There are two parts in this chapter. The first part is to study the feasibility of producing a fully amorphous ribbon via rapid solidification by melt spinning process. The second part involves the study of the microstructure and the crystallization process of the as-spun ribbons. In addition, the magnetic properties of the ribbons will also be characterized and the results will be compared to the alloys prepared by HEBM.

Finally in Chapter 7, the main conclusions are drawn from this work and suggestions for future work are made.

Chapter 2 Literature Review

Over the past several decades, amorphous and nanocrystalline materials have been investigated for application in magnetic devices requiring magnetically soft materials. Most recently, research interest in nanocrystalline soft magnetic alloys has dramatically increased (McHenry et al, 1999a; McHenry and Laughlin, 2000; Arrott, 2001; Coey, 2001a and 2001b). The vast majority of soft magnetic materials have one or more of the ferromagnetic transition elements Fe, Co or Ni, or the rare earth metal Gd as a majority component. In this project, our focus is on Ni-based Permalloy which is commonly used as soft magnetic materials. They exhibit high permeability, low coercivity and high saturation magnetization. In this chapter, general information on magnetism will first be provided. Secondly, a brief summary of the recent research work on amorphous and nanostructured magnetic materials, random anisotropy model and the fabrication methods to prepare these materials will be presented. Thirdly, special attention will be given to Ni-Fe Permalloy and the effects of additional Mo atoms will also be provided.

2.1 Magnetism

The fascinating aspect of magnetism is its ability to generate forces between objects that are not in physical contact with each other (Lall, 1992). *Magnetic field* $\boldsymbol{H}$*, magnetization* $\boldsymbol{M}$*, magnetic induction* $\boldsymbol{B}$*, permeability* $\boldsymbol{\mu}$*, Curie temperature* $\boldsymbol{T_c}$ *and coercivity* $\boldsymbol{H_c}$ are the fundamental properties that quantify all types of magnetism.

2.1.1 Types of Magnetism

Magnetic materials can be classified into five basic types of magnetism: diamagnetism, paramagnetism, ferromagnetism, antiferromagnetism and ferrimagnetism. All materials can be classified in terms of their magnetic behavior falling into one of five categories depending on their bulk magnetic susceptibility. The two common types of magnetism are diamagnetism and paramagnetism, which account for the magnetic properties of most of the periodic table of elements at room temperature. The value of magnetic susceptible falls into a particular range for each type material and this is shown in Table 2.1 with some examples.

Diamagnetism — Diamagnetism is a very weak form of magnetism in the presence of an applied external field. When a magnetic field is applied, the orbital motion of electrons is changed. The magnitude of the induced magnetic moment is extremely small, and is in an opposite direction to the applied field. Thus, the relative permeability μ_r is less than unity, and the magnetic susceptibility is negative. The volume susceptibility χ_m for diamagnetic solid materials is of the order of -10^{-5} (Callister, 2003; Willard, 1996).

Paramagnetism — Paramagnetic materials have a small and positive susceptibility (or permeability of nearly unity). Susceptibility for paramagnetic materials ranges from about 10^{-3} to 10^{-5} (Callister, 1994; Willard, 1996; Host et al, 1998). Materials exhibiting paramagnetism are usually atoms and molecules with an odd number of electrons so that there is an unpaired electron spin, giving rise to a net magnetic moment.

Ferromagnetism — Certain metallic materials possess a permanent magnetic moment in the absence of an external field, and manifest very large and permanent magnetizations. These are the characteristics of ferromagnetism, and they are displayed by transition metals such as Fe (as BCC α ferrite), Co and Ni, and some of the rare earth metals such as Gd. Ferromagnetism is only possible when atoms are arranged in a lattice and the atomic magnetic moments can interact to align parallel to each other.

Table 2.1 Summary of different types of magnetic behavior (Goldman, 1999).

Type of Magnetism	***Susceptibility***	***Atomic / Magnetic Behavior***	***Example / Susceptibility***
Diamagnetism	Small&negative.	Atoms have no magnetic moment 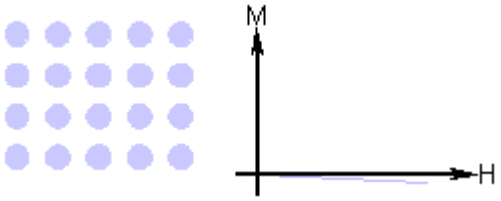	Au -2.74×10^{-6} Cu -0.77×10^{-6}
Paramagnetism	Small& positive.	Atoms have randomly oriented magnetic moments 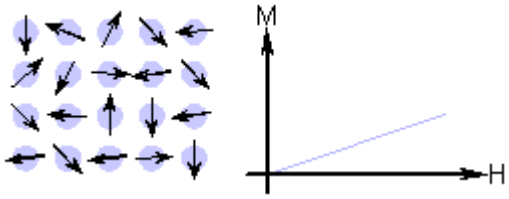	β-Sn 0.19×10^{-6} Pt 21.04×10^{-6} Mn 66.10×10^{-6}
Ferromagnetism	Large& positive, function of applied field, microstructure dependent.	Atoms have parallel aligned magnetic moments 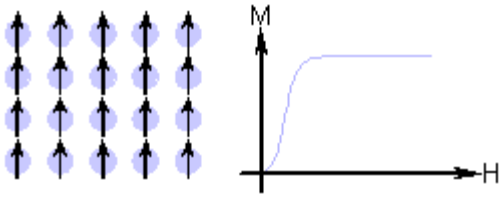	Fe ~100,000
Antiferromagnetism	Small& positive.	Atoms have mixed parallel and anti-parallel aligned magnetic moments 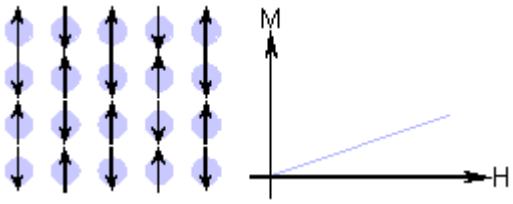	Cr 3.6×10^{-6}
Ferrimagnetism	Large&positive, function of applied field, microstructure dependent	Atoms have anti-parallel aligned magnetic moments 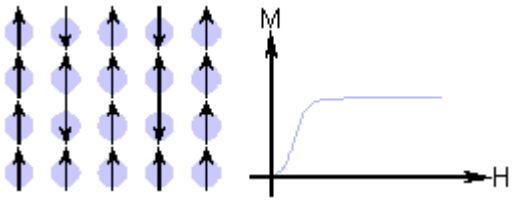	Ba ferrite ~3

Ferromagnetism is found in materials with positive exchange interactions between magnetic moments in the materials either in a direct or indirect manner. A direct exchange involves the overlap of atomic orbital and the interactions of the electron spins with one another to form positive interactions. Superexchange is a form of indirect exchange that involves interactions mediated by intermediate atoms, such as anions in ferromagnetic spinals.

Antiferromagnetism — Magnetic moment coupling between adjacent atoms or ions can also occur in materials other than ferromagnetic materials. In one such group, this coupling results in an antiparallel alignment of the spin moments of neighboring atoms or ions in exactly opposite directions. This is termed antiferromagnetism. The opposing magnetic moments cancel one another, and as a result, the material as a whole possesses no net magnetic moment. The magnetic susceptibility for antiferromagnets is slightly greater than one. Manganese oxide is a material that displays such behavior (Callister, 1994; Willard, 1996).

Ferrimagnetism — Ferrimagnetism is only observed in compounds, which have more complex crystal structures than pure elements. Within these materials the exchange interactions lead to parallel alignment of atoms in some of the crystal sites and anti-parallel alignment of others. The material breaks down into magnetic domains, just like a ferromagnetic material and the magnetic behavior is also very similar, although ferromagnetic materials usually have lower saturation magnetizations.

2.1.2 Magnetic Properties

Although all magnetic properties are dependent on composition and temperature, not all are sensitive to the metallurgical conditions of the material (Chen, 1977), which include:

(1) The size, shape and orientation of grains;
(2) The concentration and distribution of various crystal imperfections;
(3) The state of the lattice with regard to impurities, residual stresses and atomic arrangement in alloys.

Depending on these conditions, the magnetic properties can be divided into two groups: (1) intrinsic properties (microstructure insensitive properties) that depend on alloy chemistry and crystal structure, and (2) extrinsic properties (microstructure sensitive properties). Saturation magnetization $\boldsymbol{M_s}$ and Curie temperature $\boldsymbol{T_c}$ are two important intrinsic magnetic properties. Microstructure sensitive properties are

numerous and can be classified further as static or dynamic, depending on whether or not the property displays frequency dependence. Induction $\boldsymbol{B}$, permeability $\boldsymbol{\mu}$, hysteresis energy loss $\boldsymbol{W_h}$, coercivity $\boldsymbol{H_c}$ and remanence $\boldsymbol{B_r}$ are structure sensitive, static properties. Eddy current loss $\boldsymbol{E_e}$ and resonance of spins and domain walls are structure sensitive, dynamic properties (Chen, 1977; McCurrie, 1994).

In this project, the emphasis is on ferromagnetic materials. A typical hysteresis loop of a ferromagnetic material is shown in Fig. 2.1. Magnetic properties namely maximum induction $\boldsymbol{B_m}$, maximum magnetic field $\boldsymbol{H_m}$, remanence $\boldsymbol{B_r}$, permeability $\boldsymbol{\mu}$ and coercivity $\boldsymbol{H_c}$ are listed in the figure. Remanence $\boldsymbol{B_r}$, permeability $\boldsymbol{\mu}$ and coercivity $\boldsymbol{H_c}$ will be discussed in detail in the following section.

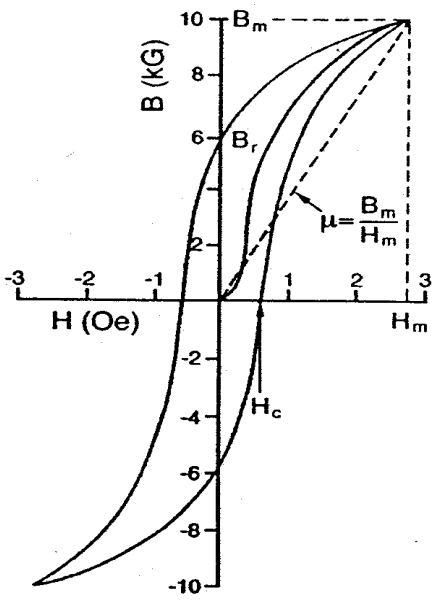

Fig. 2.1 Typical hysteresis loop of a ferromagnetic material.

2.1.2.1 Intrinsic Properties

Saturation magnetization M_s — The saturation magnetization ($\boldsymbol{M_s}$) is a measure of the maximum amount of field that can be generated by a material. It will depend on the strength of the dipole moments on the atoms that make up the material and how densely they are packed together. The atomic dipole moment will be affected by the nature of the atom and the overall electronic structure within the compound. The

packing density of the atomic moments will be determined by the crystal structure and the presence of any non-magnetic elements within the structure.

Curie temperature T_c — The Curie temperature T_c is the critical temperature at which thermal energy is just enough to remove the spontaneous magnetization. T_c marks the transition point at which a ferromagnet is converted to a paramagnet upon heating. At this temperature, the permeability of the material drops suddenly and both coercivity and remnant induction become zero (Callister, 1994; McHenry et al, 1999a; McHenry and Laughlin, 2000).

2.1.2.2 Extrinsic Properties

- ***Static properties***

Permeability μ — Magnetic permeability can be defined as:

$$\mu = B / H = 1 + \chi \qquad (2.1)$$

where μ is the magnetic permeability,
B is the magnetic induction,
H is the magnetic field,
χ is the susceptibility.
μ is equal to B/H, the ratio of the magnetic induction to the amplitude or strength of the applied field. This definition refers to the normal permeability when the material is in a "cyclic" state.

The initial permeability is strongly dependent upon the structural conditions of the specimen. These conditions include defects and internal stresses. In order to improve the magnetic properties, especially to obtain high permeability, heat treatment and magnetic annealing have been found to improve the permeability (Chen, 1977; Bozorth, 1978).

Hysteresis loss — Hysteresis loss is the energy consumed in cycling a material between a field H and $-H$ and then back again. The energy consumed in one cycle is

$W_h = \int HdB$ or the area inside the hysteresis loop. The hysteresis energy loss is due to the irreversible movement of domain walls.

Coercivity H_c — The magnetic induction can be reduced to zero by applying a reverse magnetic field of strength $\boldsymbol{H_c}$. This field strength is known as the coercivity. It is strongly dependent on the condition of the sample, being affected by such factors as heat treatment or deformation (Jiles, 1998). Coercivity $\boldsymbol{H_c}$ is often used as the most important single criterion to determine whether a ferromagnetic material is soft or hard. Keeping coercivity at a minimum is a primary goal in the preparation of soft magnetic materials.

Remanence B_r — When the field is reduced to zero after magnetizing a magnetic material, the remaining magnetic induction is called the remanent induction $\boldsymbol{B_r}$ and the remaining magnetization is called the remnant magnetization $\boldsymbol{M_r}$.

$$B_r = \mu_0 M_r \qquad (2.2)$$

The remanence is used to describe the value of either the remaining induction or magnetization when the field has been removed after the magnetic material has been magnetized to saturation. The remanence therefore becomes the upper limit for all remanent inductions or magnetizations (Jiles, 1998).

- ***Dynamic properties***

Eddy currents energy losses E_e — When an alternating field is applied to magnetize a ferromagnetic body, an electromagnetic force (emf) is set up in the body. If the material is also a good conductor, as with metals and alloys, the induced force will produce appreciable amount of currents in different regions. These currents are known as the eddy currents, and their occurrences give rise to an energy loss, $\boldsymbol{E_e}$, through resistance heating. Thus, in alternative current applications, metallic ferromagnets suffer hysteresis as well as eddy-current losses. Eddy current loss becomes even more burdensome than hysteresis loss at intermediate and high frequencies.

The eddy current energy loss E_e is dependent on several factors and is described by the well-known Steinmetz equation (Bozorth, 1978):

$$E_e = \alpha f^2 B^2 t^2 / \rho \qquad (2.3)$$

where α is a proportionality constant,
f is frequency in Hertz,
B is flux density in Tesla,
t is the sample thickness in meters, and
ρ is the resistivity in ohm·meters.

In practical terms, only the electrical resistivity ρ and the sample thickness t can be modified to minimize eddy current loss.

2.2 Amorphous and Nanostructured Magnetic Materials

2.2.1 Introduction

2.2.1.1 Amorphous materials

Amorphous metallic alloys are alloys with no long range atomic order. They have also been called glassy alloys or non-crystalline alloys. They are made by a variety of techniques, all of which involve the rapid solidification of the alloying constituents from either the gas or liquid phase. The solidification occurs so rapidly that the atoms are frozen in their liquid configuration. There are clear structural indications and indications from their various properties that nearest neighbor, or local, order does exist in most amorphous metallic alloys, but there is no long range atomic order (Luborsky, 1983).

The materials exhibit unique magnetic, mechanical, electrical and corrosion behaviors which results from the amorphous structure. They are exceptionally hard and have extremely high tensile strengths and in some alloys the coefficient of the thermal expansion can be made to be zero. They have electrical resistivities which

are three to four times higher than those of conventional iron or iron-nickel alloys. Some of the amorphous alloys are also found to be exceptionally corrosion resistant. Amorphous alloys have been shown to have vastly superior magnetic properties for application in large transformers. Moreover, having a combination of mechanical and magnetic properties makes them extremely likely candidates for application in recording heads, in some electronic size transformers and various types of sensor. Thus, the application of amorphous alloys in various magnetic devices appears to be assured. Although amorphous alloys have many merits compared to the traditional bulk materials, it is difficult to produce the amorphous alloys. The request of high cooling rate and the narrow range of the sample compositions to produce amorphous alloys are the most important limitations.

2.2.1.2 Nanostructured materials

Nanocrystalline materials can be obtained from the amorphous precursor by controlling the experiment conditions and by other techniques. Nanocrystalline materials are used to describe materials that have a majority of grain diameters in the typical range from ~1nm to 50nm. These materials can be divided into three categories (Gleiter, 1995 and 2000; Greer, 1998; Gusev, 1998; McHenry and Laughlin, 2000):

The first category comprises of materials and/or devices with reduced dimensions and/or dimensionality in the form of nanometer-sized particles, thin wires or thin films. Well-known examples of technological applications of materials with properties dependent on this type of microstructure are catalysts and semiconductor devices utilizing single or multilayer quantum well structures.

The second category comprises of materials and/or devices in which the nanometer-sized microstructure is limited to a thin surface region of a bulk material. The properties of a thin surface layer are improved by means of creating a nanometer-sized microstructure in a thin surface region.

The third category comprises of bulk solids with a nanometer-scale microstructure.

In this project, our attention is focused on the third category. In bulk solids, the chemical composition, the atomic arrangement and/or the size of the building blocks vary on a length scale of a few nanometers throughout the bulk.

Two classes of such solids can be distinguished. In the first class, the atomic structure and/or the chemical composition varies in space continuously throughout the solid on an atomic scale. Glasses, gels, supersaturated solid solution or implant materials are examples of this type. The second class of materials has a nanometer-sized microstructure, and has been synthesized and studied in the last two decades. These materials are assemblies of nanometer-sized building blocks — mostly crystallites — as shown in Fig. 2.2. These building blocks may differ in atomic structure, crystallographic orientation and chemical composition. If the building blocks are crystallites, incoherent or coherent interfaces may be formed between them, depending on the atomic structure, the crystallographic orientation and chemical composition of adjacent crystallites. In other words, materials assembled from nanometer-sized building blocks are microstructurally heterogeneous consisting of building blocks (e.g. crystallites) and regions between adjacent building blocks (e.g. grain boundaries). It is this inherently heterogeneous structure on a nanometer scale that is crucial for many of their properties and distinguished them from glasses, gels, etc.

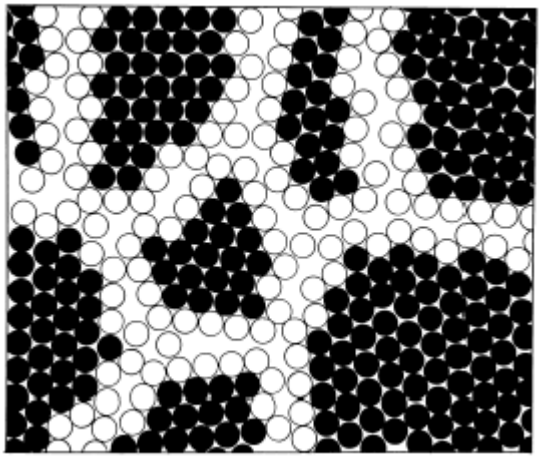

Fig. 2.2 Two-dimensional model of a nanostructured material, the atoms in the centers of the crystals are indicated in black. The ones in the boundary core regions are represented as open circles (Gleiter, 2000).

Since the properties of solids are dependent on size, atomic structure and chemical composition, increased strength or hardness, enhanced diffusivity, improved ductility or toughness, reduced density, reduced elastic modulus, higher electrical resistivity, increased specific heat, higher thermal expansion coefficient, lower thermal conductivity and superior magnetic properties may be expected in nanostructured materials compared to conventional coarse grained materials (Edelstein et al, 1998; Gleiter, 2000).

As the grain size is in the range of nanometer, a specific parameter introduced by nanomaterials is the surface / interface-to-volume ratio. A high percentage of surface atoms introduce many size-dependent phenomena, and the properties of the materials are affected by controlling the grain size and interfaces. The most important application of nanocrystals has been in catalysis (Ahmadi et al, 1996). A larger percentage of surface atoms greatly increase surface activities. The unique surface structure, electronic states and largely exposed surface area are required for stimulating and promoting chemical reactions.

Mechanical properties are also affected by nanocrystals. The grain boundary structure, boundary angle, boundary sliding and movement of dislocations are important factors that determine the mechanical properties of the nanostructured materials. A decrease in grain size significantly had been reported to affect the yield strength and hardness (Weertman and Averback, 1996). It was predicted using Hall-Petch law (Tabor, 1951; Lai, 1998) that the material's strength grows as grain size decreases including microstress and microhardness, and diffusion-controlled creep is important even at room temperature for nanometer grains. An increase in microhardness caused by a drop of grain size of nc-Cu, nc-Fe and nc-Ni was observed by a number of researchers (Chokshi et al, 1989; Jang and Koch, 1990; Ganapathi et al, 1991).

Thermodynamic properties are also influenced by the large surface-to-volume ratio of nanocrystals. The reduced coordination number of the surface atoms greatly increases the surface energy so that atom diffusion occurs at relatively lower temperatures. The melting temperature of Au particles dropped to as low as ~300°C for particles with diameters of smaller than 5 nm, much lower than the

bulk melting temperature 1063°C for Au (Buffat and Borel, 1976). The heat capacity of sample of nanocrystalline Pd and Cu produced by compacting nanoclusters was measured, and it was revealed that the capacity of the nanocrystalline Pd and Cu samples were 53% and 9-11% higher than those of ordinary polycrystalline Pd and Cu, respectively (Rupp and Birringer, 1987). Later, measurements of the temperature dependence of the heat capacity of compacted samples of nanocrystalline nickel with an average grain size of roughly 70 nm had shown that at T≤600 K nanocrystalline Ni had a much higher heat capacity than coarse-grained nickel (Valiev et al, 1989).

The nanostructured materials also have unique magnetic properties compared to the bulk materials, and the reasons for the large difference lie in two points. The large surface-to-volume ratio results in a different local environment for the surface atoms in their magnetic coupling interaction with neighboring atoms. In the case of a single particle being a single domain, the superparamagnetism occurs, in which the magnetizations of the particles are randomly distributed and they are aligned only under an applied magnetic field, and the alignment disappears once the external field is withdrawn. In ultra-compact information storage, the size of the domain determines the limit of storage density. Valiev et al (1989) reported a reduction in the Curie temperature for nanocrystalline Ni (70-100 nm) by 30-40 K in comparison to the value for ordinary coarse-grained nickel. Later, the study of the temperature dependence of the coercive force $\boldsymbol{H_c}$ of nickel-copper alloys was made by Korolev et al (1990). They found that the coercivity force $\boldsymbol{H_c}$ of the nanocrystalline Ni was several times stronger than those of the initial alloy and coarse-grained nickel. In recent years, ferromagnetic nanocrystalline alloys based on Fe with additions of Nb, Cu, Si, and B and based on Co or Fe-Co with additions of Si and B have drawn a lot of interest. These will be discussed in section 2.2.1 in detail.

2.2.2 Alloy systems

2.2.2.1 Amorphous magnetic materials

Amorphous magnetic materials can be divided into three major classes: Fe-based, Fe-Ni based and Co based. Their magnetic properties are summarized in Table 2.2.

- Fe-based alloys of saturation induction in the range of 1.2-1.8 T: these are originally developed as low-loss substitutes for the grain-oriented silicon steels for power distribution applications, but with suitable composition modifications and heat treatment have also found to possess good high-frequency characteristics.

- Fe-Ni based alloys of saturation induction in the 0.9 T range. They have lower magnetostriction and better corrosion resistance than the iron-based alloys.

- Co-based alloys with near-zero magnetostriction properties: they have the highest permeabilities and lowest losses coupled with stress insensitivity.

There are three empirical rules for synthesis of these alloy systems with large glass forming abilities: multicomponent systems with three or more constituent elements, different atomic size ratios typically with difference exceeding ~13% and negative heats of mixing among the constituent alloying elements (McHenry et al, 1999a; McHenry and Laughlin, 2000).

Table 2.2 Magnetic properties of some amorphous magnetic materials.

Alloy	Composition	B_s (T)	H_c (A/m)	T_c (°C)	Ref.
Iron- based	$Fe_{73.5}Cu_2Nb_3Si_{13.5}B_9$	1.24	0.53	843	Zhang et al, 1996
	$Fe_{83}Nb_7B_6Cu_1$	1.42	2.24	---	Perepesko and Paik, 1982
	$Fe_{78}Cu_1Nb_5Al_4B_{12}$	1.38	0.96	---	Perepesko and Paik, 1982
	$Fe_{73.5}Al_2Cu_1Nb_3Si_{13.5}B_9$	1.3	0.32	---	Varga et al, 1997
	$Fe_{80}B_{11}Si_9$	1.59	2	392	DeCristofaro, 1998
	$Fe_{91}Zr_7B_2$	1.70	7.2	---	Suzuki et al, 1998
	$Fe_{90}Zr_7B_2Cu_1$	1.65	2.4	---	Suzuki and Cadogan, 1998
	$Fe_{87}Zr_4Nb_3B_6$	1.50	15.9	---	Suzuki and Cadogan, 1998
	$Fe_{91}Hf_7B_2$	1.65	4.1	---	Suzuki et al, 1998
	$Fe_{73.5}Si_{13.5}B_9Nb_3Cu_1$	1.24	0.53	---	Suzuki and Cadogan, 1999
	$Fe_{67}Co_{18}B_{14}Si_1$	1.8	4.0	415	Chin, 1992
Fe-Ni based	$Fe_{40}Ni_{40}P_{14}B_6$	0.82	46	300	Surinach et al, 1994
	$Fe_{40}Ni_{38}Mo_4B_{18}$	0.88	1.2	353	Chin, 1992
	$Fe_{29}Ni_{49}P_{14}B_6Si_2$	0.42	56	---	DeCristofaro, 1998
	$Fe_{39}Ni_{39}Mo_2Si_{12}B_8$	0.8	2.0	533	Boll, 1994
Cobalt-based	$Co_{67}Fe_4Mo_1Si_{17}B_{11}$	0.55	0.3	483	Boll, 1994
	$Co_{74}Fe_2Mn_4Si_{11}B_9$	1.0	1.0	753	Boll, 1994
	$Co_{72}Fe_3P_{16}B_6Al_3$	0.63	1.2	350	Bordin et al, 1996
	$Co_{63}Fe_4Si_{10}B_{15}Nb_1Ni_7$	0.70	0.3	540	Bordin et al, 1996

2.2.2.2 Nanostructured magnetic materials

Nanostructured magnetic materials can be obtained from various techniques and divided into three classes: hard magnetic materials, magnetic recording media and soft magnetic materials.

- Hard magnetic materials have a magnetic transition metal as the majority species and a rare earth metal as the minority species. The large size difference between the rare earth and transition metal species gives rise to the observation of many anisotropic crystal structures. In these systems, the transition metal is responsible for most of the magnetization and the rare earth species determine the magnetocrystalline anisotropy. Systems based on Sm-Co (Wallace, 1973; Wallace and Nasasimhan, 1980; Strnat, 1988) and Fe-Nd-B (Gong et al, 1994; Billoni et al, 2000; Gao et al, 2000) have been of considerable recent interest. The nanocrystalline microstructure includes soft magnetic phases such as α-Fe, bcc (Fe, Co) and hard magnetic phases $SmCo_5$, Sm_2Co_7 and $Nd_2Fe_{14}B$. These two types of phases can be coupled when the dimension of the microstructure is less than about 20 nm. The soft magnetic grains are pinned to the hard magnetic ones by the exchange interaction at the interfaces while the center of the soft magnetic grains can rotate in a reversed magnetic field.

- The magnetic materials used as recording media are usually Co-based alloy films with the h.c.p. crystal structure. Various alloy additions to the Co (Cr, Ta, Pt et al) change some of the intrinsic magnetic properties of the alloy (Bate, 1980; Maeda et al, 1985; Chapman et al, 1986; Kemner et al, 1996). Pt increases the magneto-crystalline anisotropy constants of the Co-based alloy. Cr tends to segregate to the grain boundaries of the Co alloy, thereby decreasing the exchange coupling between the grains, which in turn tends to decrease the noise of the media. Ta has been found to promote the segregation of Cr.

- Soft magnetic materials have three families: FINEMET, NANOPERM and HITPERM. All these alloys are produced by quenching into amorphous ribbons, followed by a heat treatment around its crystallization temperature. Typical

attributes of nanocrystalline ferromagnetic materials produced by an amorphous pre-cursor route are summarized in Table 2.3.

Table 2.3 Attributes of nanocrystalline ferromagnetic materials produced by an amorphous precursor route (McHenry et al, 1999a, 1999b, 2000, 2003).

Alloy name	Typical composition	Nanocrystalline phase	B_s (T)	T_c (°C)
FINEMET	$Fe_{73.5}Si_{13.5}B_9Nb_3Cu_1$	α-FeSi, $FeSi(DO_3)$	1.0-1.2	<770
NANOPERM	$Fe_{88}Zr_7B_4Cu_1$	α-Fe (b.c.c)	1.5-1.8	770
HITPERM	$Fe_{44}Co_{44}Zr_7B_4Cu_1$	α-FeCo (b.c.c), α′-FeCo (B2)	1.6-2.1	>965

Thermodynamic, transformation kinetic considerations, microstructure, intrinsic and extrinsic magnetic properties of these three alloys have been well done (McHenry et al, 1999a, 2003; Manivel Raja et al, 2000; McHenry and Laughlin, 2000; Johnson et al, 2001; Barandiaran et al, 2003; Kwapulinski et al, 2003; Ponpandian et al, 2003; Skorvanek et al, 2003). The reason to study these properties is to understand the transformation kinetics of nanocrystalline alloy and the microstructure effect on the magnetic properties. Different addition elements that affected the microstructure and magnetic properties have also been reported for these three types' materials.

A significant issue in the use of nanocrystalline soft magnetic materials is the strength of this material and especially the temperature dependence of the exchange coupling between the nanocrystalline grains. The intergranular amorphous phase, left after the primary crystallization in FINEMET and NANOPERM, has a lower Curie temperature than the nanocrystalline ferromagnetic phase. This can give rise to exchange decoupling of the nanocrystalline grains, and resulting magnetic hardening, at relatively low temperatures. HITPERM has been developed with the aim of not only increasing the Curie temperature of the nanocrystals but also in the intragranular amorphous phase.

2.2.3 Random anisotropy model

The magnetic anisotropy represents a barrier to switching the magnetization (Cullity, 1972; Heck, 1974; Bozorth, 1978). For soft magnetic materials, a small magnetic anisotropy is desired so as to minimize the hysteretic losses and maximize the permeability. It was found that the benefits of nanocrystalline alloys for soft magnetic applications are discussed in terms of extrinsic properties — low coercivity $\boldsymbol{H_c}$ and high permeability $\boldsymbol{\mu}$ (McHenry et al, 1999a). It was also found that a measure of the magnetic hardness (coercivity, $\boldsymbol{H_c}$) is roughly proportional to the grain size ($\boldsymbol{D_g}$), and the relationship between the grain size and coercivity is described by the random anisotropy model which suggests that nanocrystaline and amorphous alloys have significant potential as soft magnetic material (Alben et al, 1978; McHenry and Laughlin, 2000). This model will be discussed in detail in the following paragraphs.

When the grain size ($\boldsymbol{D_g}$) exceeds ~0.1-1 μm (where the grain size exceeds the domain (Bloch) wall thickness, $\boldsymbol{\delta_w}$), coercivity $\boldsymbol{H_c}$ is roughly inversely proportional to the grain size [Fig. 2.3 (a)]. In such cases, grain boundaries act as impediments to domain wall motion, and thus fine-grained materials are usually magnetically harder than large grained materials. Significant developments (Herzer, 1989 and 1990; Herzer and Hilzinger, 1986 and 1992; Herzer and Warlimont, 1992) in the understanding of magnetic coercivity mechanisms have led to the realization that for very small grain sizes $\boldsymbol{D_g}$<~100 nm, $\boldsymbol{H_c}$ decreases rapidly with decreasing grain size [Fig. 2.3 (a)]. This can be understood by the fact that the domain wall, whose thickness, $\boldsymbol{\delta_w}$, exceeds the grain size, now samples several (or many) grains so that fluctuations in magnetic anisotropy on the grain size length scale are irrelevant to domain wall pinning. This is the important concept of random anisotropy model which suggests that nanocrystalline and amorphous alloys have significant potential as soft magnetic materials (Yoshizawa et al, 1988; Gleiter, 1995; Suzuki and Cadogan, 1998; Suzuki, 1999). Random anisotropy has been used in a variety of amorphous and nanocrystalline ferromagnets as illustrated in Fig. 2.3 (b) which shows two important figures of merit for soft magnetic materials their magnetic permeability and their inductions.

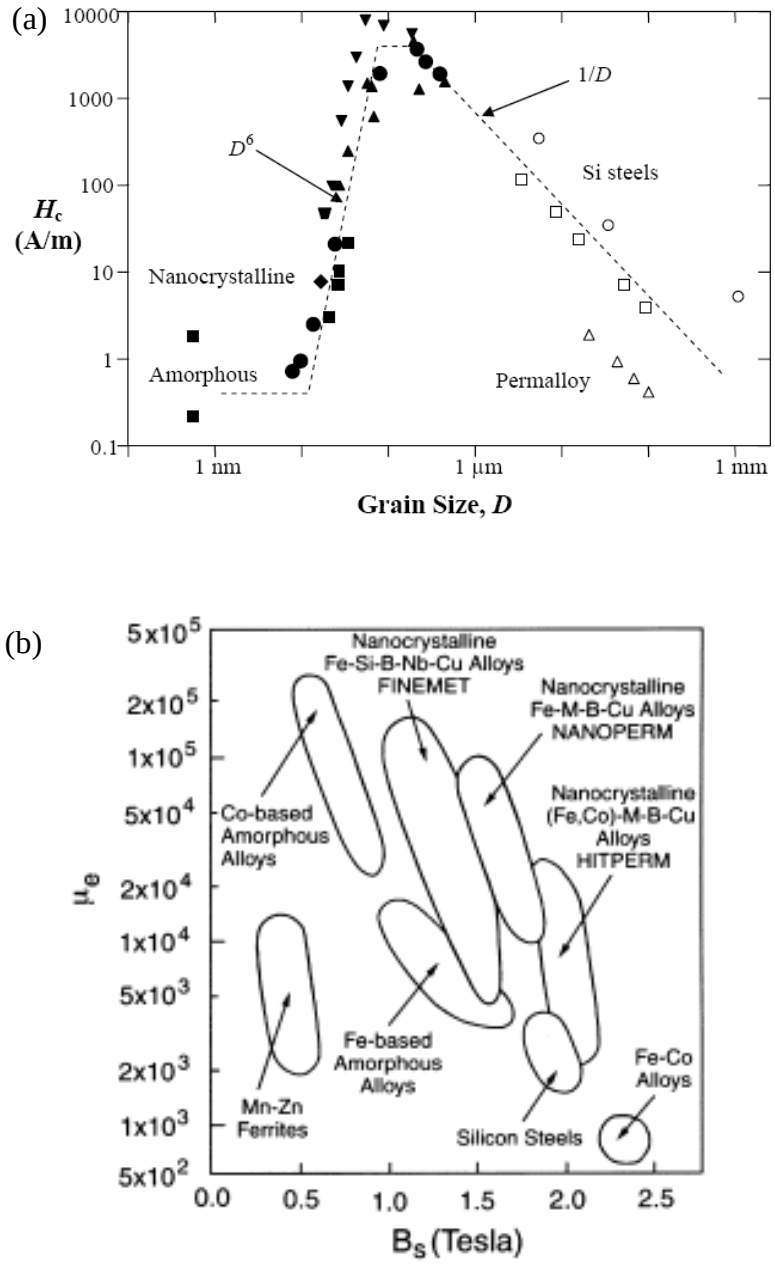

Fig. 2.3 (a) Herzer diagram (Herzer and Hilzinger, 1986; Herzer, 1997) illustrating dependence of the coercivity, H_c, with grain size in magnetic alloys, and (b) relationship between permeability, μ_e (at 1 kHz) and saturation polarization for soft magnetic materials (Makino et al, 1991)

In order to understand the random anisotropy in nanostructured materials, the magnetic exchange length should be mentioned. The concept of a magnetic exchange length and its relationship to the domain wall width and monodomain size is important in the consideration of magnetic anisotropy in nanocrystalline soft magnetic materials (Bertotti et al, 1997). These can be defined by applying to the

function as described by Coey (1996). These length scales are:

$$\delta_w = \pi\sqrt{\frac{A}{K}}, \text{ and } \quad L_{ex} = \sqrt{\frac{A}{4\pi M_s^{\,2}}} \qquad (2.4)$$

where δ_w is the domain (Bloch) wall width,

$\boldsymbol{A}$ is the exchange stiffness,

$\boldsymbol{K}$ is the magnetic anisotropy,

$\boldsymbol{L_{ex}}$ is the exchange correlation length,

$\boldsymbol{M_s}$ is the saturation magnetization.

The extension of the random anisotropy model to nanocrystalline alloys has also been used as the premise for explaining the soft magnetic properties of these materials (Herzer and Hilzinger, 1986 and 1992; Herzer and Warlimont, 1992; Herzer, 1989, 1990 and 1995). The Herzer argument for effective anisotropies in nanocrystalline materials builds on the arguments of the random anisotropy model presented for amorphous alloys. Herzer considers a characteristic volume whose linear dimension is the magnetic exchange length, $L_{ex} \sim (A/K)^{1/2}$ schematically shown in Fig. 2.4.

The Herzer argument considers $\boldsymbol{N}$ grains, with random easy axes, within a volume of $\boldsymbol{L_{ex}}$ to be exchange coupled. Since the easy axes are randomly oriented, a random walk over all $\boldsymbol{N}$ grains will yield an effective anisotropy which is reduced by a factor of $1/(N)^{1/2}$ from the value $\boldsymbol{K}$ for any one grain, thus the effective magnetic anisotropy $K_{eff} = K/(N)^{1/2}$. Now the number of grains in this exchange coupled volume is just $N = (L_{ex}/D)^3$, where $\boldsymbol{D}$ is the average diameter of individual grains. Treating the anisotropy self-consistently, then:

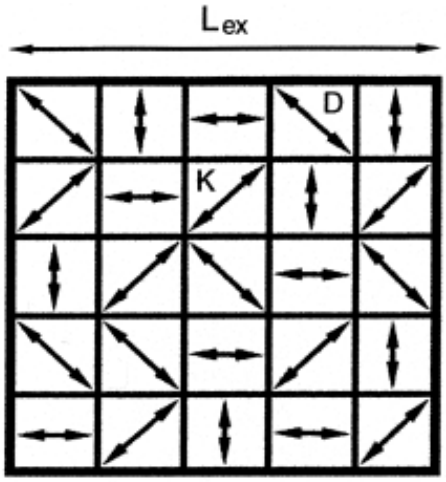

Fig. 2.4 Schematic illustration of N nanocrystalline grains of dimension ***D*** in a volume $\boldsymbol{L_{ex}}^3$ (McHenry et al, 1999a)

$$K_{eff} \sim KD^{3/2} \sim \left(K_{eff}/A\right)^{3/2} \sim \left(K^4 D^6/A^3\right) \qquad (2.5)$$

Since the coercivity can be taken as proportional to the effective anisotropy, this analysis leads to Herzer's prediction that the effective anisotropy and therefore the coercivity is a function of the 6th power of the grain size:

$$H_c \sim D^6 \qquad (2.6)$$

For such a reduction in the coercivity to be realized, Herzer noted that the nanocrystalline grains must be exchange coupled. This is to be contrasted with uncoupled particles that have an exchange length comparable to the particle diameter and are susceptible to superparamagnetic responses.

2.2.4 Fabrication methods

In principle, methods capable of producing very fine grain sized polycrystalline materials can be used to produce nanostructured material. The synthesis of nanostructured materials from atomic or molecular sources depends on the control of a variety of "nanoscale" attributes to the final product. In general, the preparation of nanostructured materials includes powder synthesis technique, deposition on

substrate and rapid solidification processing. In the current discussion, we will limit our discussion to powder synthesis technique and rapid solidification processing which will be generally discussed in the following paragraphs.

Powder synthesis technique: Nanocrystal may be synthesized as free standing powders or nanoencapsulates which must then be compacted to form a bulk alloy with nanocrystalline grains. Examples of these techniques include carbon-arc synthesis (Kratschmer et al, 1990), plasma torch synthesis (Scott et al, 1997) and gas atomization techniques (Cardoso et al, 1999). Among of these techniques, mechanical milling is commonly used as a synthesis route for nanoparticles (Koch and Whittenberger, 1996; Edelstein, 1998; McHenry et al, 1999; EI-Eskandarany, 2001), and it is a non-equilibrium processing tool to widen the composition range of easy amorphization and have high crystallization temperatures. The emphasis of this report will be on mechanical milling technique and this technique will be further discussed in section 2.2.3.1.

Rapid solidification processing: Nanocrystalline metallic alloys can also be produced by rapid solidification processing techniques (RSP). However, a subsequent controlled heat treatment after rapid solidification processing is necessary to produce the nanocrystalline structure. The types of rapid solidification processing techniques include splat quenching, melt spinning, gas atomization and condensation from the gas phase (Umakoshi et al, 2000; Tkatch et al, 2002). These typically require cooling rates of $>10^4$ K/s for typical alloys at eutectic composition. Among the most common rapid solidification processing technique is melt spinning which yields amorphous metallic ribbons typically 20 μm in thickness (McHenry et al, 1999). In this project, melt spinning will be employed and this method will be discussed in more detail in section 2.2.3.2.

2.2.4.1 Mechanical Alloying

Mechanical alloying (MA) is a solid-state powder process technique involving repeated welding, fracturing, and rewelding of powder particles in a high-energy

ball mill. Originally it was developed to produce oxide-dispersion strengthened (ODS) nickel- and iron-base superalloys for applications in the aerospace industry; however MA has now been shown to be capable of synthesizing a variety of equilibrium and non-equilibrium alloy phases starting from blended elemental or prealloyed powders. The attributes of mechanical alloying include: (1) production of fine dispersion of second phase particles, (2) extension of solid solubility limits, (3) refinement of grain size down to nanometer range, (4) development of amorphous phases, (5) disordering of ordered intermetallics and (6) possibility of alloying of difficult to alloy elements (Lai, 1998; El-Eskandarany, 2001; Suryanarayana, 2001). The entire process of mechanical alloying includes blending of the powder mixture prior to the ball milling, vacuuming and/or filling with protective gases to prevent oxidation and contamination, and the ball milling process itself.

The MA process is affected by several factors that are playing the important roles in the fabrication of homogeneous materials. The properties of the final milled powders, such as the particle size distribution, the degree of disorder, or amorphization, depend on these factors, which include: (1) type of milling media and milling tool, (2) milling atmosphere and environment, (3) ball to powder weight ration and (4) milling temperature and milling time. It was reported that when the milling intensity is increased either by increasing the weight of the ball and/or density of the ball materials or by increasing the speed of collision, more energy will be transferred to the powder particles and more energy will be dissipated in the form of heat, which is crucial for the formation of amorphous alloys (El-Eskandarany, 2001; Suryanarayana, 2001). It was also reported that when the temperature exceeds the critical temperature of crystallization, partial crystallization can occur during mechanical alloying (Suryanarayana, 2001; Zhang, 2004). Hence, high milling intensity may lead to partial crystallization of amorphous alloys.

Two requirements proposed for the solid-state amorphization reaction have been reported (El-Eskandarany, 2001; Suryanarayana, 2001; Zhang, 2004):

- The two reacting metals must have a large negative heat of mixing.
- The two metals must have vastly different diffusivities in each other and in the

amorphous alloy to be formed.

The first condition ensures that a thermodynamic driving force for the reaction exists. The second condition ensures that the amorphous alloy will form in preference to crystalline intermetallics, which have lower free energies (El-Eskandarany, 2001).

As mechanical alloying is commonly used as a synthesis route for nanoparticles, following are some examples of mechanical alloying as applied to interesting soft magnetic alloys. Investigations showed that nanostructures can be easily formed by mechanical alloying in soft magnetic Fe-Co and Fe-Ni alloys (Bruning et al, 1992; Kuhrt and Schultz, 1992, 1993; Elkalkouli et al, 1995; Kim et al, 2000). The alloying of these elemental powders depends on the intensity of milling. At low intensity, alloying is difficult; however at high intensity, alloying can be completed in about 10 h. The phases formed after alloying are affected by the compositions. In the Fe-Co system, a b.c.c phase formed when Co content is less than 80 at%, a f.c.c phase formed when Co content is 90 at% (Kuhrt and Schultz, 1992). In the Fe-Ni system, a b.c.c phase formed for 15 at% and 30 at% of Ni, a f.c.c phase formed at 80 at% of Ni and mixture of b.c.c and f.c.c phases formed at 50 at% of Ni. The average grain size reached by mechanical alloying is about 20 nm. Zhang et al (1996) have prepared $Fe_{80}Zr_8B_{11}Cu_1$ alloy powders by ball milling mixtures of Fe-Zr, Fe-B and elemental Fe and Cu powders. They monitored crystallization using XRD, electron microscopy and Mossbauer spectroscopy. Annealing temperatures of 400-900°C were employed.

However, large internal strain induced by mechanical milling is a limitation of this technique to produce materials with good soft magnetic properties, despite the formation of amorphous phase or nanocrystalline structure. One pathway to process soft magnetic materials by mechanical milling is to retain the amorphous phase or nanostructure during annealing and at the same time relieve the strain (Arrott, 1999). Stabilization of the microstructure can be achieved by suitable elemental additions. Some examples have been reported. In a mechanically alloyed multi-component $Fe_{80}Zr_8B_{11}Cu_1$ alloy, a nanosized b.c.c soft magnetic phase (about 15 nm) in an

amorphous matrix could be obtained after heat treatment (Zhang et al, 1996a), such a microstructure is predicted to have good soft magnetic properties.

In order to process soft magnetic materials, the following challenges should be overcome: large stress, contamination and inhomogeneity. To reduce stress, proper annealing conditions and alloy compositions should be selected. Contamination can be introduced by the balls and vial, thus proper materials to coat the balls and vial should be selected. Contamination can be also caused by the atmosphere since fine particles are very reactive and will react with the air or gas, selection of milling atmosphere is important.

2.2.4.2 Melt Spinning

Melt spinning (MS) is a rapid solidification process that allows for cooling rates of approximately 10^{6}°C/s and it is the main technique to produce metallic glass (Edelstein, 1998; Greer, 1998; Gleiter, 2000). Fig. 2.5 shows a schematic diagram of a melt-spinning apparatus used to produce metallic ribbons. During solidification, the liquid phase remains metastable to low temperatures due to the chosen composition and the high cooling rate. The process involves ejecting a superheated molten alloy through the orifice of the crucible onto a rapidly rotating copper wheel. This yields amorphous metallic ribbons ~20 μm in thickness and a few to several mm in width. For melt spinning, the melt temperature influences the ribbon thickness and therefore the final nanocrystal size distribution throughout the transformed ribbon after nanocrystallization (Perepesko and Pair, 1982; Host et al, 1998).

The melt spinning process may require the optimization of many parameters including: wheel speeds, orifice size, melt temperature (superheat), injection pressure of back-gas, etc., to result in amorphous and nanocrystalline alloy. Of these, the most easily controlled parameters are the wheel speed and the melt superheat (McHenry et al, 1999a).

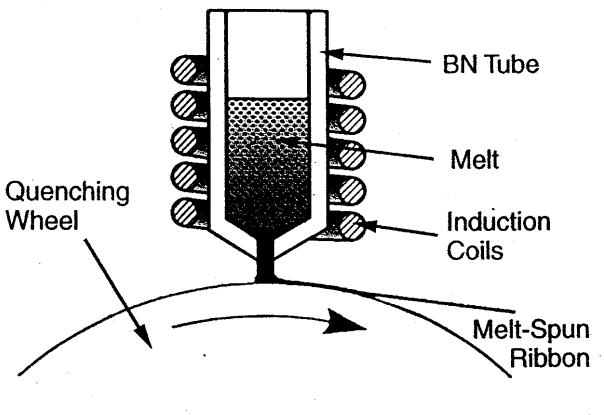

Fig. 2.5 Schematic diagram of melt-spinning apparatus (McHenry et al, 1999a).

Melt spinning can form nanostructures since grain growth can be reduced at low temperature due to the decreased diffusivity. In the conventional solidification process, the grain size is determined by a balance between the nucleation and growth rates. The grain size decreases rapidly, reaches a minimum and then increases rapidly again with increasing undercooling. However, in some alloys, due to solute segregation and trapping during rapid solidification, nanostructures can be form. Controlled crystallization from an amorphous precursor, for example, melt-spun amorphous ribbon, can also be used to produce nanocrystalline materials. In fact, this is the most common and effective method to prepare bulk nanostructured materials. The obvious advantages of the nanostructured magnetic materials are the higher magnetic induction and Curie temperatures compared to the amorphous precursors, which indicates a wider range of commercial applications (McHenry et al, 1999). In particular the recently developed HiTperm alloys have very high Curie temperature and are candidates for high temperature electromagnetic applications (McHenry et al, 2003). A few other systems and compositions are being studied to form nanostructures from amorphous precursors and thus improve the magnetic properties.

2.3 Nickel-Iron (Ni-Fe) based soft magnetic materials

2.3.1 Bulk Ni-Fe alloys

In the second decade of last century, as workers sought a magnetic material whose permeability would exceed that of iron, Fe-Ni alloys were found to have valuable magnetic properties. It was discovered that these materials had a higher specific electrical resistance than iron and that they could be readily worked, so thin strip could be made from them. In the years which followed, Fe-Ni alloys not only gave excellent service at low field strengths but had found a wide range of usefulness at medium and high intensities (Heck, 1974). In this project, attentions are focused on permalloy — nickel-iron alloys with 50-80% percent nickel which is characterized by high initial, maximum permeabilities and low coercivity.

The phase diagram of the Iron-Nickel system is given in Fig. 2.6. It can be seen that at low temperature, in the range of 65 to 90 percent Ni, the alloys form $FeNi_3$ solid solutions. This solid solution has face-centered structure. Near the $FeNi_3$ composition, the alloys can undergo long-range ordering below a temperature of 503°C (Cullity, 1972) and have an extended range of solid solubility (Massalski, 1986). It was also reported that the order-disorder transformation point of $FeNi_3$ at 506°C (Bozorth, 1978). As the magnetic properties of the disordered alloys are inferior to those of the ordered alloys, disordered alloys are more preferred. The ordered and disordered structures are shown in Fig. 2.7.

For disordered $FeNi_3$ (also called $Fe_{25}Ni_{75}$) cell belonging to the Cu type structure described by the space group $Fm\bar{3}m$, both the Fe atom and Ni atom can occupy any point of the lattice, but the atom ratio of Fe and Ni remains as 1:3. This is to say, at any point, that ratio of Fe and Ni is matched. Ordered and disordered $FeNi_3$ crystals have great difference in magnetic properties. For disordered $FeNi_3$, permeability is optimized. For ordered phase, the permeability is very small. The kinetics of this phenomenon has yet to be investigated further. In fact, there is no absolutely ordered and disordered structure. It is not possible to achieve perfect ordered phase even with a cooling rate of 1°C/h under the ordered temperature

point, so-called ordered phase is actually partially short-range ordered phase. Therefore, to obtain excellent magnetic properties of the alloy, high cooling rate process should be employed, such as quenching at the ordered temperature point or by using the melt spinning process.

As anisotropy is the main concern when choosing soft magnetic materials, the manner of Ni-Fe magnetic materials in which the anisotropy constant K_1, the saturation magnetization M_s and the Curie temperature T_c vary with composition is shown in Fig. 2.8. The anisotropy constant K_1 is seen to pass through zero at about 75 percent Ni. The magnetostriction constant λ is given in Fig. 2.9. The value of λ_{100} is zero at two compositions, near 46 and 83 percent Ni, while λ_{111} is zero at about 80 percent (Bozorth, 1978). A low value of K decreases domain-wall energy, and inclusions then become less effective hindrances to wall motion. A low value of λ means that microstress becomes less effective. Fig. 2.8 and Fig.2.9 show that both K_1 and λ_{111} are nearly zero just below 80 percent Ni and λ_{100} are not very large. At these conditions, the optimum magnetic properties can be obtained.

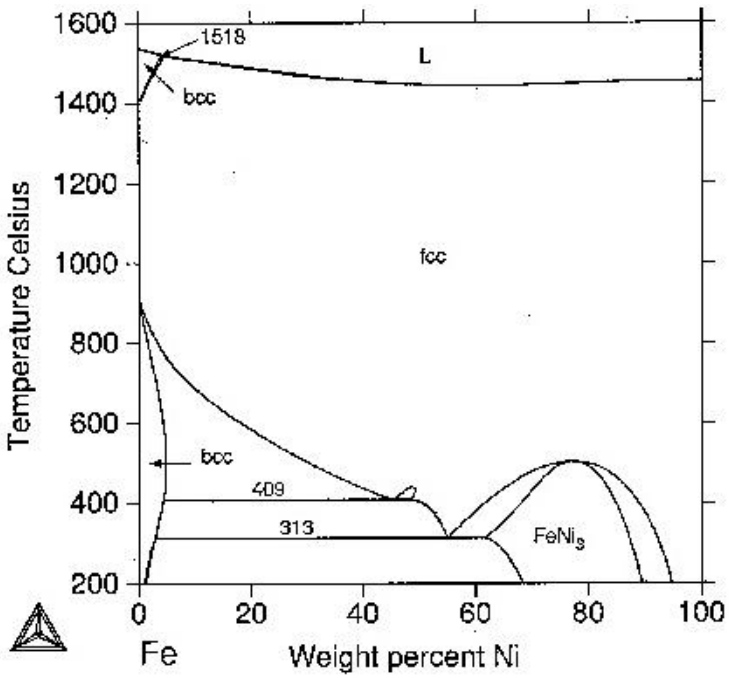

Fig. 2.6 Phase diagram of the iron-nickel system (Bozorth, 1978).

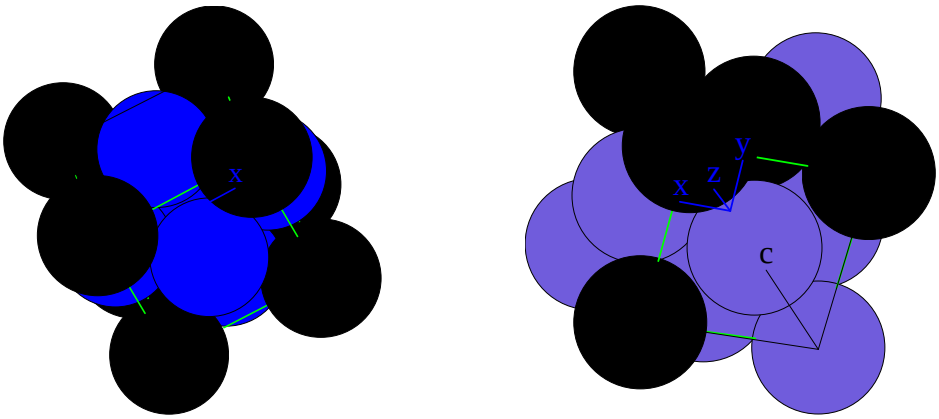

Ordered structure Disordered structure

Fig. 2.7 Ordered and disordered $FeNi_3$ crystal cell (Black balls present Fe atoms and blue balls represent Ni atoms).

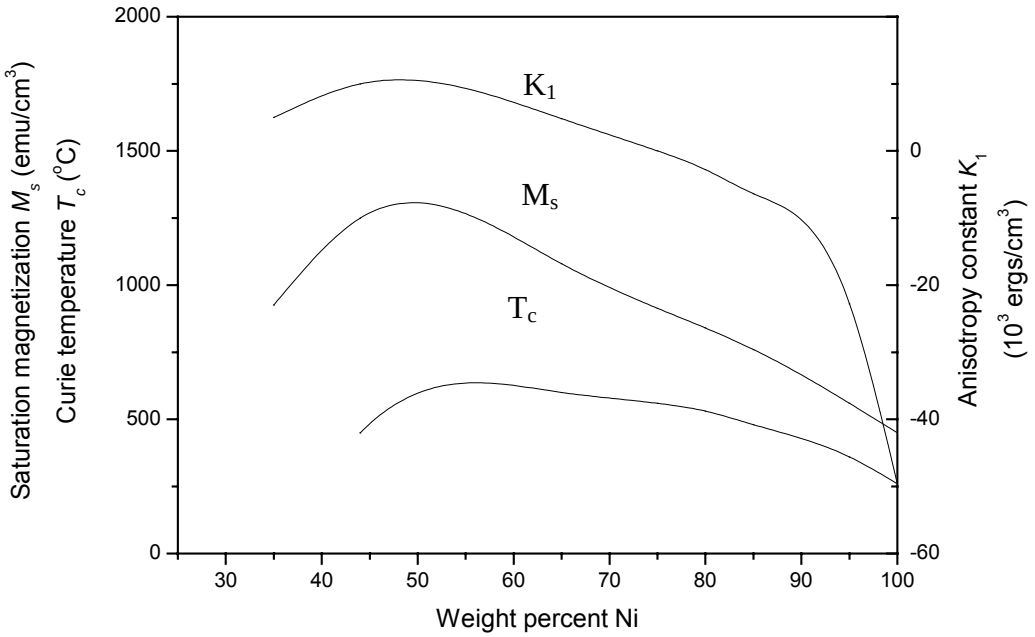

Fig. 2.8 Variation of saturation magnetization $\boldsymbol{M_s}$, Curie temperature $\boldsymbol{T_c}$ and crystal anisotropy $\boldsymbol{K_1}$ with nickel content in Fe-Ni alloy (Cullity, 1972).

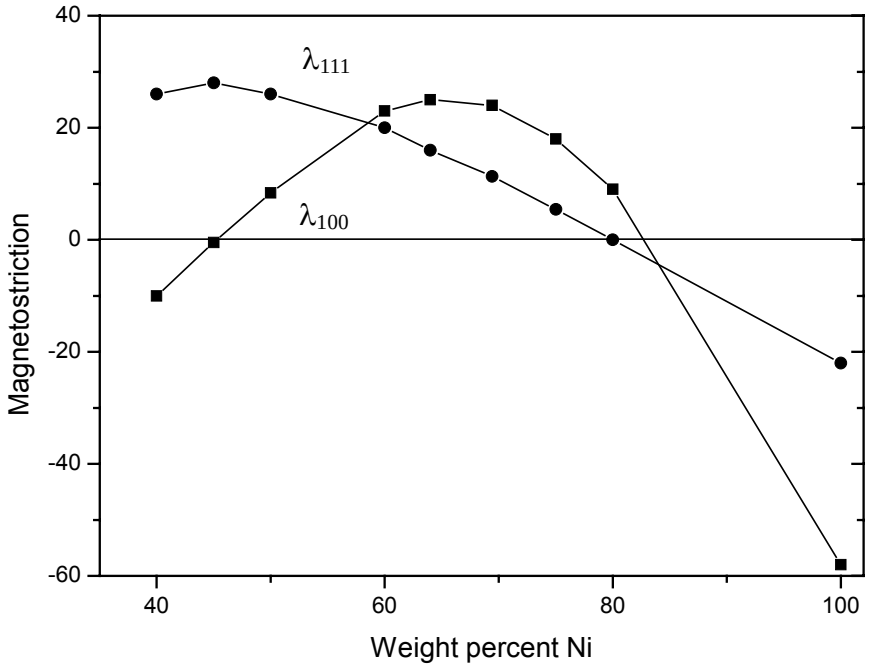

Fig. 2.9 Variation of saturation magnetostriction with nickel content in Fe-Ni alloys (Cullity, 1972)

2.3.2 Nanostructured and amorphous Ni-Fe based alloys

Most research work on nanostructured and amorphous Ni-Fe based alloys are mainly based on FeN_3 solid solution and Ni-Fe (atomic ratio nearly 1:1) multicomponent systems with metalloid elements. These research works are briefly summarized in the following paragraphs.

Nanostructured $FeNi_3$ solid solution has been studied in recent years by Frase (1997, 1998, 1999a, 1999b, 2000) and others (Fultz et al, 1995; Chinnasamy et la, 2001). $FeNi_3$ alloy was synthesized by mechanical attrition in a high-energy ball milling, and the aim was to study the effect of grain size and residual strain on the magnetic properties of the nanostructured magnetic properties. They found that the as-milled powders had high value of coercivity due to the presence of residual strain. When the residual strain was released, coercivity decreased and the relationship between coercivity and grain size was accordance with the Herzer diagram. In addition, in

order to study the local structure of grain boundary, structural relaxation and physical properties of nanocrystalline $FeNi_3$ was also studied. They found that the nanocrystalline material had the large vibration entropy and this observation was explained by the density of grain boundaries in the nanostructured materials. The increase in the grain boundary magnetic moments after low-temperature thermal treatments caused the rearrangements of atom involving a reduction in the number of atoms in highly disordered regions and a sharper density gradient between the crystalline region and the grain boundary region.

Multicomponent Ni-Fe (atomic ratio nearly 1:1) alloy system was first studied in $Fe_{40}Ni_{40}B_{20}$ alloy (Miura and Omuro, 1990; Kursumovic and Cantor, 1996). The aim was to investigate the possibility of amorphizing this alloy system by high-energy ball milling. It was found that amorphous $Fe_{40}Ni_{40}B_{20}$ powders could be produced easily by the ball milling process. Elemental B in $Fe_{40}Ni_{40}B_{20}$ alloy was also replaced by Si and P to form $Fe_{40}Ni_{40}P_xSi(B)_{20-x}$ alloy systems (Miura and Omuro, 1990; Surinach et al, 1994; Zhang and Yi, 1996; Lee et al, 1997 and 2001; Knorr et al, 1999; Pradell et al, 2000; Sui et al, 2000l; Tejedor et al, 2002). The aim was to study the possibility of amorphizing the alloys by replacing B with Si (P), the properties change after the replacement and the crystallization process of these amorphous alloys. It was found that the final crystallite size of the powders was dependent on the composition of the material as well as on the precursors utilized. The use of Fe and Ni in the alloy reduced both the energy formation of the amorphous phase and the time necessary to produce this phase. The incorporation of Si into the Ni-Fe based alloy favored the formation of a more stable amorphous phase. From the analysis of the crystallization products, it was found that Ni-rich silicides and Fe (Si) bcc phases were formed in the early stages and Fe-rich phosphides and ferromagnetic Fe (Ni) fcc phases were formed at higher temperature.

Commercial $Fe_{40}Ni_{38}Mo_4B_{18}$ alloy named METGLAS 2825MB was also studied in recent years (Ok and Morrish, 1981; Chan and Chiang, 1997; Li et al, 1999; Nunes et al, 2002). The study on this type material was mainly focused on the crystallization stages and microstructure changes after crystallization. The presence of Mo in this type of alloy was reported to prevent grain growth and play a crucial

role in the nanostructure formation process. Depending on the annealing temperature, the nanostructured $Fe_{40}Ni_{38}Mo_4B_{18}$ specimens with different microstructure can be produced by annealing the amorphous alloy. In general, $(Fe, Ni, Mo)_{23}B_6$ crystallites were formed at low annealing temperatures, and high annealing temperatures caused the formation of the magnetic phase.

The main focus of Ni-Fe alloys are nearly based on equal atomic percentage of Ni and Fe elements. Although nanostructured $FeNi_3$ solid solution has been studied by MA (Frase et al, 1997, 1998, 1999a, 1999b, 2000), more research work need to be done on this solid solution with the addition of other elements in order to form amorphous and nanocrystalline materials. In addition in order to get optimal magnetic properties and fine microstructure materials, an amorphous phase may be required to act as an exchange coupling medium. This is because from the previous research on FINEMET, NANOPERM, HITPERM and Fe-Co alloys, it was found that these alloys were generally two phase materials with a nanocrystalline ferromagnetic phase and a residual amorphous phase at the grain boundaries (McHenry et al, 1999a; McHenry and Laughlin, 2000). Some general properties can be observed in these alloys, such as (1) relatively high resistivity (2) low magnetocrystalline anisotropy (3) increased mechanical strength. With properties such as these, nanocrystalline alloys have great potential as soft magnetic materials.

In order to obtain the amorphous phase, elements such as Boron and Phosphorous are added to the Ni-Fe based alloys. These elements are metalloids and they are added to a pure metal to ensure that significant diffusive rearrangement occur during crystallization of the glass phase, i.e. to stabilize the glass, especially these elements are of different size and chemical character from the host atoms (Luborsky, 1983). As mentioned earlier, the effect of elemental Boron, Phosphorous and Silicon in Ni-Fe based alloys on the microstructure change have been studied (Surinach et al, 1994; Sunol et al, 2001). However, more research on the amorphous phase need to be done, especially for Ni content of more than 60%, and not just Ni-Fe alloys of nearly 1:1 atomic ratio.

2.3.3 Addition of Molybdenum in Ni-Fe alloys

In the bulk form, Molybdenum is added to Ni-Fe alloy system for two main reasons: (1) to increase the electrical resistivity and thus decrease the eddy-current losses; (2) to increase the initial permeability and to simplify the heat treatment necessary to obtain high initial permeability (Heck, 1974; Bozorth, 1978; McCurrie, 1994).

Fig. 2.10 shows the effect of Mo content on intrinsic magnetization at room temperature. As expected, intrinsic magnetization decreases uniformly with Mo content, and approaches zero at about 15% Mo. Fig. 2.11 shows the effect of Mo content on the maximum permeability of Fe-Ni-Mo alloys which undego two standard treatments, namely double treatment and furnace cooled. Double treatment involves heating and cooling as before reheating to 600°C, and cooling in open air by placing it on a copper plate. While furnace cooled involves heating to 900-950°C, maintaining at that temperature for about one hour, and cooling at the maximum rate of 100°C per hour. It can be seen that as the Mo content increases, the maximum permeability of 78%Ni-x%Fe-(22-x)%Mo (x=10~22) alloy system decreases rapidly for double treatment. However, for furnace cooled samples, maximum permeability occurs at about 3.8% Mo content. It can be concluded from these two figures that, the addition of Mo in Fe-Ni alloy systems can cause the decrease in magnetization and maximum permeability. With the decrease in the maximum permeability, the heat treatment necessary to obtain high permeability is simplified.

The effect of Mo atoms to magnetic properties can be also explained from the electron consideration (Wakelin and Yates, 1953). The increase in the magnetic moment per atom on ordering is indicative of an increase in the number of vacancies in the 3d shells, and thus possibly an increase in the number of free electrons available for conduction. Ferromagnetism is due to an excess number of electrons spins in a given direction in the 3d shell. There are a number of vacant sites or “positive holes” in this shell. These vacancies have been identified with the saturation magnetic moment in Bohr magnetons, 0.6 per atom for nickel and 2.2 per atoms for iron. It is found that the “spare” electrons of the added elements enter the

3d shell of the nickel atoms only which play the major role at this condition, the contribution of the iron atoms to the total magnetic moment being unaltered only a simple dilution effect. As the decrease of vacancies in 3d shells, permeability will decrease then.

In recent years, effects of Mo content and baking temperature on permeability of Ni-Mo-Cu-Fe and Ni-Mo-Fe permalloys in the tape form had been studied by Li and Masteller (1997). They found that the primary function of Mo was to retard the ordering process therefore the optimum ordering parameter would be easier to achieve. It was also found that when the Ni content was fixed, the higher Mo gain resulted in the lower optimum baking temperature. By adjusting Mo and/or Ni contents, the peak maximum permeability at the desired baking temperature could be obtained. Inoue and Gook (1995) have investigated the effects of Mo substitutions in $Fe_{72-x}Al_5Ga_2P_{11}C_6B_4M_x$ (M=Mo, x=5) bulk amorphous alloys. This substitution was found to extend the supercooled liquid region, ΔT_x. ΔT_x was determined to be 60 K for the parent alloy and 62 k for M=Mo.

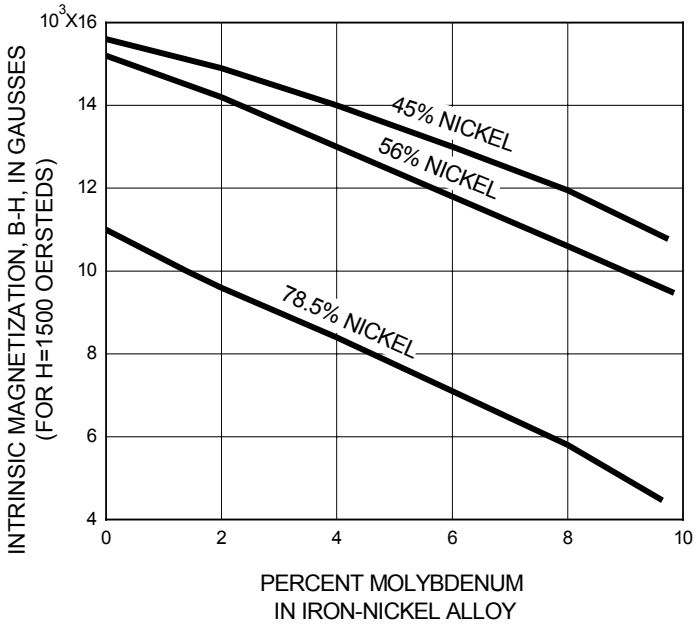

Fig. 2.10 Dependence of intrinsic magnetization on molybdenum content (Bozorth, 1978).

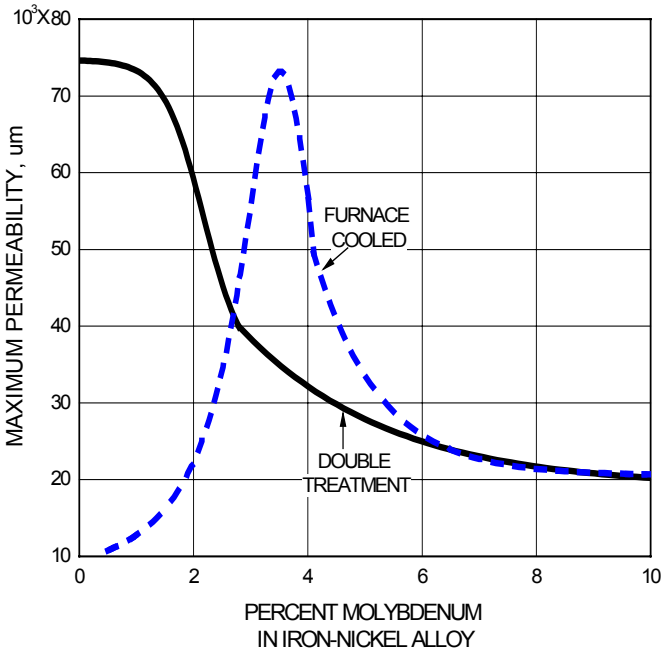

Fig. 2.11 Maximum permeability of Fe-Ni-Mo alloys with the two standard treatments (Nickel content about 78%) (Bozorth, 1978).

The effects of Mo in nanostructured samples have also been studied in recent years. Li et al (1999) studied the effects of Mo for the crystallization of the amorphous $Fe_{40}Ni_{38}Mo_4B_{18}$ ribbon. In the presence of Mo element, they studied the amorphous ribbon in an attempt to understand the details of the complex crystallization process leading to the formation of new fcc-structure based soft magnetic nanostructured systems. The presence of Mo in the precursor alloy was found to prevent grain growth and play the crucial role in the nanostructure formation process. The effects of Zr and Mo additions on the crystallization process, structure, and magnetic properties of (NdPr)-Fe-B amorphous ribbons were later studied by Wang and Davies (2003). Their results indicated that the addition of Zr or Mo did not change the phase composition of the ribbons after crystallization but significantly improved the thermal stability of the amorphous phase. They explained the observation as that the decrease of atomic diffusivity on substituting Zr or Mo for Fe led to higher transformation temperature. They also found that the lower values of activation energy of crystallization at small x for the Zr and Mo containing amorphous alloys promoted higher rates of crystal nucleation, while the subsequent increase in

activation energy for both alloys was helpful in impeding the growth of the crystals. Consequently, these factors contributed to the formation of a finer grained and probably more homogeneous structure in the Zr- or Mo- containing alloys than in the Zr- and Mo-free alloy.

2.4 Summary

Nickel-Iron alloys are traditional soft magnetic materials. They have low coercivity, high permeability and low energy loss so that they can be used in various fields, for making audio coils, transformers, magnetic shields etc. Before 1990s, research is focused on bulk materials. In recent years, attentions are changed to nanostructured and amorphous materials because of the chemical and structural variations on a nanoscale which are important for developing optimal magnetic properties.

From the literature review, most work on nanostructured magnetic materials are focused on Fe-based, Fe-Ni based and Co-based alloys. Ni-based alloy has not been investigated. In this project, Ni-15%Fe-5%Mo alloy was chosen since in the bulk system, this alloy composition exhibits good magnetic properties such as low coercivity and high permeability. The reason to add Mo atoms is because they can promote the formation of nanocrystalline structure. The main aim of this project is to study the processing and properties relationship for this alloy system by two nano-processing techniques, namely high energy ball milling and melt spinning.

As discussed in section 2.2.2, nanocrystalline alloys produced by partial crystallization of the amorphous precursors exhibit a multiphase structure with nanograins dispersed into the residual amorphous matrix. In order to produce an amorphous phase, Boron will also be added to the alloy system. This element is metalloids and is often added to alloys to cause significant diffusive rearrangement to occur during crystallization of the glass phase. A detailed study of the crystallization phases from an amorphous phase will also be included in this project.

Chapter 3 Experimental Methods

3.1 Introduction

Details of sample preparation, experimental conditions, techniques used for analyses, specimen preparation for the respective techniques and methods of data evaluations are outlined in this chapter.

3.2 Sample Preparation

In this study, two compositions of Ni-based magnetic materials were chosen. They are Ni-15%Fe-5%Mo and Ni-15%Fe-5%Mo-5%B. High purity powders starting materials were used to prepare the samples. The powders were obtained from Alfa Aesar of purity as indicated in wt %: Ni (>99%), Fe (>99%), Mo (>99%) and B (>99%). Two processing techniques were employed to prepare the samples. Mechanical alloying by high energy ball milling (HEBM) was used to prepare Ni-15%Fe-5%Mo and Ni-15%Fe-5%Mo-5%B alloys. Melt spinning (MS) were used to prepare Ni-15%Fe-5%Mo-5%B sample. The details of the sample preparation for each alloy system are described in the respective chapters.

In order to study the crystallization process of the as-prepared alloys, the samples were also subjected to a series of heat treatment process. The heat treatment was carried out in vacuum furnace with a vacuum of about 1×10^{-5} Torr and temperature fluctuation ±3°C. Different holding times and temperatures were selected. A heating rate of 10°C/min was used and the samples were furnace cooled.

3.3 Characterization Techniques

The samples were subjected to various kinds of analysis and characterization techniques. The characterization techniques and the corresponding specimen preparation methods are summarized in the following sections.

3.3.1 X-ray Diffraction (XRD)

X-ray diffraction (XRD-6000, Shimadzu) using CuK_α radiation (λ = 0.15405 nm) was used to characterize the phases present in the samples. The parameters set for the XRD equipment were listed in Table 3.1:

Table 3.1 XRD parameters.

X-ray target	CuK_α
X-ray tube voltage and current	50 kV and 20mA
Scan range (2θ)	30~100 degree
Scan speed	4 degree/min

3.3.2 Scanning Electron Microscopy (SEM)

The as-milled and annealed powders were examined directly using SEM equipped with energy dispersive X-ray (EDX) analysis facilities (JSM-5410) at 20 kV. For cross section observation, the powders were mixed with epoxy, and then hot mounted, grinded, polished and etched before SEM observation.

3.3.3 Transmission Electron Microscopy (TEM)

For TEM characterization, the as-milled powders prepared by HEBM were immersed into alcohol and dispersed using ultrasonic vibrator for about 30 min. Holey carbon grids were then used to hold the dispersed powders. Although this method is simple, it is difficult to find a thin area. For the annealed powders, different sample preparation technique was used. The annealed powders were first

mixed with epoxy and then inserted in a copper tube. After heating for about 15 min, a 1 mm thick sample was cut from the copper tube. After grinding, polishing and dimpling, the sample was finally thinned using ion milling. For the ribbon samples prepared by MS, 3 mm diameter disk was punched from the ribbon. After that, TEM samples were prepared using an Ar ion milling equipped with liquid-nitrogen cooled cold stage to ensure minimal heating of the sample during milling.

The main study of microstructure was through the use of TEM, using various modes of analysis. In conventional TEM, these were mainly bright field (BF), dark field (DF), selected area diffraction patterns (SADP), energy dispersive X-ray analysis (EDX). These were performed on a JEOL 2010 at 200 kV having an ultra-thin BE window for EDX.

3.3.4 Differential Scanning Calorimetry (DSC)

DSC (NETZCH 404C) with temperature accuracy of ±1°C in vacuum was used to study the crystallization behavior of the powders and ribbons. These measurements during the heating process were performed from 200°C to 800°C using heating rates of 5°C /min, 10°C /min, 20°C/min, 30°C/min and 40°C/min.

3.3.5 Vibrating Sample Magnetometer (VSM)

Magnetic properties characterization in this project was performed using a Lake Shore Vibrating Sample Magnetometer (VSM 736). During the experiment, the magnetic field was increased from zero to 10 kOe, and then cycled to negative and positive values at room temperature. The properties obtained from the experiment were coercivity $\boldsymbol{H_c}$ (Oe) and saturation magnetization $\boldsymbol{M_s}$ (emu/g). Saturation magnetization, $\boldsymbol{M_s}$, was taken as the measured values at the highest magnetic field.

3.4 Powder Analysis

3.4.1 Powder size determination

For the powder size determination, the powders were directly observed by measuring the diameter from representative SEM micrographs. The size of more than 200 powders was measured using AIS image analysis software.

3.4.2 Determination of Grain Size and Residual Strain

Nanocrystalline size and residual strain of the mechanical alloyed samples were determined from the XRD data. Williamson-Hall method (Gayle and Biancaniello, 1996; Klug and Alexander, 1974; Ungar and Borbely, 1996) was used and described as follows:

Each X-ray diffraction line profile obtained in a diffractometer is broadened due to instrumental and physical factors including crystallite size and lattice strain. Therefore, the first indispensable step preparatory to the calculation of crystallite size and lattice strain from the recorded XRD scan is to determine the pure diffraction line profile for a given reflection whose breadth depends solely on the physical factors. This line profile is extracted by removing the instrumental broadening factor from the experimental line profile. Only then the pure line profile can be used for calculating the crystallite size and lattice strain. Simple equations or graphs based on line profiles of assumed analytical forms can be used for the instrumental broadening correction. In the present work, the instrumental broadening corrected pure line profile breadth of each reflection was calculated from the parabolic approximation correction:

$$\delta(2\theta) = B\left(1 - \frac{b^2}{B^2}\right) \text{ (rad)} \qquad (3.1)$$

where ***B*** and ***b*** are the breadths (in radians) of the same Bragg peak from the XRD scans of the experimental and reference powder, respectively. The reference powder

is the same powder of $FeNi_3$ annealed at 700°C for 1 h. Both ***B*** and ***b*** are calculated by the computer software Origin as the full-widths at half maximum (FWHM) after automatic background removal and K_α stripping.

The method is based on the assumption that the crystallite size and strain line profiles are both presumed to be Cauchy and the appropriate equation for the separation of crystallite size and strain takes the following form (Klug and Alexander, 1974; Ungar and Borbely, 1996):

$$\delta(2\theta)\cos\theta_0 = \frac{0.9\lambda}{L} + 4e\sin\theta_0 \qquad (3.2)$$

where θ_0 is the position of the analyzed peak maximum, λ is the X-ray wavelength, ***L*** is the crystallite size and ***e*** is the maximum strain. Any available orders of a given reflection may be used to construct a linear plot of $\sin\theta_0$ against $\delta(2\theta)\cos\theta_0$. From this plot, the crystallite size ***L*** can be obtained from the intercept and the strain ***e*** from the slope.

3.5 Determination of Activation Energy

To determine the reaction mechanism, the values of the degree of transformation have been introduced into the reaction equation. There are several types of reaction models based on different consideration. Among them, Wilhelmy model is often used (Lai, 1998):

$$k = k_0 \exp\left(-\frac{Q^*}{RT}\right) \qquad (3.3)$$

where k_0, in s^{-1}, is frequency factor or rate constant at infinite temperature, Q^* active energy in J mol^{-1}, ***R*** gas constant and ***T*** temperature of the reaction in K.

Activation energy Q^*, may be calculated using measurements from differential scanning, calorimeter or differential thermal analysis. Based on Kissinger equation,

the calculation procedures using a suitable thermal instrument may be carried out as follows:

Thermal analysis using a DSC or DTA was done on the milled powders and ribbons using a minimum of four different heating rates. The heating rates were selected from 1 to 40°C/min. The peak temperatures of the transition of the powders were measured. A plot of $-\ln(T/T_p^{\,2})$ versus $1000/T_p$, where $\boldsymbol{T}$ is the heating rate and $\boldsymbol{T_p}$, the peak temperature was obtained, $\boldsymbol{Q}^*$ was then determined from the slope of the linear straight line.

3.6 Analysis of data obtained from VSM

Vibrating Sample Magnetometer (VSM) measures the magnetic properties of materials. When a material is placed within a uniform magnetic field and is justified to sinusoidal motion (i.e. mechanically vibrated), there is some magnetic flux change. This induces a voltage in the pick-up coils, which is proportional to the magnetic moment of the sample.

The magnetization, $\boldsymbol{M}$, is determined by dividing the sample moment, $\boldsymbol{m}$, by the sample volume, $\boldsymbol{V}$:

$$M\left(Am^{-1}\right) = m\left(emu = Am^{-1} \times m^3\right) / V(m^3) \qquad (3.4)$$

However, the volume cannot be obtained for these samples; thus, an alternative method is used which make use of the magnetic moment per kilogram $\boldsymbol{\sigma}$. Magnetic moment per kilogram, $\boldsymbol{\sigma}$, is determined by dividing the moment, $\boldsymbol{m}$, by the sample mass:

$$\sigma\left(Am^{-1} \times m^3/kg\right) = m\left(Am^{-1} \times m^3\right) / mass(kg) \qquad (3.5)$$

The two quantities M and $\boldsymbol{\sigma}$ are related by the sample density, ρ:

$$M\left(Am^{-1}\right)=\sigma\left(Am^{-1}\times m^{3}/kg\right)*\rho\left(kg/m^{3}\right) \qquad (3.6)$$

Thus, the saturation magnetization, M_s, can be obtained by multiplying the saturation magnetic moment with density. The saturation magnetic induction, $\boldsymbol{B_s}$, is obtained by using the following equation:

$$B(T)=\mu_0(H(Am^{-1})+M(Am^{-1})) \qquad (3.7)$$

where $\boldsymbol{B}$ is the magnetic induction, $\boldsymbol{H}$ is the magnetic field and $\boldsymbol{M}$ is the magnetization.

Since $H << M$ at $M = M_s$

$$B_s(T)=\mu_0 M_s\left(Am^{-1}\right) \qquad (3.8)$$

Coercivity $\boldsymbol{H_c}$ is taken when the magnetization is equal to zero. Thus, the saturation magnetization $\boldsymbol{M_s}$, saturation induction $\boldsymbol{B_s}$ and coercivity $\boldsymbol{H_c}$ can be obtained from VSM.

Chapter 4 Mechanically Alloyed Ni-Fe-Mo Magnetic powders

4.1 Introduction

Synthesis of intermetallic and other compounds by mechanical alloying (MA) of elemental blends has been the subject of interest (Koch and Whittenberger, 1996; Lai, 1998; Murty and Ranganathan, 1998; Suryanarayana, 2001). Most of the studies reported the formation of one or more compounds in the nanocrystalline form. The resulting materials exhibited improved mechanical and chemical properties due to the large fraction of grain boundaries in comparison to materials with conventional grain size (Frase et al, 1999a; Jiang et al, 2001).

In recent years, extensive studies have been carried out towards the development of soft magnetic materials for various applications (Arrott, 2000; Coey, 2001a, 2001b). Most of the attention has been focused on Fe-based and Fe-Co based materials (McHenry et al, 1999a, 1999b, 2003; Willard et al, 1999). Very little attention has been focused on Ni-based soft magnetic materials. Ni-based soft magnetic materials containing around 75-82 wt% Ni, known as Permalloys, have higher permeability and lower coercivity, and are widely used in electrical and electronic industries for the making of audio coils, transformers and magnetic shields. Most of the work on Ni-based soft magnetic materials found in the literature is on bulk materials, and very little has been focused on the nanoscale. Hence, in this chapter, the main objective is to study the nanostructured Ni-Fe-Mo magnetic powders using high energy ball milling (HEBM).

High energy ball milling is a mechanical alloying technology, and has been successfully used to obtain nanocrystalline materials. In general, there are three mechanical stages during the milling process: the early stage, the intermediate stage and the completion stage (Lai, 1998). The transformation kinetics of ball milling has been the target of investigation for some researchers, and John-Mehl-Avrami (JMA) method is often used to study the kinetics of phase transformation (Jiang et al, 1996; Grandi et al, 1999; De Lima et al, 2000; Liu and Chang, 2002a, 2002b). Hence, JMA equation will be used in this work to study the kinetics of nucleation and growth of a second phase from an initial parent phase during the milling process.

Therefore, in order to have a better understanding of the Ni-Fe-Mo nanostructured soft magnetic materials prepared by HEBM, this chapter will be divided into three parts. First, the formation kinetics of Mo atoms substituted into the pre-alloyed $FeNi_3$ powders will be studied and this will be presented in Section 4.3.2. Secondly, the mechanical stages during the ball milling process will be discussed in Section 4.3.3. Lastly, the effects of milling time on the magnetic properties will be covered in Section 4.3.4. This chapter will end with some concluding remarks.

4.2 Sample Preparation

The pre-alloyed intermetallic $FeNi_3$ was initially prepared using a planetary mill (Fritsch, Pulverisette 5) for 10 h at 300 rpm at room temperature. The starting powders were a mixture of Ni (purity>99%, mesh size≤150 μm) and Fe powders (purity>99%, mesh size≤10 μm) with a weight ratio of 16: 3. 19g of the starting powder mixture and 50 tungsten carbon (WC) balls of diameter 10 mm were loaded into a 250 ml WC container inside a glove bag that was evacuated first and then back-filled with purified argon. The ball to powder charge ratio was maintained at 20:1. The milling program was set to pause for 3 min for every 5 min of milling to prevent excessive heating during the milling process. Prior to milling, ~0.2 wt% of ethanol was added to the powders as a processing control agent to inhibit cold welding process. An O-ring was fitted between the container and the cover to prevent any possible ingress of oxygen into the container from the surrounding

atmosphere. In order to minimize oxidation, the "entire operation" was performed in a dried argon atmosphere. Fig. 4.1 shows the XRPD patterns of the Ni-Fe powders before and after 10 h of milling. The three diffraction peaks corresponding to Ni were found to slightly shift to the left after 10 h of milling. This indicated the formation of the $FeNi_3$ phase, which has the same face-centered cubic crystal structure as Ni, but with a slightly larger lattice parameter.

The as-milled Ni-Fe powders were then annealed at 700°C for 1 h under vacuum to release the micro-strain and other defects. Mo powders (purity>99%, mesh size≤10 μm) were then added to the annealed Ni-Fe powders to prepare the Ni-15%Fe-5%Mo powders. These powders were milled again in the planetary ball mill for different milling time varying from 1 h to 100 h. The ball to powder charge ratio and the milling environment were the same as described above.

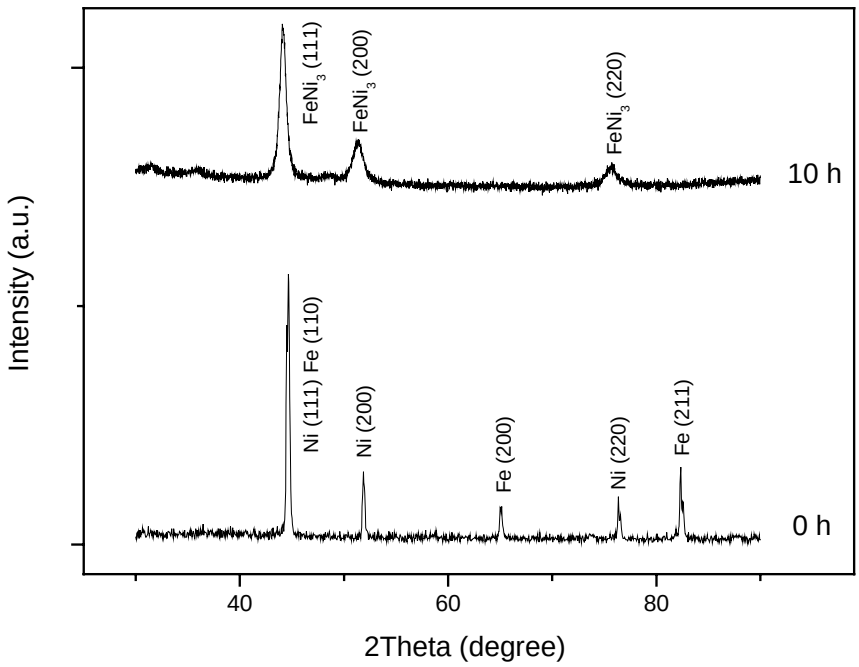

Fig. 4.1 XRPD patterns of Ni-Fe powders before and after 10 h of milling.

4.3 Results and Discussion

4.3.1 XRPD results

XRPD patterns of Ni-15%Fe-5%Mo powders milled for different durations varying from 0 h to 100 h are presented in Fig. 4.2. XRPD pattern of the powder mixture before milling shows the peaks corresponding to the phases of $FeNi_3$ and Mo only. As milling time increased, the intensity of all the peaks decreased and the peaks became broader indicating the decrease in grain size and increase in residual strain. It was also found that as the milling time increased, the intensity of the diffraction peaks corresponding to the elemental Mo decreased gradually and after 20 h of milling, they disappeared. This observation indicates that most of the Mo had dissolved into the $FeNi_3$ phase after 20 h of milling.

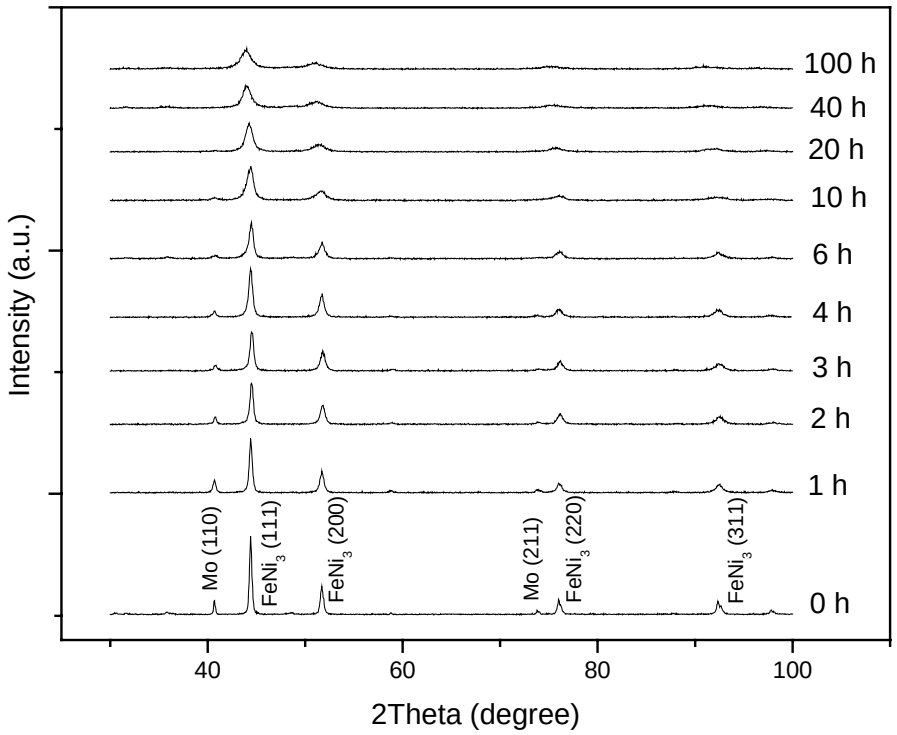

Fig. 4.2 XRPD patterns of Ni-15%Fe-5%Mo powders milled for different times from 1 h to 100 h.

Using the XRPD data, the Williamson-Hall method (refer to section 3.4.2) was used to determine the grain size and the residual strain of the milled sample. The instrumental broadening was first determined from the annealed Ni-Fe powders. The grain size and residual strain of Ni-15%Fe-5%Mo powders that were milled for different hours were then determined using Equation 3.2. The results are summarized in Table 4.1 and graphically presented in Fig. 4.3 and Fig. 4.4. The grain size was found to decrease rapidly at the beginning of the milling and remained constant at about 15 nm for 10 h to 40 h of milling. Further milling caused the grain size to decrease further to about 8 nm. The decrease of grain size during the milling process is the common observation and it has been reported by other researches (Pan et al, 1994; Surinach et al, 1994; Chen et al, 1999; Chiriac et al, 2001; Liu and Chang, 2002a). The rapid decrease of grain size during the initial milling process and the slight decrease of grain size in the late stage have also been reported. The possible reason for this observation was explained that the small crystal size itself provided a limit for the glide of dislocations (Surinach et al, 1994).

The residual strain of the milled powders shows a different trend. The strain was found to remain more or less constant with increasing milling time up to 4 h, and then increased significantly with increasing milling time. A maximum residual strain was reached after milling for 10 h. Further milling up to 100 h caused the strain to decrease gradually.

The increase in residual strain with milling time during the early stage of ball milling caused by the increased plastic deformation produced by ball milling process has been reported by many researchers (Eckert et al, 1993; Surinach et al, 1994; Chen et al, 1999; Chiriac et al, 2001; Liu and Chang, 2002a). In addition, it was also found that the increase of grain boundary due to the decrease of grain size also contributed to the residual strain observed in the ball milled powders (Frase et al, 1999b; Chen et al, 1999; Liu and Chang, 2002a). The slight decrease in residual strain for longer milling hours was reported (Chen et al, 1999; Liu and Chang, 2002a). The reason for this observation was reported as the decrease in mechanical deformation caused by crystal disintegration.

According to these researches, it could be concluded that in general, the increase in lattice strain during ball milling can be due to the following 3 factors: (1) the size mismatch between the constituents, (2) the increasing grain boundary fraction due to the decrease in grain size and (3) the increasing mechanical deformation in the powders from the macrostructure view. In the current experiment, although the size mismatch between Mo and Ni is about 8.8 %, the percentage of Mo atom in the powders is only 5 wt%. Hence, this type of lattice strain contribution to the measured strain values is likely to be small. From our experiment, the increase in residual strain should be contributed to the increase of grain boundary and mechanical deformation during the initial ball milling process. And the slight decrease after 10 h of milling was attributed to mechanical deformation caused by crystal disintegration.

The lattice parameters of Ni-15%Fe-5%Mo powders were also calculated from the XRPD data as a function of milling time and presented as a plot in Fig. 4.5. During the first 10 h of milling, the lattice parameter was found to remain nearly constant. A significant increase, from ~ 0.3547 nm to ~0.3567 nm, was observed when milling time increased from 10 h to 20 h. The lattice parameter increased further to 0.3580 nm after 40 h of milling, and remained nearly constant with further milling.

Table 4.1 Average grain size and residual strain of Ni-15%Fe-5%Mo powders after different milling time.

Milling time (hours)	Average grain size (nm)	Residual strain (%)
1	100	0.112
2	68	0.206
3	40	0.329
4	37	0.425
6	22	0.711
10	15	0.971
20	12	0.803
40	10	0.711
100	7	0.628

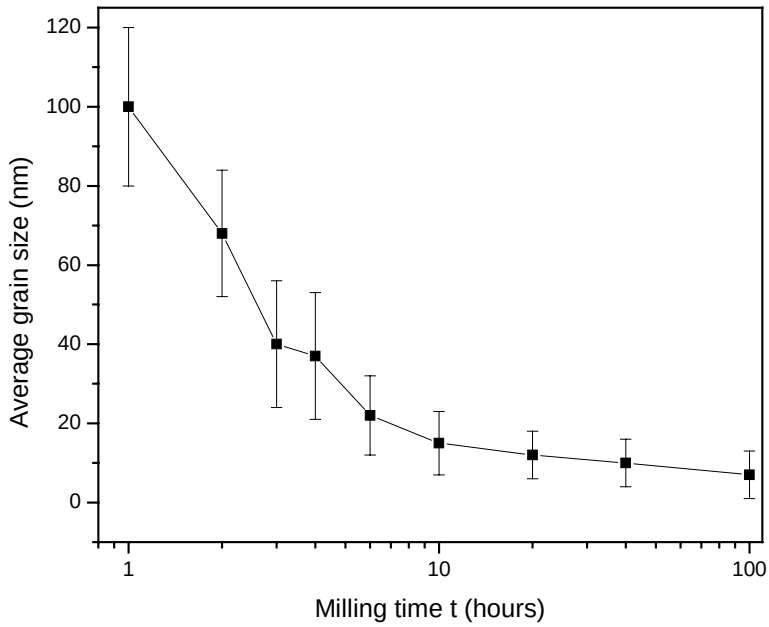

Fig. 4.3 Variation of average grain size of Ni-15%Fe-5%Mo powders as a function of milling time.

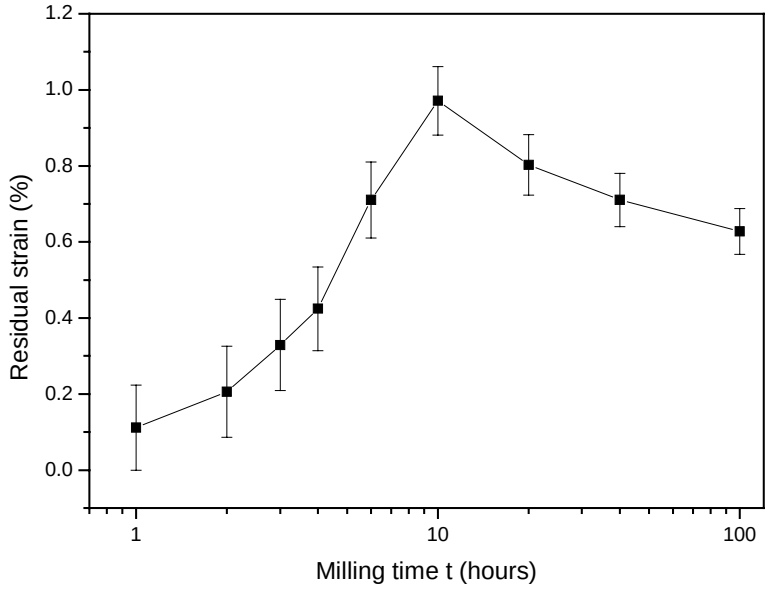

Fig. 4.4 Variation of average residual strain of Ni-15%Fe-5%Mo powders as a function of milling time.

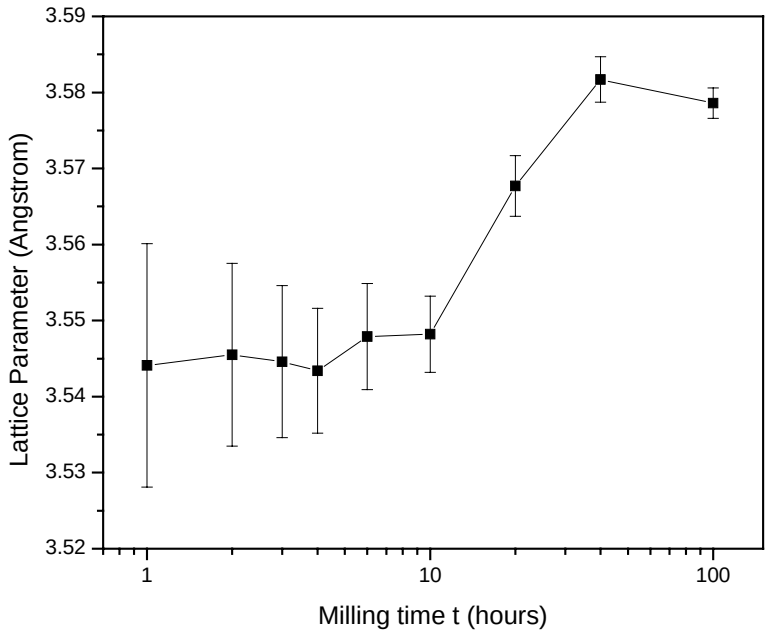

Fig. 4.5 Lattice parameter of Ni-15%Fe-5%Mo powders as a function of milling time.

The nearly constant lattice parameter during the first 10 h of milling shows that during this stage of milling, the effect of ball milling was nearly to change the powder particle morphology and to refine the particle size. During this stage, the substitution process between Mo and Fe, Ni atom is very low. This is reasonable, because milling of less than 10 h involves only the mixing of the Mo and $FeNi_3$ powders. The increase in lattice parameter after 10 h of milling indicates that alloying took place mainly from 10 h of milling to 40 h of milling, and a steady state was reached after 40 h of milling as observed in Fig. 4.5. Such observation could be explained by considering the atomic radii of Fe, Ni and Mo atoms which are 0.124 nm, 0.125 nm and 0.136 nm respectively (Callister, 2003). When the Mo atoms substitute for Ni or Fe atoms in the $FeNi_3$ crystal structure, the lattice parameter will increase. The change in lattice parameter during the milling process suggested that the dissolution of Mo into the $FeNi_3$ structure was completed within 40 h of milling.

4.3.2 Microstructure observation

4.3.2.1 SEM observations

Fig. 4.6 shows the morphologies of the elemental Fe and Ni powders before ball milling. The powder size of elemental Ni before milling was about 20-50 μm and the surface was rough. The average powder size of elemental Fe was less than 5 μm and the surface was smoother compared to the Ni powder. The morphologies of the pre-alloyed $FeNi_3$ powders after annealing and elemental Mo powders are also shown in Fig. 4.7. The pre-alloyed $FeNi_3$ was agglomerated. The powder surface was smoother compared to the elemental Fe and Ni powders and the powders were of uniform size of about 15 μm. The average size of the elemental Mo powders was less than 3 μm.

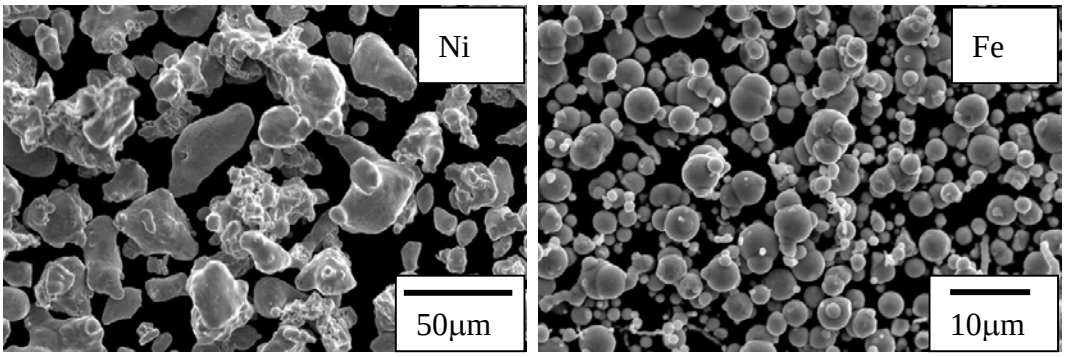

Fig. 4.6 Morphology of the elemental Ni and Fe powders before ball milling.

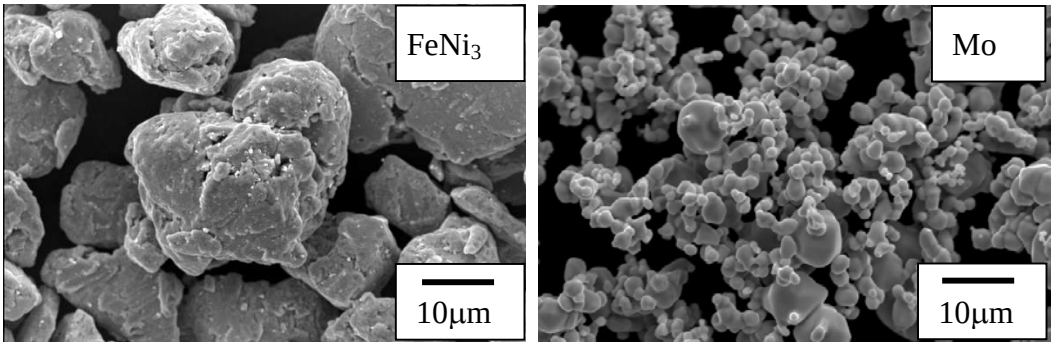

Fig. 4.7 Morphology of the annealed $FeNi_3$ and elemental Mo powders.

The morphology of the milled Ni-15%Fe-5%Mo powders produced at different milling times was investigated via SEM analysis. In general, there are three stages during mechanical alloying, which are the early stage, the intermediate stage and

the completion stage (Lai, 1998). Due to the softness of the powders in the early stage, it was very easy for them to become flat and to form layered structure consisting of various combinations of the starting constituents. Micro-forging led to changes in the shapes of individual particles, or cluster of particles being impacted repeatedly by the milling balls with high kinetic energy. Powders of ductile materials could easily be plastic deformed under compressive loading, and hence they became flattened into thin flakes. The characteristic of the powders in this stage was platelike particles as shown in Fig. 4.8 for 1 h to 6 h of milling.

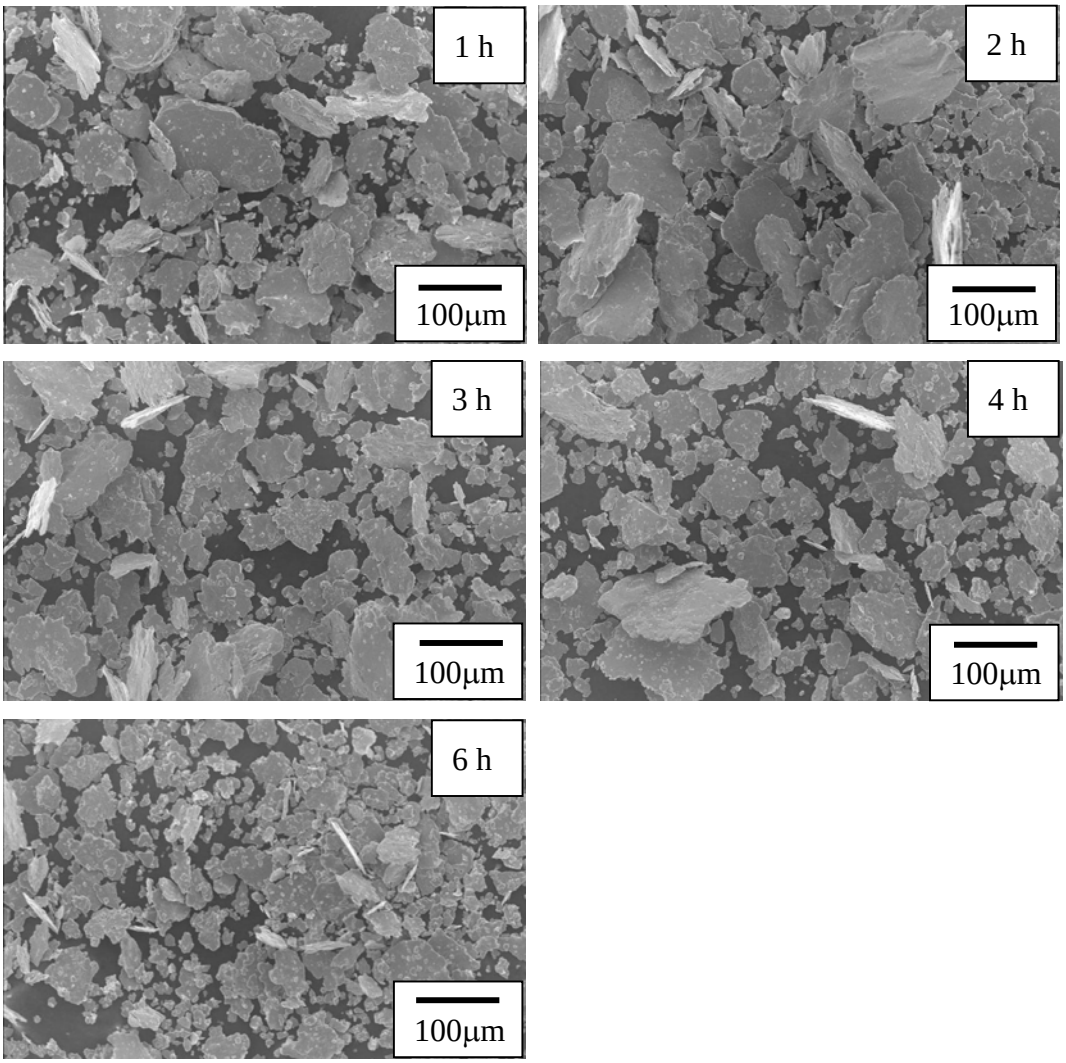

Fig. 4.8 Early stages of ball milling (milling time 1– 6 h) for Ni-15%Fe-5%Mo powders.

The early stage of the milling process was also studied using X-ray mapping. Fig. 4.9 shows the elemental mapping of the powders milled for 2 h and 6 h. Since the powders used for this experiment was pre-alloyed $FeNi_3$ powders, the mapping intensity of elemental Ni and Fe was homogeneous. However, the mapping intensity for Mo was different; some regions were brighter than others indicating that Mo had not dissolved into $FeNi_3$ after 2 h of milling. Similar observations were also observed for the powders milled for 6 h (Fig. 4.9 (b)). However, the mapping intensity for Mo was slightly more homogeneous compared to the powders milled for 2 h. This showed that the mixing of Mo and $FeNi_3$ had proceeded to some extent, but total dissolution of Mo atoms was not reached after 6 h of milling.

At the intermediate stage of the mechanical alloying process, significant changes occurred as evidence from the morphology difference of the particles compared with those in the initial stage, as shown in Fig. 4.10 for 10 h to 40 h of milling. At this stage, fracturing and cold welding were the two dominant milling processes. Fracture tends to break the individual particles into smaller pieces and de-agglomerate particles that were cold welded. Particles that became finer in size due to fracturing might alternatively become cold welded together since these two processes were operating in cycle. However, the cold welded particles required a larger force to fracture them again since the forces that bind them together were stronger when the particles size was finer. On the other hand, some particles that were cold welded might undergo de-agglomeration because the forces that broke them apart were much stronger than those that bound them together. Fracture was the main process, and the powders were finer in size in comparison with those in the initial stage and some agglomerates were formed as shown in Fig. 4.10. However, flattened powders could still be observed in these powders. X-ray mapping (Fig. 4.11) shows that the intensity of the Mo atoms for 10 h of milling was almost homogeneous in this stage of milling.

(a) 2 h milling

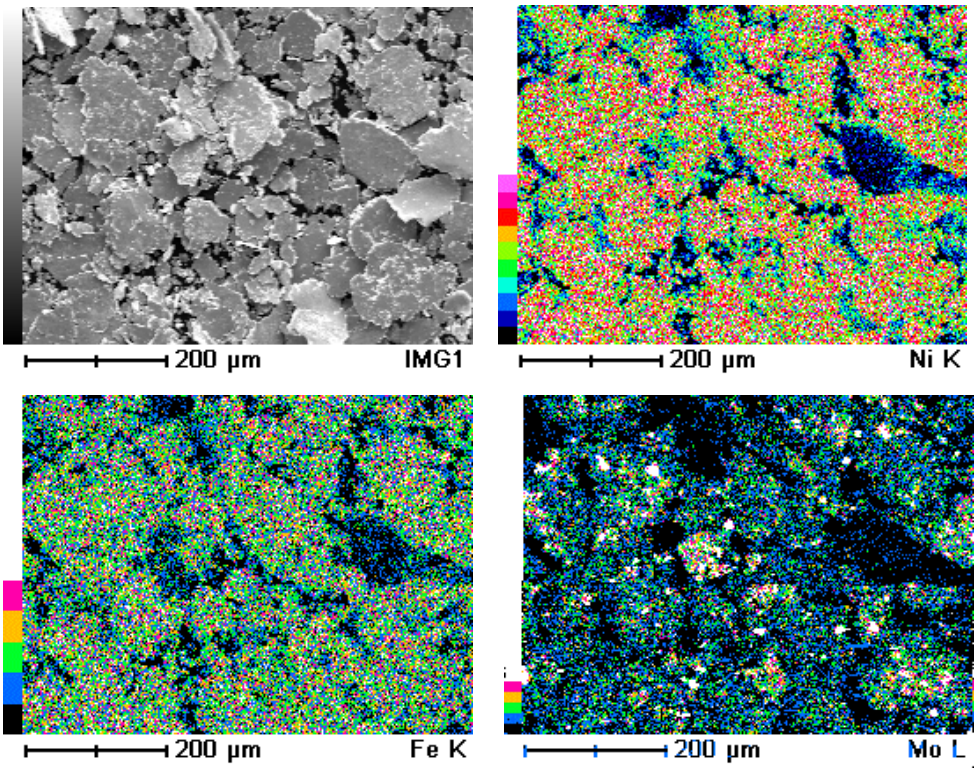

(b) 6 h milling

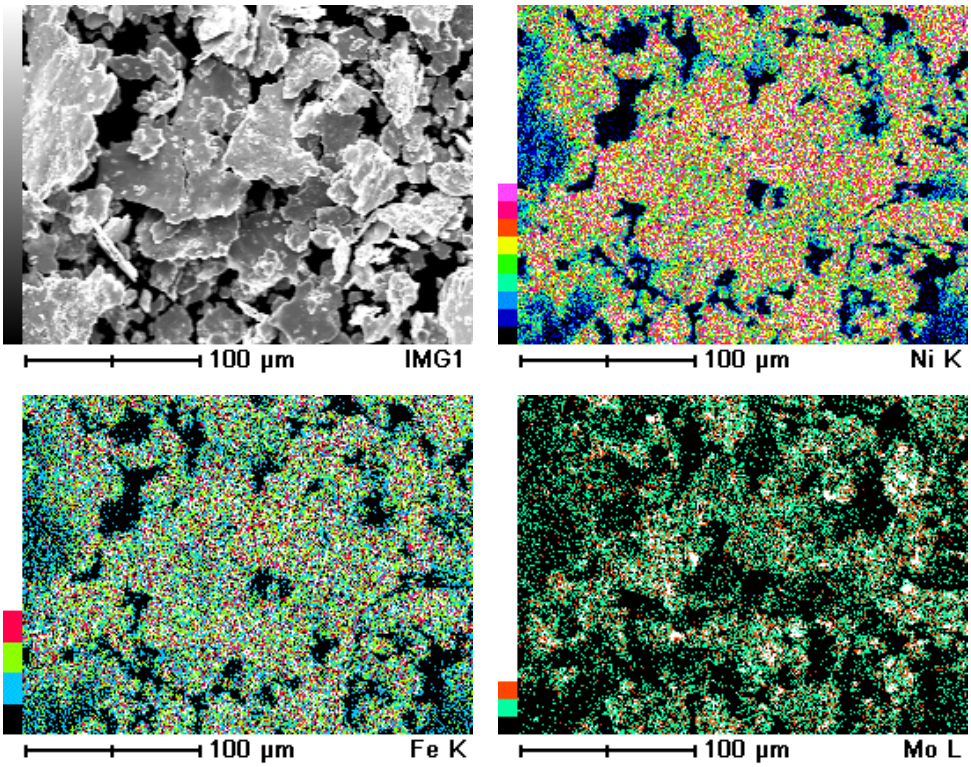

Fig. 4.9 X-ray images of Ni-15%Fe-5%Mo powders during the early stages of ball milling of (a) 2 h and (b) 6 h.

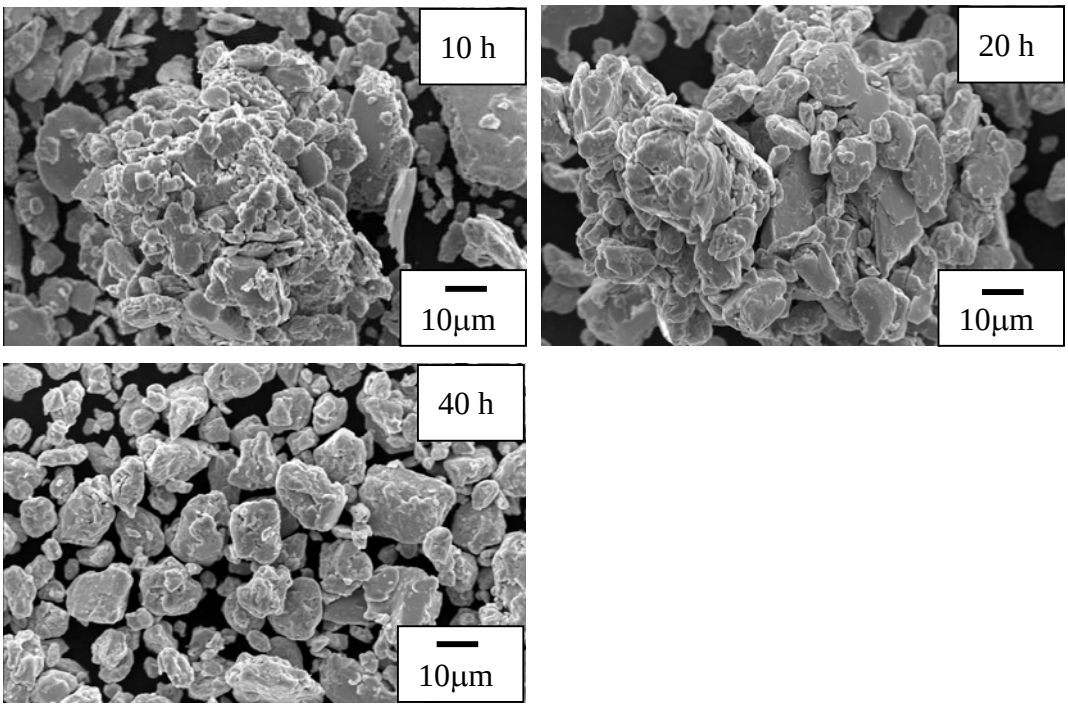

Fig. 4.10 Intermediate stage of ball milling (milling time 10 – 40 h) for Ni-15%Fe-5%Mo powders.

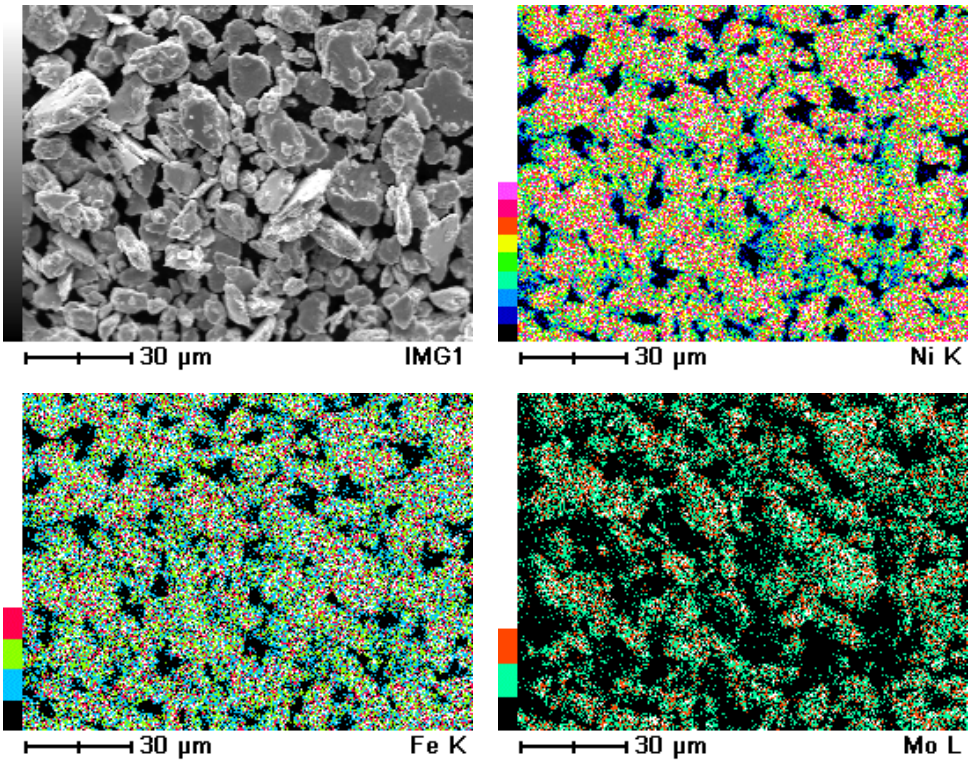

Fig. 4.11 X-ray images of Ni-15%Fe-5%Mo powders during the intermediate stage of ball milling (10 h milling time).

After further milling, steady-state equilibrium was attained when a balance was achieved between cold welding and fracture. This is called the completion stage of the mechanical alloying. In this stage, smaller particles were able to withstand deformation without fracturing and tend to be welded into larger pieces, with an overall tendency to drive both very fine and very large particles towards an intermediate size as shown in Fig. 4.12 for powders milled for 100 h. At the completion of the mechanical alloying process, the powder particles possessed an extremely deformed metastable structure. Further mechanical alloying beyond this stage could not physically improve the dispersion distribution. Real alloy with composition similar to the starting constituents was thus formed. X-ray images (Fig. 4.13) of the powders after 100 h of milling showed homogeneous distribution of the elements.

The particle size distribution of the as-milled powders was also obtained from the SEM micrographs. The analysis was performed using the AIS software to obtain data from more than 200 powders observed in SEM micrographs. The results are graphically presented in Fig. 4.14. The mean powder size calculated from the powder size analysis is summarized in Table 4.2 and graphically presented in Fig. 4.15. The powder size distribution shown in Fig. 4.14 (a) indicates that during the early stage of ball milling, flattening was the main process since no significant powder size reduction was observed. It was also noted that the powder size distribution was almost the same during the early stage of milling (1-6 h). The mean powder size during the early stage of milling varied from 20 μm to 30 μm. As milling time increased, the mean powder size decreased accordingly. However, as milling time increased further to the intermediate stage (10 h to 40 h milling), a significant reduction in powder size was observed as shown in Fig. 4.14 (b). The powder size distribution was between 2 μm to 30 μm and the mean powder size decreased to about 10 μm. In the completion stage, the powder size distribution became narrower (2 μm to 10 μm), and the mean size decreased sharply to 4 μm.

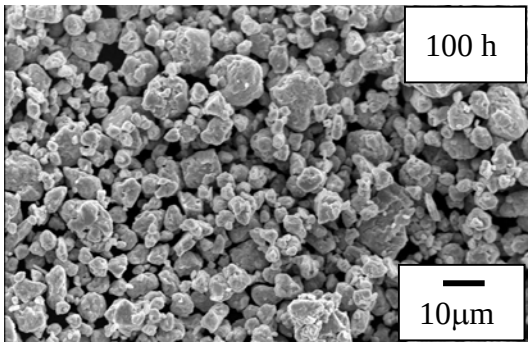

Fig. 4.12 Completion stage of ball milling (milling time 100 h) for Ni-15%Fe-5%Mo powders.

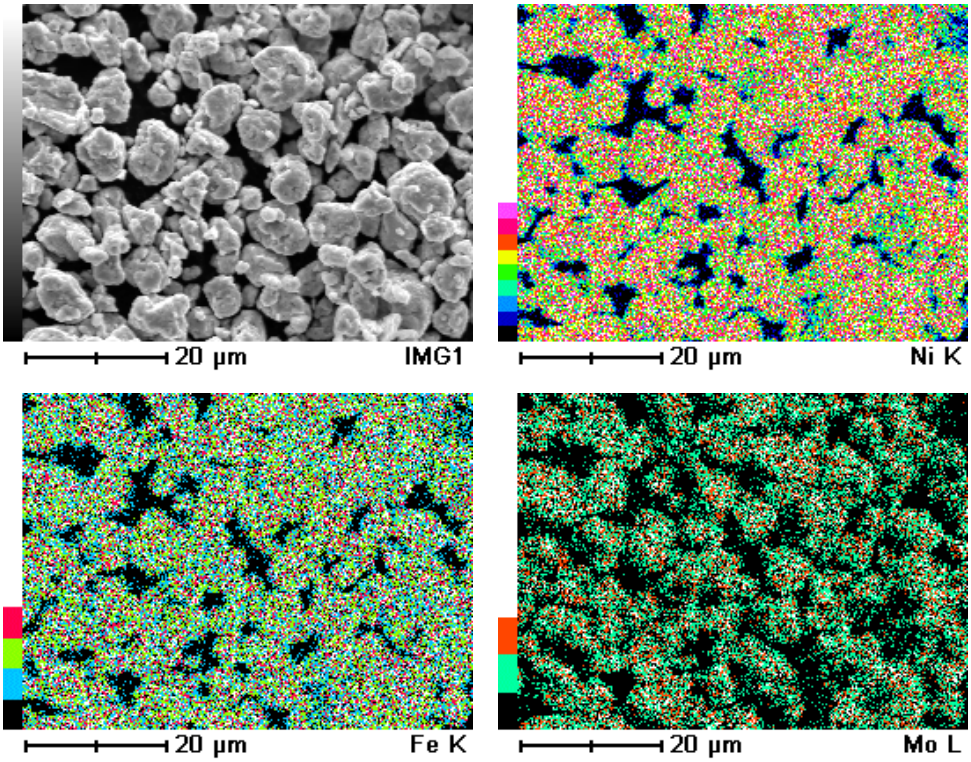

Fig. 4.13 X-ray images of Ni-15%Fe-5%Mo powders at the completion stage of ball milling (100 h milling).

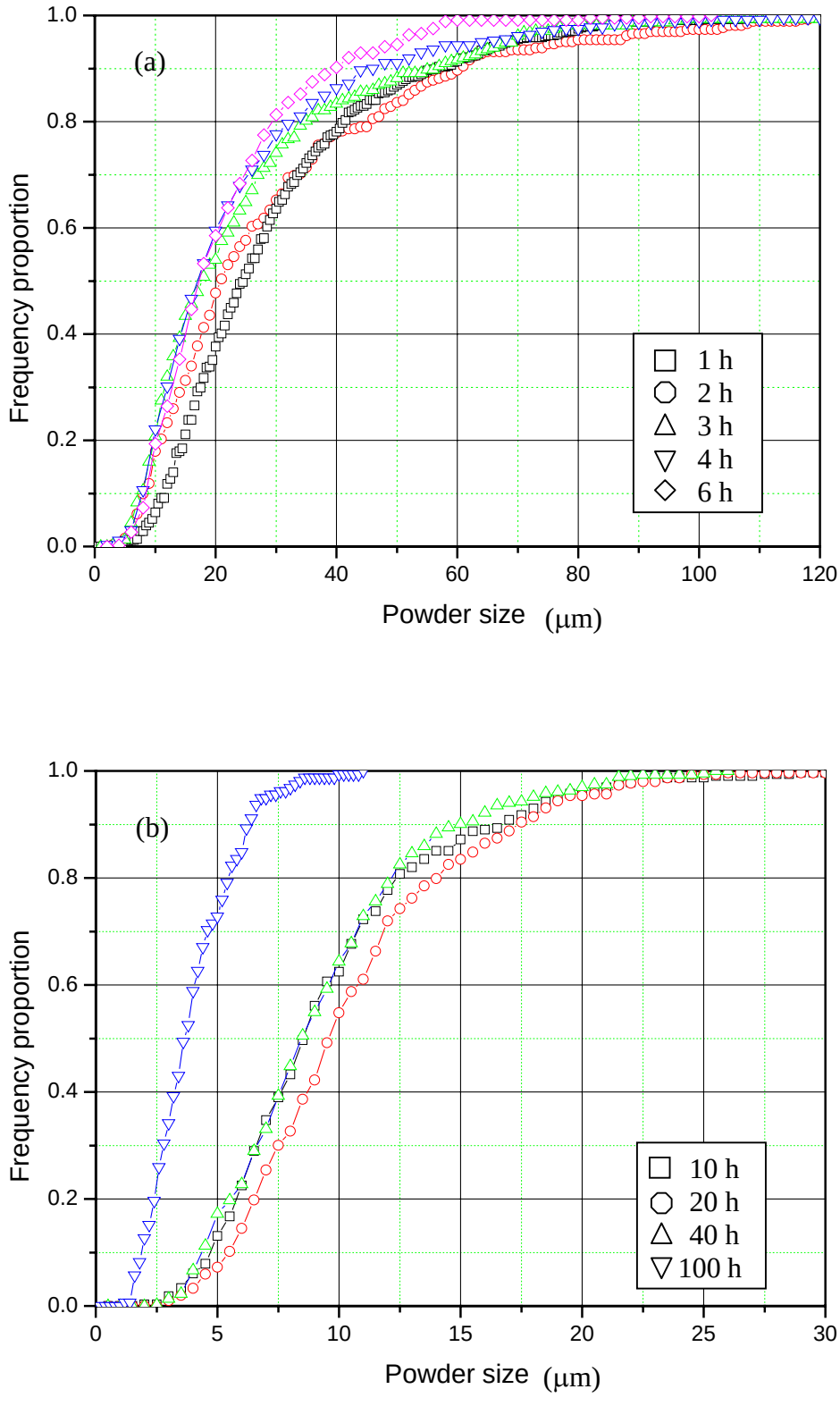

Fig. 4.14 Particle size distribution of the as milled Ni-15%Fe-5%Mo powders (a) 1 h to 6 h and (b) 10 h to 100 h.

Table 4.2 Powder size distribution range and mean powder size of the as-milled Ni-15%Fe-5%Mo powders for different milling time.

Milling time (h)	Size distribution range (μm)	Mean powder size (μm)
0	1 ~ 30	20
1	10 ~ 100	29.7
2	5 ~ 120	29.1
3	5 ~ 90	24.7
4	3 ~ 110	23.3
6	3 ~ 90	21.2
10	2 ~ 27	9.6
20	3 ~ 25	10.6
40	2 ~ 21	9.3
100	2 ~ 10.5	3.9

Previous researches had also studied the different mechanical stages during ball milling of different alloy systems including ductile-ductile systems (Benjamin and Volin, 1974; Benjamin, 1976; Lee et al, 1998; Suryanarayana, 2001), ductile-brittle systems (Gilman and Benjamin, 1983; Lee and Koch, 1988) and brittle-brittle systems (Davis and Koch, 1987; Davis et al, 1988; Lee and Koch, 1987). Different alloy systems have different morphologies during the milling process, however, the milling stages namely the early stage, the intermediate stage and the completion stage are still observed in all systems. A common observation is the increase in the average particle size after milling for a certain length of time. This was also observed in the current study for the early stages when compared to the raw powders shown in Fig. 4.15.

From the above observations, it can be concluded that in the early stage of milling, cold welding is the main process compared to the powders without milling. However, in the intermediate stage, fracture is the dominant process and cold welding is not as effective. This may be due to the fact that the alloyed phase is not ductile. As the powder size is reduced, further fracture would need higher enerreak the powders, therefore frac ture and cold welding are balanced in the final stage of ball milling. The mechanical stages of the ball milled Co-Fe-P-B

powders observed by the analysis of powder size distribution were also reported by Li and Ramanujan (2004), and the similar conclusions were also given.

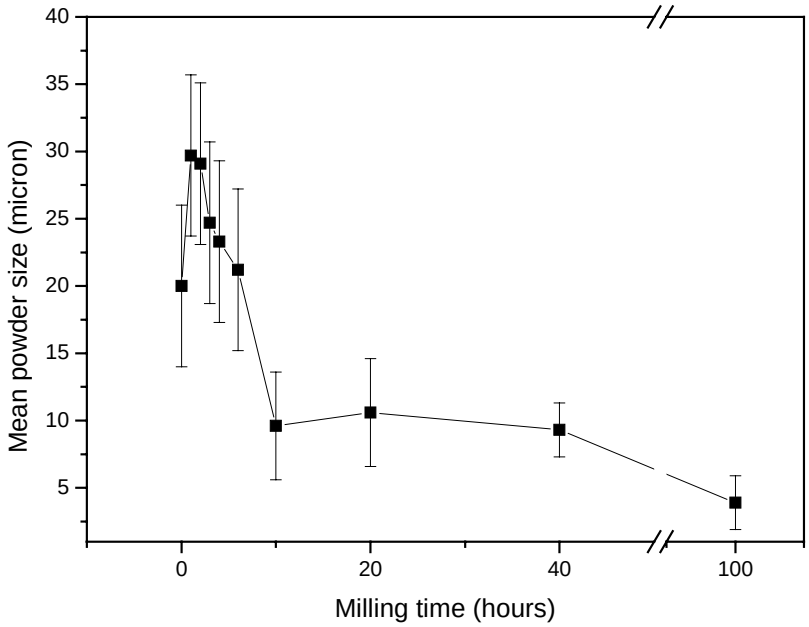

Fig. 4.15 Mean powder size of the as-milled Ni-15%Fe-5%Mo powders for different milling time.

4.3.2.2 TEM observations

The nanocrystalline structure of the powders was confirmed from TEM observations. TEM bright-field (BF) image and the corresponding diffraction pattern of the powder milled for different times were obtained. TEM BF images of Ni-15%Fe-5%Mo powders after 2, 4 and 6 h of milling are shown in Fig. 4.16. The grains were not well-defined in these images. Similar microstructures were also observed for powders milled for 10 h (Fig. 4.17) and 20 h (Fig. 4.18). Such non-uniform microstructures became less obvious as the milling time increased. Non-uniform microstructure and random distribution of equiaxed grains were also observed for mechanically alloyed Al-Mg powders (Zhou et al, 2003), with the diameter of grains varying from less than 10 nm to more than 200 nm. Li and Ramanujan (2004, 2005) also reported non-uniform microstructure for their Fe-Co powders milled for less than 10 h. The formation of the non-uniform microstructure

was explained to be due to the ball milling process. During ball milling process, the powders between the balls would receive the highest force along the vertical direction. This caused the formation of texture. The existence of the texture gave rise to the non-uniform microstructure of the powders, which was observed in the early and intermediate stages of ball milling.

The grains could be distinguished clearly after 40 and 100 h of milling as shown in Fig. 4.19 and Fig. 4.20. The average grain size for these two samples was about 10 nm. This value is consistent with the value obtained from the XRPD results. The diffraction rings shown in Fig. 4.20 for the powders milled for 100 h was indexed as the FCC $FeNi_3$ crystal structure. The orientation of the crystallites was quite random and the grain size was small, as demonstrated by the uniformity of the diffraction rings. The random orientation of the crystallites and the small grain size was further confirmed from high resolution TEM image (HRTEM) (Fig. 4.21).

In general, during the process of ball milling, large deformation is introduced which can produce distorted regions within subgrains, grain boundaries and even across entire grains. The existence of high dislocation is just a typical example. HRTEM image of the 10 h milled Ni-15%Fe-5%Mo powders (Fig. 4.22) revealed the presence of moiré fringes at the grain boundaries and the grains had different crystallographic orientations. Dislocation, moiré fringes and increased grain boundaries have been observed by Chen et al (1999) in their NiAl intermetallic sample. They reported that the formation of the shear bands and moiré fringes were responsible for breakdown of the grains and generation of nanostructure during the mechanical alloying process. Zhou et al (2003) observed a high density of dislocation in the Al-Mg powders. They found that the defect structures could affect subgrain coarsening during the recovery process and lead to a heterogeneous state in microstructures from large to small-sized grains. From those reported research, it would be concluded that the formation of these defects was responsible for the breakdown of grains, and the defects observed in the powders would promote the formation of nanostructure during ball milling.

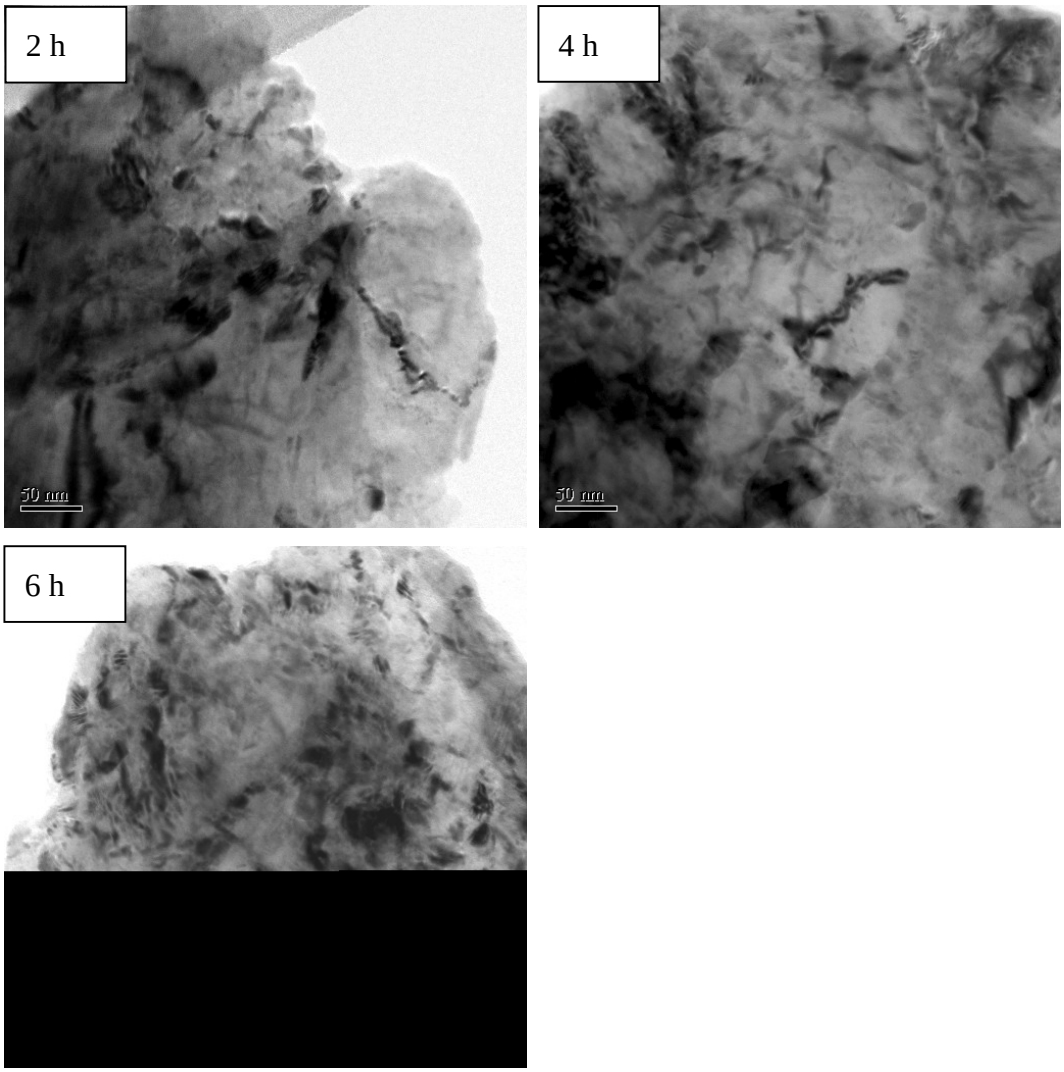

Fig. 4.16 TEM bright field image of Ni-15%Fe-5%Mo powder after 2 h, 4 h and 6 h of milling.

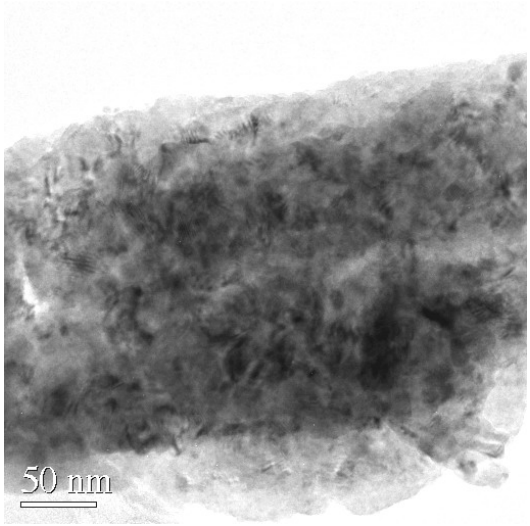

Fig. 4.17 TEM bright field image of Ni-15%Fe-5%Mo powder after 10 h of milling.

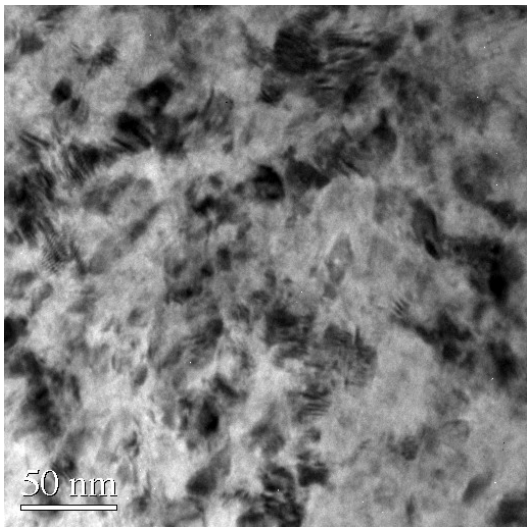

Fig. 4.18 TEM bright field image of Ni-15%Fe-5%Mo powder after 20 h of milling.

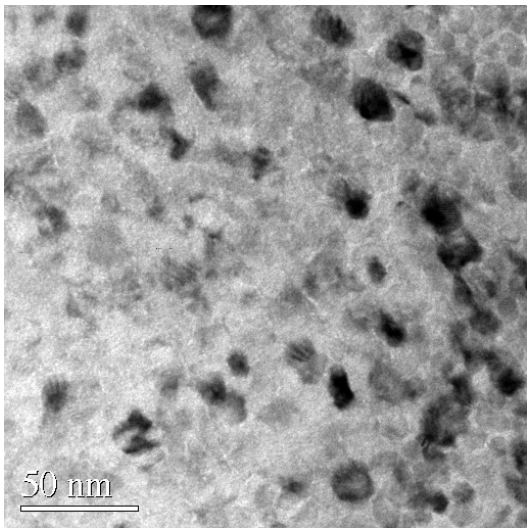

Fig. 4.19 TEM bright field image and dark field image of Ni-15%Fe-5%Mo powder after 40 h of milling.

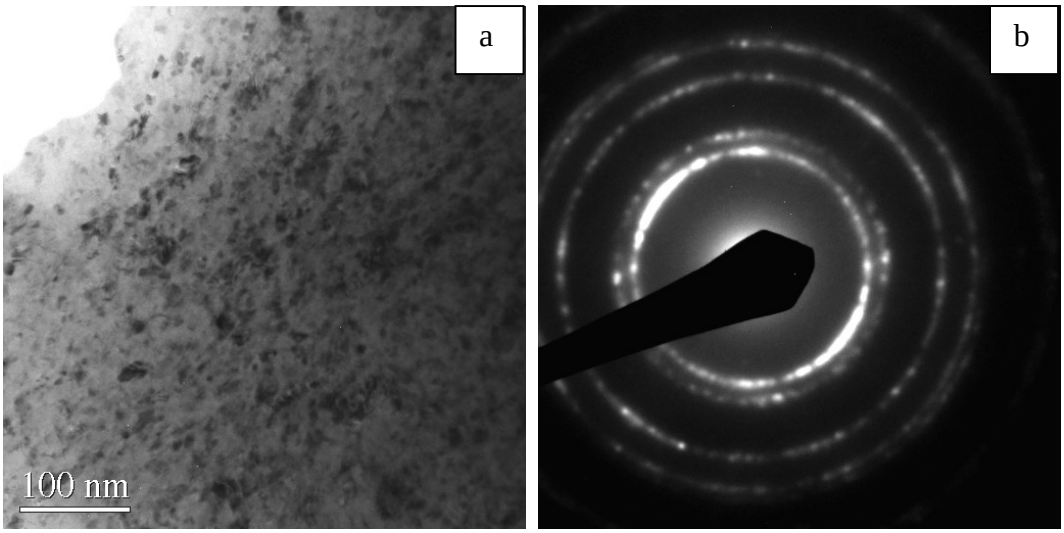

Fig. 4.20 TEM micrographs of Ni-15%Fe-5%Mo powders after 100 h of milling (a) bright field image and (b) corresponding diffraction pattern for $FeNi_3$ phase.

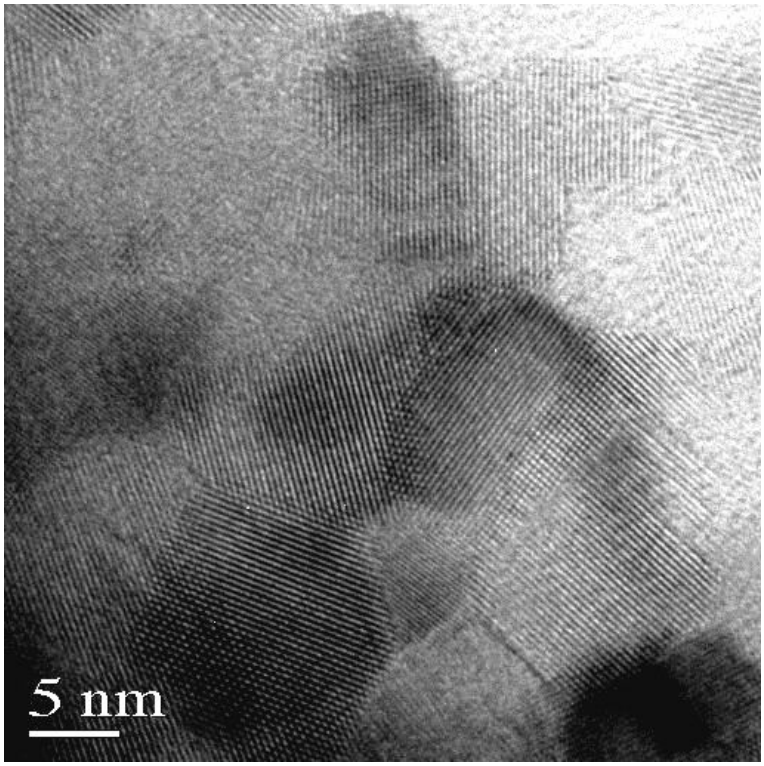

Fig. 4.21 HRTEM of Ni-15%Fe-5%Mo powders after 100 h of milling.

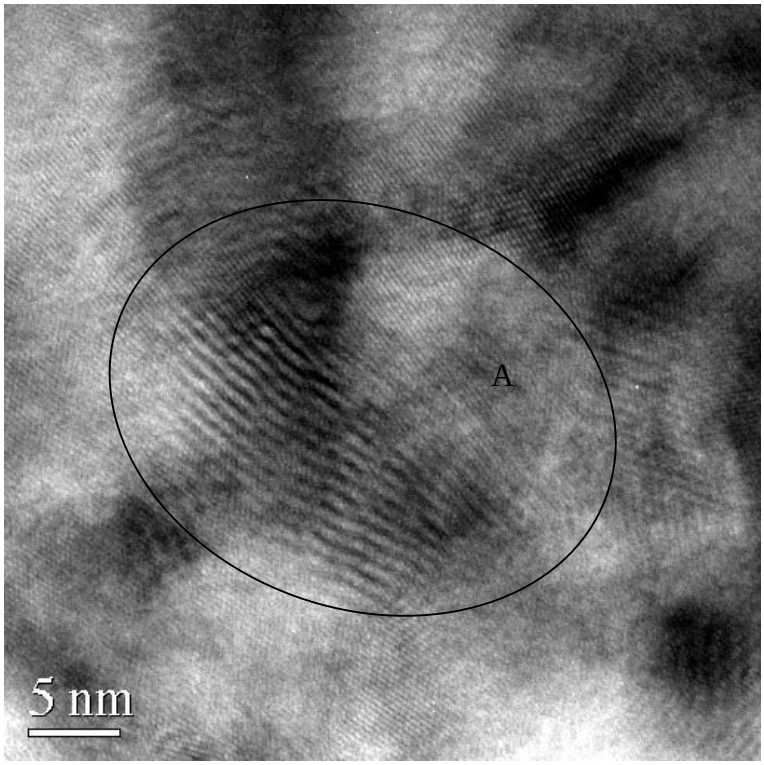

Fig. 4.22 HRTEM of 10 h milled Ni-15%Fe-5%Mo powders showing the presence of moiré fringes as marked in area A.

4.3.3 Magnetic Properties

Saturation magnetization $\boldsymbol{M_s}$ and coercivity $\boldsymbol{H_c}$ were determined from the hysteresis loops and are summarized in Table 4.3. Fig. 4.23 shows the variation of saturation magnetization $\boldsymbol{M_s}$ with milling time at room temperature. It was observed that $\boldsymbol{M_s}$ remained constant at about 80 emu/g for 1 h to 4 h of milling. There was a slight decrease to about 70 emu/g for 6 and 10 h milling, after which $\boldsymbol{M_s}$ decreased steadily to 42 emu/g for 100 h of milling.

As elemental Mo powders and pre-alloyed $FeNi_3$ powders were used to prepare Ni-15%Fe-5%Mo alloy, the $\boldsymbol{M_s}$ of the pre-milled powders were contributed by the pure $FeNi_3$ phase. It was reported that the $\boldsymbol{M_s}$ of $FeNi_3$ powder and pellet prepared by high energy ball milling with the composition of Ni-25 at. % Fe was nearly 100 emu/g (Frase et al, 1999b). The observed value of the annealed $FeNi_3$ phase in our experiment was about 88 emu/g which was slightly lower than the reported one. A possible reason for the difference is the different composition used to prepare the

powder sample. The atomic Fe and Ni ratio of our sample was less than 1:3 as compared to the reported one.

Table 4.3 Saturation magnetization $\boldsymbol{M_s}$ and coercivity $\boldsymbol{H_c}$ of the Ni-15%Fe-5%Mo powders milled for different time.

Milling time (hours)	Saturation magnetization (emu/g)	Coercivity (Oe)
1	82.2	17.7
2	82.8	20.2
3	79.6	19.6
4	80.8	19.5
6	71.8	19.4
10	68.4	25.9
20	64.2	14.8
40	53.1	13.8
100	42.5	13.5

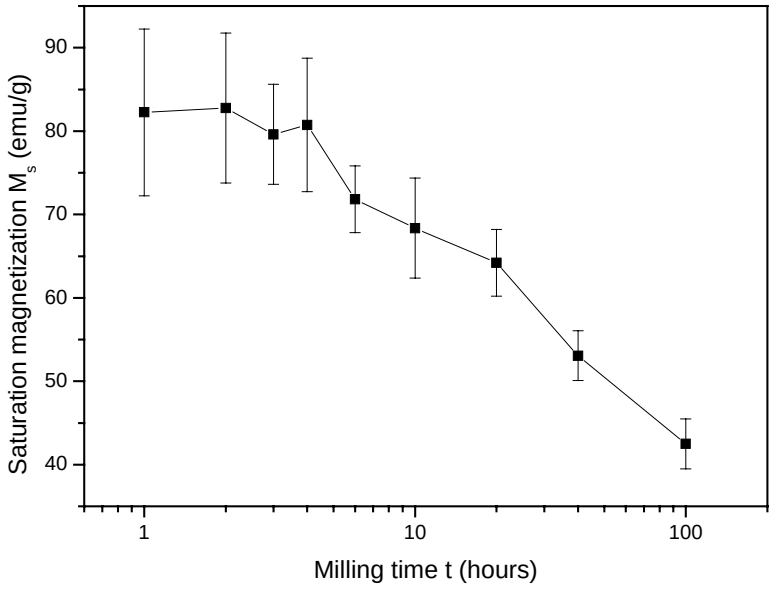

Fig. 4.23 Saturation Magnetization of Ni-15%Fe-5%Mo powders as a function of milling time.

Mo atoms were observed to dissolve into $FeNi_3$ phase during the ball milling process. It has been reported that Mo atoms replaced Fe atoms and bonded strongly

with Ni atoms, causing the destruction of the NiFe bonds and the formation of NiMo bonds (Wohlfarth, 1980). As milling time increased, more and more Mo atoms were observed to dissolve in $FeNi_3$ phase. Of prime importance to the magnetic behavior of Ni-Fe alloys is the appearance of the long-range ordered LI_2 structure at the $FeNi_3$ composition (Wohlfarth, 1980). When this long-range ordered structure is destroyed, the magnetic properties will change. In this investigation, the additional Mo atoms tend to replace Fe or Ni atoms. From literature review, it is found that the "spare" electrons of the added elements enter the 3d shell of the nickel atoms only which play the major role at this condition, the contribution of the iron atoms to the total magnetic moment being unaltered only a simple dilution effect. As Mo atoms either replace the Fe or Ni atoms, the final result is the decrease of M_s as more and more Mo atoms substituted.

From the XRPD data on the variation of lattice parameter during the milling process (Fig. 4.5), it was deduced that the dissolution of Mo atoms was completed within 40 h of milling. If all the Mo atoms were to dissolve after 40 h of milling, $\boldsymbol{M_s}$ would be expected to remain constant after further milling. However, $\boldsymbol{M_s}$ continued to decrease when the milling time was increased to 100 h. Hence, there are other reasons that caused the decrease in $\boldsymbol{M_s}$.

Chinnasamy et al (1999) reported the decrease in $\boldsymbol{M_s}$ for their ball milled $FeNi_3$ samples. They explained the decrease in the saturation magnetization from 94 emu/g to 73 emu/g with milling time to three factors: (1) dead layers on the surface, (2) increase in the volume fraction of superparamagnetic particles and (3) surface oxidation. Frase et al (1999b) also observed a decrease in $\boldsymbol{M_s}$, and explained the decrease in $\boldsymbol{M_s}$ for their $FeNi_3$ alloy system to be due to the dissolution of Fe impurities. Hence, a possible explanation for the decrease in $\boldsymbol{M_s}$ observed in the current experiment after 40 h of milling could be due to contamination during the ball milling process.

From the XRPD results, the substitution of Mo atoms would have completed after 40 h of milling. At this condition, the saturation magnetization is about 53.1 emu/g (5840 Gauss), which is lower than the reported values of 8700 Gauss for Ni-15%Fe-4%Mo and 8000 Gauss for Ni-16%Fe-5%Mo bulk materials (Cullity,

1972; Chen, 1977). These bulk materials are cast, swaged, drawn, and rolled in the usual way and tested in the form of 0.006-in strip after heat treatment with furnace cooling or air quenching. Hence, the difference in $\boldsymbol{M_s}$ value is mainly due to the difference in the preparation process.

The coercivity of the powders milled for different times is shown in Fig. 4.24. The coercivity increased gradually during the first 10 h of milling. A maximum coercivity of 26 Oe was obtained for the powders that were milled for 10 h. Further milling for 20 h caused the coercivity to decrease rapidly to about 15 Oe. The coercivity remained constant at about 14 Oe for powders that were milled for more than 20 h.

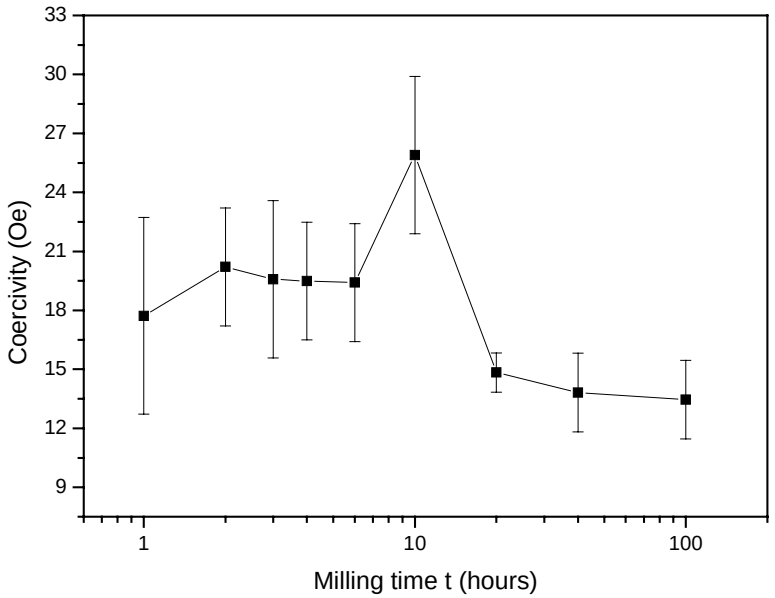

Fig. 4.24 Coercivity of Ni-15%Fe-5%Mo powders as a function of milling time.

The coercivity is an extrinsic property and microstructure sensitive. Its value will be affected by ambient environment factors such as contamination, and microstructural features including grain size, defect concentrations, compositional inhomogeneities and magnetic domains. Contamination from the milling material cannot be prevented. It has been reported that contamination from the milling bowls and balls have caused an increase in coercivity as milling time increased (Frase et al, 1999b). In the current study, contamination from WC vials could cause the increase in coercivity as the milling time increases. However, the volume fraction of the

contamination was too small to account for the large increase observed at 10 h of milling. The effects of contamination would be small, but perhaps not negligible.

The variation of coercivity with milling time as observed in the current study is attributed mainly to the microstructure effects. The effects of residual strain on H_c in HEBM powders have been reported by some researchers (Frase et al, 1999b; Chiriac et al, 2001). In general, it was found that H_c increases as residual strain increases. Such an observation is consistent with our results (Fig. 4.29). As the residual strain increased, H_c increased up to 10 h of milling. The residual strain had the maximum value at 10 h of milling, and this corresponded to the highest H_c. For the powders milled for more than 10 h, the residual strain decreased, and this corresponded to a decreased in H_c too. However, the amount of decrease in strain does not warrant the sharp decrease in H_c for powders milled for 20 h. Another factor that needs to be considered is the grain size, which will be considered in detail in the following paragraphs.

The variation of coercivity and average grain size with milling time is presented in Fig. 4.26. Grain size was observed to decrease with milling time, and the sharp decrease of coercivity at 20 h of milling which could not be explained by residual strain could be due to the decrease of grain size during the milling process. In general, the effect of grain size on coercivity has two trends. When a polycrystalline grain size is smaller than the width of a magnetic domain wall, there will be little tendency for crystalline orientations to affect the energy of magnetic orientation in the materials. For small grain sizes, $H_c \approx d^6$. However, when a grain is large enough to contain a domain wall, magnetization is dominated by domain wall movement, causing $H_c \approx d^{-1}$. This effect of small grain size on coercivity was described by Herzer and Hilzinger (1986), and random anisotropy model was set up. This model can be used in the current project to explain the variation of coercivity of Ni-15%Fe-5%Mo powders with grain size (Fig. 4.27). The coercivity reached a maximum value when the grain size was about 15 nm. Coercivity was plotted as a function of sixth power of grain size for grain size less than 20 nm is shown in Fig. 4.28. This line fits reasonably well to the random anisotropy model. In addition, coercivity was also plotted as a function of the reciprocal of grain size for grain size

larger than 20 nm (other than the last point), and is shown in Fig. 4.29. For this case, the H_c did not fit d^{-1} very well. This is because other than the grain size effect, there is also the residual strain effect which is not considered in the random anisotropy model.

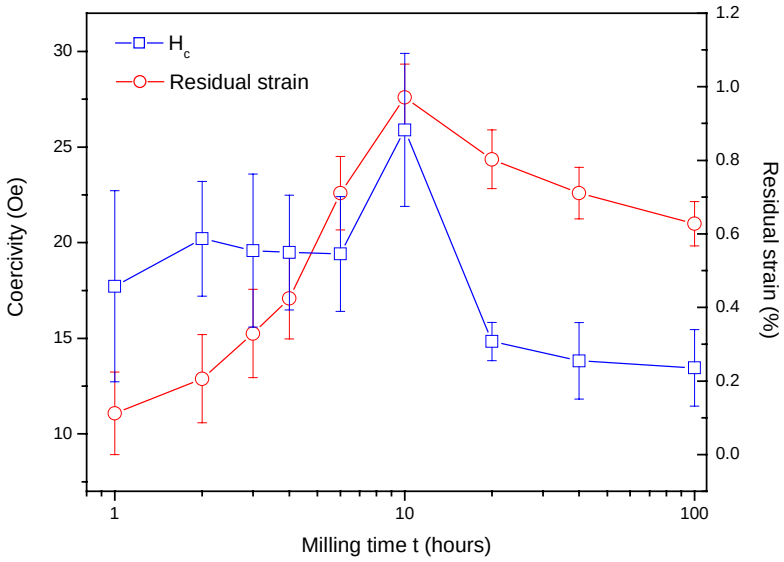

Fig. 4.25 Variation of coercivity and residual strain with milling time.

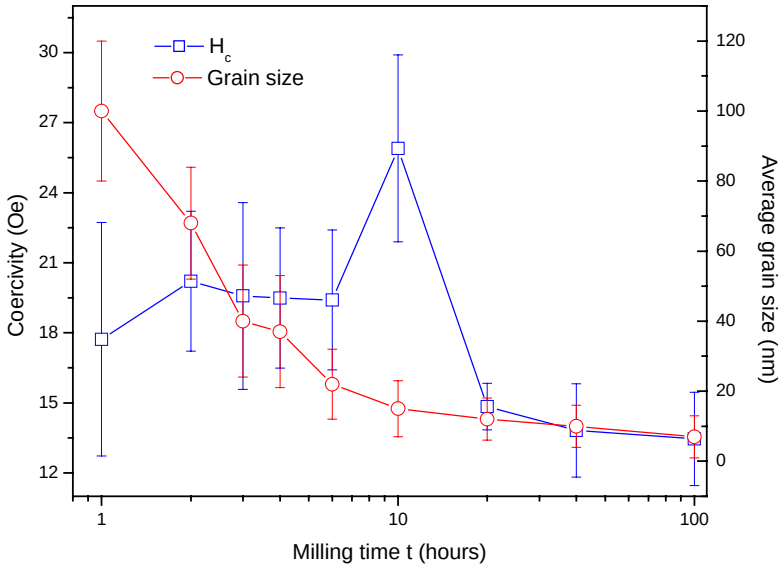

Fig. 4.26 Variation of coericivity and average grain size with milling time.

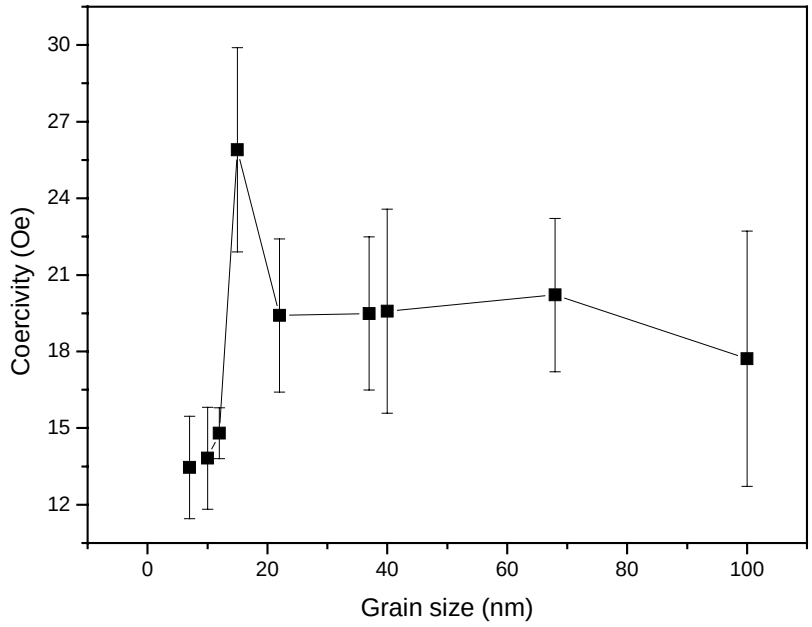

Fig. 4.27 Coercivity of Ni-15%Fe-5%Mo powders as a function of grain size.

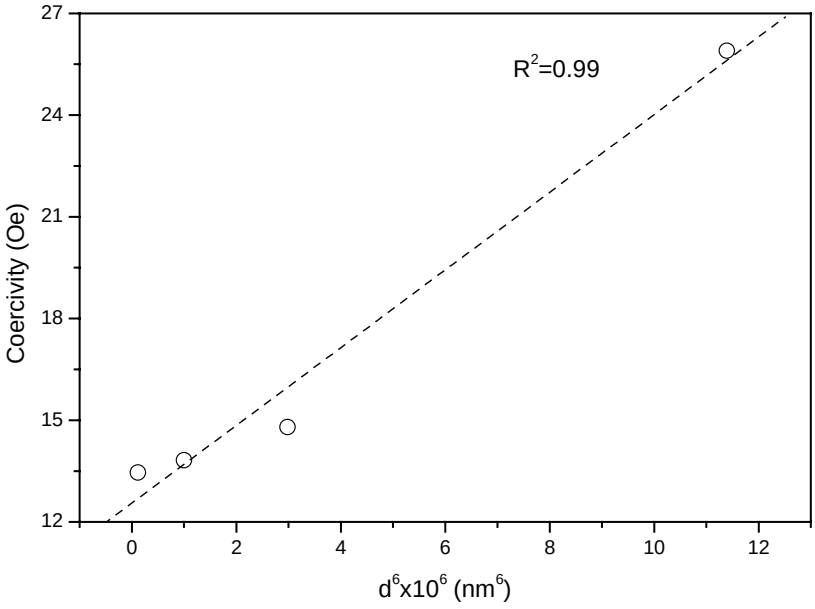

Fig. 4.28 Coercivity $\boldsymbol{H_c}$ against sixth power of grain size $\boldsymbol{d^6}$.

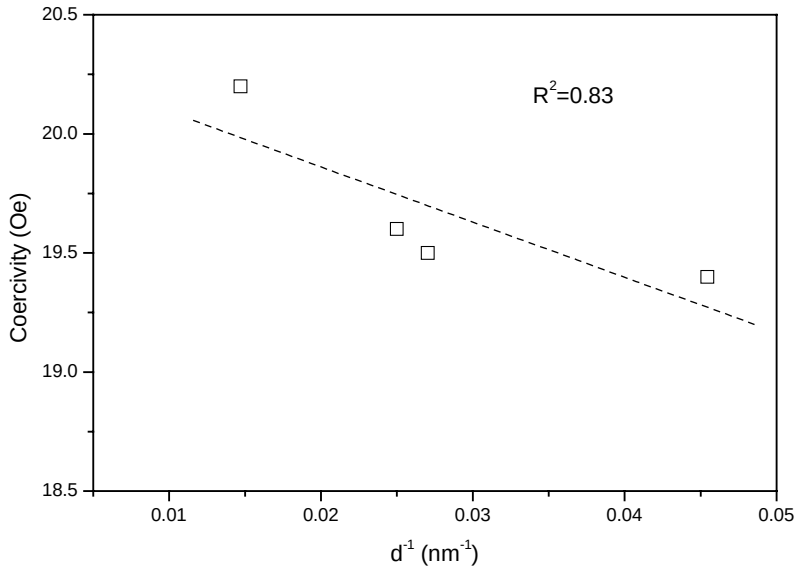

Fig. 4.29 Coercivity $\boldsymbol{H_c}$ against the reciprocal of grain size $\boldsymbol{d^{-1}}$.

It should also be noted that coercivity is also affected by the presence of pores between the powders particles during the magnetic properties measurement. Frase et al (1999b) compared the coercivity of $FeNi_3$ powders and compressed pellets, and found that in general compressed pellets had lower coercivity than powders. This is because compressed pellets reduce the volume of voids, cracks and gaps between particles. The increase in packing density would reduce the energy associated with the magnetic fields in the voids. There was lower energy cost associated with the rotation of the magnetic field into the gaps between particles for the compressed pellets. Hence, the porosity of the powder sample would cause a higher value of coercivity as compared to a bulk sample.

In general, the coercivities of the powders milled for various times are larger than the values reported for bulk Ni-17%Fe-4%Mo permalloy (0.05 Oe) and Ni-16%Fe-5%Mo supermalloy (0.002 Oe) (Cullity, 1972; Chen, 1977). The difference in values is expected since the value obtained from the literature is for bulk materials which have undergone different treatments to improve their magnetic properties. In this experiment, the as-milled powder samples have residual strain and as well as pores. This will give rise to higher coercivity as compared to the bulk sample.

4.4 Conclusions

Nanocrystalline Ni-15%Fe-5%Mo solid solution was synthesized by mechanical alloying via high energy ball milling, using elemental Mo powders and pre-alloyed $FeNi_3$ powders. This milling process could not produce the amorphous phase, no matter how long these powders were milled.

It was concluded from the XRPD analysis that 40 h of milling was required to complete the substituting process of the Mo atoms into the $FeNi_3$ lattice to form Ni-15%Fe-5%Mo solid solution. A diffusion controlled mechanism was responsible for the formation of the Ni-15%Fe-5%Mo solid solution.

As Mo atoms dissolved into Ni-Fe alloys, they destroyed the $FeNi_3$ lattice. This caused saturation magnetization to decrease during the substitution process. The coercivity of the milled powders was mainly affected by residual strain and grain size of the powders. The observation of coercivity was consistent with random anisotropy model that with increasing grain size, $\boldsymbol{H_c}$ should increase to a maximum and then decrease.

Chapter 5 Mechanically alloyed and Annealed Ni-Fe-Mo-B magnetic powders

5.1 Introduction

Mechanical alloying (MA) is a popular powder- metallurgy route to produce precursor amorphous alloy powders with a large supercooled liquid region sufficient for subsequent consolidation into the bulk form (Koch and Whittenberger, 1996; Suryanarayana, 2001; Manna et al, 2004; Zhang, 2004). Most of the work on the amorphous magnetic materials produced by mechanical alloying is mainly focused on Fe-based, Co-based and Fe-Co based alloys (Bednarcik et al, 2003; McHenry et al, 2003). Although Ni-based amorphous alloy produced by mechanical alloying have also been studied, they are mainly on binary systems such as Ni-Nb, Ni-Ti and Ni-Zr systems (Koch et al, 1983; Hellstern and Schultz, 1987; Schwarz and Koch, 1986; Lee and Koch, 1987; Wang et al, 1991; Sun et al, 1992). The only work found on the multicomponent Ni-Fe amorphous alloys produced by ball milling are based on $Fe_{40}Ni_{40}B_{20}$ (Miura et al, 1990) and $Fe_{40}Ni_{40}P_xSi(B)_{20-x}$ metal-metalloid systems (Miura et al,1990; Surinach et al, 1994; Sunol et al, 2001). The aim to produce these materials is to study the feasibility to form the amorphous phase by mechanical alloying and compare them with the ones produced by melt spinning. From the reported research work, the main focus on Ni-Fe alloys are based on nearly equal atomic percentage of Ni and Fe. No research work based on Ni-Fe-Mo permalloy with 70-80 wt. %Ni has been reported.

In addition, in order to obtain optimal magnetic properties and fine microstructure materials, an amorphous phase may be required to act as an exchange coupling medium. This is because from the previous research on FINEMET, NANOPERM,

HITPER and Fe-Co alloys, it was found that these alloys were generally two phase materials with a nanocrystalline ferromagnetic phase and a residual amorphous phase at the grain boundaries (McHenry et al, 1999a; McHenry and Laughlin, 2000). Some general properties can be observed in these alloys, such as (1) relatively high resistivity (2) low magnetocrystalline anisotropy (3) increased mechanical strength. With properties such as these, nanocrystalline alloys have great potential as soft magnetic materials. In order to obtain this type structure, the amorphous materials have to undergo a series of annealing process. Hence, many research works have also been reported on the microstructure evolution of the annealed samples (Herzer and Warlimont, 1992; Surinach et al, 1994; Zhang and Yi, 1996; Zhang et al, 1996; Chiriac et al, 2001; Sunol et al, 2001; Zhou et al, 2002).

In the previous chapter, it has been shown that nanostructured Ni-Fe-Mo alloys based on permalloy composition can be produced by mechanical alloying. However, an amorphous phase could not be formed even after 100 h of high energy ball milling. In order to obtain the amorphous phase, some elements such as Boron and Phosphorous can be added to the Ni-Fe based alloys. These elements are metalloids and are often added to alloys to cause significant diffusive rearrangement to occur during crystallization of the glass phase. Hence, in this chapter, Boron is added to induce the formation of amorphous phase in Ni-15%Fe-5%Mo-5%B alloy by high energy ball milling process.

There are basically three aims to be accomplished in this investigation of the mechanically alloyed Ni-15%Fe-5%Mo-5%B system. The first one is to study the feasibility of producing an amorphous phase by the addition of B to Ni-15%Fe-5%Mo alloy using HEBM process and this will be presented in section 5.3.1. The second aim is to study the crystallization process of the as-milled powders so as to understand the annealing process to produce nanostructured soft magnetic materials, and this will be covered in section 5.3.2. Lastly, the magnetic properties of the as-milled and annealed powders will be studied and related to the microstructure, and this will be discussed in the respective sections.

5.2 Sample Preparation

Mechanical alloying of Ni-15%Fe-5%Mo-5%B (weight percentage) powders were performed using a planetary mill (Fritsch, Pulverisette 5) for different milling time varying from 1 to 100 h at 300 rpm at room temperature. The starting powders were a mixture of Ni powder (purity>99%, mesh size≤150 μm), Fe powder (purity>99%, mesh size≤10 μm), Mo powder (purity>99%, mesh size≤10 μm) and B powder (purity>99%, mesh size≤150 μm) with a weight ratio of 15: 3: 1: 1. 40 g of the starting mixture and 50 WC balls of 10 mm diameter were loaded into a 250 ml WC container inside a glove bag that was evacuated first and then back-filled with purified argon. The ball to powder charge ratio was maintained at 10:1. The milling program was set up to pause for 3 min for every 5 min of milling to prevent excessive heating during the milling process. Prior to milling, ~0.2 wt% of ethanol was added to the powders as a processing control agent to inhibit a cold welding process. An O-ring was fitted between the container and the cover to prevent any possible ingress of oxygen into the container from the surrounding atmosphere. In order to minimize oxidation, the “entire operation” was performed in a dried argon atmosphere.

In order to study the crystallization process, the as-milled powders were annealed in a vacuum furnace with a vacuum of about 10^{-5} Torr and temperature fluctuation ±3°C. Different holding times and holding temperatures were selected based on the DSC results of the as-milled powders. The heating rate was set at 10°C/min and the samples were furnace cooled.

5.3 Results and Discussion

The study of the mechanical alloyed Ni-Fe-Mo-B system is divided into two parts. The first part involves the study of the high energy ball milling process of the Ni-Fe-Mo-B alloy system, which will be covered in Section 5.3.1. The second part involves the study of crystallization process by annealing the as-milled powders at various temperatures and durations, which will be presented in Section 5.3.2.

overlapped exothermic peaks which became more pronounced with increasing milling times for the milled Fe-Ni based metal-metalloid amorphous powders. Sunol et al (2001) also reported similar observation for their ball milled Fe-Ni-P-Si alloys. The reason for such observation was explained to be due to the fact that more amorphous phase was produced with prolonged milling time and hence, causing the exothermic peak to become more obvious.

In order to determine the activation energy (***E***) for the crystallization process corresponding to the exothermic peak, the Kissinger's method (Kissinger, 1957) will be used. The Kissinger's equation is expressed as:

$$\ln\frac{T_p^{\,2}}{T} = \frac{E}{RT_p} + \text{Constant}, \qquad (5.1)$$

where $\boldsymbol{T_p}$ is the peak temperature obtained from the DSC measurement at the heating rate of ***T*** and ***R*** is the gas constant. Fig. 5.2 shows the typical non-isothermal DSC traces for the Ni-15%Fe-5%Mo-5%B powders milled for 10 h at different heating rates. Activation energy (***E***) for this process can be calculated using the Kissinger's method. The plot of $\ln T_p^{\,2}/T$ versus $1/T_p$ for 10 h milled powders is shown in Fig. 5.3 and the activation energy was determined to be about 187 kJ/mol. Using this method, the average activation energies of the powders milled for different times were also determined and the results are summarized in Table 5.1 and graphically presented in Fig. 5.4. The activation energy of the milled powders was found to increase from 187 kJ/mol for the 10 h milled sample to 261 kJ/mol for the 60 h milled samples.

Liu et al (2001a, 2001b and 2001c) also determined the activation energy for the crystallization of their multicomponent $(Fe, Ni)_{70}Zr_{10}B_{20}$ amorphous powders milled for different hours. They found that the activation energy for crystallization is strongly dependent on the degree of amorphous phase (or the fraction of crystalline phase in the amorphous matrix). ***E*** is significantly reduced where a high degree of nanostructured crystalline phases existed in the amorphous matrix. Hence, the increase in ***E*** for the powders milled for longer hours in our samples can be

explained to be due to the increase in amorphous phase content as milling time increased.

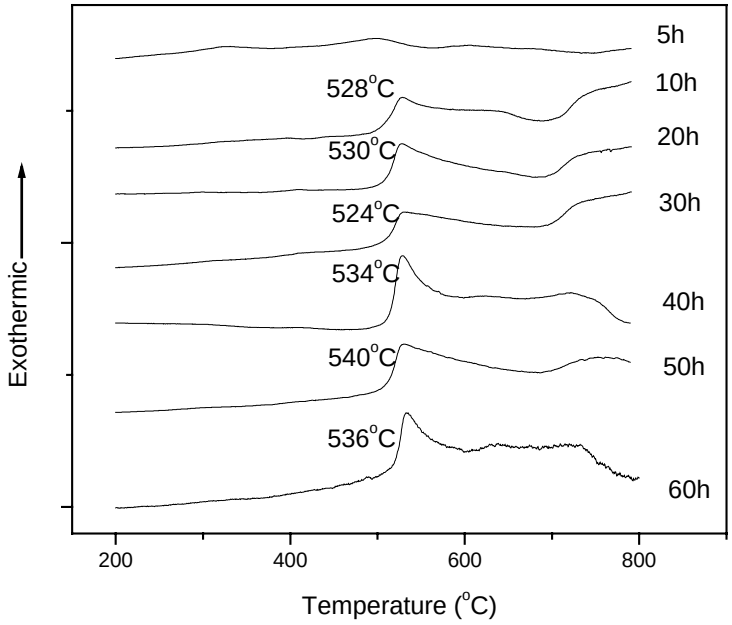

Fig. 5.1 DSC curves obtained at a heating rate of 10°C/min for the Ni-15%Fe-5%Mo-5%B powders milled for different times.

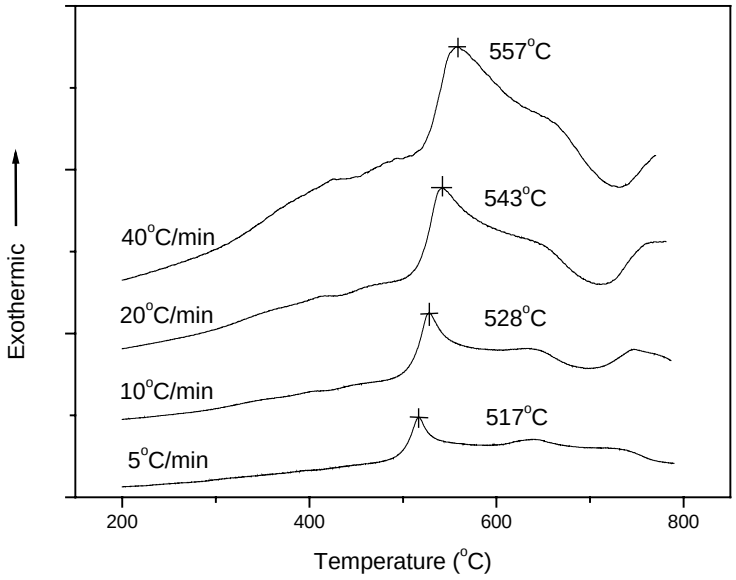

Fig. 5.2 Non-isothermal DSC curves obtained using different heating rates for the Ni-15%Fe-5%Mo-5%B powders milled for 10 h.

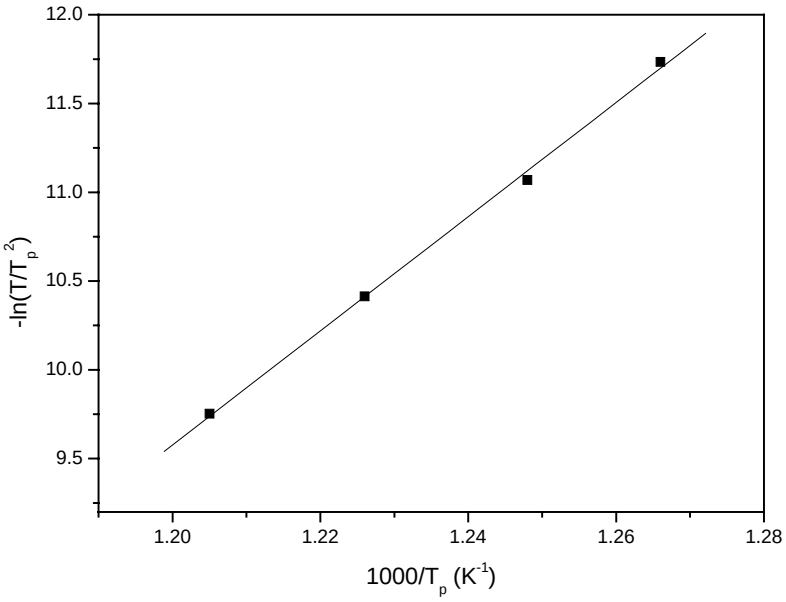

Fig. 5.3 Kissinger's plot of $-\ln(T/T_p^2)$ versus $1000/T_p$ for the Ni-15%Fe-5%Mo-5%B powders milled for 10 h.

Table 5.1 Activation energy for the crystallization of the powders milled for different hours.

Milling time (hours)	Activation energy (kJ/mol)
10	187
20	196
30	194
40	230
50	234
60	261

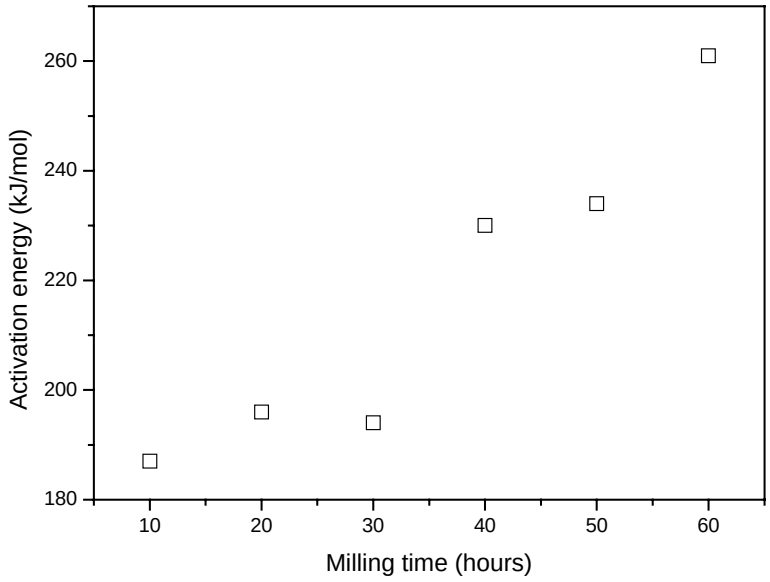

Fig. 5.4 Activation energy for the crystallization of the powders.

5.3.1.2 XRPD results

Fig. 5.5 shows the XRPD patterns of the Ni-15%Fe-5%Mo-5%B powders milled for different durations varying from 5 to 60 h. For the powders milled for 5 h, the diffraction peaks observed corresponded to the elemental powders of Ni, Fe and Mo. No diffraction peaks corresponding to B were detected, which is attributed to the small scattering factor of B (Chiriac et al, 2001). After 10 h of milling, the intensity of the diffraction peaks which corresponded to pure Ni decreased and their peak positions shifted to smaller 2θ angle. These diffraction peaks corresponded to the intermetallic $FeNi_3$ phase, which has the same face-centered cubic structure as Ni, but with a slightly larger lattice parameter. This observation indicated that the formation of the intermetallic $FeNi_3$ took place mainly during the first 10 h of milling. Further milling did not cause any shift in the peaks, but only broadened the peaks and decreased the intensity of the peaks. It was also found that the diffraction peaks of Mo atoms disappeared after 30 h of milling.

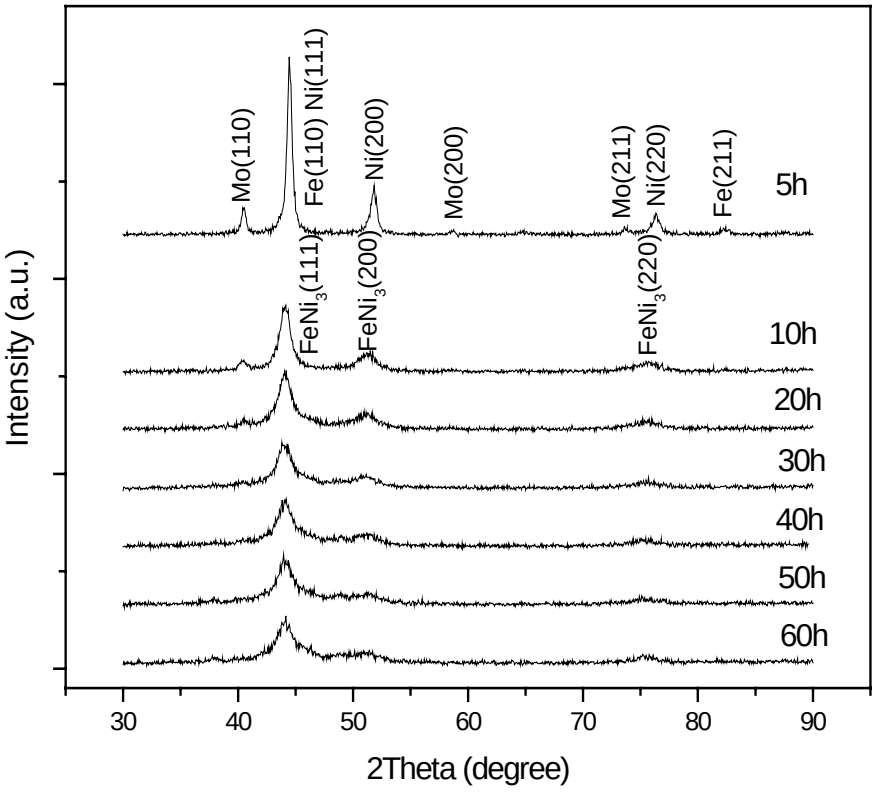

Fig. 5.5 XRPD patterns of Ni-15%Fe-5%Mo-5%B powders milled for different times from 5 h to 60 h.

An exothermic peak for the crystallization of the amorphous phase had already been observed for the powders milled for 10 h (Fig. 5.2). However, from the XRPD observation (Fig. 5.5), $FeNi_3$ was observed to form during 5 to 10 h of milling and further milling only caused the broadened peaks and decreased intensity of the peaks. The presence of the amorphous phase was not obvious from the XRPD results. Combined the observation of DSC and XRPD, partially amorphous powders might be obtained after 10 h of milling, and this assumption will be further confirmed using TEM.

Grain size and residual strain of the milled powders with different milling times were also calculated from the XRPD data using the William-Hall method as described in Chapter 3. The results are summarized in Table 5.2 and graphically presented in Fig. 5.6 and Fig. 5.7 respectively. The grain size decreased rapidly

after 10 h of milling, and decreased slightly with further milling. After 60 h of milling, the average grain size was about 10 nm. This value is similar to the one reported in chapter 4 for Ni-15%Fe-5%Mo powders milled for more than 40 h. This suggests that steady-state milling might be attained at this point.

Table 5.2 Average grain size and residual strain of Ni-15%Fe-5%Mo-5%B powders after different milling time.

Milling time (hours)	Average grain size (nm)	Residual strain (%)
5	50	0.7
10	20	1
20	18	0.8
30	15	0.75
40	12	0.77
50	10	0.76
60	10	0.75

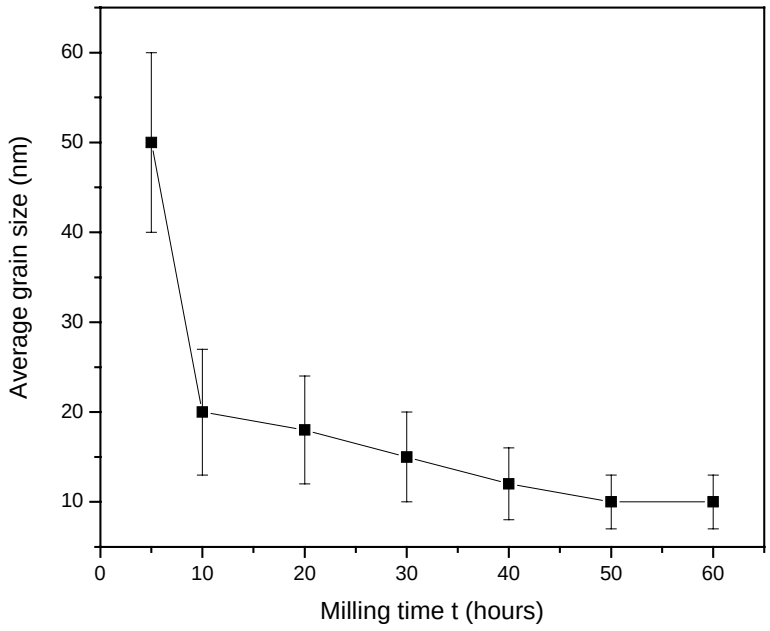

Fig. 5.6 Variation of average grain size of Ni-15%Fe-5%Mo-5%B powders as a function of milling time.

The decrease in grain size was not significant after more than 10 h of milling in the current research. Such an observation was also reported by Surinach et al (1994) for their ball milled $Fe_{40}Ni_{40}B_6P_{14}$ powders, in which average crystalline size remained constant after 30 h of milling and prolonged milling time (up to 156 h) did not reduce the crystallite size. The possible reason for this observation was explained that the small crystal size itself provided a limit for the glide of dislocations and, therefore, for further crystal size refinement, since the forces required to maintain plastic deformation via dislocation movement might be very large in a polycrystalline material with decreasing crystal size.

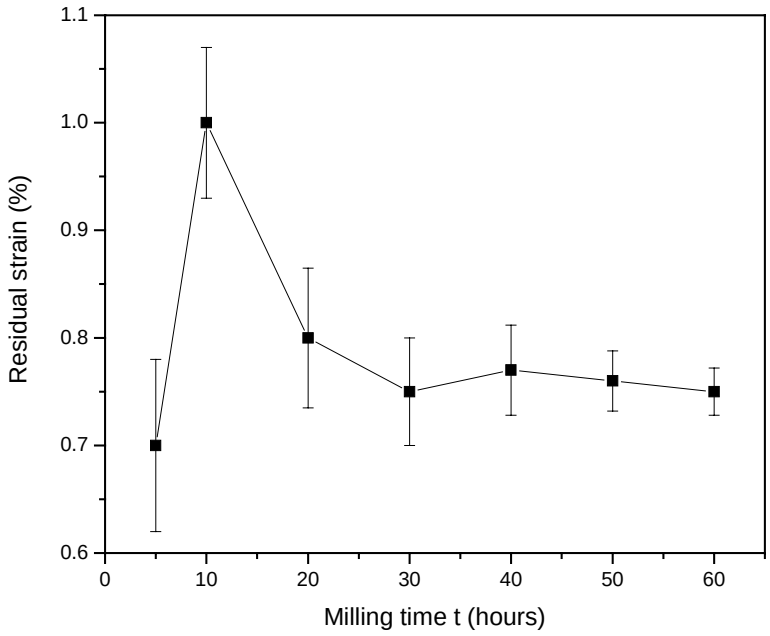

Fig. 5.7 Variation of residual strain of Ni-15%Fe-5%Mo-5%B powders as a function of milling time.

The residual strain of ball milled Ni-15%Fe-5%Mo-5%B powders (Fig. 5.7) follows the same trend as the ball milled Ni-15%Fe-5%Mo powders (Fig. 4.4). The maximum residual strain was observed for 10 h of milling, and further milling caused a decrease in the residual strain to about 0.7%. The reason for such observation during the milling process is the same as the one described in chapter 4 for the ball-milled Ni-Fe-Mo powders. The increase in the residual strain during

the first 10 h of milling was due to the increase in mechanical deformation and the decrease in grain size. The decrease in residual strain after 10 h milling was caused by the change in mechanical deformation due to crystal disintegration and the formation of the amorphous phase.

5.3.1.3 Microstructural observations

(A) SEM observation

The morphology of the Ni-15%Fe-5%Mo-5%B powders produced at different milling times was investigated via SEM analysis and the images are shown in Fig. 5.8. After 5 h of milling, the powders appeared to agglomerate. Further milling caused the disintegration of the agglomerates and a more uniform size distribution was observed after 10 h of milling. However, some agglomeration was still observed. Agglomeration disappeared after 20 h or longer milling time and the powder size became more uniform.

The particle size distribution was also obtained from the SEM micrographs and the results are presented in Fig. 5.9. The mean powder size calculated from the powder size analysis is summarized in Table 5.3. The powder size distribution range was very narrow (0.5 μm to 12 μm), and the mean powder size was about 3 μm for all the powders milled for different times.

X-ray mappings of the powders milled for 5 h, 10 h and 40 h milling were obtained and are shown in Fig. 5.10-5.12, respectively. Due to the small scattering factor of B, the X-ray mapping of B could not be obtained, and only the mappings of Ni, Fe and Mo were obtained. After 5 h of milling, Ni, Fe and Mo were not alloyed since the mappings for Fe and Mo were not homogeneous (Fig. 5.10). This observation is consistent with the XRPD results which showed that after 5 h of milling, the powders still existed as the elemental powders. However, after 10 h of milling, the mappings of Fe and Mo were nearly homogeneous as shown in Fig. 5.11, which indicated that mechanical alloying happened during 5 h to 10 h of milling. Further milling produced homogeneous mappings of these elements as shown in Fig. 5.12 for the powders milled for 40 h.

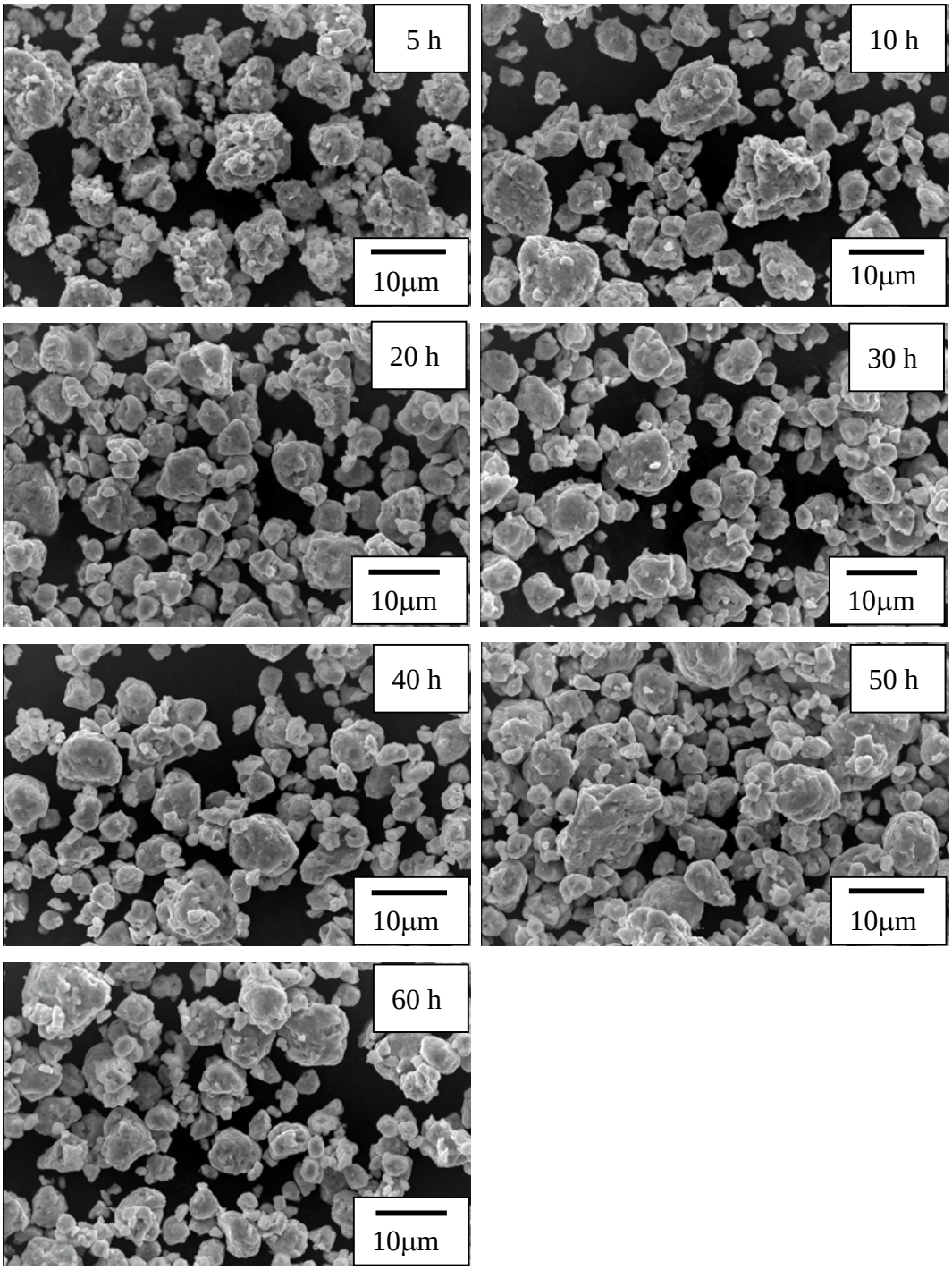

Fig. 5.8 Morphology of Ni-15%Fe-5%Mo-5%B powders milled for different times.

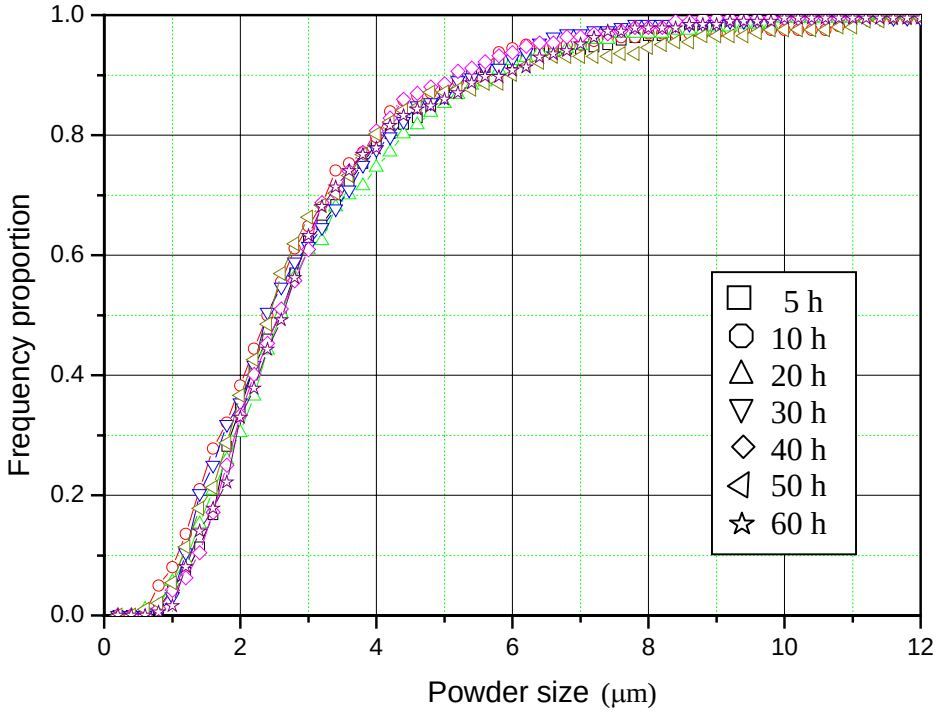

Fig. 5.9 Particle size distribution of the as milled Ni-15%Fe-5%Mo-5%B powders.

Table 5.3 Powder size distribution range and mean powder size of the as milled Ni-15%Fe-5%Mo-5%B powders for different time.

Milling time (h)	Size distribution range (μm)	Mean powder size (μm)
5	1 ~ 10	3.1
10	0.5 ~ 11	2.9
20	0.5 ~ 10	3.1
30	0.5 ~ 10	3.0
40	0.5 ~ 9	3.0
50	0.5 ~ 11	3.1
60	0.8 ~ 10	3.1

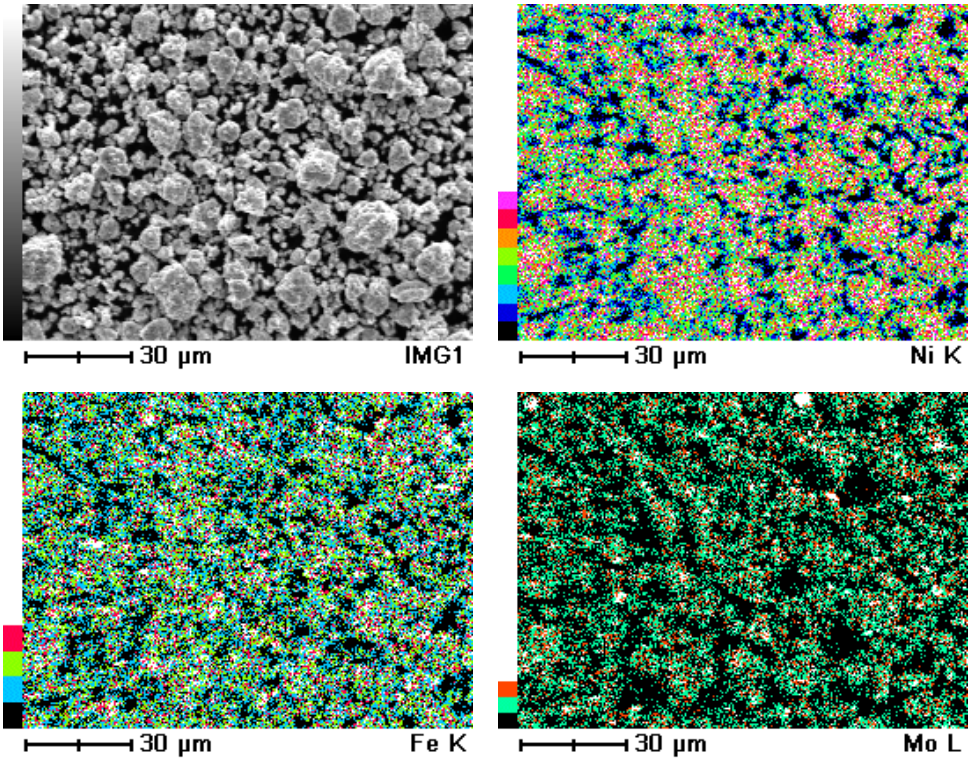

Fig. 5.10 X-ray images of Ni-15%Fe-5%Mo-5%B powders during early stages of ball milling (5 h milling time).

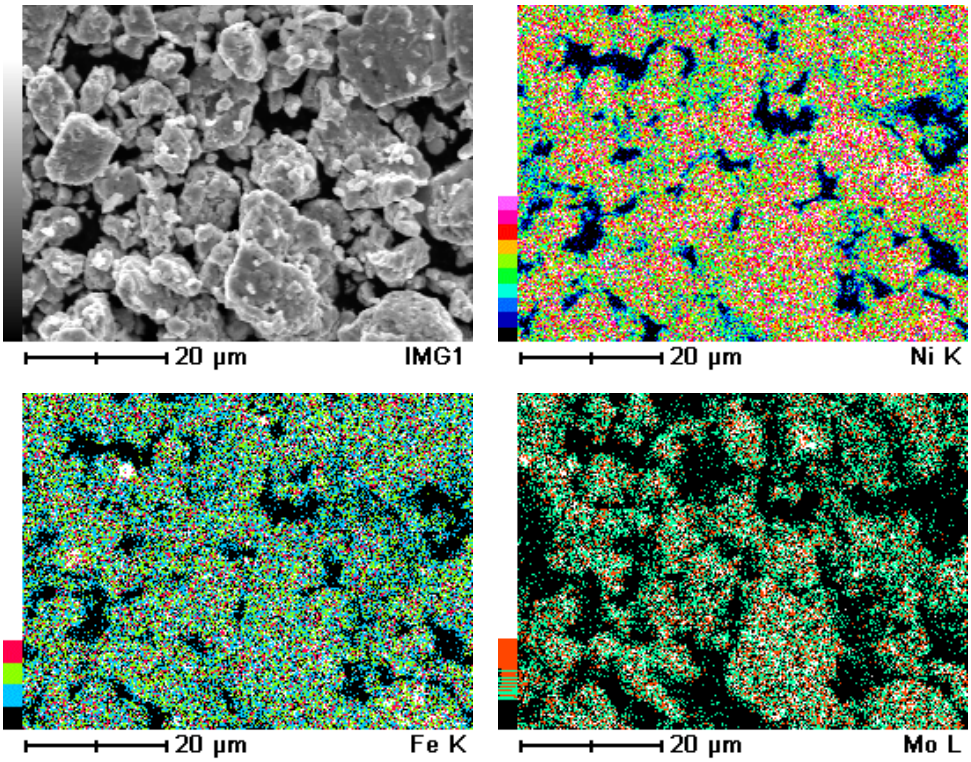

Fig. 5.11 X-ray images of Ni-15%Fe-5%Mo-5%B powders at the intermediate stage of ball milling (10 h milling time).

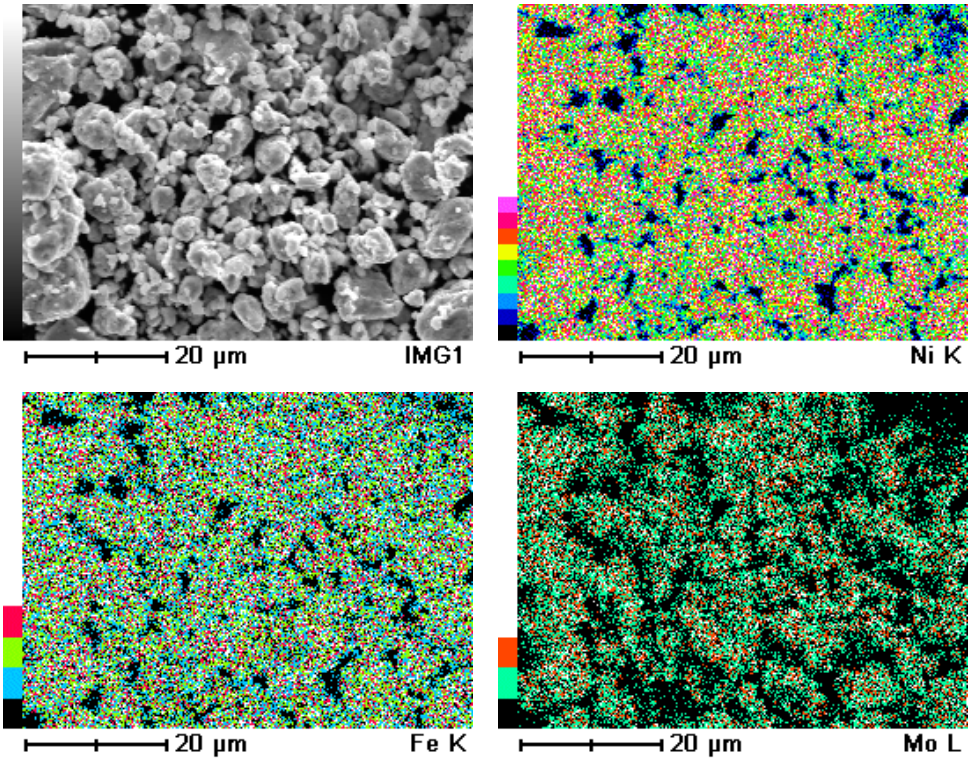

Fig. 5.12 X-ray images of Ni-15%Fe-5%Mo-5%B powders at the completion stage of ball milling (40 h milling time).

In order to study the microstructure of the powders, cross-section images of the powders after polishing and etching were also obtained and are shown in Fig. 5.13. The lamellar structures of the powders are marked in the circle area. The powders contained many intimate layers when they were milled for 5 h and 10 h. However, these intimate layers were not observed for the 40 h milled powder. This observation indicated that although the mechanical alloying took place mainly during the first 10 h of milling, the composition was still heterogeneous as shown in the cross section images of the powders milled for 10 h. Homogeneity was only obtained after further milling and a true alloy was finally obtained. Such lamellar structure was also observed during the initial milling stage of ductile-ductile alloy system in Ag-Cu alloy (Suryanarayana, 2001).

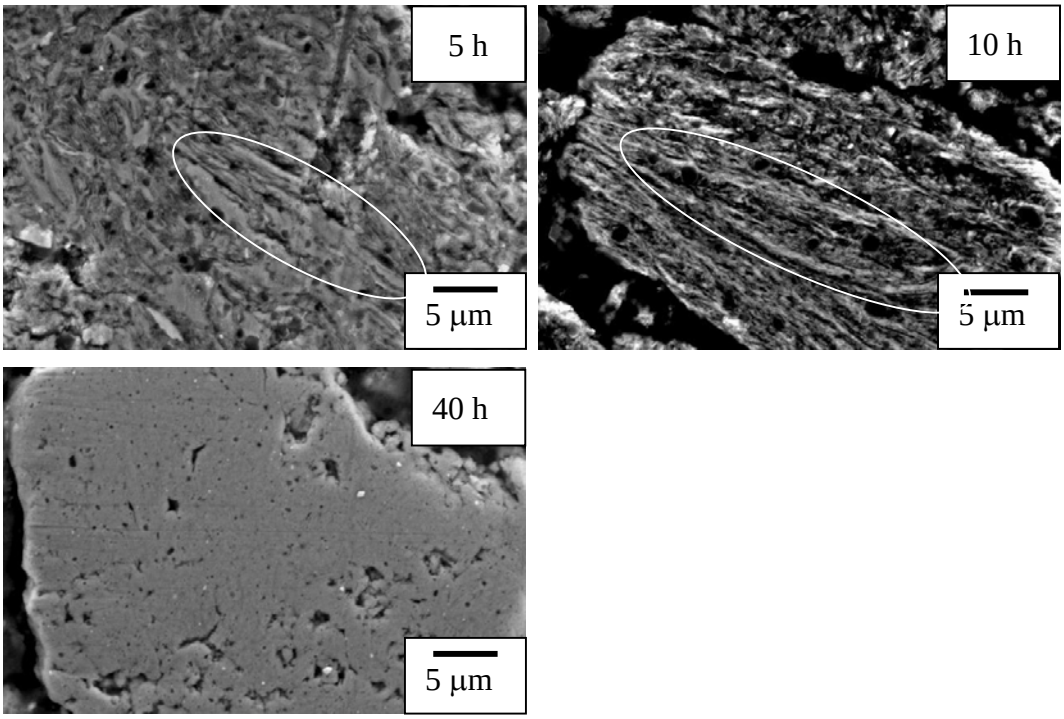

Fig. 5.13 Cross section images of Ni-15%Fe-5%Mo-5%B powders milled for different times (lamellar structure indicated in the circles).

Based on the results obtained for the powder morphology, powder size distribution, X-ray mapping and cross-section images, the milling stages of Ni-15%Fe-5%Mo-5%B powders can also be divided into 3 stages: first, intermediate and final stages. In the first stage of milling, the powders were very soft and they would get flattened very easily by a micro-forging process, and agglomeration would be formed as shown in the powders milled for 5 h. During this stage of ball milling, almost all the initial elements of Ni, Fe and Mo were agglomerated to form powder particles containing coarse layers of the metallic diffusion couples. Further milling led to the formation of composite particles containing numerous narrow layers of Ni, Fe and Mo in good arrangement as a result of the shear force generated by the balls (Fig. 5.13 for the powders milled for 5 h). However, as milling time increased, fracture and welding became the two main processes. Agglomeration would disintegrate gradually as shown from the morphology of the powders milled for 10 h. At the intermediate stage of milling, the elemental layers of Ni, Fe and Mo of the composite powders became very thin and had excellent arrangement with numerous numbers of interfaces between the diffusion couples (Fig. 5.13). When the balance of fracture and welding was

achieved, the powders size would not change with further milling, and this will be considered as the completion stage. According to this, the powders would have reached the steady state after 20 h of milling. Towards the final stage, the elemental layers of Ni and Fe gradually disappeared, and the powder particles no longer had layered-structure morphology, and homogenous powders were obtained.

It was noted that the morphologies of the Ni-15%Fe-5%Mo powders (Fig. 4.12) and the Ni-15%Fe-5%Mo-5%B powders (Fig. 5.8) in the early milling stage were different and the powder size of Ni-15%Fe-5%Mo-5%B was much smaller than the Ni-15%Fe-5%Mo powders. There are two possible reasons for this observation. The first reason is that pre-alloyed and annealed $FeNi_3$ powders were used as the starting powders to prepare the Ni-15%Fe-5%Mo alloy. Although the $FeNi_3$ powders were annealed to release the defects before milling, these powders were still harder than the elemental powders. It was difficult to fracture these powders. The second reason was due to the addition of Boron. It has been reported that the addition of B and P can produce a more uniform distribution of particles and smaller particle size are obtained for Co-Fe-B (P) alloy systems (Li and Ramanujan, 2004).

(B) TEM observation

TEM was used to study the microstructure of the as-milled Ni-15%Fe-5%Mo-5%B powders in detail. Fig. 5.14 shows the BF image and the corresponding diffraction pattern of the Ni-15%Fe-5%Mo-5%B powder sample milled for 5 h. The average grain size was about 15 nm as observed from the BF image. This value is much smaller than the one obtained from the XRPD results, which was about 50 nm. The difference may be due to the fact for TEM only observed from a small area of the sample, which XRPD is a bulk measurement.

The powders were polycrystalline as indicated by the sharp spots in the diffraction pattern shown in Fig. 5.14 (b). The diffraction pattern was indexed as the FCC crystal structure. No diffuse broad ring was observed from the diffraction pattern, indicating that an amorphous phase was not formed at this stage of milling. From the XRPD observation, the powders after 5 h of milling still existed as a mixture

of the elemental powders. It is known that Ni and $FeNi_3$ have FCC crystal structure, while Fe and Mo have BCC crystal structure. Hence, the diffraction pattern shown in Fig. 5.14 (b) can be indexed as the Ni phase.

In general, during the ball milling process, severe plastic deformation is introduced, which can produce distorted regions within subgrains, grain boundaries and even across entire grains. Dislocations were often observed in the milled powders. An example is shown in Fig. 5.15 of HRTEM image of the powders milled for 5 h.

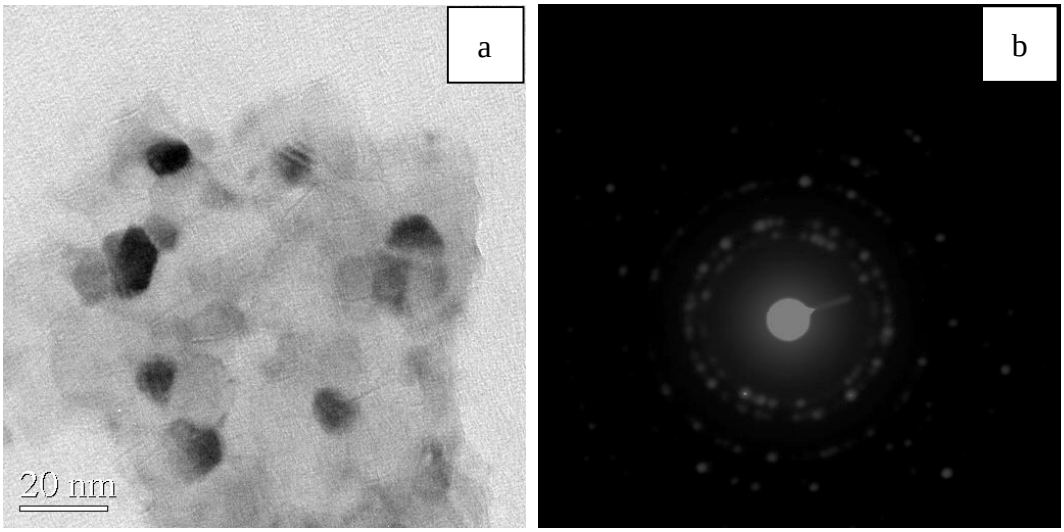

Fig. 5.14 TEM micrographs of Ni-Fe-Mo-B powders after 5 h of milling, (a) BF image and (b) corresponding diffraction pattern.

The TEM micrographs of the Ni-15%Fe-5%Mo-5%B powders milled for 20 h, 40 h and 60 h are shown from Fig. 5.16 to Fig. 5.18 respectively. The average grain size was about 10 nm as observed for these three milled powders. Bright spots as well as broad diffuse rings were observed for the diffraction patterns obtained for the powders milled for 20, 40 and 60 h. Bright dots observed for the diffraction patterns confirmed that crystallites existed in these powders. This is consistent with the XRPD results, which showed that $FeNi_3$ phase was formed after 10 h milling. The broad diffuse rings indicated the presence of an amorphous phase in these powders. The broad diffused rings became more pronounced as the milling time increased. This observation indicated that more amorphous phase was formed with longer milling time. Hence, by combining the DSC and TEM results, it is confirmed that partially amorphous Ni-15%Fe-5%Mo-5%B powders were produced by HEBM,

and as milling time increased, more amorphous phase was formed.

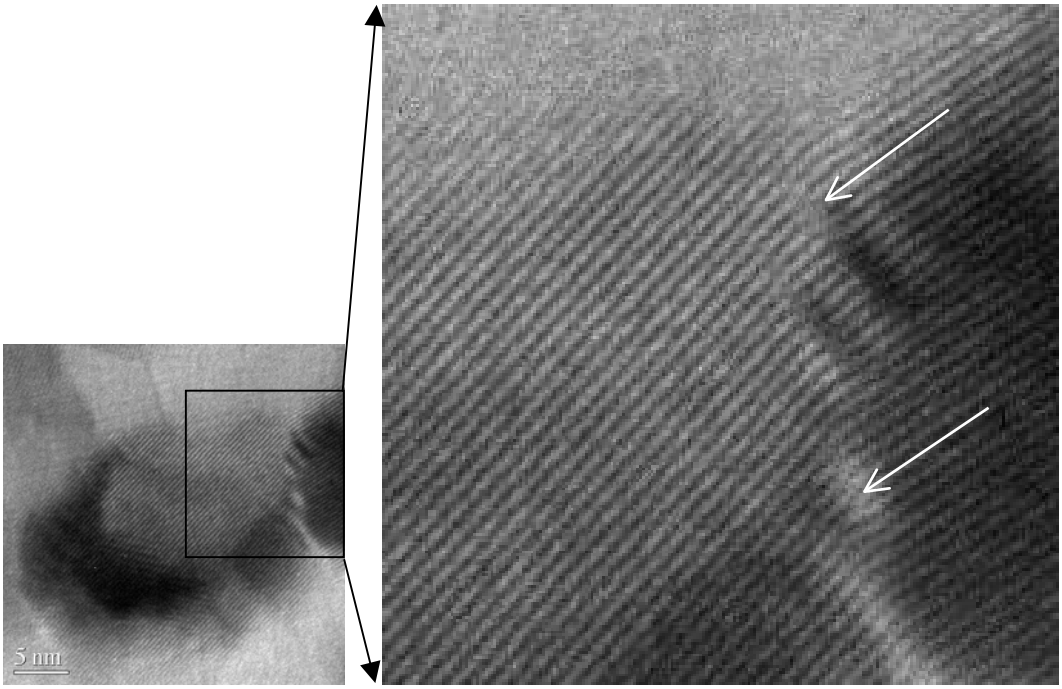

Fig. 5.15 HRTEM and the enlarged image of the Ni-15%Fe-5%Mo-5%B powders milled for 5 h.

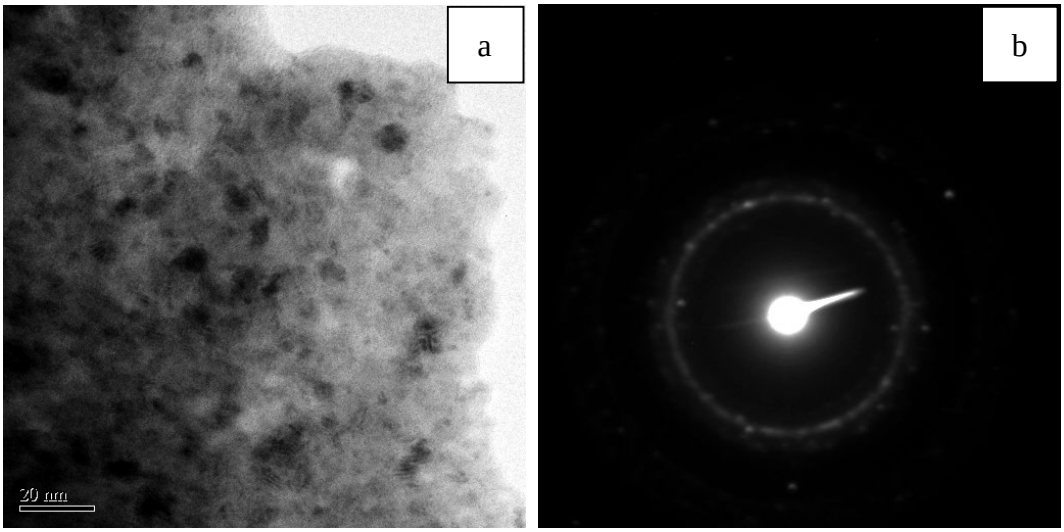

Fig. 5.16 TEM micrographs of the Ni-Fe-Mo-B powders after 20 h of milling, (a) BF image and (b) corresponding diffraction pattern.

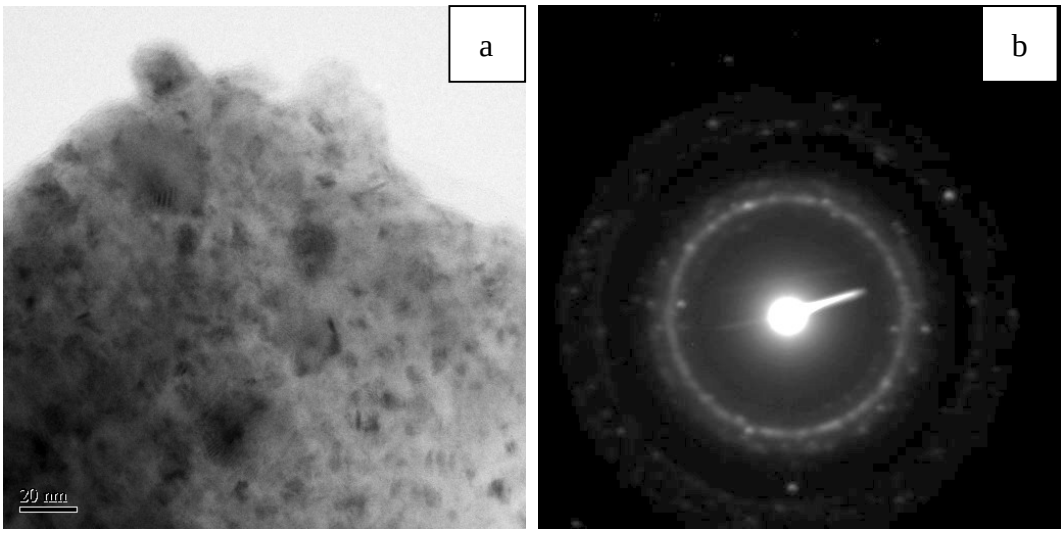

Fig. 5.17 (a) BF image and (b) corresponding diffraction pattern of Ni-Fe-Mo-B powders milled for 40 h.

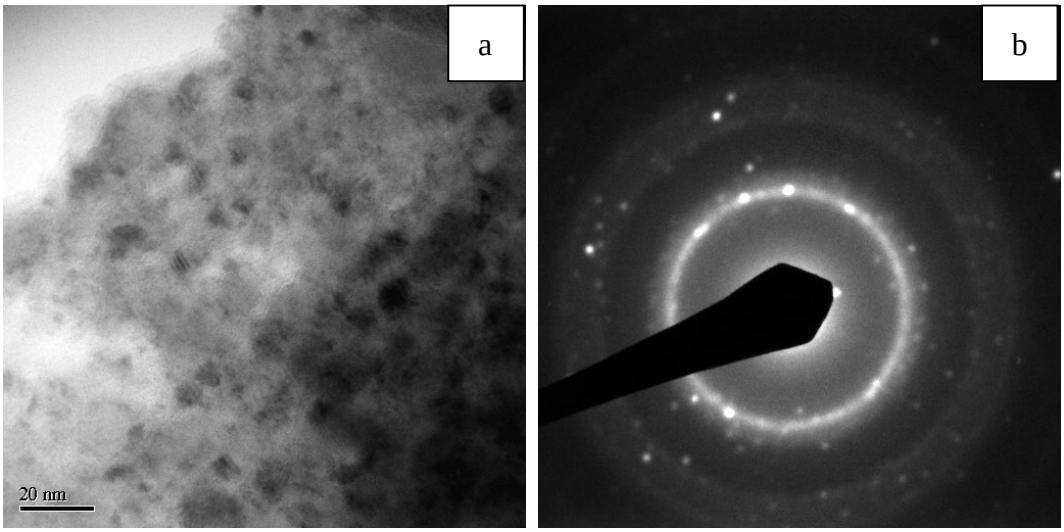

Fig. 5.18 (a) BF image and (b) corresponding diffraction pattern of Ni-Fe-Mo-B powders after 60 h of milling.

From DSC, XRD and TEM observations, it was found that partially amorphous powders were formed after 10 h of milling, and the final products of Ni-15%Fe-5%Mo-5%B powders after 60 h of milling were $FeNi_3$ and amorphous phase. This amorphization process without passing through the liquid state was known as solid-state amorphization reactions (SSAR), including irradiation, interdiffusion of elemental metals, pressure-induced vitrification, and mechanical deformation (Koch, 1996; Koch and Whittenberger, 1996; Suryanarayana, 2001; Manna et al, 2004; Zhang, 2004). In chapter 4, microstructure observation of

Ni-15%Fe-5%Mo powders showed that after 100 h of milling, the powders remained polycrystalline and no amorphous phase was observed for the Ni-15%Fe-5%Mo powders prepared from the pre-alloyed $FeNi_3$ and Mo powders. The observed amorphous phase would attribute to two reasons: the addition of B powders and the mechanical alloying process. And these two effects would be explained in the following paragraphs.

(A) Effect of B

It was mentioned in chapter 2 that two conditions are required for solid-state amorphization reaction. Firstly, the two reacting metals must have a large negative heat of mixing in the liquid (amorphous) state to provide the thermodynamic driving force for the reaction to occur. Accordingly, the two metals must have largely different diffusion rates into each other and in the amorphous alloy to be formed (Koch and Whittenberger, 1996; Suryanarayana, 2001; Zhang, 2004). The second condition requires that the amorphous alloy will form in preference to crystalline intermetallics which have lower free energies. In the current system, the amorphization process is due to the addition of Boron powders. The reason for the formed amorphous phase by the addition of B was explained by many researches (Koch and Whittenberger, 1996; Suryanarayana, 2001; Manna et al, 2004; Zhang, 2004). Due to the small atomic size of B, it can penetrate into the interstitial sites and distort the lattice locally during the initial stage of MA. With further milling time, the powders were subjected to heavy deformations (shear bands, dislocation, etc.), leading to lattice and point defects. When the local distortions caused by the substitution of B atoms reached some critical value, the long-range order of the lattice was destroyed and an amorphous phase was formed. This amorphous phase formed at this stage was still heterogeneous in its composition and structure. With further milling would homogenize the powders and more amorphous phase would be formed. The increase in the amount of amorphous phase with further milling was observed in the current system from the DSC (Table 5.1) and TEM results (Fig. 5.17 and Fig. 5.18).

(B) Effect of mechanical alloying process

From the current study, it was found that the addition of B facilitates the formation of an amorphous phase in the Ni-Fe-Mo alloy system by HEBM. However, only partially amorphous powders were obtained after 60 h of milling. The incomplete amorphization process could be explained by considering the mechanical alloying process.

The thermodynamics and kinetics of amorphous phase formation had been studied (Gilman and Benjamin, 1983; Lee and Koch, 1988; Koch and Whittenberger, 1996; Lai, 1998). The formation of the amorphous phase from A and B elemental metallic powders is rationalized with reference to Fig. 5.19. A hypothetical binary phase diagram featuring some solid solubility on either end and also exhibiting the presence of an intermetallic phase is shown in Fig. 5.19 (a). α and β are the terminal solid solutions, γ is the intermetallic and L represents the liquid phase. The Gibbs free energies of the different phases at a temperature T_r are shown as a function of composition in Fig. 5.19 (b), assuming that the free energy of the undercooled liquid fairly accurately represents the free energy of the amorphous phase. At this temperature, α, β, γ and mixtures of these phases are thermodynamically stable, whereas L is metastable.

The blended elemental powder mixture has a free energy, G_c corresponding to point 1 in Fig. 5.19 (b), half way along the straight line joining the free energies of pure metals A and B. If the two components are allowed to interdiffuse freely, then the lowest free energy state corresponding to the formation of the γ phase, G_i (point 3) will be obtained. Even though thermodynamically this is the lowest free energy state, this can be kinetically prevented from occurring when the free energy G_a, corresponding to the formation of an amorphous phase (point 2), is reached.

Preventing the reaction $c \rightarrow i$ from occurring and favoring $c \rightarrow a$ to occur is possible by the proper choice of metals A and B, the reaction temperature T_r and the reaction time t_r. Two conditions need to satisfy for an amorphous phase to form from a blended elemental powder mixture. First, the two metals must have a large negative heat of mixing in the liquid stage (Koch and Whittenberger, 1996;

Suryanarayana, 2001; Zhang, 2004). The second criterion is that the two metals must have largely different diffusion rates into each other and in the amorphous alloy phase. This favors the kinetics of reaction path $\boldsymbol{c \rightarrow a}$ in Fig. 5.19 (b) over that of reaction path $\boldsymbol{c \rightarrow i}$.

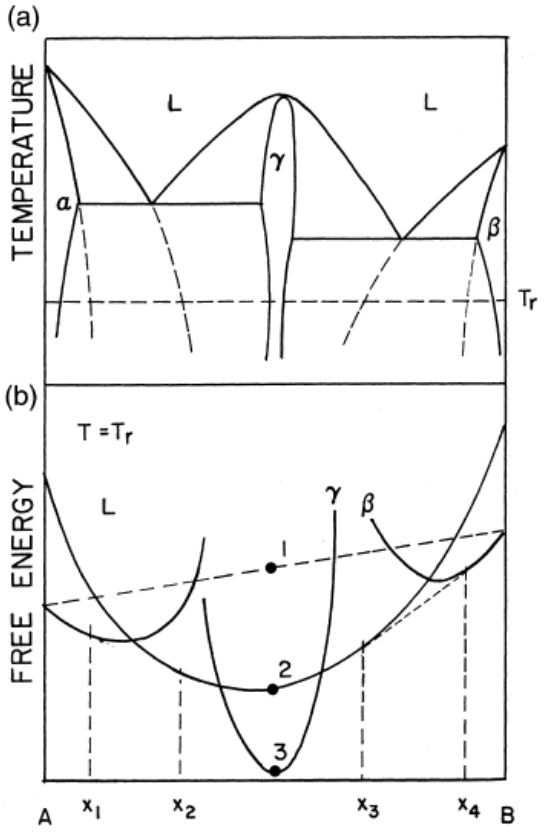

Fig. 5.19 (a) Hypothetical binary phase diagram featuring some solid solubility on either end and showing the presence of an intermetallic phase. (b) Gibbs free energy versus composition at a temperature corresponding to T_r in the above diagram.

The reaction time scales are important because not only should one allow the formation of the amorphous phase, but also maintains it without transforming to the equilibrium phases. These concepts could be explained with reference to Fig. 5.20. It is assumed that the free energy of the blended elemental mixture is $\boldsymbol{G_c}$, that of the amorphous phase is $\boldsymbol{G_a}$, and that of the intermetallic is $\boldsymbol{G_i}$, then these are schematically shown in Fig. 5.20. To prevent the stable intermetallic from forming, the time scale for the formation of the amorphous phase from the blended elemental mixture, $\boldsymbol{t_{c \rightarrow a}}$ should be much shorter than $\boldsymbol{t_{c \rightarrow i}}$. Further, since the amorphous phase

is metastable, $t_{a\to i}$ should be much longer than $t_{c\to a}$ so that the stability of the amorphous phase can be increased. Thus, the kinetics conditions for the formation of an amorphous phase by solid-state reactions can be summarized as:

$t_{c\to a} \le t_{c\to i}$ and $t_{a\to i} \ge t_{c\to a}$

In our experiment, it was observed that the $FeNi_3$ intermetallic phase had already formed after 10 h of milling and some partially amorphous phase began to form at this condition. From the Gibbs energy consideration according to Fig. 5.20, it can be concluded that the $FeNi_3$ intermetallic phase has lower Gibbs energy and it needs less time to form as compared to the amorphous phase. This intermetallic phase is stable at this condition and will not transform to the amorphous phase. However, from broader and higher intensity exothermic peaks obtained from DSC, and the more obvious diffusion rings observed from TEM diffraction pattern, it was found that more amorphous phase was formed with further milling. This observation contradicted with the thermodynamic and kinetic considerations showed in Fig. 5.19 and Fig. 5.20. Hence, the mechanism of amorphization by ball milling should be considered.

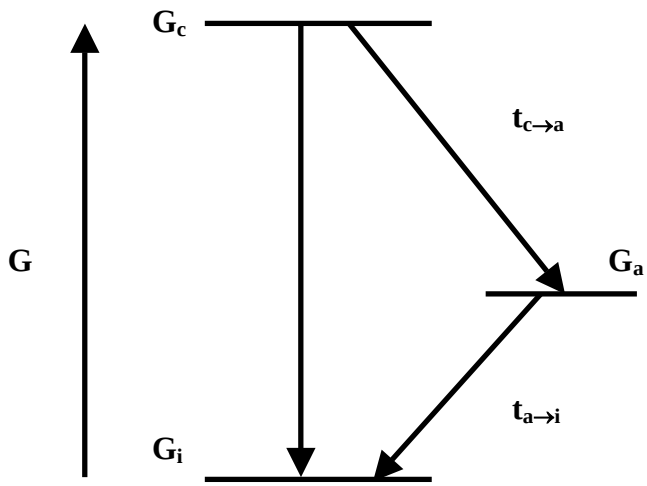

Fig. 5.20 Schematic free energy diagram indicating the criteria to be met for solid state amorphization

Mechanical amorphization process by mechanical alloying works through the absorption of mechanical energy. The realization of amorphization by mechanical

alloy is through collision and mixing of atoms. During the milling process, the atoms will be shifted away from their initial lattice points after impact during milling: they will then be trapped by other atoms. The trapped atoms can be located at new lattice points which may cause structural defects such as vacancies, dislocations, grain boundaries, and anti-phase boundaries. The continuous decreased in grain size (and consequent increase in grain boundary area) and a lattice expansion would also contribute to the increase in free energy of the system. These defects raised the free energy of the intermetallic system to a level higher than that of the amorphous phase and consequently, it became possible for the amorphous phase to form.

However, higher milling energies also produced more heat (and higher temperatures) and this could result in the crystallization of the amorphous phase. The ball milling caused the crystallization of amorphous phase was reported by Eckert et al (1988) in their Ni-Zr system. It was found that milling in a planetary ball mill at an intensity of 3 did not produce any amorphous phase due to the insufficient energy available at low intensities. When the intensity was increased to 5, amorphous phase formation was observed in a wide composition range of 30-83 at.% Ni. At an intensity of 7, amorphous phase formation was observed, but only between 66 and 72 at.% Ni. These observations suggested that that with increasing milling energy, the heat generated was also high, which crystallizes the amorphous phase.

The steady-state dynamical equilibrium between amorphization and crystallization was also reported by Calka and Radlinski (1991) for Mg-Zn alloys. To produce fully amorphous $Mg_{70}Zn_{30}$ alloys from the crystalline master alloy a two-step ball-milling procedure was used. Initially, the milling was performed using the high-energy mode, which resulted in a mixture of the amorphous phase and the metastable crystalline phase $Mg_{51}Zn_{20}$. Under the high-energy milling conditions this mixture corresponded to a steady-state dynamical equilibrium between amorphization and crystallization. Full amorphization could only be achieved by switching to the low energy mode.

Therefore, a balance between the increased defect concentration due to addition of B and the production of heat due to the milling process would determine the nature of the final product phases. Too low an intensity will not provide enough energy to produce an amorphous phase while too high intensities, the amorphous phase formed would crystallize. The formation of the partially amorphous phase in the current experiment can be due to two reasons: insufficient milling intensity and heat produced from the milling process.

5.3.1.4 Magnetic properties

Saturation magnetization $\boldsymbol{M_s}$ and coercivity $\boldsymbol{H_c}$ were determined from the hysteresis loops and the results are summarized in Table 5.4. Fig. 5.21 shows the variation of $\boldsymbol{M_s}$ of the Ni-15%Fe-5%Mo-5%B powders with milling time. $\boldsymbol{M_s}$ for the powders milled for 5 h and 10 h was about 62 emu/g. $\boldsymbol{M_s}$ decreased gradually with further milling to about 40 emu/g for the 40 h milled powders. $\boldsymbol{M_s}$ remained more or less constant with further milling up to 60 h.

As mentioned earlier in chapter 4 for the ball milled Ni-Fe-Mo powders, the appearance of the LI_2 structure in the $FeNi_3$ composition is the main contribution to the magnetic properties of $FeNi_3$ based alloy. Saturation magnetization decreases with the destruction of this structure. For the current Ni-Fe-Mo-B system, the destruction of this structure can be caused by the substitution of Mo atoms into the $FeNi_3$ structure and the amorphization of the powders. The decrease in saturation magnetization caused by the amorphization of the powders was reported by Pan et al (1994) for their mechanical alloyed Fe_3Sn powders. They found that $\boldsymbol{M_s}$ decreased with increasing milling time up to 30 h when an amorphous phase was formed.

In this experiment, the amorphous phase began to form after 10 h of milling, and more amorphous phase was formed with further milling time as deduced from the DSC results. However, the increase in the amount of amorphous phase with milling time could not explain the nearly constant saturation magnetization after 40 h of milling. Hence, the effect of the substitution of Mo atoms into the $FeNi_3$ structure is

likely to be the main reason for the decrease in $\boldsymbol{M_s}$. From the XRPD results, the substitution of Mo atoms were completed after 30 h of milling, however saturation magnetization was observed to decrease further after 40 h of milling. Combining the results obtained from XRPD and VSM, it could be concluded that Mo atoms took 40 h of milling to complete the substitution process, and the decrease in $\boldsymbol{M_s}$ with milling time was mainly due to the destruction of the long-rang order caused by the substitution of Mo atoms into the $FeNi_3$ structure.

The saturation magnetization of the Ni-Fe-Mo powders after 100 h of milling (Fig. 4.23) is nearly same as the Ni-Fe-Mo-B powders after 40 h of milling. This observation further confirmed that the Mo substitution process is the main reason for the decrease in the $\boldsymbol{M_s}$, and the amorphization process has less effect on $\boldsymbol{M_s}$.

The coercivity of the Ni-15%Fe-5%Mo-5%B powders milled for different times is shown in Fig. 5.22. The coercivity of the 5 h milled powders was about 135 Oe. $\boldsymbol{H_c}$ decreased sharply when the milling time increased to 10 h. Further increase in milling time to 20 h caused a slight decrease in $\boldsymbol{H_c}$ to about 20 Oe. The coercivity remained constant at around this value when milling time increased up to 60 h.

The variation of coercivity with residual strain and average grain size are shown in Fig. 5.23 and Fig. 5.24 respectively. The high coercivity obtained for the 5 h mechanically alloyed powders could be caused by several factors: internal stress, the status of the elemental powders and the presence of the contaminated surface. During the milling process, the powders were flattened and deformed by the colliding media. The flattened surface might experience a much higher strain rate deformation than the core (Liu and Chang, 2001a). Since there was a limited plastic strain in the powder, the impact load from the colliding balls might not transfer into the core. This might induce a variation in the residual stress across the flattened powder. Consequently, the residual stress on the surface of the flattened powder was likely to be compressive. Furthermore, the flattened powders with different degrees of deformation were mechanically keyed together but without sufficient time for the atomic diffusion to complete between them. This resulted in the formation of the imperfect interfaces between the flattened powders. In addition, the powders were still the elemental powders after 5 h of milling, the composition of the powders were

heterogeneous with a multi-layered structure (Fig. 5.13). These imperfect interfaces might act as pinning sites for domain walls and cause a high $\boldsymbol{H_c}$ for the powders milled for 5 h of milling.

Table 5.4 Saturation magnetization $\boldsymbol{M_s}$ and coercivity $\boldsymbol{H_c}$ of the Ni-15%Fe-5%Mo-5%B powders milled for different time.

Milling time (hours)	Saturation magnetization (emu/g)	Coercivity (Oe)
5	62.2	135.3
10	61.8	36.9
20	53.8	20.1
30	47.5	18.5
40	41.1	17.9
50	40.5	18.0
60	39.5	18.2

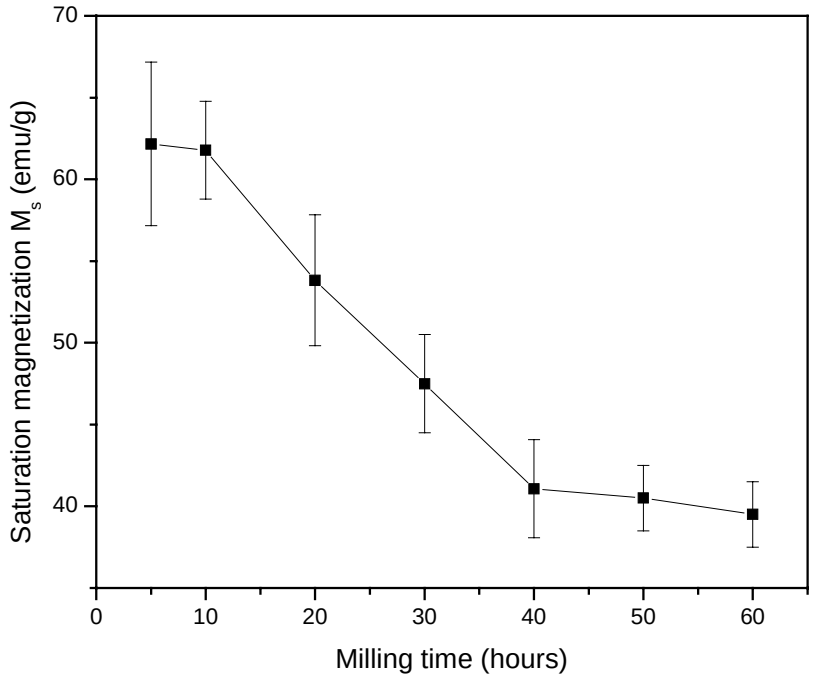

Fig. 5.21 Saturation Magnetization of Ni-15%Fe-5%Mo-5%B powders as a function of milling time.

The sharp decrease in coercivity after 10 h of milling is most likely due to the

decrease of grain size (Fig. 5.24). As milling time increased to 10 h, the residual strain reached a maximum value (Fig. 5.23). This would cause an increase in coercivity. The decrease in coercivity for powders milled for more than 10 h was attributed to the decrease of grain size. It was reported when a polycrystalline grain size was smaller than the width of a magnetic domain wall, there would be little tendency for crystalline orientations to affect the energy of magnetic orientation in the materials (Herzer, 1990). This was especially so when the materials became amorphous, and there was no impedance in the movement of the domains in the amorphous situation. Hence, a relatively low coercivity was observed for amorphous powders. Coercivity plotted as a function of sixth power of grain size (for >10 h of milling) is shown in Fig. 5.25. This line fits reasonably well to the random anisotropy model that when the grain size is smaller than the width of a magnetic domain wall, coercivity is sixth power of grain size.

It is noted that the coercivity of the Ni-Fe-Mo-B powders after 60 h of milling is larger than the Ni-Fe-Mo powders after 100 h of milling (Fig. 4.24). The Ni-Fe-Mo-B powders were partially amorphous, and should have lower coercivity compared to the nanocrystalline Ni-Fe-Mo powders. A possible reason for the high coercivity observed in the Ni-Fe-Mo-B powders could be due to the higher residual strain.

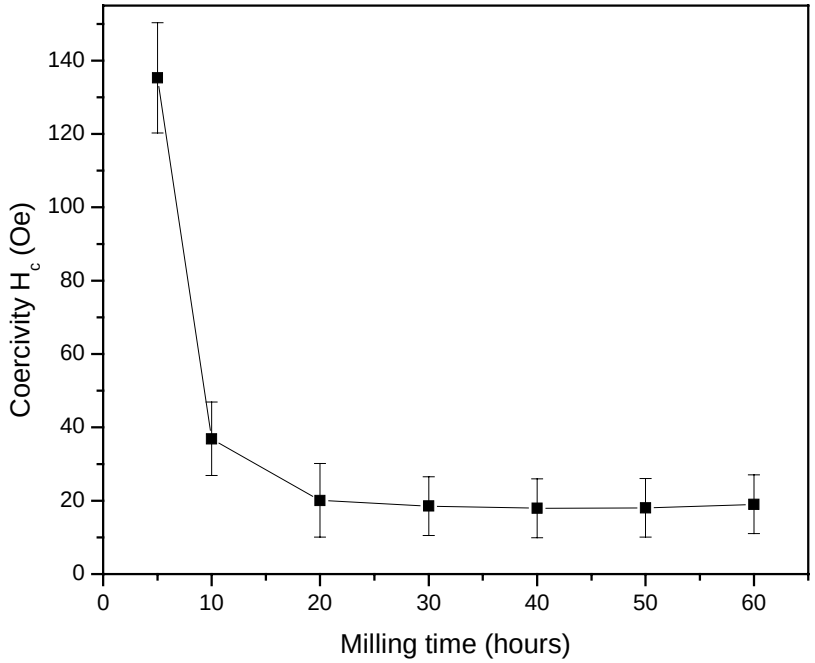

Fig. 5.22 Coercivity of Ni-15%Fe-5%Mo-5%B powders as a function of milling time.

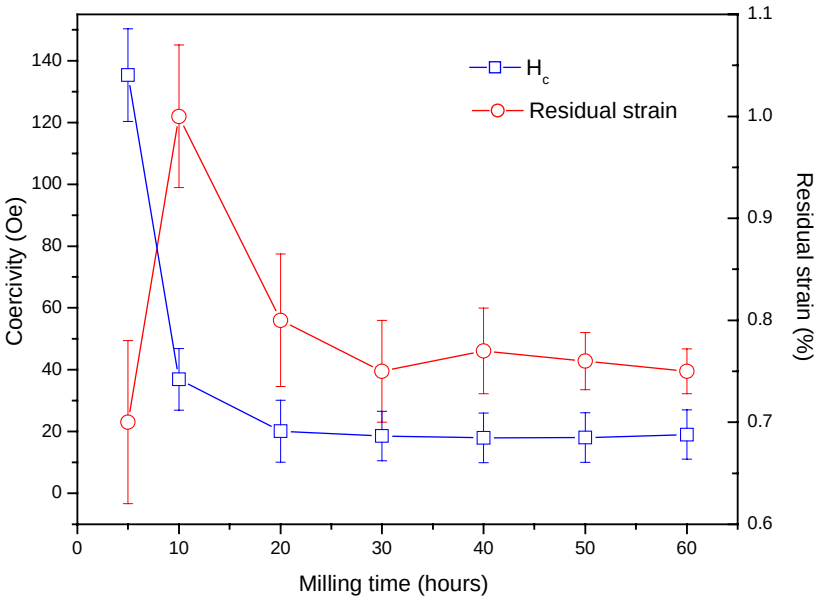

Fig. 5.23 Variation of coercivity and residual strain with milling time.

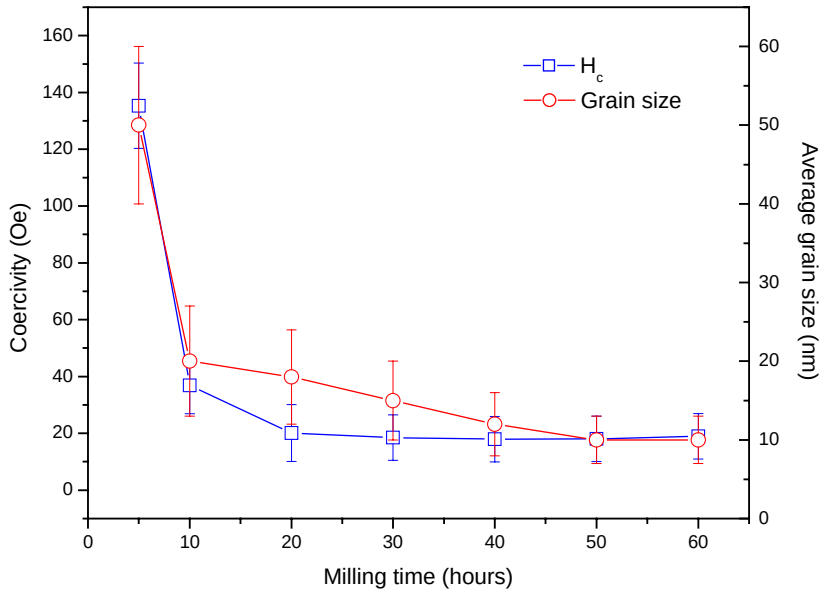

Fig. 5.24 Variation of coericivity and average grain size with milling time.

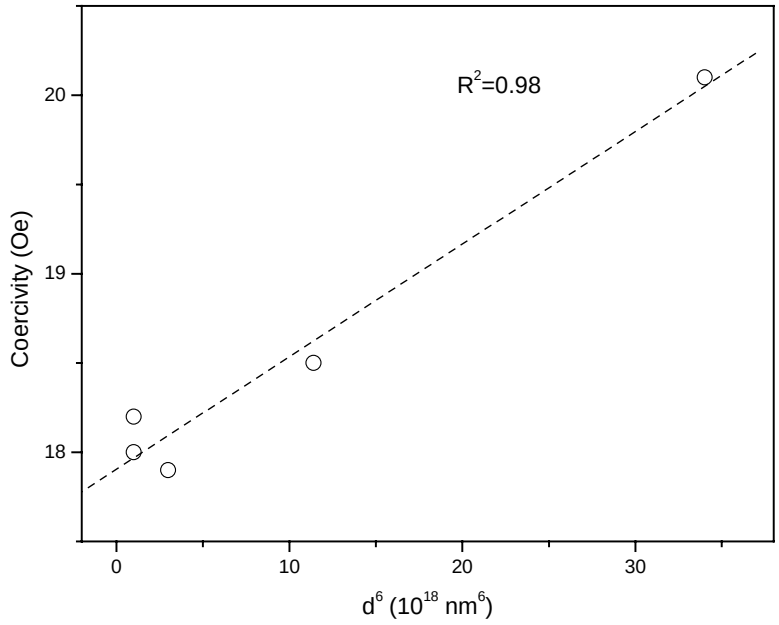

Fig. 5.25 Coercivity $\boldsymbol{H_c}$ against sixth power of grain size $\boldsymbol{d^6}$.

5.3.2 Annealed powders

Based on the DSC results (refer to section 5.3.1.1), the exothermic peaks observed were assumed to be the crystallization of the amorphous phase that was formed during the milling process. In order to study in detail the crystallization process of the amorphous phase, the powders milled for 40 h were subjected to a series of annealing experiments. The onset temperature was around 510°C when a heating rate of 10°C /min was used (Fig. 5.1). Hence, four annealing temperatures (480, 520, 600 and 700°C) were chosen, and the powders were annealed at these temperatures for 30 min in a vacuum furnace.

5.3.2.1 XRD results

Fig. 5.26 shows the crystallization process of the milled powders before and after annealing. When the powders were annealed at 480°C for 30 min, the major phase was still $FeNi_3$. However, small peaks corresponding to metastable $(Fe, Ni, Mo)_{23}B_6$ (JCPDS 38-888) phase started to appear. As the annealing temperatures increased further, the peaks corresponding to this metastable phase became more pronounced. In addition, as the annealing temperatures increased, the intensity of all the peaks increased and the peaks became sharper, which indicated an increase in grain size. From these observations, the crystallization process of the partially amorphous powders could be summarized as follows:

$$amorphous + FeNi_3 \xrightarrow{530^{o}C} (Fe, Ni, Mo)_{23} B_6 + FeNi_3$$

From the XRPD results, the metastable $(Fe, Ni, Mo)_{23}B_6$ phase crystallized from the amorphous phase and coexisted with the $FeNi_3$ phase after annealing. The crystallization of $(Fe, Ni, Mo)_{23}B_6$ phase from the amorphous phase was also reported by Li et al (1999) in their $Fe_{40}Ni_{38}Mo_4B_{18}$ amorphous ribbon. They annealed their amorphous ribbon from 700 K to 1060 K (427 to 787°C). They found that the fcc (Fe, Ni) solid solution was the primary phase to crystallize from the amorphous matrix and the cubic $(Fe, Ni, Mo)_{23}B_6$ phase was the secondary phase to crystallize from the amorphous matrix. However, very little was mentioned with

regard to the $(Fe, Ni, Mo)_{23}B_6$ phase.

According to the JCPDS records, $(Fe, Ni, Mo)_{23}B_6$ was first reported by Kamzeeva et al (1984) when they compared the process of crystallization of $Fe_{40}Ni_{38}Mo_4B_{18}$ alloy from the liquid and amorphous phase by means of X-ray structure analysis and diffraction electron microscopy. $(Fe, Ni, Mo)_{23}B_6$ was one of the metastable phase formed, and was found to have a FCC structure with a lattice parameter of 1.055 nm. The exact atomic ratio for Fe, Ni and Mo was not indicated. It was also reported the cubic boride $(Fe, Ni, Mo)_{23}B_6$ is isomorphic with that of the carbide $Cr_{23}B_6$ which has the space group Fm3m and contains four formula units or 116 atoms per unit cell. The presence and identification of this metalstable phase was obtained by electron diffraction, usually obtained from local microregions.

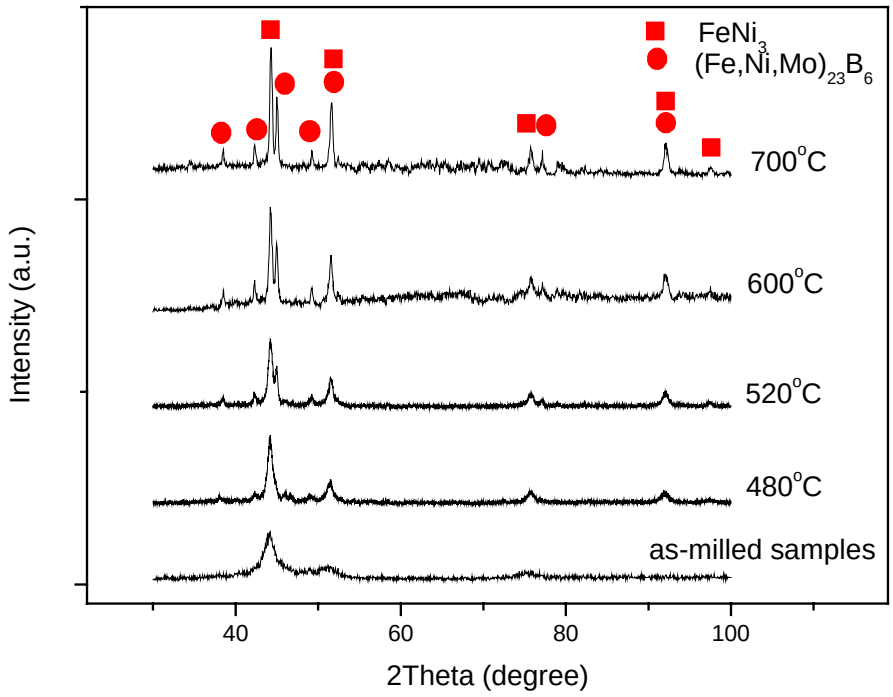

Fig. 5.26 XRPD data of 40 h milled Ni-15%Fe-5%Mo-5%B powders annealed at different temperatures for 30 min.

5.3.2.2 Microstructure observation

Detailed microstructural studies of the powders annealed at different temperatures were performed using TEM. Fig. 5.27 shows the BF image and the corresponding diffraction pattern of the Ni-15%Fe-5%Mo-5%B powders annealed at 480°C for 30 min. The average grain size was about 20-30 nm as observed from the BF image. The diffraction rings in the diffraction pattern showed that the powders were polycrystalline and the grains were very small. The first two slightly diffused rings suggested the possible existence of the amorphous phase. The diffraction pattern was indexed as a mixture of $FeNi_3$, $(Fe, Ni, Mo)_{23}B_6$ and amorphous phase. Comparing the microstructure of the powders milled for 40 h (Fig. 5.17) and the one annealed at 480°C for 30 min (Fig. 5.27), grain growth could be observed from 10 nm to 20-30 nm. In addition, the diffused rings in the DP became less distinct and more bright dots were observed after annealing. The disappearance of the diffused rings meant that amorphous phase began to crystallize. When the powders were annealed at 520°C (Fig. 5.28), the diffused rings observed in Fig. 5.27 could no longer be observed, which indicated that the crystallization of the amorphous phase had completed. The grain size of the powders annealed at 520°C did not change when compared to the powders annealed at 480°C.

The grains remained small after annealing at 480°C and 520°C. SADP could not be obtained for a single grain. High resolution TEM (HRTEM) was used to obtain the lattice information of the annealed powders. HRTEM of the Ni-15%Fe-5%Mo-5%B powders annealed at 480°C for 30 min is presented in Fig. 5.29. The grain size was about 20 nm. This lattice image was indexed as the $(Fe, Ni, Mo)_{23}B_6$ (200) plane. These observations confirmed the XRPD results that after annealing, the metastable $(Fe, Ni, Mo)_{23}B_6$ phase was crystallized from the amorphous phase.

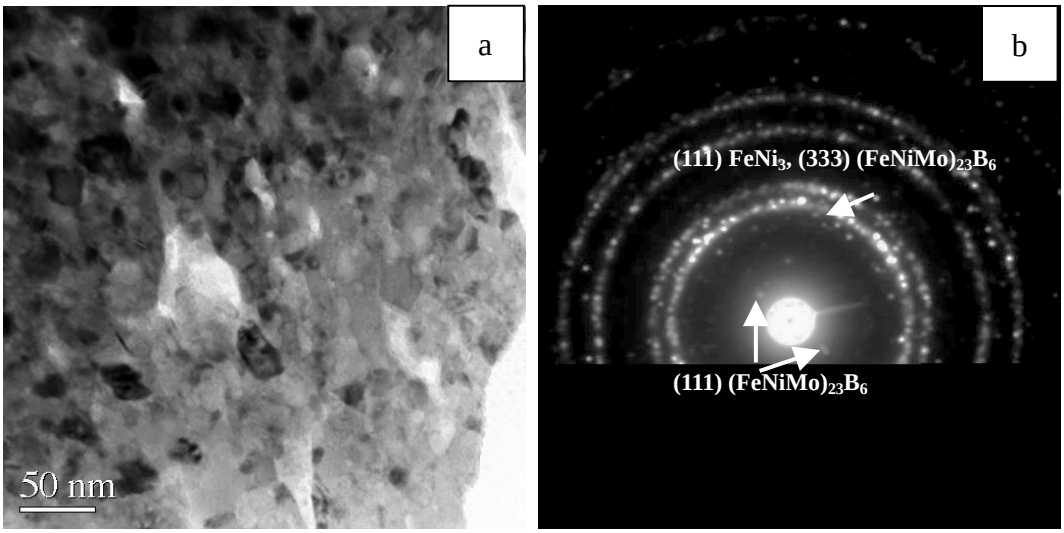

Fig. 5.27 TEM micrographs of Ni-Fe-Mo-B powders annealed at 480°C for 30 min. (a) bright field image and (b) corresponding diffraction pattern.

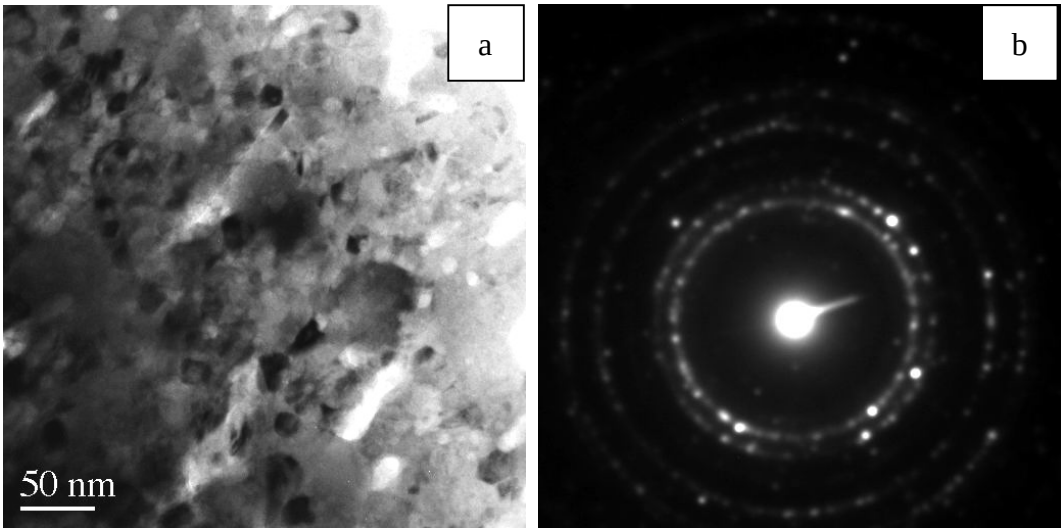

Fig. 5.28 TEM micrographs of Ni-Fe-Mo-B powders annealed at 520°C for 30 min. (a) bright field image and (b) corresponding diffraction pattern.

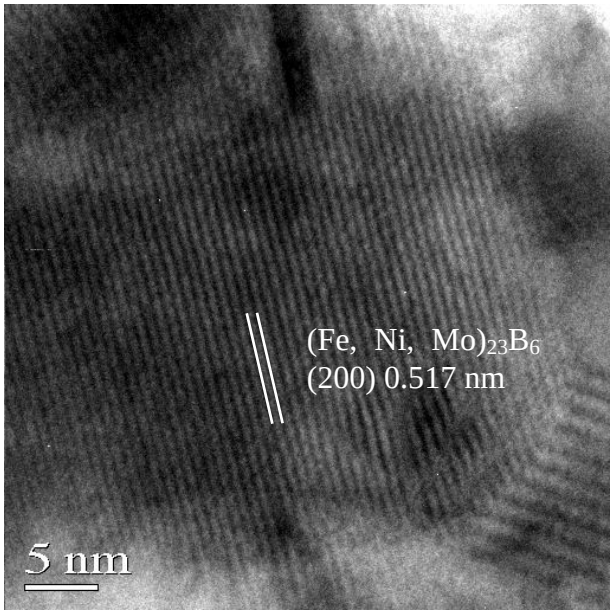

Fig. 5.29 HRTEM of the Ni-15%Fe-5%Mo-5%B powders annealed at 480°C for 30 min showing the existence of the metastable $(Fe, Ni, Mo)_{23}B_6$ phase.

Fig. 5.30 shows some typical DF images of the Ni-15%Fe-5%Mo-5%B powders annealed at 600°C and 700°C. The grains were observed to grow from 20-30 nm for low annealing temperature of 480°C and 500°C to about 50 nm for high annealing temperature of 600°C and 700°C. The average grain size after annealing at the various temperatures is summarized in Table 5.5. From the average grain size observation, it could be concluded that the metastable $(Fe, Ni, Mo)_{23}B_6$ phase began to crystallize at 480°C, and the crystallization process was completed when the powders were held at 520°C for 30 min. Further annealing at 600°C and 700°C only caused the grain to grow.

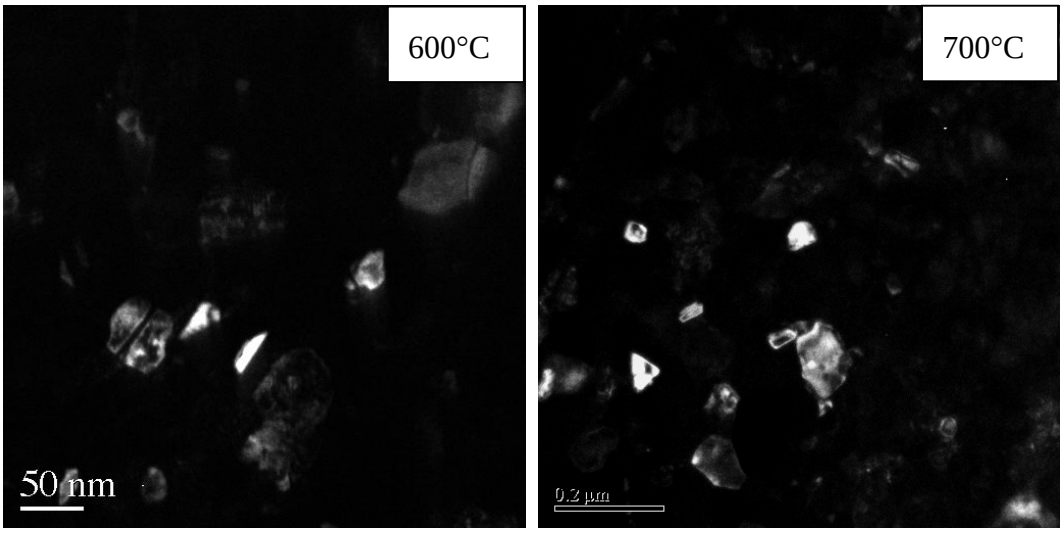

Fig. 5.30 Typical TEM dark field images of the milled Ni-15%Fe-5%Mo-5%B powders annealed at 600°C and 700°C for 30 min.

Table 5.5 Average grain size after annealing.

Annealing temperatures (°C)	Average grain size (nm)
480	20
520	30
600	55
700	80

5.3.2.3 Magnetic properties

Saturation magnetization and coercivity of the annealed powders are summarized in Table 5.6. Fig. 5.31 shows the saturation magnetization of the annealed Ni-Fe-Mo-B powders as a function of annealing temperatures. In general, the saturation magnetization $\boldsymbol{M_s}$ increased after the annealing process. $\boldsymbol{M_s}$ increased from about 42 emu/g to about 54 emu/g after annealing at 480°C for 30 min. The $\boldsymbol{M_s}$ value kept nearly constant after that.

It was observed that the annealing process caused the crystallization process of the amorphous phase and in general, the $\boldsymbol{M_s}$ values of the annealed samples were larger than the as-milled (unannealed) powder. The reason for the increase of $\boldsymbol{M_s}$ after annealing was mainly due to the obvious of $FeNi_3$ phase after annealing. After

annealing at 480°C, most of the existing phase was $FeNi_3$, and only a very small amount of (Fe, Ni, Mo)$_{23}B_6$ phase existed, as evident from the XRPD results. The increase in $\boldsymbol{M_s}$ was purely due to the crystallization process. An increase in $\boldsymbol{M_s}$ was also reported for ball milled amorphous Fe-Sn powders after the annealing process that crystallized the amorphous phase (Pan et al, 1994). However, as annealing temperature increased further, more and more (Fe, Ni, Mo)$_{23}B_6$ phase crystallized from the amorphous phase and coexisted with the $FeNi_3$ phase. The presence of (Fe, Ni, Mo)$_{23}B_6$ phase caused a slight decrease in the saturation magnetization.

The annealing process at the various temperatures had a different effect on the coercivity of the milled powders, and this is presented in Fig. 5.32. After annealing at 480°C, the coercivity decreased slightly from about 18 Oe to 12 Oe. The coercivity increased dramatically to about 75 Oe when the annealing temperature was increased to 520°C. When the annealing temperature was increased further to 600°C, a significant decrease in the coercivity was observed. A gradual decrease in coercivity was then observed when the annealing temperature was further increased to 700°C.

Table 5.6 Saturation magnetization $\boldsymbol{M_s}$ and coercivity $\boldsymbol{H_c}$ of the Ni-15%Fe-5%Mo-5%B powders annealed at different temperatures.

Annealing temperature (°C)	Saturation magnetization (emu/g)	Coercivity (Oe)
As-milled	41.1	17.9
480	53.9	12.7
520	53.4	72.9
600	52.7	30.7
700	52.4	23.3

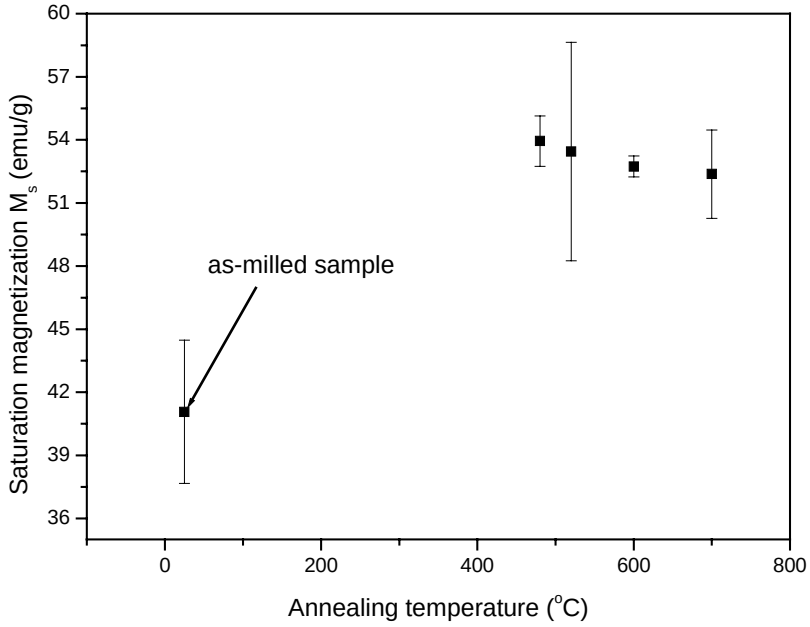

Fig. 5.31 Saturation magnetization of Ni-15%Fe-5%Mo-5%B powders as a function of annealing temperature.

The initial slight decrease in coercivity at 480°C was due to the release of strain through the annealing process. Many defects existed in the as-milled powders due to the milling process which involved repeated cold welding and fracturing, and these defects would inhibit the movement of domain wall. When the powders were annealed at low temperature, the strain stored in the powders was released, and a lower coercivity was observed. Although (Fe, Ni, Mo)$_{23}$B$_6$ phase began to crystallize from the amorphous phase, the amount was small as evident from the XRPD results. The effect of the (Fe, Ni, Mo)$_{23}$B$_6$ phase on coercivity is negligible for this annealed sample.

As the annealing temperature increased further, the grain size would increase along with the release of the defects. According to Herzer's diagram, when the grain size was in the range of nanometer, an increase in grain size would cause an increase in coercivity. The release of defects would be completed by annealing at low temperature, so the high annealing temperature only caused an increase in grain size. Thus, this explained the exceptionally high coercivity observed for the sample annealed at 520°C. In addition, as more and more (Fe, Ni, Mo)$_{23}$B$_6$ phase

crystallized and grew, it would also caused an increase in coercivity.

The sharp decrease in coercivity for the sample annealed at 600°C was solely due to grain size effect. When a grain is large enough to contain a domain wall, magnetization is dominated by domain wall movement. At this stage, the coercivity of the powders will decrease as the grain size increases. So, the coercivity of the powders decreased as the annealing temperature increased when the powders were annealed at 600°C and above.

Fig. 5.33 shows the coercivity variation of Ni-15%Fe-5%Mo-5%B powders with grain size. The low coercivity observed for annealing at 480°C was attributed to the release of defects and the high coercivity observed for annealing at 520°C was caused by the increase in grain size. The decrease in coercivity for higher annealing temperature was attributed to the growth in grain size.

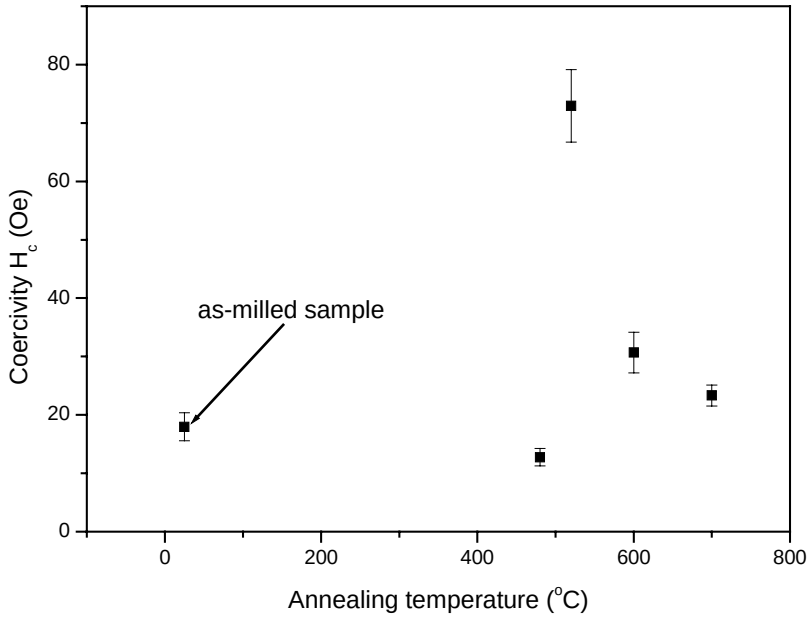

Fig. 5.32 Coercivity of Ni-15%Fe-5%Mo-5%B powders as a function of annealing temperatures.

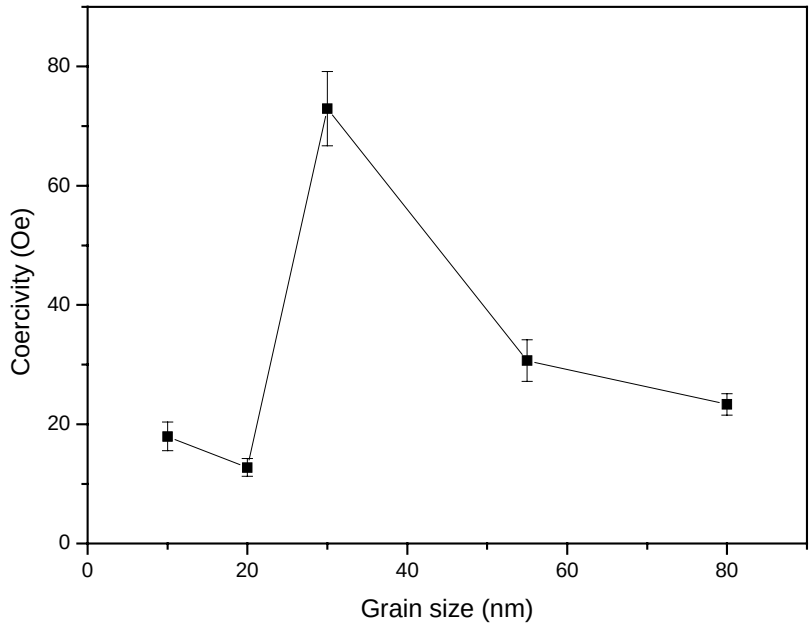

Fig. 5.33 Coercivity of Ni-15%Fe-5%Mo-5%B powders as a function of grain size

5.4 Conclusions

Partially amorphous Ni-15%Fe-5%Mo-5%B powders prepared by elemental Fe, Ni, Mo and B powders have been obtained by high energy ball milling for 10 h. The formation of the amorphous phase was attributed to the addition of B to the Ni-Fe-Mo alloys. A balance between the increased defect concentration and the production of heat during the milling process caused the formation of a partially amorphous powder sample. Magnetic properties were found to be affected by the amorphization of the powders. The sharp decrease in the saturation magnetization of the as-milled Ni-15%Fe-5%Mo-5%B powders was related to the substitution of the Mo atoms. The lower coercivity after 20 h of milling was caused by the appearance of the amorphous phase. Although the amorphous phase was formed after 10 h of milling, the saturation magnetization value of the partially amorphous Ni-15%Fe-5%Mo-5%B powders was similar to the nanocrystalline Ni-15%Fe-5%Mo powders.

After annealing, the phase transformation observed in the DSC results was confirmed to be due to the crystallization of the amorphous phase. $(Fe, Ni, Mo)_{23}B_6$ phase crystallized from the amorphous phase and co-existed with the $FeNi_3$ phase. The magnetic properties were affected by the appearance of the $(Fe, Ni, Mo)_{23}B_6$ phase accordingly. In general, saturation magnetization increased after annealing. However, the coercivity decreased initially due to the release of residual strain after annealing. The coercivity increased sharply as the grain size and the amount of $(Fe, Ni, Mo)_{23}B_6$ phase increased. The decrease in coercivity annealed at 600 and 700°C was attributed to strong pinning of domain walls of the interaction domains at the grain boundaries.

From the current study, it could be concluded that the addition of B could induce the formation of amorphous Ni-15%Fe-5%Mo-5%B alloys. However, only partially amorphous alloy could be produced via the high energy ball milling process. In order to produce a fully amorphous alloy, a different processing method is required. Hence, in the next chapter, melt spinning technique, which is a rapid solidification technique, will be employed to prepare the amorphous ribbon.

Chapter 6 Melt spun Ni-Fe-Mo-B ribbons

6.1 Introduction

Amorphous and nanocrystalline materials have been investigated for applications in magnetic devices requiring magnetically soft materials such as transformers, inductive devices, etc. Most recently, research interest in nanocrystalline soft magnetic alloys has dramatically increased. The benefits found in the nanocrystalline alloys stem from their chemical and structural variations on a nanoscale which are important for developing optimum magnetic properties. Accordingly, research work on amorphous Fe- and Co- based magnets with the development of FINEMET, NANOPERM and HITPERM in ribbon form have been obtained (McHenry et al, 1999a, 1999b, 2000, 2003). Detailed crystallization studies of these amorphous alloys have been performed, and it was found that optimum magnetic properties could be obtained through careful control of the crystallization process.

On the other hand, very little has been reported on Ni-based multicomponent amorphous ribbon. The only available researches were on $Fe_{40}Ni_{38}Mo_4B_{18}$ (Li et al, 1999) and $Fe_{40}Ni_{40}P_xSi(B)_{20-x}$ alloy systems (Miura et al, 1990; Surinach et al, 1994; Zhang and Yi, 1996; Pradell et al, 2000; Sui et al, 2000; Tejedor et al, 2002). The crystallization process of $Fe_{40}Ni_{38}Mo_4B_{18}$ amorphous ribbon was studied, and it was found that magnetic phase was formed at low annealing temperatures, and high annealing temperatures caused the formation of $(Fe, Ni, Mo)_{23}B_6$ crystallites (Li et al, 1999). By controlling the annealing temperatures, different microstructure could be obtained which gave rise to different magnetic properties. From the analysis of the crystallization products of $Fe_{40}Ni_{40}P_xSi(B)_{20-x}$ alloy systems, it was found that Ni-rich silicides and Fe (Si) bcc phases were formed in the early stages and Fe-rich

phosphides and ferromagnetic Fe (Ni) fcc phases were formed at higher temperature.

However, there is no report for amorphous Ni permalloy. As mentioned in the literature review, permalloy has good magnetic properties. It will be of great interest to study the feasibility of producing completely amorphous Ni-based alloy based on permalloy composition. In chapter 5, it was shown that high energy ball milling (HEBM) was not able to produce a completely amorphous Ni-Fe-Mo-B alloy system. Hence, in this chapter, rapid solidification by melt spinning technique will be used in an attempt to produce a fully amorphous system for the same Ni-15%Fe-5%Mo-5%B composition.

The investigation of melt-spun Ni-15%Fe-5%Mo-5%B alloy system is divided into two parts. The first part is to study the feasibility of producing a fully amorphous ribbon via rapid solidification by melt spinning process. This will be covered in section 6.3.1. The second part involves the study of the microstructure and the crystallization process of the as-spun ribbons. In addition, the magnetic properties of the ribbons will also be characterized and the results will be compared to the alloys prepared by HEBM. This will be covered in section 6.3.2. Finally, a conclusion summarizing the results for melt-spun ribbons will be given in section 6.4.

6.2 Sample Preparation

Multicomponent alloy with composition Ni-15%Fe-5%Mo-5%B was prepared by arc-melting technique from elemental Ni, Fe, Mo and B powders in a pure argon atmosphere. The ingots of the alloys were remelted several times to ensure the homogeneity of the samples. Ribbons were obtained by using a single-roller melt-spinner (HIT 6) with a diameter of 20 cm copper wheel and a gas pressure of 600 mbar. The average holding temperature was between 1200°C and 1300°C, and the holding time was about 20 seconds.

The processing parameters of the melt-spinning process can affect the type of the produced ribbons. The distance between the bottom of the nozzle and the surface of the copper wheel, and the rolling rate of the wheel has been reported to affect the character of the ribbons (McHenry et al, 1999b; Al-Khafaji et al, 2001). High rolling rate produces the amorphous ribbon, while a low rate produces the partially amorphous ribbon (Wu et al, 2000). In this experiment, two types of ribbons, namely sample A and sample B were obtained by changing the rolling rate and the distance between the bottom of the nozzle and the surface of the wheel. For the preparation of sample A, the distance was set at 0.5 mm and the rolling rate was 38 m/s. For sample B, the distance and the speed were 0.8 mm and 30 m/s respectively. Both types of ribbons were 25 μm thick and 5 mm wide. Sample A was found to be flexible, while sample B was more brittle.

In order to study the crystallization process of these as-spun ribbons, heat treatment was done on these two samples in a vacuum furnace set at about 10^{-5} Torr and with temperature fluctuation ±3°C. Based on the DSC results obtained for the melt-spun ribbons, different holding times and temperatures were selected. The heating rate was set at 10°C/min and the samples were furnace-cooled.

6.3 Results and Discussion

6.3.1 As-spun ribbons

6.3.1.1 Sample A

XRD pattern of the as-spun sample A is shown in Fig. 6.1. Only a broad and low intensity hump was observed. No other diffraction peaks were observed. This is the characteristic of an amorphous sample. Hence, it could be concluded that sample A is a completely amorphous ribbon.

TEM observations confirmed the formation of a completely amorphous ribbon in sample A. Fig. 6.2 shows the BF image and corresponding diffraction pattern of sample A. The TEM BF image does not show any significant contrast and the

electron diffraction pattern shows an intense diffuse halo followed by another one of lower intensity. These are characteristics of an amorphous phase.

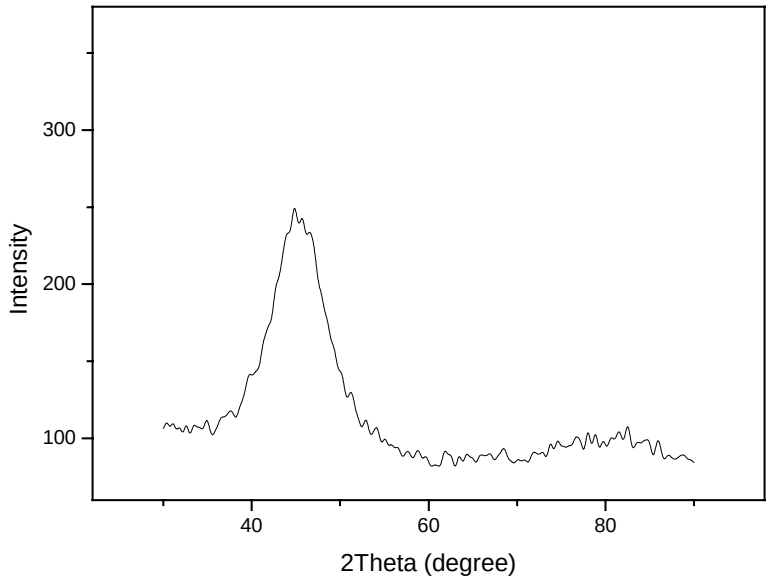

Fig.6.1 XRD pattern of sample A.

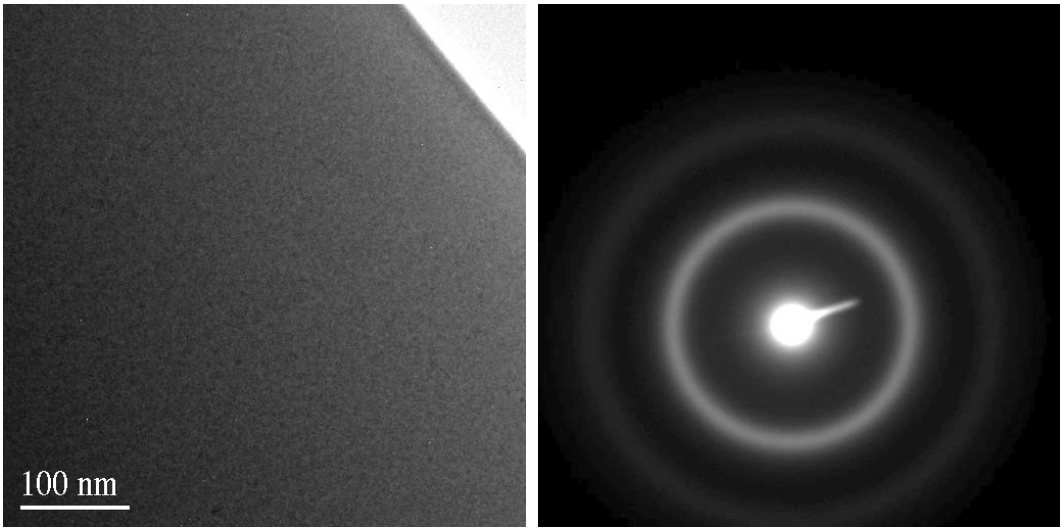

Fig.6.2 Bright field image and corresponding diffraction pattern of sample A.

DSC was also obtained for sample A, in order to study the crystallization of the amorphous ribbon. Fig. 6.3 shows the non-isothermal DSC curve obtained at a heating rate of 10°C/min. A sharp exothermic peak at a peak temperature of about 432°C was observed during the heating process. Another non-obvious peak

appearing at around 601°C was also observed. The observation of exothermic peaks during the heating process of as-spun ribbon was often reported for different alloy systems, and these peaks were related to the crystallization process. Inoue (2000) has studied the crystallization process of Zr-Al-Ni-Cu amorphous alloys containing Ag, Ti or Pd elements, and found that the crystallization process changed from a single-stage mode to two-stage mode by the addition of different elements. A two-stage crystallization of amorphous $Fe_{54}Co_{26}Si_6B_{14}$ ribbon was also reported by Rho et al (2003).

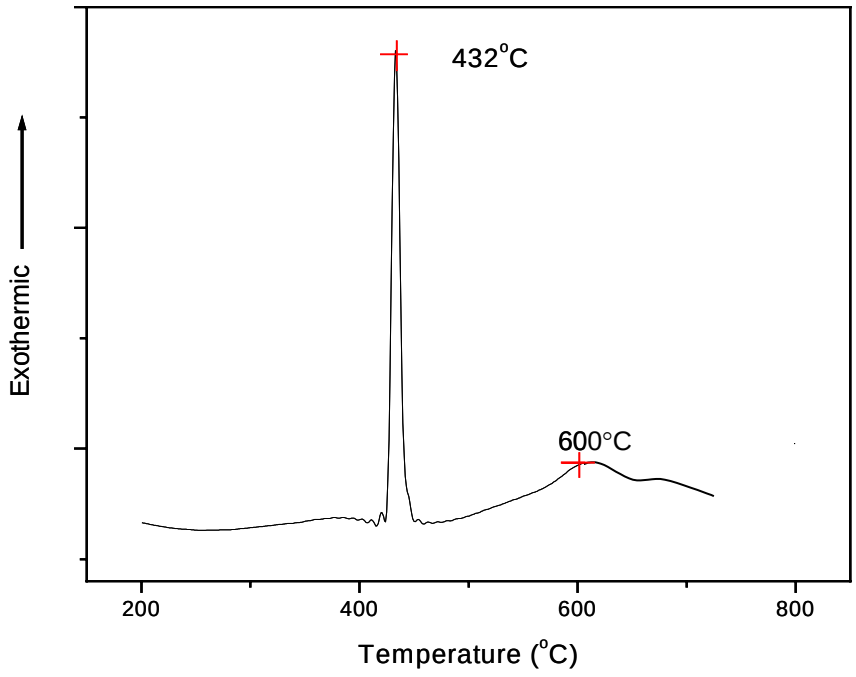

Fig.6.3 DSC scan obtained at a heating rate of 10°C/min for sample A.

TEM EDX was performed on this sample and the spectrum is shown in Fig. 6.4. Due to the small scattering factor of B, no peaks representative of B were detected from the EDX spectrum. Hence, only the atomic ratio for Ni, Fe and Mo could be obtained. The average atomic ratio for Ni, Fe and Mo was about 78.7±0.6: 17.7±0.5: 3.6±0.2 for the completely amorphous ribbon (sample A).

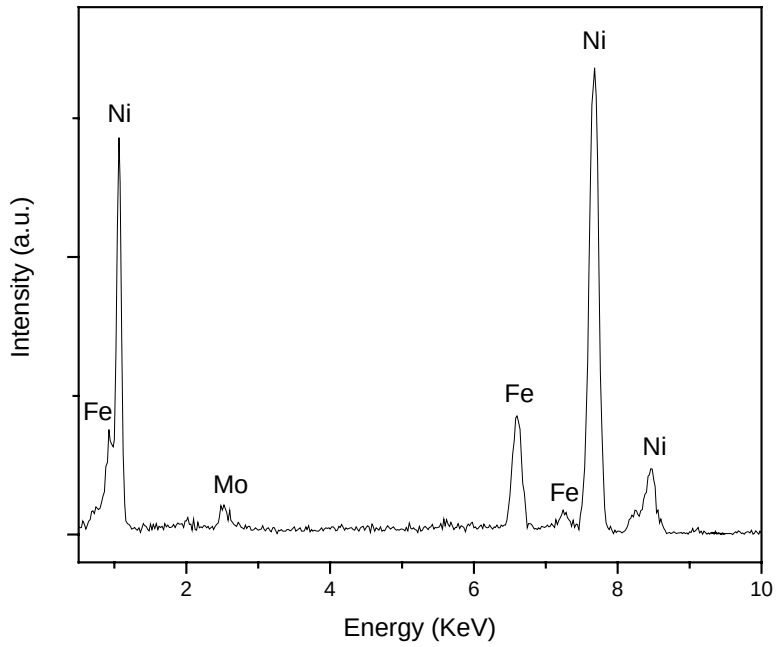

Fig.6.4 EDX spectrum of sample A.

6.3.1.2 Sample B

Fig. 6.5 shows the XRD pattern of sample B. The appearance of a broad and low intensity hump observed for sample A was not obvious for sample B. Only sharp diffraction peaks corresponding to crystalline phases were observed. The diffraction peaks were indexed as $FeNi_3$ and $(Fe, Ni, Mo)_{23}B_6$ phases, and $FeNi_3$ was the major phase.

TEM observations (Fig. 6.6) also confirmed the presence of crystalline phases in sample B. In the BF image of the as-spun sample B (Fig. 6.6a), grain boundaries were not clearly observed. However, the SADP pattern (Fig. 6.6b) contained a halo ring in addition to sharp diffraction spots, which corresponds to the $FeNi_3$ and $(Fe, Ni, Mo)_{23}B_6$ phases. The existence of the halo rings suggested that a substantial amount of amorphous phase existed in this as-spun ribbon. Hence, sample B was a partially amorphous ribbon. The average grain size of the crystalline phase was about 30 nm. Due to the small grain size, it is difficult to distinguish the $FeNi_3$ and

$(Fe, Ni, Mo)_{23}B_6$ phases.

Comparing the XRD results obtained for the partially amorphous ribbon and the partially amorphous powders in chapter 5, $(Fe, Ni, Mo)_{23}B_6$ phase was not detected in the partially amorphous powders. Such a difference in phases might be due to the different amorphization process involved in HEBM and melt-spinning process. For the HEBM process, the partially amorphous powders were formed directly from the crystalline phase through solid-state amorphization without going through the liquid phase. The amorphization process by mechanical alloying works through absorption of mechanical energy. The relatization of amorphization by mechanical alloy is through collision and mixing of atoms. During the milling process, the atoms will be shifted away from their initial lattice points after impact during milling: they will then be trapped by other atoms. The trapped atoms can be located at new lattice points which may cause structural defects such as vacancies, dislocations, grain boundaries, and anti-phase boundaries. These defects raised the free energy of the intermetallic system to a level higher than that of the amorphous phase and consequently, it became possible for the amorphous phase to form. However, for the melt-spinning process, the partially amorphous ribbon was obtained by rapid cooling from a liquid melt. The formation of a partially amorphous phase in this process was due to the insufficient cooling rate to prevent the crystallization in some parts of the ribbon.

Fig. 6.7 shows the non-isothermal DSC curve obtained at 10°C/min for sample B. Two exothermic peaks were observed during the heating process. The peak temperatures obtained for both samples A and B were similar, which indicated that these two types of ribbons exhibited the same crystallization process. However, it was noted that the first peak of sample B was wider and less sharp than sample A, and the second peak of sample B was more obvious than sample A. Such a difference might be due to the different amorphization status of sample A and sample B. For sample B, some partial of $FeNi_3$ and $(Fe, Ni, Mo)_{23}B_6$ crystals have already crystallized, and these crystallizes will work as the crystal center for the future crystallization. This was the reason for the wider and less sharp exothermic peaks observed in the DSC results as compared to sample A, which was completely

amorphous ribbon.

The first exothermic peak corresponding to the primary crystallization step for sample A and sample B was detected to be about 435°C at a heating rate of 10°C/min. Compared to the partially amorphous powders prepared by HEBM (Chapter 5), the exothermic peak obtained was about 530°C at the same heating rate. In addition, the secondary crystallization peak appearing at 600°C for the two ribbons was not observed for the milled powders. The difference in the crystallization temperatures for ribbons and powders could be attributed to the difference in the characteristics between the milled powders and the as-spun ribbons. El-Eskandarany (2001) has summarized the general factors that affect the crystallization peak temperature, which includes the composition of the samples, the sample preparation methods and the effect of the working environment. In the current study, the samples were prepared by different techniques. The amorphous phase obtained by HEBM and melt-spinning might be of different composition and stability. Hence, crystallization temperature was expected to be different for the as-milled powders and the as-spun ribbons.

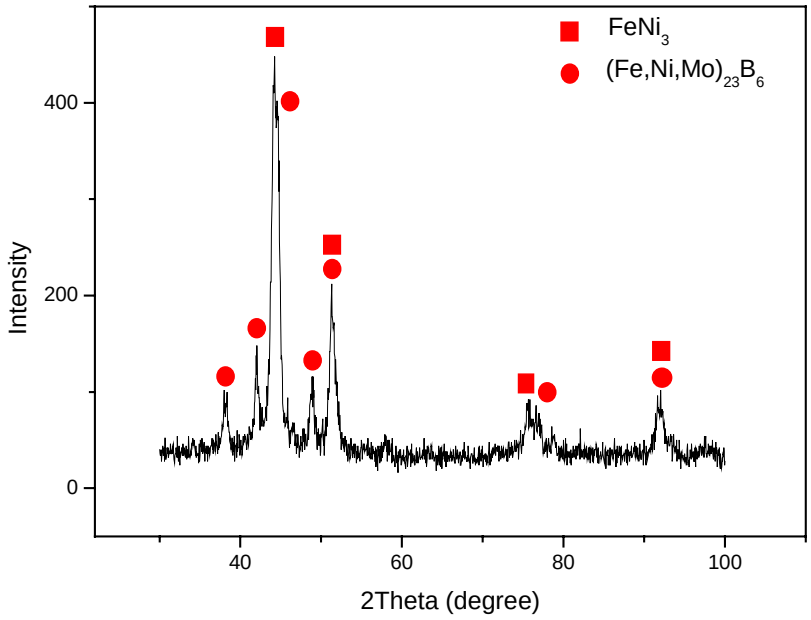

Fig.6.5 XRD pattern of sample B.

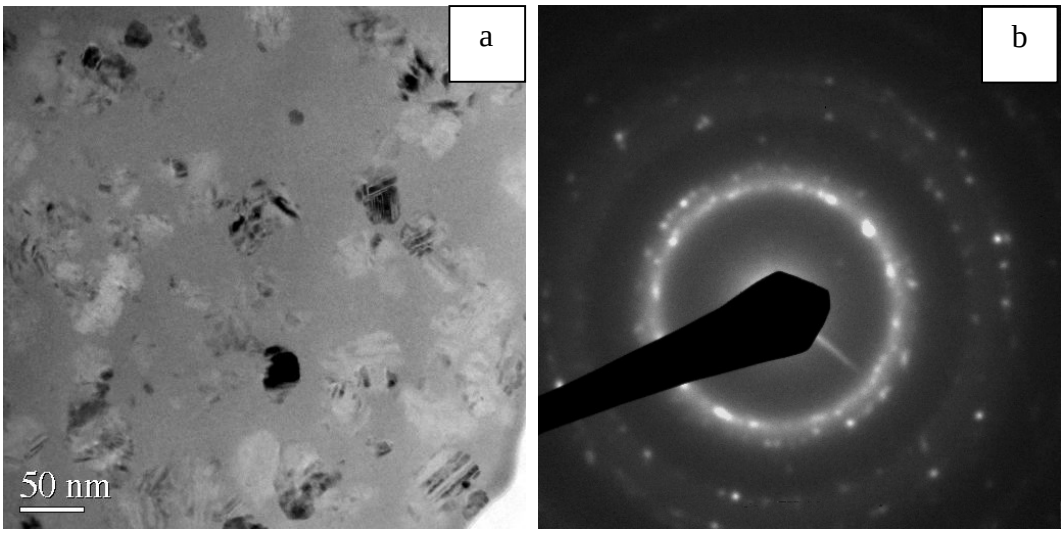

Fig.6.6 (a) BF image and (b) corresponding diffraction pattern of sample B.

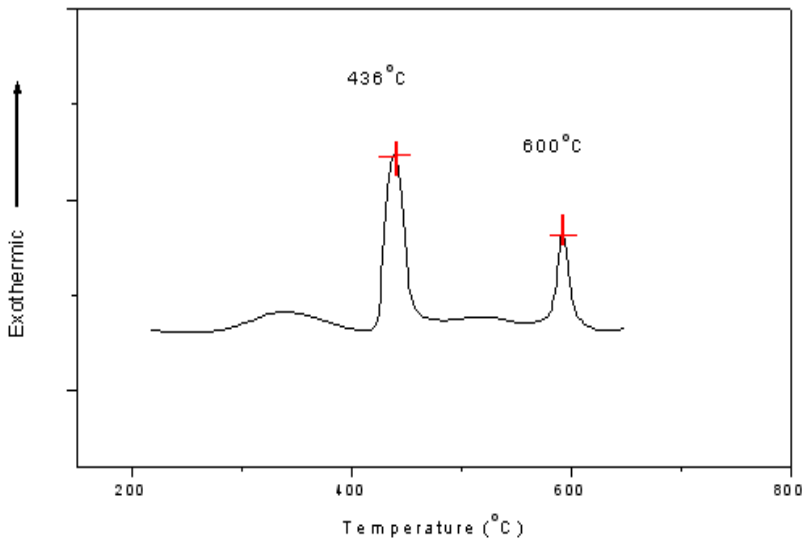

Fig.6.7 DSC scan obtained at a heating rate of 10°C/min for sample B.

It was also noted that the exothermic peaks of the partially amorphous powders (chapter 5) were broader and less sharp than those obtained for the melt-spun samples. The broader and less sharp peaks of the milled powders were also observed for mechanically alloyed multicomponent Fe-Co-Ni-Zr-B alloys (Liu and Chang, 2002a). There are two reasons for the difference. The first reason might be caused by the fact that the partially amorphous powders had a particle size distribution in the amorphous phase. The second reason was the high residual strain in the powders due to the ball milling process.

In order to determine the activation energy of the two crystallization processes by Kissinger method, DSC scan were also done on sample B for different heating rates (Fig. 6.8). The Kissinger's plots for these two peaks are shown in Fig. 6.9 and Fig. 6.10 respectively. The activation energy was found to be about 422 kJ/mol for the first crystallization peak and 257 kJ/mol for the second peak.

Although samples A and B had the same composition, sample A was completely amorphous while sample B was partially amorphous. The difference in microstructure was caused by the different rolling rates used to produce the two samples. The effects of rolling rates on the morphologies of the ribbons have been reported (Wu et al, 2000). Different rolling speed caused different grain morphology of the produced ribbon has also been reported (Al-Khafaji et al, 2001). In general, high rolling rates would facilitate the formation of amorphous ribbon.

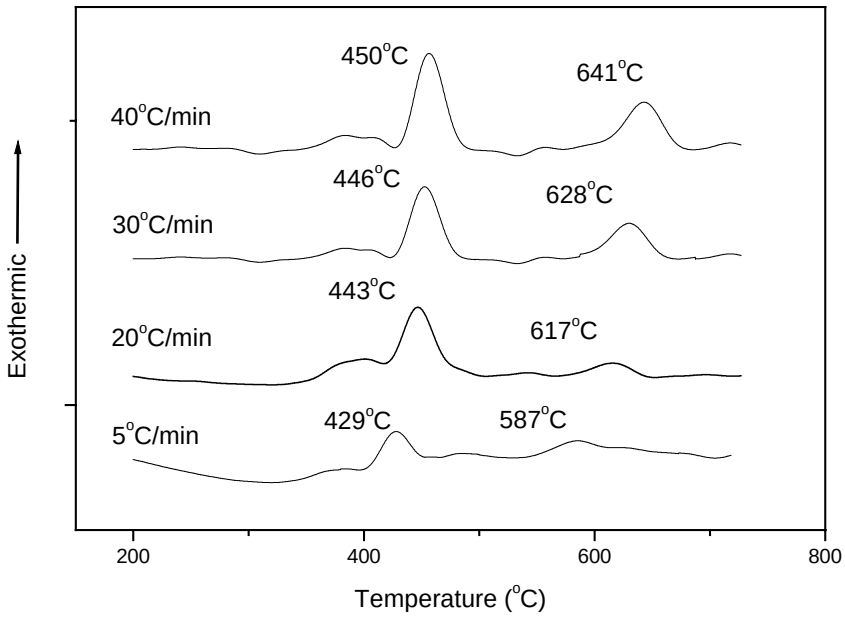

Fig.6.8 DSC scan obtained at a heating rate of 5°C/min, 20°C/min, 30°C/min and 40°C/min for sample B.

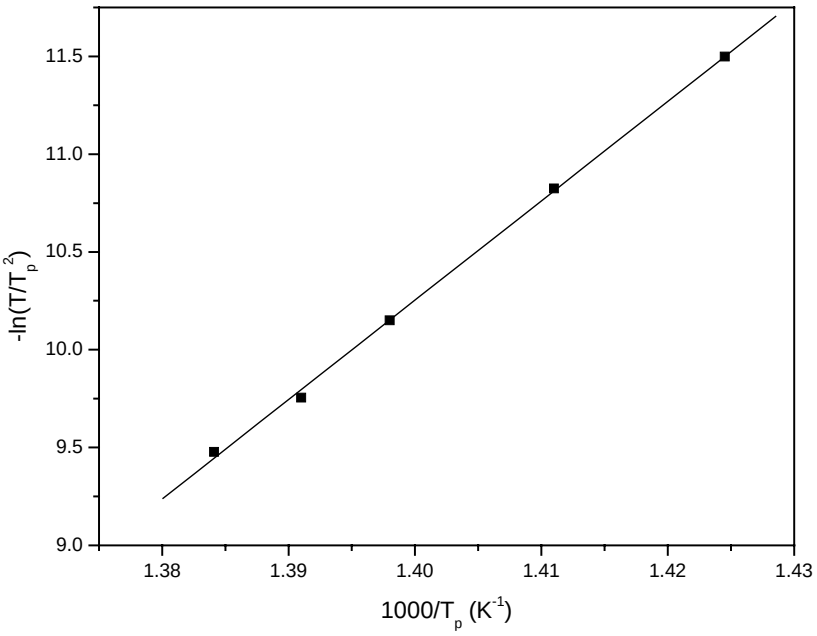

Fig.6.9 Kissinger's plot of $-\ln(T/T_p{}^2)$ versus $1000/T_p$ for the first crystallization peak for sample B.

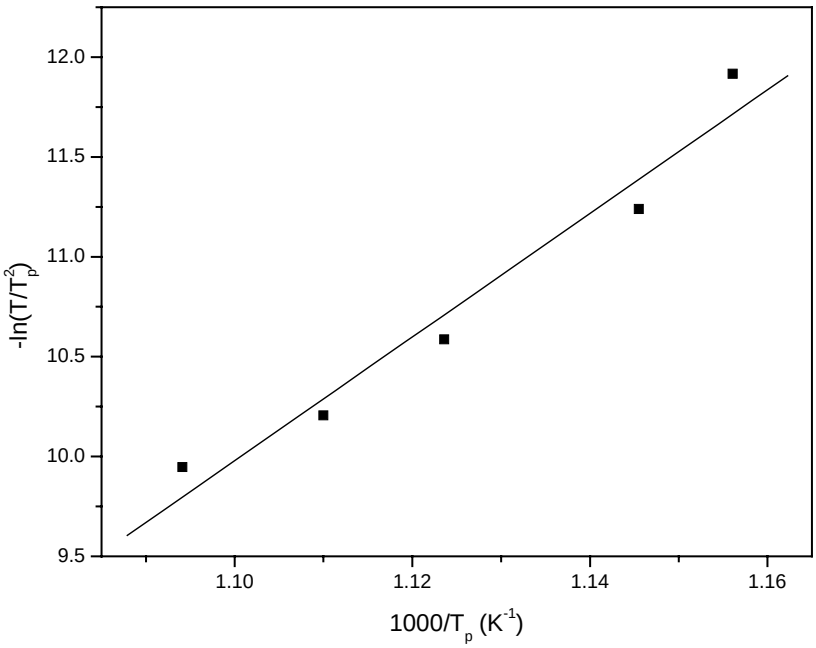

Fig.6.10 Kissinger's plot of $-\ln(T/T_p{}^2)$ versus $1000/T_p$ for the second crystallization peak for sample B.

6.3.2 Crystallization studies for Sample A (completely amorphous ribbon)

Based on the DSC results obtained at annealing rate of 10°C/min for sample A (completely amorphous ribbon), the onset temperatures of the two crystallization steps occurred at about 420°C and 570°C respectively. According to this result, annealing temperatures ranging from 350°C to 550°C were chosen to study the first step crystallization, and temperatures ranging from 600°C to 700°C were chosen to study the second step crystallization. The effects of annealing temperature on the two step crystallization will be shown in section 6.3.2.1, and the effects of annealing time will be presented in section 6.3.2.2.

6.3.2.1 Effects of annealing temperature

(A) XRD observation

XRD results of the completely amorphous ribbon annealed at 350°C, and 400 to 550°C for 1 h are shown in Fig. 6.11 and Fig. 6.12 respectively. These temperatures were lower than the secondary crystallization temperature. After annealing at 350°C for 1 h (Fig. 6.11), the broad hump indicating the presence of an amorphous phase was still evident. However, some small sharp peaks were also observed. These precipitated peaks were few and the intensities were low, and they could not be indexed. However, when the annealing temperature increased to 400°C, which was slightly lower than the onset temperature of the primary crystallization, the broad hump indicating the presence of the amorphous phase was no longer observed. Instead, a few sharp diffraction peaks appeared. No new phase was formed when the annealing temperature was increased to 450°C. Further increase in the annealing temperature up to 550°C only caused the intensities of these peaks to increase, without changing the positions of the peaks.

XRD results of the completely amorphous ribbon annealed at temperatures close to the secondary crystallization temperature (600°C) are shown in Fig. 6.13. The sharp

peaks observed at 550°C annealing temperature were still observed when the ribbon was annealed at 600°C. However, a small new peak appearing at about 43.6° was detected, which meant that a new phase began to form at this temperature. As the annealing temperature increased further to 700°C, the new peak that appeared at 600°C became more pronounced. This indicated the growth of a new phase during the second-stage crystallization. This new phase was indexed as the $FeNi_3$ phase.

Although the first crystallization temperature appeared at 432°C, the ribbon began to crystallize at 350°C and annealing at 400°C for 1 h caused the fully crystallization of the ribbon. Further annealing at temperatures less than 600°C only caused the growth of the crystallized phase. $FeNi_3$ phase crystallized from the ribbon during the secondary crystallization process. From these observations, the crystallization process of the completely amorphous ribbon could be summarized as follows:

$$amorphous \xrightarrow{432^{o}C} (Fe,Ni,Mo)_{23}B_6 \xrightarrow{600^{o}C} (Fe,Ni,Mo)_{23}B_6 + FeNi_3$$

Similar two stages crystallization process was also reported for some amorphous Fe-Ni based ribbons during the annealing process (Li et al, 1999; Pradell et al, 2000; Sui et al, 2000; Nunes et al, 2002). However, depending on the alloy composition, different phases were obtained. In the current research, since $(Fe, Ni, Mo)_{23}B_6$ is a metastable phase, it is easy to crystallize from the amorphous phase during the primary crystallization. $FeNi_3$ phase is more stable compared to $(Fe, Ni, Mo)_{23}B_6$ phase, and it crystallized at higher annealing temperature.

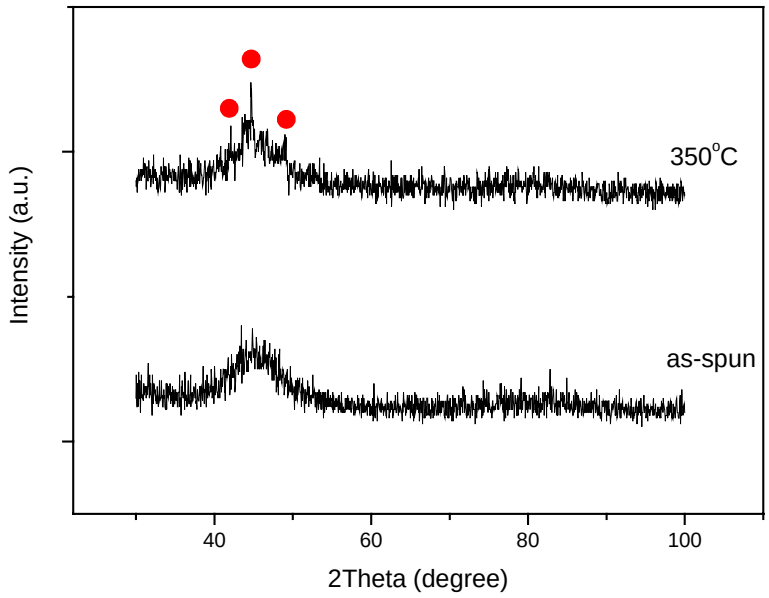

Fig.6.11 XRD results of the initially completely amorphous ribbon annealed at 350°C for 1 h.

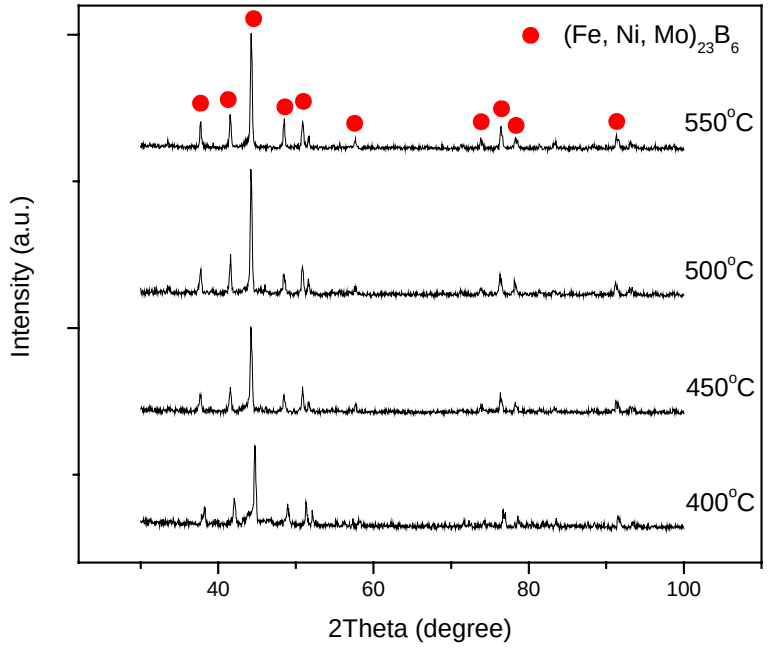

Fig.6.12 XRD results of the initially completely amorphous ribbon annealed at 400 to 550°C for 1 h.

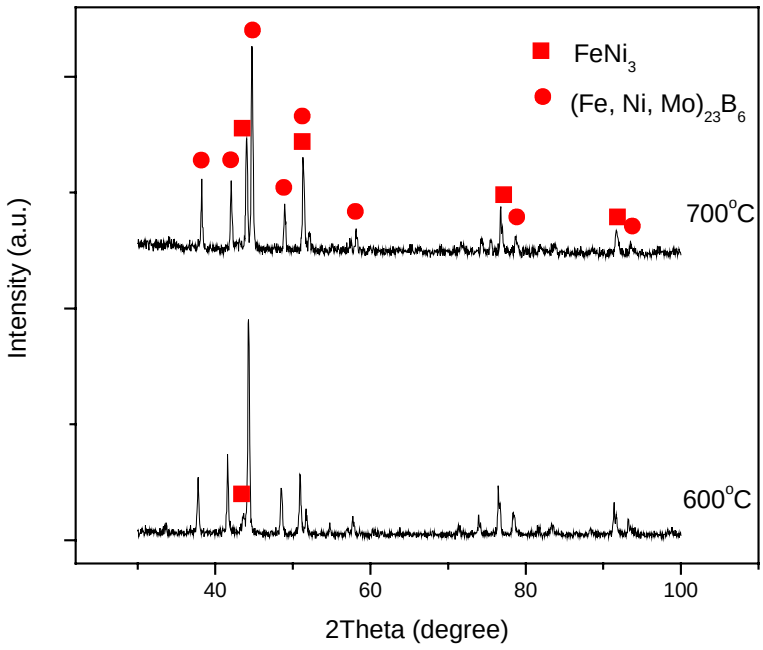

Fig.6.13 XRD results of the initially completely amorphous ribbon annealed at 600 and 700°C for 1 h.

(B) Microstructure observation

The microstructures of the ribbon annealed at different temperatures were studied by TEM. Fig. 6.14 (a) shows the general microstructure of sample A (completely amorphous ribbon) annealed at 350°C for 1 h. An amorphous matrix phase with some grains was observed. The grains were nearly 100 nm, and the shape of the grains was quadrangle. The grains were confirmed to be (Fe, Ni, Mo)$_{23}$B$_6$ phase by indexing SADP obtained from the grains. A typical SADP of the grain is shown in Fig. 6.14 (b).

EDX spectra were also obtained for both the grains and the amorphous matrix (Fig. 6.15). The average compositions of these two phases obtained from EDX analyses are summarized in Table 6.1. It was noted that the compositions of these two phases were similar. Compared the annealed ribbon with the as-spun completely amorphous ribbon, there is also no difference in the composition of the amorphous

phase in the as-spun and the annealed ribbons.

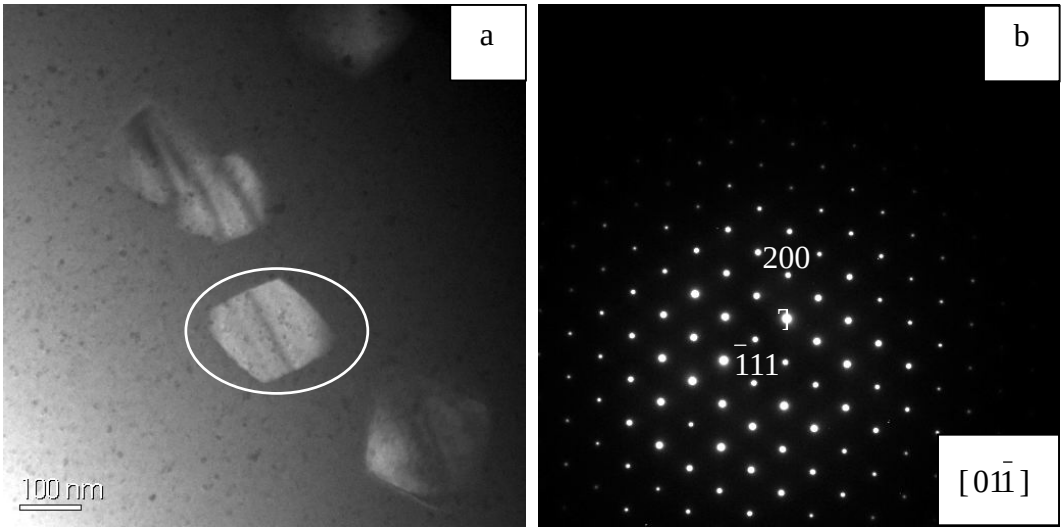

Fig.6.14 (a) BF image and (b) typical diffraction pattern of the crystals (grain in the circle) of the initially completely amorphous ribbon annealed at 350°C for 1 h.

The microstructures of the fully crystallized ribbon annealed at 400°C and 500°C for 1 h are shown in Fig. 6.16. The ribbons exhibited similar microstructure. The shape of the grains was irregular and the grain size ranged from 100 nm to 300 nm. The grains were confirmed to be $(Fe, Ni, Mo)_{23}B_6$ by indexing SADP. SADP of the major zone axes of these crystals are shown in Fig. 6.17. EDX analysis was also performed for these two samples. The average composition of the grains was found to be 79.1±0.6, 17.5±0.5 and 3.4±0.2 for Ni, Fe and Mo respectively.

The microstructures shown in Fig. 6.14 and 6.16 are classified as the primary crystallization stage since the annealing temperatures were lower than the secondary crystallization temperature of 600°C. The primary crystallization stage could be distinguished by two stages, namely the early-stage crystallization and the large-grained crystallization. The early stage crystallization could be observed for the amorphous ribbon annealed at 350°C for 1 h shown in Fig. 6.14. Several grains with grain size of 100 nm were observed, and they were of the same composition as the amorphous phase.

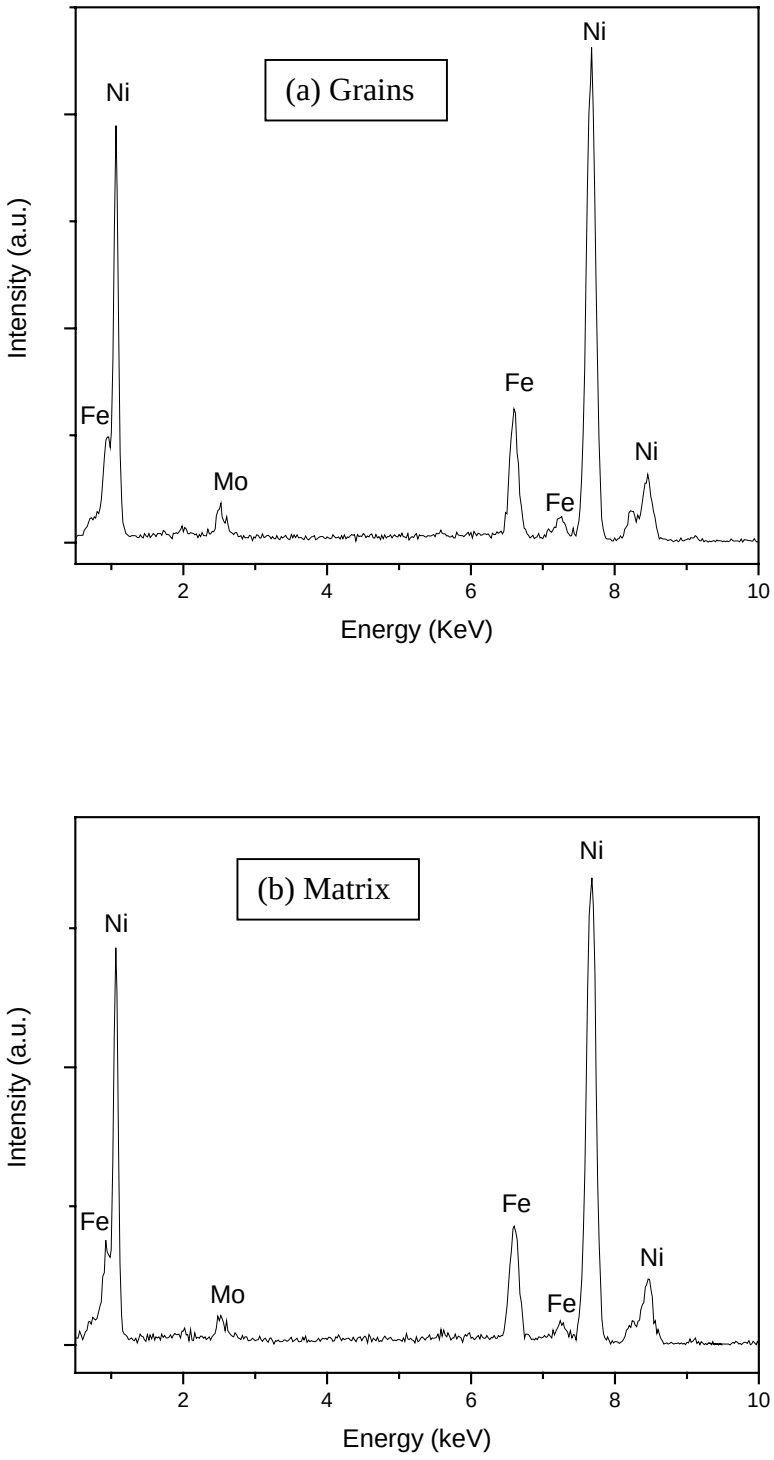

Fig.6.15 Typical EDX spectra of (a) grains and (b) amorphous matrix of the initially completely amorphous ribbon annealed at 350°C for 1 h.

Table 6.1 Average composition (at. % metallic elements) obtained using TEM/EDX analysis of the grains and the amorphous matrix of the completely amorphous ribbon after annealing at 350°C for 1 h.

Name	Composition (atomic %)		
	Ni	Fe	Mo
Matrix	78.8±0.6	17.6±0.5	3.6±0.2
Grains	78.7±0.6	17.9±0.5	3.4±0.2

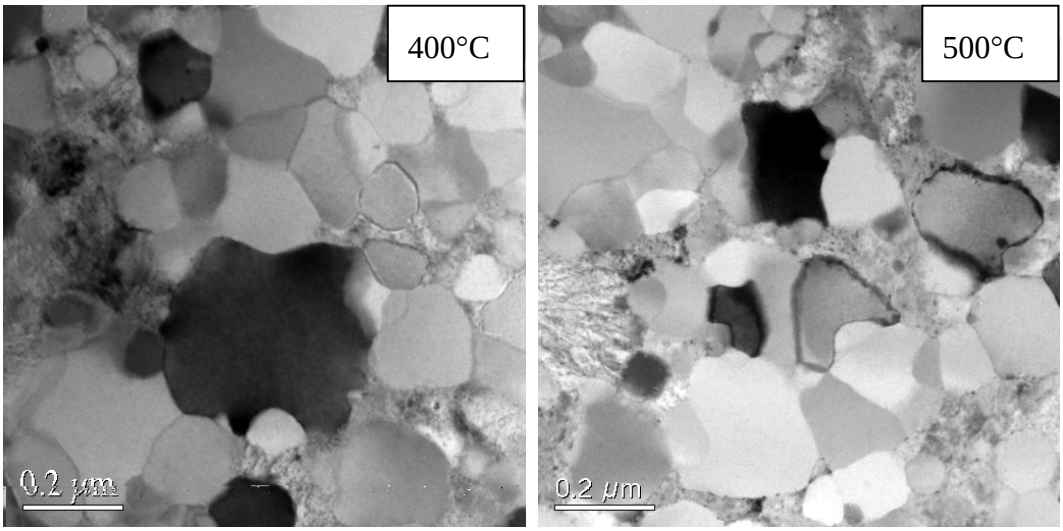

Fig.6.16 BF images of the initially completely amorphous ribbon after annealing at 400°C and 500°C for 1 h.

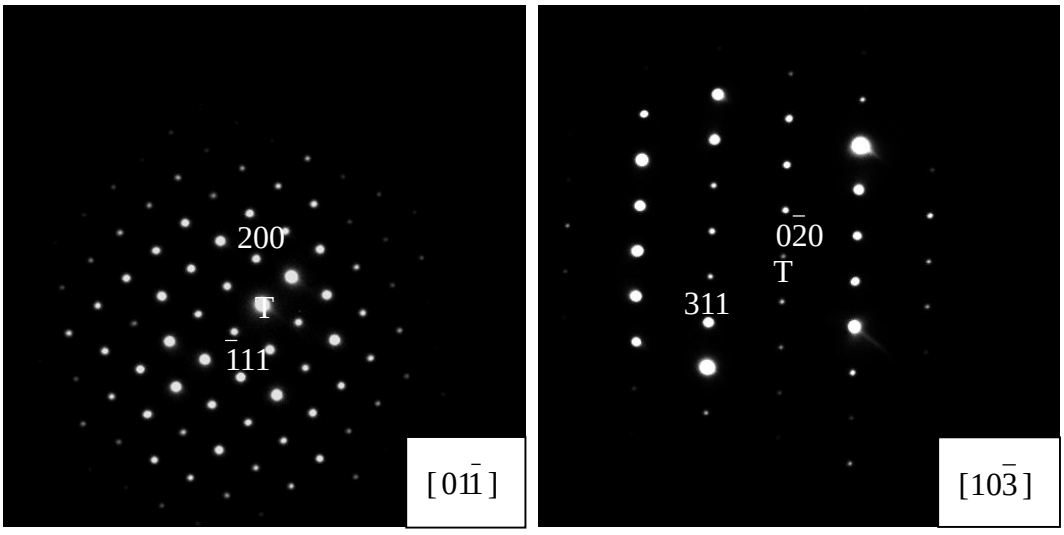

Fig.6.17 Selected area diffraction patterns of the $(Fe, Ni, Mo)_{23}B_6$ phase obtained from the initially completely amorphous ribbons annealed at 400°C and 500°C for 1 h.

The large-grained crystallization was observed when the ribbon was annealed at 400°C and higher temperatures. The grains grew significantly in this stage, and full crystallization of the ribbon was observed when the ribbon was annealed at 400°C for 1 h. The grains had the same composition as the amorphous phase.

Modes in crystallization of amorphous alloys have been studied by many researchers (Ye and Lu, 1998; Hono, 2002; Rho et al, 2003). In general, according to the composition of the crystal phase and the amorphous phase, three crystallization modes were built. If the amorphous alloy can decrease its free energy by changing the structure from amorphous to crystalline phase without any change in composition, this type of crystallization is known as polymorphous crystallization (Ye and Lu, 1998; Hono, 2002; Rho et al, 2003). If the polymorphously crystallized phase is still metastable, precipitation of more stable phase should follow from the polymorphously crystallized phase. When the composition of the product phase is different from that of the amorphous phase, crystallization occurs with compositional change. For such cases, two crystallization modes, eutectic crystallization and primary crystallization are possible.

According to the definition of the crystallization modes, the crystallization of the completely amorphous ribbon would be polymorphous crystallization, and can be presented by a schematic free energy-composition curve shown in Fig. 6.18, and F represented metastable (Fe, Ni, Mo)$_{23}$B$_6$ phase. The driving force for the crystallization of (Fe, Ni, Mo)$_{23}$B$_6$ phase from the amorphous phase was due to the difference in free energy of these two phases. The amorphous alloy with composition Ni-15%Fe-5%Mo-5%B could decrease its free energy by changing the structure from amorphous to (Fe, Ni, Mo)$_{23}$B$_6$ crystalline phase without any change in composition. In such a case, crystallization would occur by changing the site of atoms in a few atomic distances at the amorphous/crystal interface without solute partitioning.

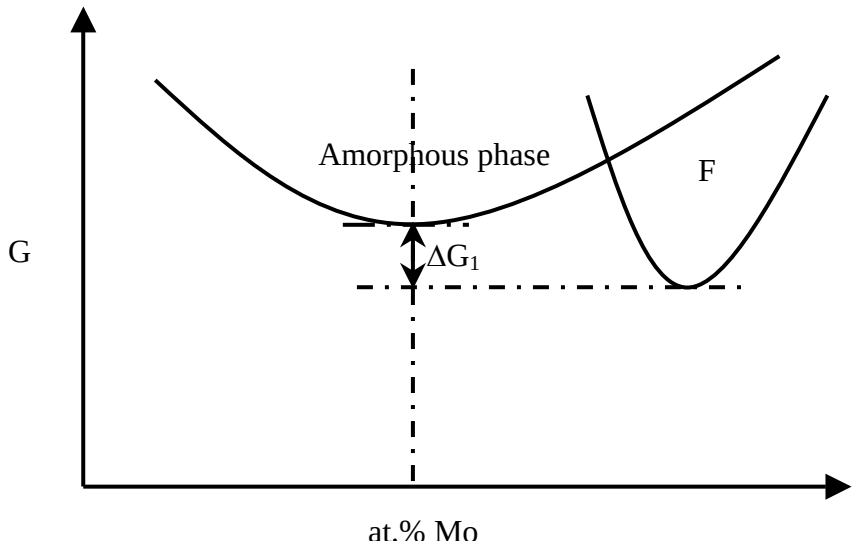

Fig.6.18 Hypothetical free-energy composition diagram to explain possible modes of the primary crystallization of Ni-15%Fe-5%Mo-5%B amorphous ribbon.

As the growth of the crystalline product is interfacial controlled, the growth rate is fast in the polymorphous crystallization mode which results in relatively gross final microstructure (Ye and Lu, 1998; Hono, 2002). This was the reason for the large grain observed in Fig. 6.14. Polymorphous crystallization of the amorphous $Ti_{50}Ni_{25}Cu_{25}$ ribbon was also reported (Louzguine and Inoue, 2000). The same composition before and after crystallization, and a rough microstructure with average grain size of 0.5 μm were reported.

For the well studied FINEMET, NANOPERM and HITPERM ribbons, which were successfully prepared by the primary crystallization from their corresponding amorphous precursors (Suzuki et al, 1994; Zbroszcyk et al, 1996; Zhang et al, 1996a; Efthimiadis et al, 1997; Iwanabe et al, 1999; McHenry et al, 1999a; Hono, 2002), the product after the primary crystallization was magnetic phase with very fine grain size that coexisted with the remaining amorphous phase. The microstructure for these ribbons was very fine, and is different from the one observed in our experiment. The reason for the difference in microstructure was due to the different crystallization mechanism. For the FINEMET, NANOPERM and HITPERM ribbons, the composition of the crystallized phase was different from the amorphous matrix, and grain growth was diffusion-controlled (Efthimiadis et al,

1997; Iwanabe et al, 1999; McHenry et al, 1999a; Hono, 2002). However, for our sample, polymorphous crystallization was interface-controlled, and full crystallization could be reached over a very short period of time and larger grains were obtained.

The microstructures of the completely amorphous ribbon after annealing at 600°C and 700°C for 1 h are shown in Fig. 6.19. Two types of grains were observed. The grain size varied from 100 nm to 400 nm for the ribbon annealed at 600°C. The grains were observed to grow to more than 500 nm when the annealing temperature was increased to 700°C. The two types of grains were identified using SADP. Typical SADP taken from these two types of grains were shown in Fig. 6.20 and Fig. 6.21. One type of grains was indexed as $FeNi_3$ phase and the other one was indexed as $(Fe, Ni, Mo)_{23}B_6$ phase. EDX was also performed on these two types of grains. It was found that one type of the grains had nearly the same composition and the average atomic Ni, Fe and Mo ratio for these grains was 74.4±0.6: 25.0±0.5: 0.5±0.2. Since the ratio of Ni and Fe for these grains was nearly 3:1, they were indexed as $FeNi_3$ phase. The composition of the other type of grains was 79.3±0.6: 17.2±0.5: 3.5±0.2, and these grains were indexed as $(Fe, Ni, Mo)_{23}B_6$ phase.

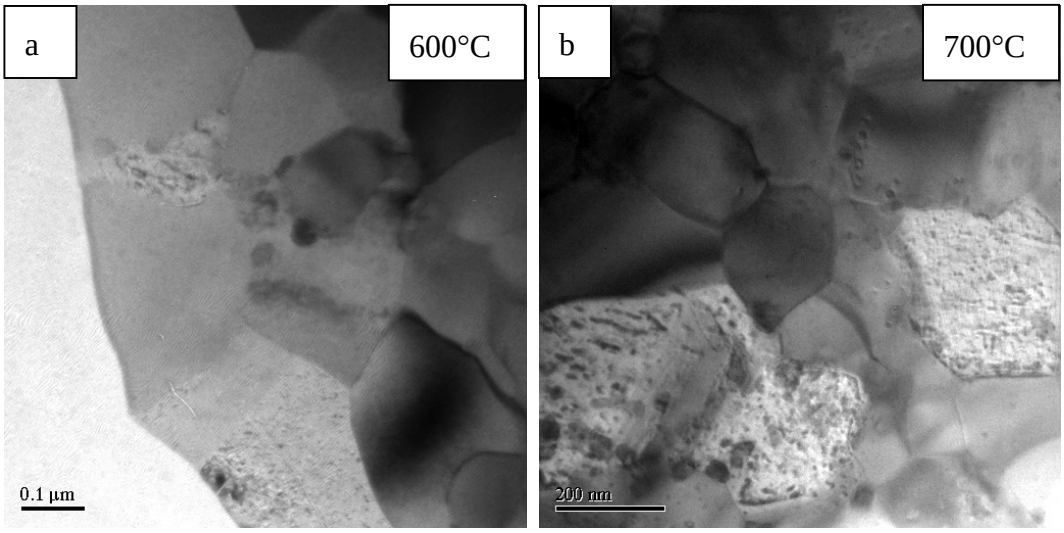

Fig.6.19 BF images of the initially completely amorphous ribbon annealed at (a) 600°C and (b) 700°C for 1 h.

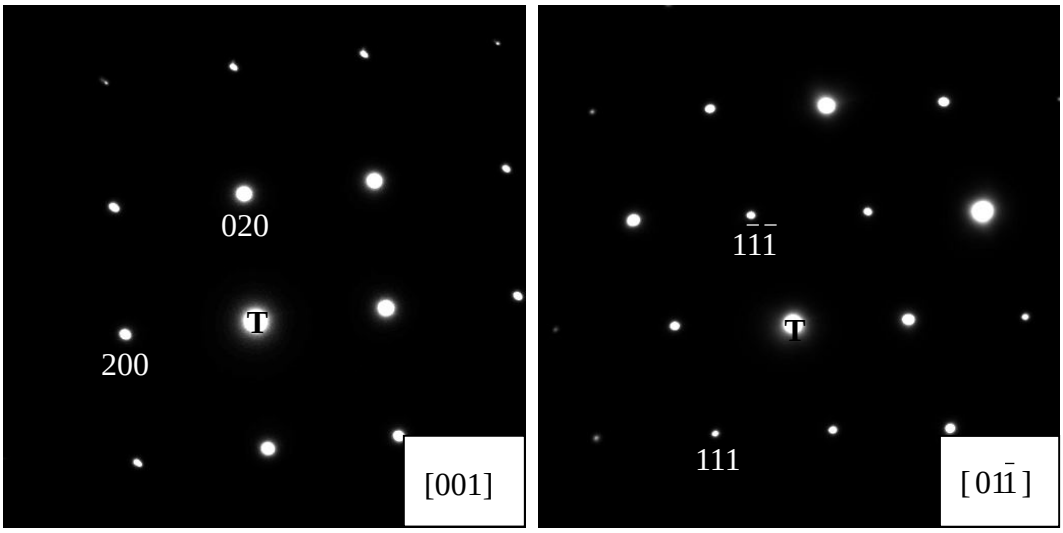

Fig.6.20 Typical SADP of one type of grains ($FeNi_3$ phase).

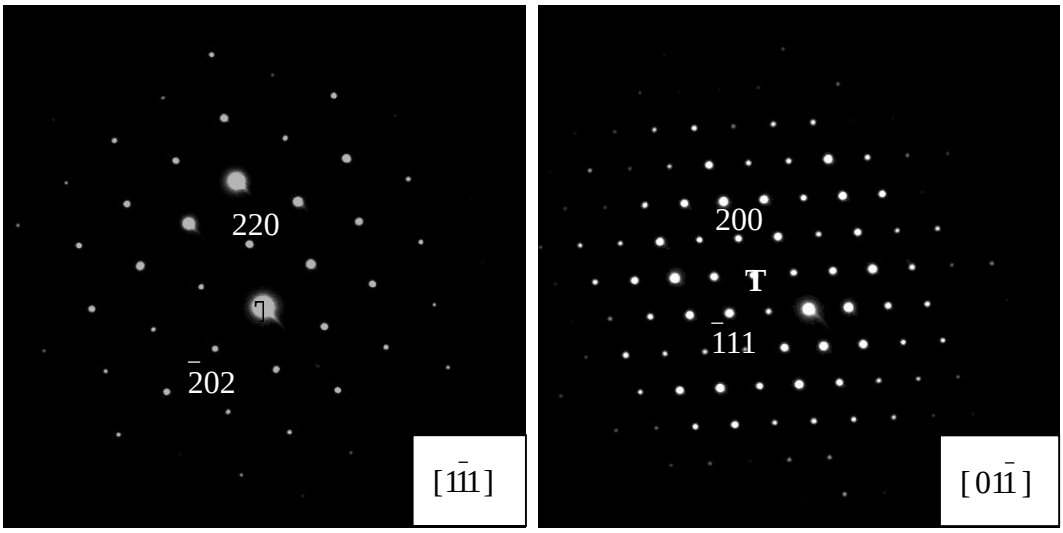

Fig.6.21 Typical SADP of the other type of grains ($(Fe, Ni, Mo)_{23}B_6$ phase).

Based on the above results, the secondary crystallization of the completely amorphous ribbon could be summarized as follows. $FeNi_3$ was the secondary phase precipitated from the $(Fe, Ni, Mo)_{23}B_6$ matrix, and became more pronounced as the annealing temperature increased. During this transformation, Mo atoms diffuse out and Fe atoms diffuse into $(Fe, Ni, Mo)_{23}B_6$ matrix to form $FeNi_3$ phase. The crystallization mode obtained in the primary crystallization should be revised as shown in Fig. 6.22. The final microstructure after the secondary crystallization stage comprised of $FeNi_3$ phase embedded in the $(Fe, Ni, Mo)_{23}B_6$ phase matrix.

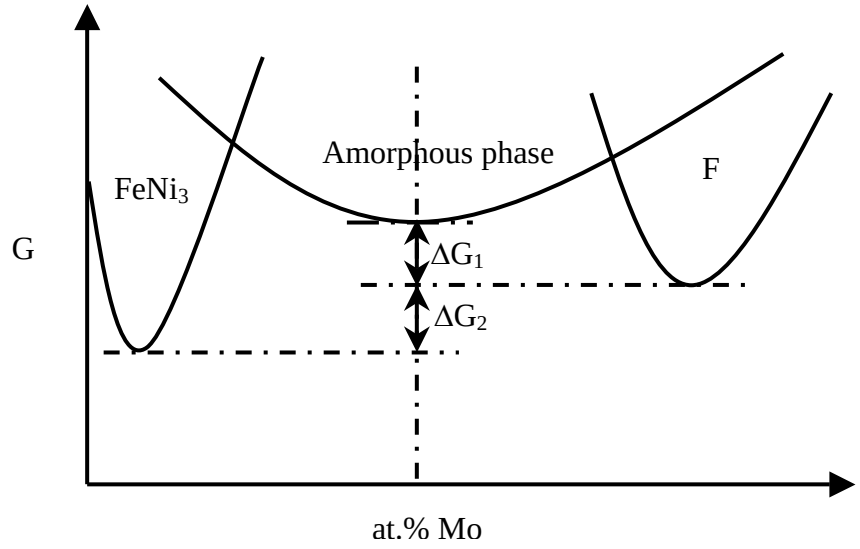

Fig.6.22 Revised hypothetical free-energy diagram showing the possible two phase transformation processes in the Ni-15%Fe-5%Mo-5%B alloy.

Phase formed in any material depend on the composition and processing conditions. For solidification from melt, the cooling rate plays a significant role in altering the products since it determines the degree of undercooling and affects the nucleation and growth process. For metallic glasses, the microstructures can be further modified by crystallization at large undercooling and slow diffusion. Crystallization from metallic glasses is a successful technique to process nanostructures from amorphous precursors (Scott, M.G. 1983; McHenry et al, 1999; Gao et al, 2000). This microstructure of the amorphous sample is related to alloy composition, atomic configuration and diffusion.

Crystallization of amorphous alloy is driven by the free energy difference between amorphous phase and the appropriate crystalline phase. Fig. 6.22 schematically illustrates the possible free energy difference between the metallic glass and the metastable phase $(Fe, Ni, Mo)_{23}B_6$ and equilibrium phase $FeNi_3$. There are two cases: formation of metastable phase followed by the formation of $FeNi_3$ phase.

From microstructure and EDX observation, it found that the primary crystallization only caused the formation of $(Fe, Ni, Mo)_{23}B_6$ which has the same composition as the amorphous matrix. The F phase in Fig. 6.22 represents $(Fe, Ni, Mo)_{23}B_6$. The formation of this metastable phase F is a polymorphic transformation. According to nucleation theory, the critical radius of nucleation γ_c is

$$\gamma_c=-2\gamma_{F\text{-}G}/\Delta G_{V\text{-}F} \quad (6.1)$$

$\gamma_{F\text{-}G}$ is the interfacial energy of metastable phase and metallic glass; $\Delta G_{V\text{-}F}$ is the volume free energy change from metallic glass to the metastable crystal, which corresponds to ΔG_1 in Fig. 6.22. From the microstructure observations, the crystal size is about 100 nm when sparse crystals are precipitated from the metallic glass. For the formation of this metastable crystal, diffusion is only required within one unit cell, it is thus preferred when the diffusion of atoms is slow.

When the annealing temperatures were increased, the mobility of atoms was increased. More stable phase will be formed. Coarsening of the metastable structure was initiated at the grain boundaries, and the atomic configuration at the grain boundary produced nucleation sites for the precipitation of the more stable $FeNi_3$ phase. The growth of precipitates at the grain boundaries induced a composition variation in the neighbouring region. This composition variation facilitates the nucleation of $FeNi_3$ phase. The final microstructure after the secondary crystallization stage comprised of $FeNi_3$ phase embedded in the $(Fe, Ni, Mo)_{23}B_6$ phase matrix. The free energy change for the formation of $FeNi_3$ phase from $(Fe, Ni, Mo)_{23}B_6$ phase is ΔG_2 in Fig. 6.22.

It can be detected that the even if the sample A is annealed at higher temperature than 700°C for longer time than 1 h, $(Fe, Ni, Mo)_{23}B_6$ phase can also exist. This is because from EDX observation, nearly no Mo atoms exist in $FeNi_3$ phase, then those Mo atoms should exist with $(Fe, Ni, Mo)_{23}B_6$ phase. The final microstructure is comprised of $FeNi_3$ and $(Fe, Ni, Mo)_{23}B_6$ phases.

(C) Magnetic properties

Saturation magnetization $\boldsymbol{M_s}$ and coercivity $\boldsymbol{H_c}$ of the completely amorphous ribbon after annealing at different temperatures were determined from the hysteresis loops and the results were summarized in Table 6.2. Fig. 6.23 shows the variation of saturation magnetization with the annealing temperature. The saturation magnetization of the as-spun ribbon was about 2.4 emu/g, and after annealing, $\boldsymbol{M_s}$

increased slightly to 4.3 emu/g at 500°C. Further annealing at 550°C and 600°C caused $\boldsymbol{M_s}$ to decrease slightly to 2 emu/g, and $\boldsymbol{M_s}$ to increase to 6 emu/g when the annealing temperature increased further to 700°C.

Since the change in saturation magnetization during annealing was not significant, it could be considered that annealing had very little effect on $\boldsymbol{M_s}$. Although (Fe, Ni, Mo)$_{23}$B$_6$ phase was found to crystallize in the primary crystallization stage, it had the same composition with the amorphous matrix. Hence, saturation magnetization did not change after the polymorphous crystallization. FeNi$_3$ phase began to precipitate during the secondary crystallization stage and $\boldsymbol{M_s}$ should increase. However, the amount of FeNi$_3$ phase was small. Hence, saturation magnetization would still keep constant after the secondary crystallization.

The magnetic properties of Fe$_x$Ni$_{23-x}$B$_6$ alloy having the same space group and structure with (Fe, Ni, Mo)$_{23}$B$_6$ phase have been reported by Idzikowski and his co-workers (Nakamura et al, 2002; Idzikowski and Szajek, 2003; Idzikowski et al, 2004). The metastable magnetically ordered fcc-Fe$_x$Ni$_{23-x}$B$_6$ phase was produced from amorphous Fe$_{81-y-z}$Ni$_y$Zr$_7$B$_{12}$Au$_y$ (y=10-40, 64; z=0, 1) precursors by heat treatment. Magnetic behavior of Fe$_x$Ni$_{23-x}$B$_6$ (x=0, 1, 22 and 23) phases were studied theoretically using the spin polarized tight binding linear muffin-tin orbital (TB-LMTO) method. It was found that the magnetic properties of this phase were highly dependent on the atomic percent of Fe atoms, and the values of the magnetic moments were dependent on the local environment of Fe atoms. Increasing the number of neighboring boron atoms reduces the magnetic moment of iron. In the case of Ni$_{23}$B$_6$ compound, the magnetic moment was reduced almost to zero. The main component in the (Fe, Ni, Mo)$_{23}$B$_6$ phase found in our experiment was Ni. Hence, according to Idzikowski and his co-workers research, the magnetic moment of this phase would be very small. This explains why low $\boldsymbol{M_s}$ value was observed during the primary crystallization process for our samples.

Table 6.2 Saturation magnetization and coercivity of the initially completely amorphous ribbon annealed at different temperatures for 1 h.

Annealing temperature (°C)	Saturation magnetization (emu/g)	Coercivity (Oe)
As-spun	2.4	30.0
350	2.6	174.3
400	3.6	69.6
450	4.1	42.4
500	4.3	99.6
550	1.9	69.1
600	2.2	40.7
700	6.0	20.0

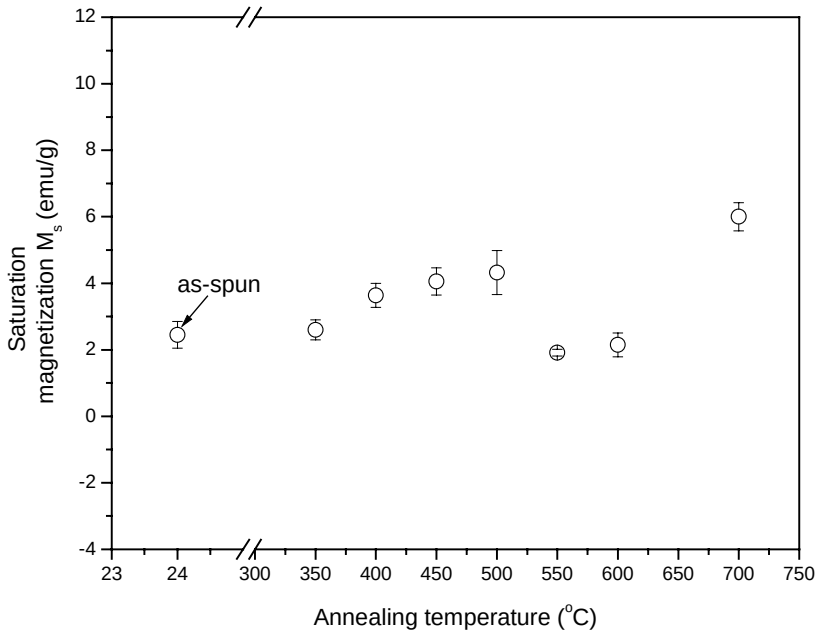

Fig.6.23 Saturation magnetization of the initially completely amorphous ribbon annealed at different temperatures for 1 h.

Coercivity of the completely amorphous ribbon annealed at different temperatures for 1 h is shown in Fig. 6.24. The coercivity of the as-spun ribbon was nearly 30 Oe. After annealing at 350°C, $\boldsymbol{H_c}$ of the ribbon increased significantly to 174 Oe. Such a large increase in $\boldsymbol{H_c}$ was due to the formation of the $(Ni, Fe, Mo)_{23}B_6$ phase and

increase of grain size. Further increase in the annealing temperatures caused a decrease in $\boldsymbol{H_c}$. This decrease is likely to be due to the increase in grain size that the grain size was in the right hand of Herzer diagram, which caused the decrease of coercivity. From this observation, it can be concluded that the critical grain size for coercivity is about 100 nm.

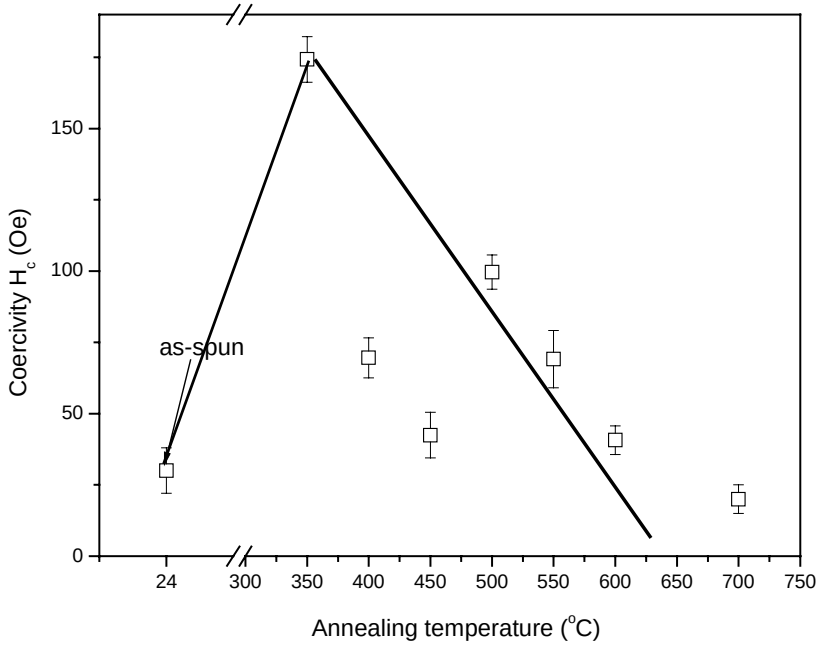

Fig.6.24 Coercivity of the initially completely amorphous ribbon annealed at different temperatures for 1 h.

6.3.2.2 Effects of annealing time

Since the $(Fe, Ni, Mo)_{23}B_6$ phase formed during the primary crystallization stage is a non-magnetic phase, the effects of annealing time will only be discussed for the secondary crystallization stage and the results are presented in the following sections.

(A) XRD observation

XRD results of the completely amorphous ribbons annealed at 600°C for different duration are shown in Fig. 6.25. In general, $(Fe, Ni, Mo)_{23}B_6$ was the main phase for these three samples. However, as the annealing time increased to 1 h, a small little peak splitting at 43.6° was observed, which indicated the presence of the $FeNi_3$ phase. As the annealing time was increased further to 10 h, this peak became more pronounced, showing that more $FeNi_3$ phase was formed with prolonged annealing.

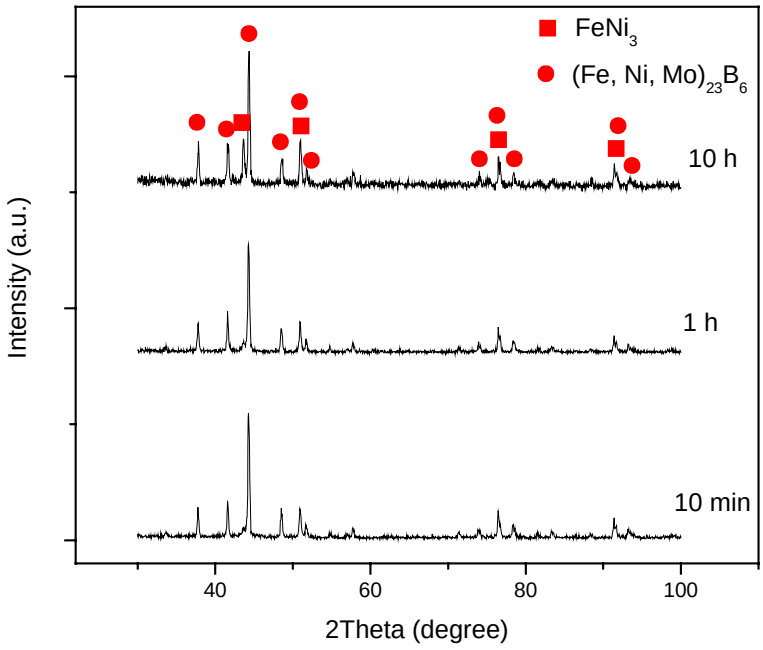

Fig.6.25 XRD results of the initially completely amorphous ribbon annealed at 600°C for 10 min, 1 h and 10 h.

(B) Microstructure observation

BF images of the completely amorphous ribbons annealed at 600°C for 10 min and 10 h are shown in Fig. 6.26. In general, the grain size varied from 100 nm to 200 nm. The grains of the ribbon annealed for 10 min were finer than the one annealed for 10 h. BF image of the ribbon annealed for 10 h was similar like the one annealed for 1 h (Fig. 6.19). Since two types of grains existed in the annealed ribbons, SADP was used to identify them. It was found that $FeNi_3$ phase was hardly found for the ribbon

annealed for 10 min because of the small amount of $FeNi_3$ phase at this condition. However, $FeNi_3$ phase could be detected from the ribbon annealed for 10 h. After indexing, it was found that the grains labeled as R shown in Fig. 6.26 were the $FeNi_3$ phase, the other type of grains in these two samples were indexed as the $(Fe, Ni, Mo)_{23}B_6$ phase. Typical diffraction patterns taken from the grains labeled as R for $FeNi_3$ phase and the grains for $(Fe, Ni, Mo)_{23}B_6$ phase are shown in Fig. 6.27 and 6.28. From the observation of microstructure and diffraction pattern, it might be concluded that the grains labeled as R observed in the BF images are $FeNi_3$ phase and the other grains are $(Fe, Ni, Mo)_{23}B_6$ phase.

EDX analysis was also performed on these two samples and the results are listed in Table 6.3. From the EDX observation, the atomic ratio of Ni and Fe in the grains labeled as R ($FeNi_3$ phase) was about 3:1. Compared to the EDX results for the primary crystallization presented in section 6.3.2.1 (B), more Ni atoms and less Fe atoms existed in the $(Fe, Ni, Mo)_{23}B_6$ phase for the secondary crystallization stage.

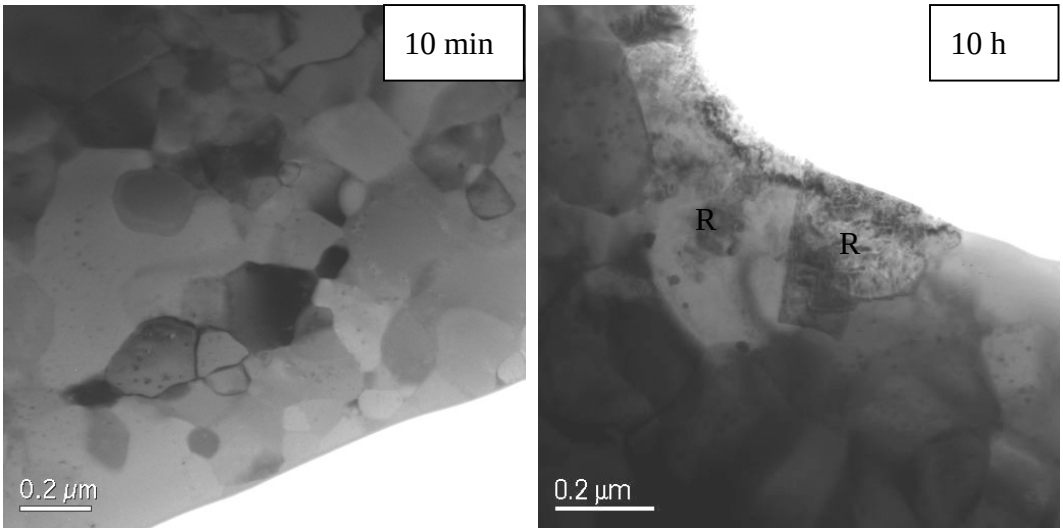

Fig.6.26 BF images of the initially completely amorphous ribbon annealed at 600°C for 10 min and 10 h.

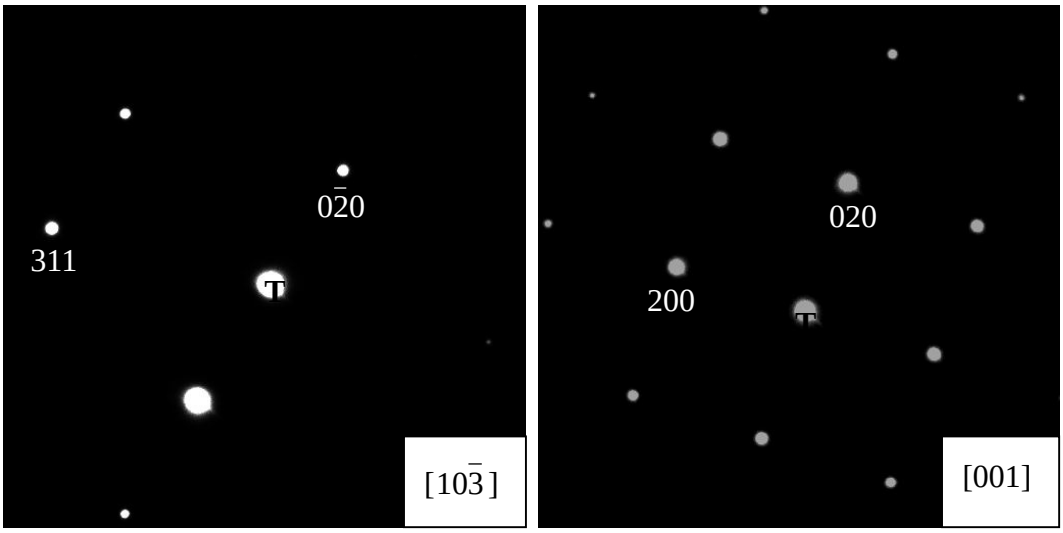

Fig.6.27 Typical diffraction patterns of $FeNi_3$ phase.

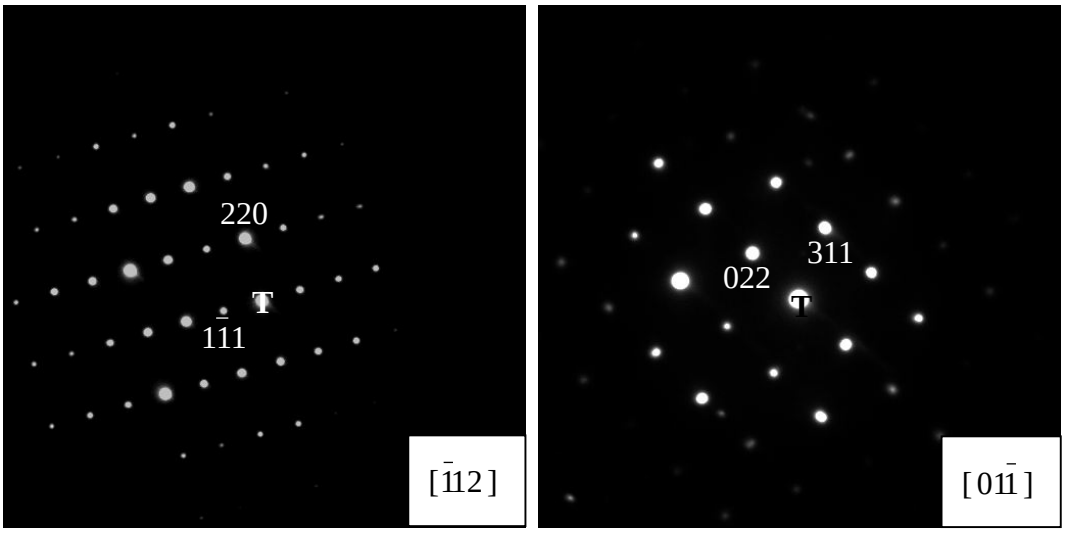

Fig.6.28 Typical diffraction patterns of $(Fe, Ni, Mo)_{23}B_6$ phase.

Table 6.3 Average composition (at. % metallic elements) obtained using TEM/EDX analysis of $FeNi_3$ and $(Fe, Ni, Mo)_{23}B_6$ grains of the initially completely amorphous ribbon after annealing at 600°C for different time.

Name	Composition (atomic %)		
	Ni	Fe	Mo
$FeNi_3$	75.1±0.6	24.4±0.5	0.5±0.2
$(Fe, Ni, Mo)_{23}B_6$	81.3±0.6	15.4±0.5	3.3±0.2

(C) Magnetic properties

Magnetic properties of the as-spun completely amorphous ribbon annealed at 600°C for different durations are listed in Table 6.4. The graphical representation of saturation magnetization is shown in Fig 6.29. It was observed that in general, as annealing time increased, saturation magnetization increased. $\boldsymbol{M_s}$ increased to 10.8 emu/g after annealing at 600°C for 10 h. The increase in saturation magnetization was attributed to the appearance of the magnetic $FeNi_3$ phase during the secondary crystallization. However, as the $FeNi_3$ phase remained to be the minor phase in these annealed ribbons as evident from the XRD results (Fig. 6.25), the value of saturation magnetization was still very small.

Saturation magnetization of the completely amorphous ribbon annealed at 600°C for different durations was compared to the $\boldsymbol{M_s}$ of the annealed partially amorphous powders. Lower $\boldsymbol{M_s}$ was observed for the annealed completely amorphous ribbon. The reason for this difference could be due to the crystallization sequence of the ferromagnetic $FeNi_3$ phase. For the as-milled powders, the main phases were the amorphous phase and the $FeNi_3$ phase. After annealing, $(Fe, Ni, Mo)_{23}B_6$ phase began to appear. However, the $FeNi_3$ phase still remained as the major phase. Hence, the saturation magnetization before and after annealing for the milled powders was similar as discussed earlier in chapter 5 (Fig. 5.31). However, as $(Fe, Ni, Mo)_{23}B_6$ was the only product during the primary crystallization of the amorphous ribbon, the annealed ribbon showed nearly no magnetic properties. $FeNi_3$ phase crystallized from the $(Fe, Ni, Mo)_{23}B_6$ matrix gradually during the secondary crystallization. Hence, the saturation magnetization increased gradually due to the increase in amount of the $FeNi_3$ phase.

Coercivity of the completely amorphous ribbon annealed at 600°C for different durations is shown in Fig. 6.30. Coercivity decreased from 80 Oe for the ribbon annealed for 10 min to 20 Oe for the ribbon annealed for 10 h. The decrease in coercivity is likely due to the crystallization of the $FeNi_3$ phase and the growth of the grain size during the secondary crystallization stage. The average grain size is larger than the critical dimension 100 nm, which means that the grain size lies in the right hand of Herzer diagram, coercivity decreased with the increase of grain size.

Table 6.4 Saturation magnetization and coercivity of the initially completely amorphous ribbon annealed at 600°C for different time.

Annealing time (minutes)	Saturation magnetization (emu/g)	Coercivity (Oe)
10	1.4	84.3
60	2.2	40.7
600	10.8	20.5

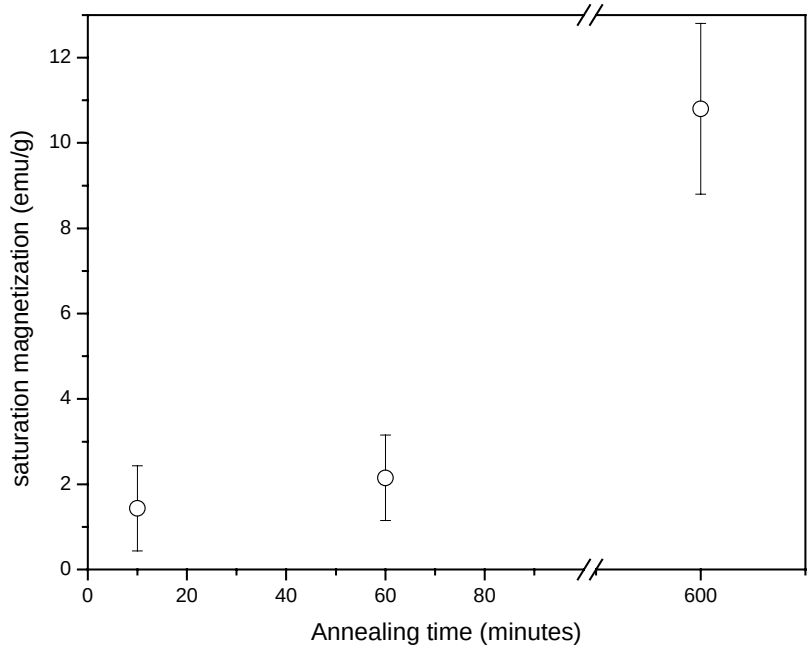

Fig.6.29 Saturation magnetization of the initially completely amorphous ribbon annealed at 600°C for different time.

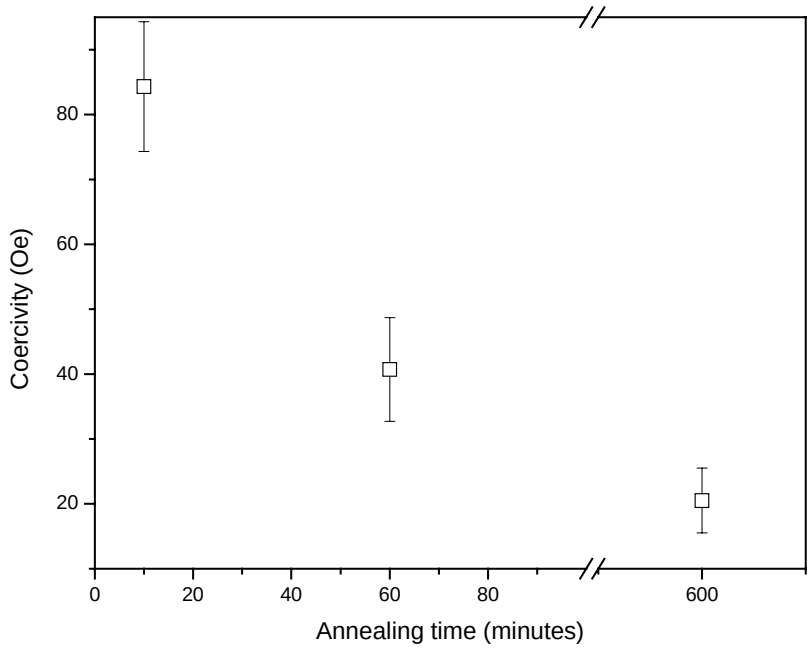

Fig.6.30 Coercivity of the initially completely amorphous ribbon annealed at 600°C for different time.

6.3.3 Crystallization studies for Sample B (partially amorphous ribbon)

Based on the DSC results obtained at a heating rate of 10°C/min for sample B (partially amorphous ribbon), the onset temperatures of the two crystallization steps were observed at about 410°C and 550°C. According to this result, annealing temperatures ranging from 400°C to 550°C were chosen to study the first step crystallization, and temperature of 600°C was chosen to study the secondary crystallization. The effects of annealing temperature at these two step crystallization will be discussed in section 6.3.3.1, and the effects of annealing time at these two stages will be covered in section 6.3.3.2.

6.3.3.1 Effects of annealing temperature

(A) XRD observation

Fig. 6.31 shows the XRD results of the partially amorphous ribbon annealed at different temperatures for 1 h in the primary crystallization stage. In general, after annealing, the diffraction peaks of $FeNi_3$ and $(Fe, Ni, Mo)_{23}B_6$ phases overlapped at about 44° for the as-spun ribbon could be distinguished clearly. As the annealing temperatures increased, the peaks became more obvious and the intensity of all the peaks increased. The XRD results were similar for the ribbons annealed at 500°C and 550°C.

The XRD result of the partially amorphous ribbon annealed at the temperature close to the secondary crystallization temperature (600°C) is shown in Fig. 6.32. More $FeNi_3$ phase was observed as compared to the annealed samples shown in Fig. 6.31.

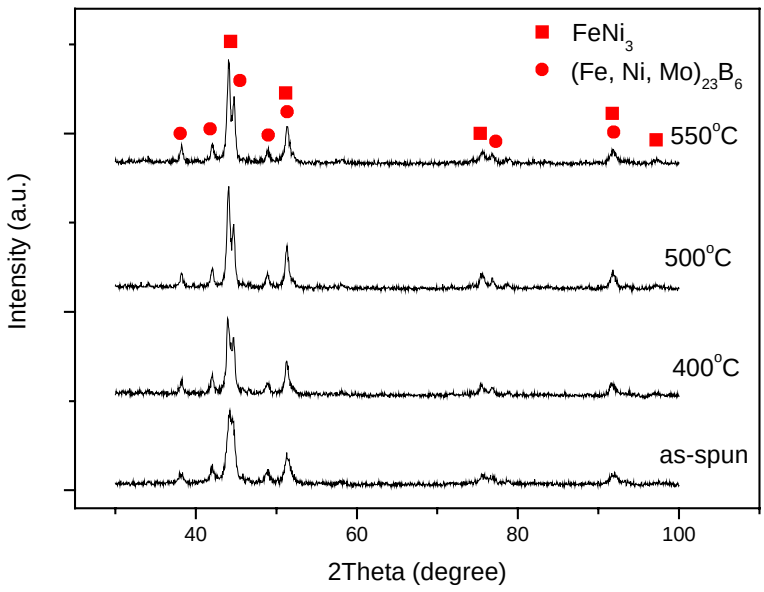

Fig.6.31 XRD results of the initially partially amorphous ribbon annealed at different temperatures for 1 h.

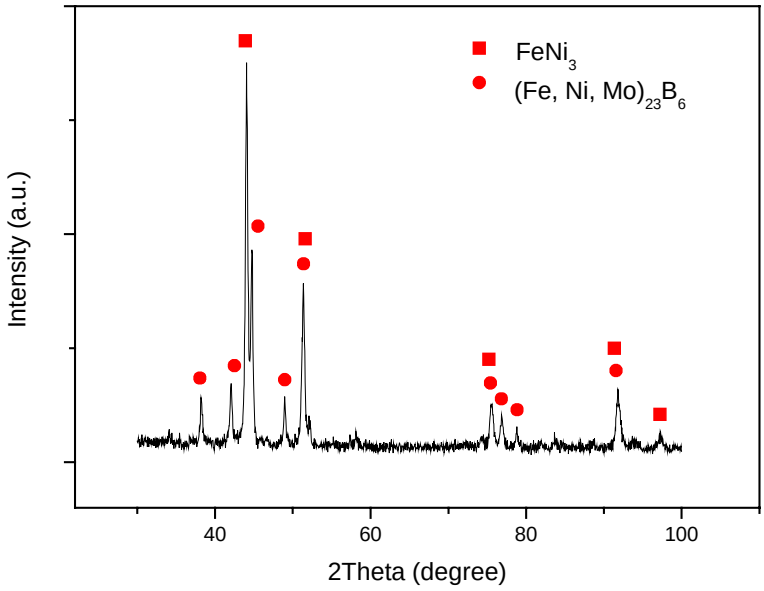

Fig.6.32 XRD results of the initially partially amorphous ribbon annealed at 600°C for 1 h.

XRD results during the primary crystallization of the partially amorphous ribbon annealed at different temperatures for 1 h were compared to the completely amorphous ribbon annealed under similar conditions (Fig. 6.12). It was found that $FeNi_3$ phase only existed in the partially amorphous ribbon. From the discussion for the crystallization process of the completely amorphous ribbon, $FeNi_3$ phase only existed in the secondary crystallization and the primary crystallization only caused the formation of $(Fe, Ni, Mo)_{23}B_6$ phase. The observed $FeNi_3$ phase in the primary crystallization of the partially amorphous ribbon should be due to the characteristic of the original partially amorphous ribbon.

(B) Microstructure observation

The microstructure of the partially amorphous ribbon annealed at 400°C for 1 h is shown in Fig. 6.33. Two types of grains were observed for the ribbon annealed at 400°C for 1 h: (1) one type of grains with grain size ranging from 30 to 80 nm, and (2) the other one with average grain size of about 50 nm. One type of grains was

found to usually exist at the grain boundary between the other type of grains. Diffraction pattern taken from this ribbon (Fig. 6.34) showed the nanosize and the random orientation of the grains, and the diffraction pattern was indexed as a mixture of the $FeNi_3$ and $(Fe, Ni, Mo)_{23}B_6$ phases. Under this condition, the grain sizes of these phases were mostly less than 50 nm, and SADP could not be obtained for a single grain.

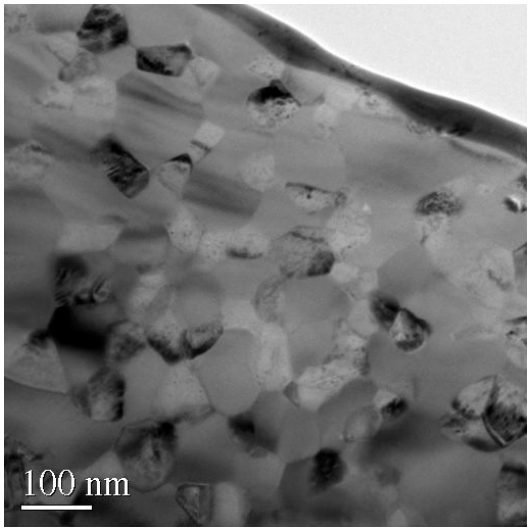

Fig.6.33 BF image of the initially partially amorphous ribbon annealed at 400°C for 1 h.

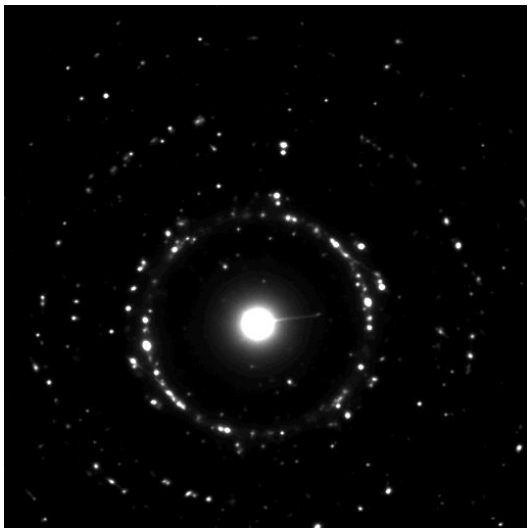

Fig.6.34 Typical diffraction pattern of the initially partially amorphous ribbon annealed at 400°C for 1 h.

Clear grain boundaries were observed for the ribbon annealed at 400°C for 1 h (Fig. 6.33) as compared to the as-spun partially amorphous ribbon (Fig. 6.6). The amorphous phase existed in the as-spun ribbon had crystallized after annealing. The crystallization of the amorphous phase was further confirmed from the diffraction pattern shown in Fig. 6.34 where no broad diffused rings indicating the presence of an amorphous phase could be observed.

The ribbons annealed at higher temperatures (Fig. 6.35) also showed similar microstructure as the one annealed at 400°C. Two types of grains were still observed. However, the grain size of these two types of grains grew to nearly 100 nm when the ribbon was annealed at 600°C (Fig. 6.36). Annealing at 600°C would mean that the ribbon was in the secondary crystallization stage when the $FeNi_3$ phase began to precipitate. From the microstructure observation, the ribbon held at 600°C for 1 h not only caused the precipitation of the $FeNi_3$ phase, but also caused the grain growth.

Although the initial composition was the same, the microstructures of the completely amorphous (sample A) and partially amorphous (sample B) ribbons after the primary crystallization at annealing temperature of less than 600°C were quite different as shown in Fig. 6.16, 6.33 and 6.35. The grain size of the completely amorphous ribbon after annealing was about 100 nm, while the average grain of sample B after annealing was about 50 nm. Two distinct features of the grains could be observed for the partially amorphous ribbon. The different microstructures observed are likely due to the presence of the $FeNi_3$ phase in the partially amorphous ribbon before annealing. According to the crystallization studies for the completely amorphous ribbons, $FeNi_3$ phase only crystallized during the secondary crystallization stage when the annealing temperature was increased to 600°C. Hence, $FeNi_3$ should be a more stable phase than $(Fe, Ni, Mo)_{23}B_6$, and the appearance of the $FeNi_3$ phase during the primary crystallization could hinder the grain growth of the $(Fe, Ni, Mo)_{23}B_6$ phase. This explains the finer microstructure observed for sample B. Such fine microstructure was also observed for the annealed partially amorphous powders obtained by HEBM, where the as-milled powders also contained $FeNi_3$ phase before the annealing process. Similar observation was also

reported for $Nd_8Fe_{76.5}Co_8B_6Nb_1Cu_{0.5}$ ribbons (Wu et al, 2000). It was found that the nanocomposite microstructure produced by annealing from a fully amorphous alloy had grain size about two times larger than that produced from a partially crystallized alloy. However, the reason why $Nd_8Fe_{76.5}Co_8B_6Nb_1Cu_{0.5}$ nanocomposite microstructure could not be obtained by the crystallization of an amorphous alloy was not clear.

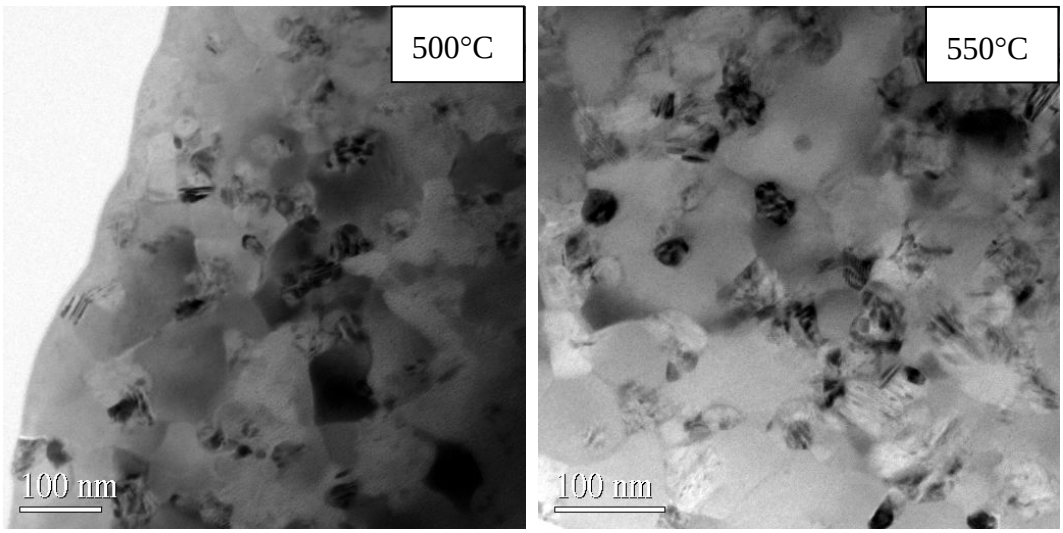

Fig.6.35 BF images of the initially partially amorphous ribbon annealed at different temperatures for 1 h.

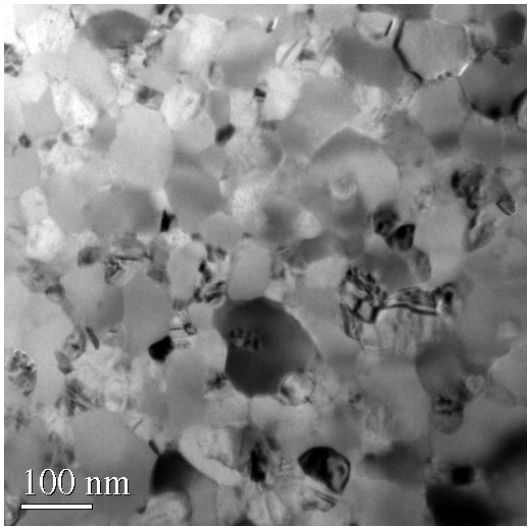

Fig.6.36 BF image of the initially partially amorphous ribbon annealed at 600°C for 1 h.

(C) Magnetic properties

Saturation magnetization $\boldsymbol{M_s}$ and coercivity $\boldsymbol{H_c}$ of the partially amorphous ribbon annealed at different temperatures for 1 h are listed in Table 6.5. Saturation magnetization is graphically presented in Fig. 6.37. In general, $\boldsymbol{M_s}$ for the annealed samples were higher than the as-spun ribbon. The increase in the saturation magnetization after annealing might be caused by the crystallization of the partially amorphous phase, and the value did not change much. This is because although the formation of the $FeNi_3$ phase would cause the increase in $\boldsymbol{M_s}$ during the annealing process, the amount of this phase does not change much after annealing. Compared to the annealed completely amorphous ribbon (Fig. 6.23), higher $\boldsymbol{M_s}$ was observed for the annealed partially amorphous ribbon. The reason for this observation was due to the presence of the $FeNi_3$ phase in the partially amorphous ribbon after the primary crystallization stage.

Coercivity of the partially amorphous ribbon annealed at different temperatures for 1 h is shown in Fig. 6.38. It was observed after annealing, coercivity increased sharply from less than 15 Oe for the as-spun ribbon to nearly 107 Oe for the ribbon annealed at 400°C for 1 h. As the annealing temperature increased further, coercivity also increased further to about 175 Oe. From microstructure observation, it was found that grain size was less than 100 nm even annealed at 600°C. It has been concluded in section 6.3.2.1 that grain size of 100 nm is the critical dimension for coercivity, which means that when the grain size is less than 100 nm, coercivity increases with the increase of grain size, on the other hand when the grain size is larger than 100 nm, coercivity decreases with the increase of grain size. According to this, the increase in $\boldsymbol{H_c}$ after annealing is likely to be caused by the increase of grain size.

It was noted that a higher coercivity was observed for the annealed partially amorphous ribbon as compared to the completely amorphous one (Fig. 6.24). Grain size might be the main reason for the high value. As described in the literature review, when the grain size was larger than the width of domain wall, larger grain size would lead to low coercivity. As the grain size of the annealed completely amorphous ribbon was much larger than the annealed partially amorphous ribbon,

high coercivity would be observed for the partially amorphous ribbon.

Table 6.5 Saturation magnetization and coercivity of the initially partially amorphous ribbon annealed at different temperatures for 1 h.

Annealing temperature (°C)	Saturation magnetization (emu/g)	Coercivity (Oe)
As-spun	24.9	14.9
400	31.6	106.7
500	30	155.6
550	27.8	174.4
600	29.3	173.5

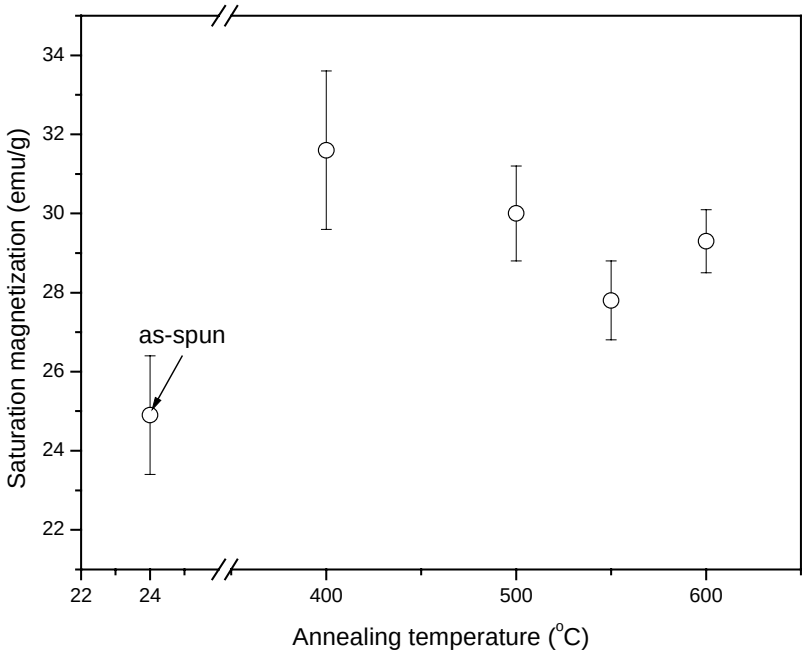

Fig.6.37 Saturation magnetization of the initially partially amorphous ribbon annealed at different temperatures for 1 h.

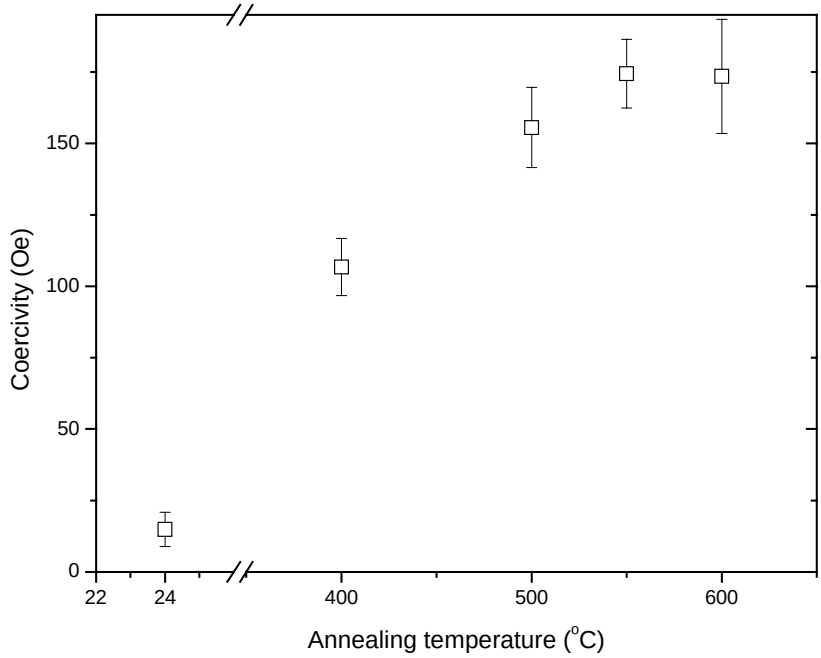

Fig.6.38 Coercivity of the initially partially amorphous ribbon annealed at different temperatures for 1 h.

6.3.3.2 Effects of annealing time

As the $FeNi_3$ phase existed in both the primary and secondary crystallization stages, effects of annealing time on the crystallization will be discussed for these two stages. The results are shown in section 6.3.3.2.1 for the primary crystallization and in section 6.3.3.2.2 for the secondary crystallization.

6.3.3.2.1 Primary Crystallization

(A) XRD observation

XRD results of the partially amorphous ribbon annealed at 500°C for different duration are shown in Fig. 6.39. In general, as the annealing time increased, all the peaks became sharper and the peaks corresponding to the two phases became more obvious which indicated the growth of these two phases. Compared to the primary crystallization of the completely amorphous ribbon (Fig. 6.12), $FeNi_3$ phase was

observed for the annealed partially amorphous ribbon. This was due to the existence of the $FeNi_3$ phase in the as-spun partially amorphous ribbon.

It was also observed that longer annealing duration at 500°C did not cause an increase in the $FeNi_3$ phase. Instead, $(Fe, Ni, Mo)_{23}B_6$ phase was observed to crystallize from the partially amorphous ribbon. This observation also confirmed the crystallization process of Ni-15%Fe-5%Mo-5%B alloy that the primary crystallization was the precipitation of $(Fe, Ni, Mo)_{23}B_6$ phase from the amorphous matrix.

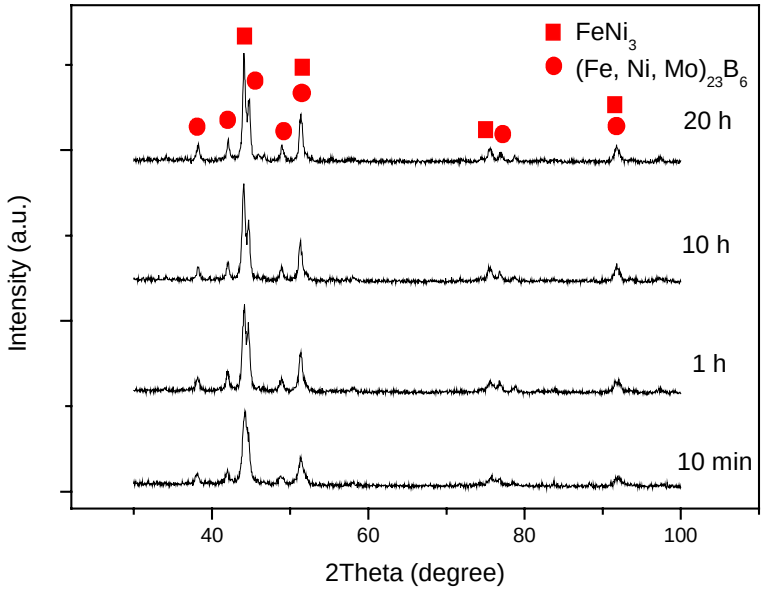

Fig.6.39 XRD results of the initially partially amorphous ribbon annealed at 500°C for different times.

(B) Microstructure observation

BF images of the partially amorphous ribbon annealed at 500°C for 10 min, 1 h, 10 h and 20 h are shown in Fig. 6.40. In general, two types of grains were still observed for these four samples. Longer annealing at 500°C for 20 h did not change the microstructure, and this microstructure was similar to the ones annealed at 500°C and 550°C for 1 h (Fig. 6.35). Annealing time seemed to have no effect on the

observed microstructure during the primary crystallization stage.

From the DSC results (Fig. 6.7), the primary crystallization of the partially amorphous ribbon (sample B) would have completed at 450°C with a heating rate of 10°C/min. It seemed that the presence of the $FeNi_3$ phase in the primary crystallization hindered grain growth, and the microstructure remained the same during the primary crystallization process even when the annealing time increased to 20 h. Hence, for the primary crystallization, annealing time has no effect on the observed microstructure for the partially amorphous ribbon.

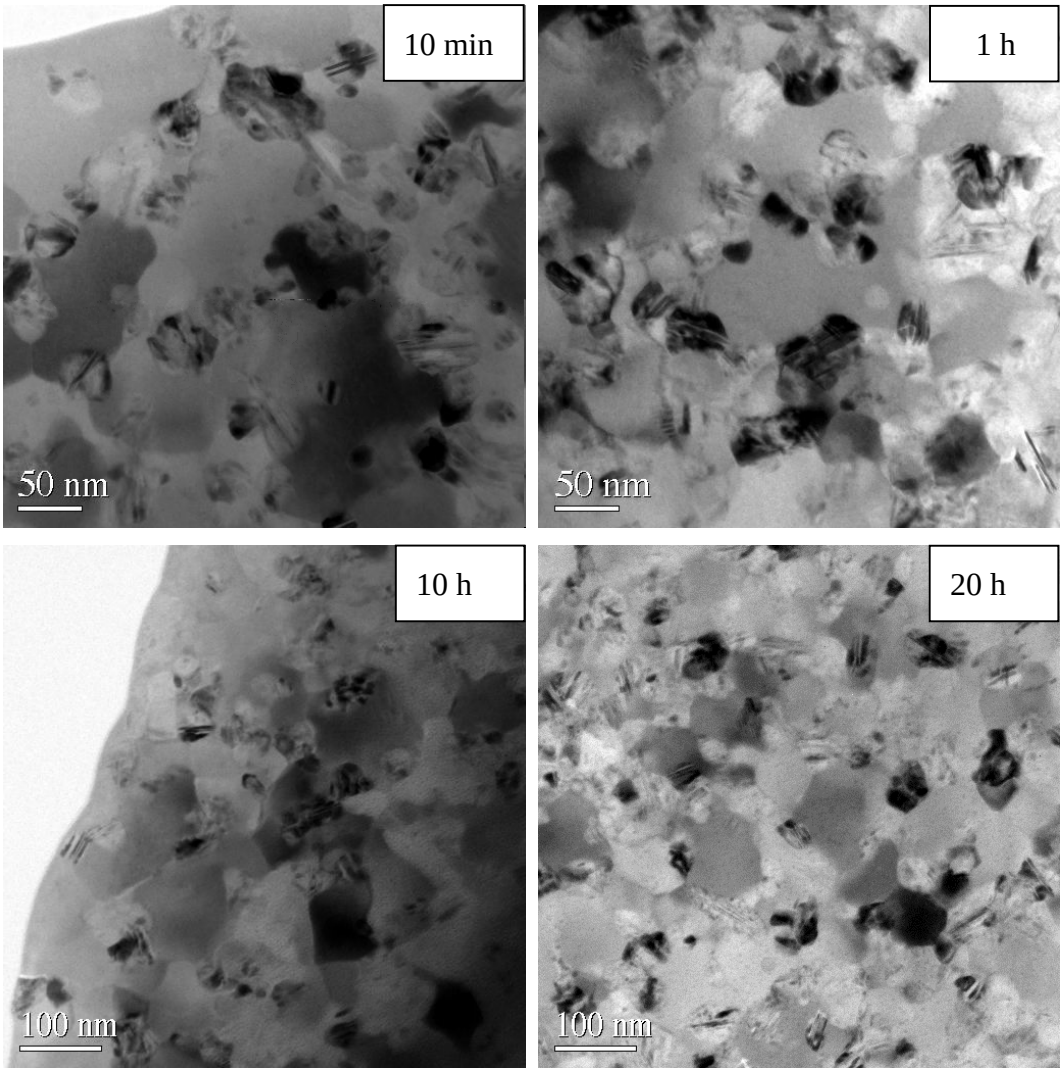

Fig.6.40 BF images of the initially partially amorphous ribbon annealed at 500°C for different times.

SADP was used to index the two types of grains and the diffraction pattern taken from one type of grain of the partially amorphous ribbon annealed at 500°C for 20 h is shown in Fig. 6.41. This diffraction was identified as $(Fe, Ni, Mo)_{23}B_6$ phase taken from $[0\bar{1}1]$ zone. Since the grain size of the other type of grains was small, it was difficult to obtain the diffraction pattern from them.

In order to confirm SADP observation, EDX spectra were done on the ribbon annealed at 500°C for 20 h. EDX spectra are shown in Fig. 6.42 and the results are listed in Table 6.6. From the ratio of Fe and Ni, one type of grains were indexed as the $FeNi_3$ phase and the other type of grains were indexed as $(Fe, Ni, Mo)_{23}B_6$ phase. From SADP and EDX observation, it could be concluded that the two types of grains were $(Fe, Ni, Mo)_{23}B_6$ and $FeNi_3$ phases.

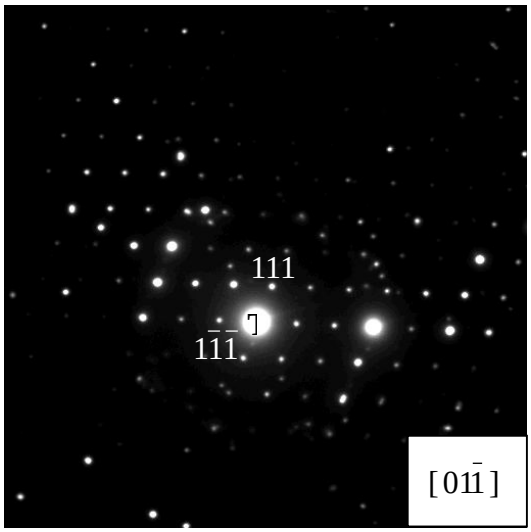

Fig.6.41 SADP taken from one type grain of the initially partially amorphous ribbon annealed at 500°C for 20 h.

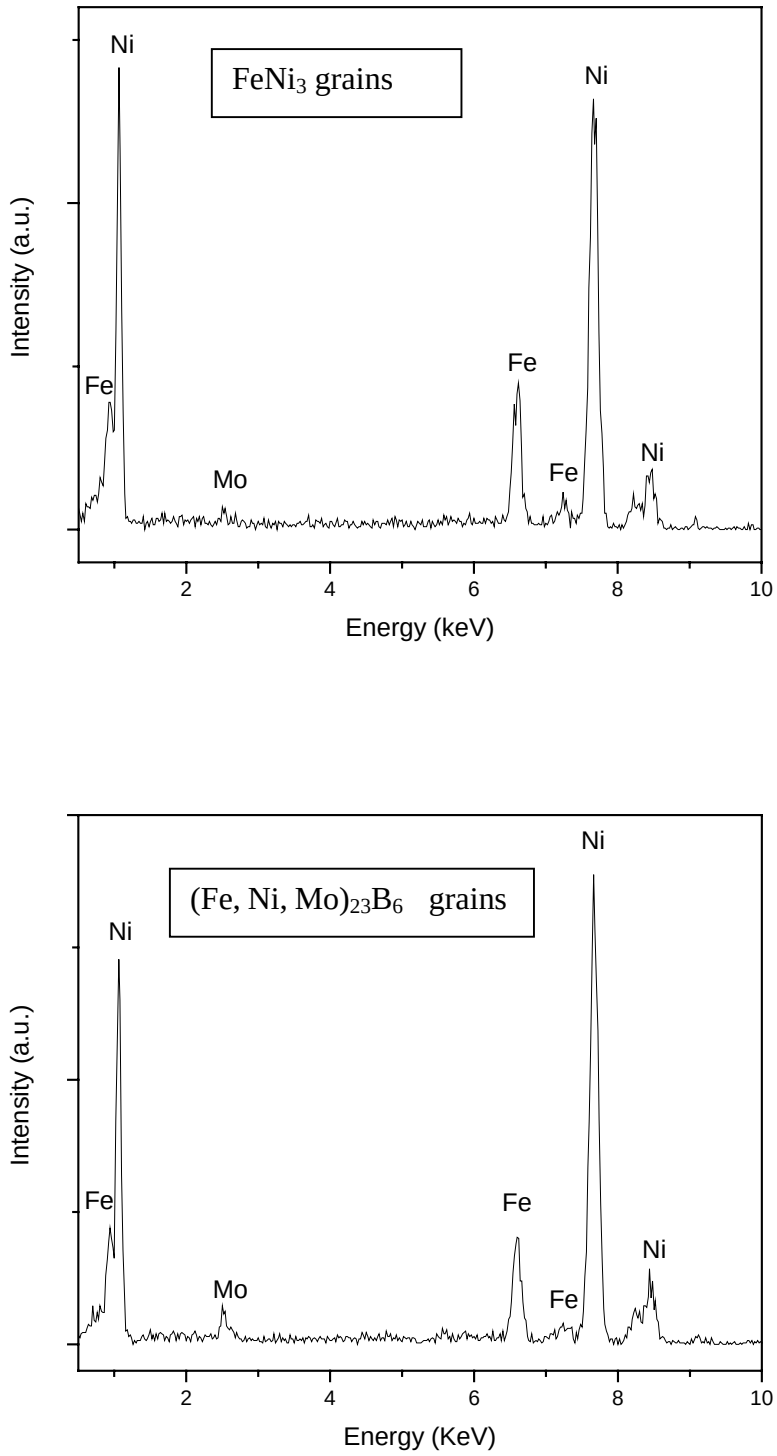

Fig.6.42 EDX spectra of the initially partially amorphous ribbon annealed at 500°C for 20 h.

Table 6.6 Composition analysis of the grains of the initially partially amorphous ribbon annealed at 500°C for 20 h.

Grain Number	Composition (atomic %)		
	Ni	Fe	Mo
$FeNi_3$ grains	74.5±0.6	24.4±0.5	1.1±0.2
$(Fe, Ni, Mo)_{23}B_6$ grains	80.7±0.6	15.7±0.5	3.6±0.2

(C) Magnetic properties

Magnetic properties of the partially amorphous ribbon annealed during the primary crystallization stage are listed in Table. 6.7. Saturation magnetization of the partially amorphous ribbon annealed at 500°C for different durations is graphically presented in Fig. 6.43. In general, saturation magnetization was observed to decrease slightly after annealing. This slight decrease was caused by the formation of $(Fe, Ni, Mo)_{23}B_6$ phase in the primary crystallization stage.

Coercivity of the partially amorphous ribbon annealed at 500°C for different durations is graphically presented in Fig. 6.44. Coercivity was observed to increase after annealing. As grain size is less than 100 nm, coercivity increased with the increase of grain size.

Table 6.7 Saturation magnetization and coercivity of the initially partially amorphous ribbon annealed at 500°C for different time.

Annealing time (minutes)	Saturation magnetization (emu/g)	Coercivity (Oe)
10	37.1	134.4
60	30	155.6
600	28.5	164.7
1200	30	166.4

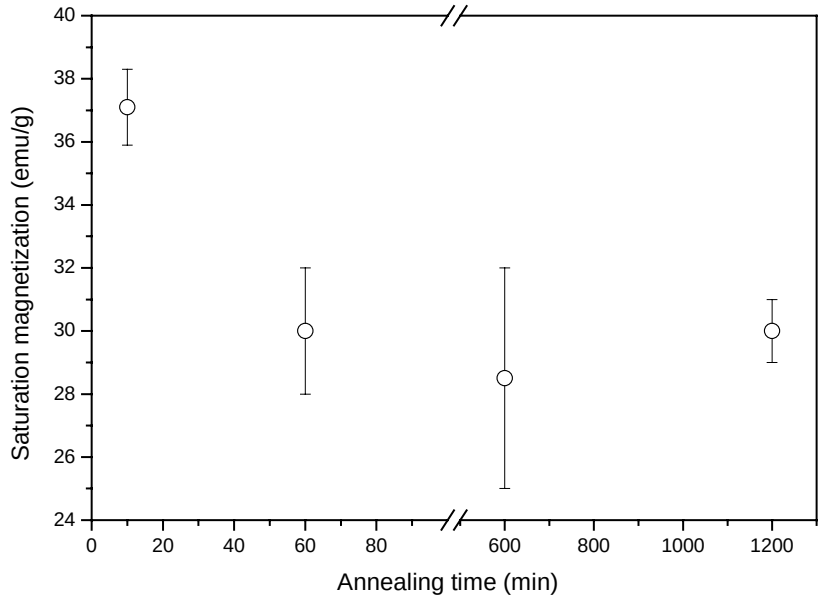

Fig.6.43 Saturation magnetization of the initially partially amorphous ribbon annealed at 500°C for different time.

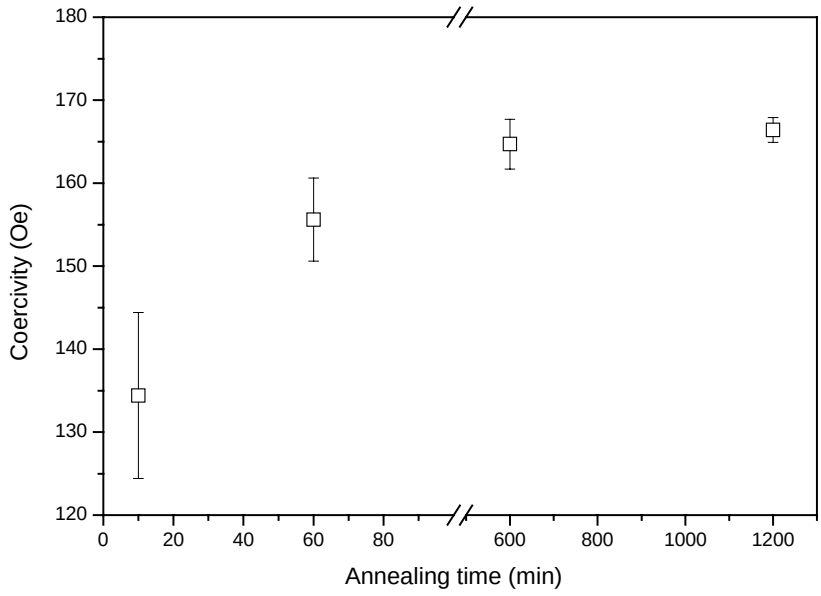

Fig.6.44 Coercivity of the initially partially amorphous ribbon annealed at 500°C for different time.

6.3.3.2.2 Secondary Crystallization

(A) XRD observation

XRD results of the partially amorphous ribbon annealed at 600°C for different durations are shown in Fig. 6.45. In general, as the annealing time increased, all the peaks became sharper and the peaks corresponding to the two phases became more obvious which indicated the growth of these two phases. Compared to the partially amorphous ribbon and the completely amorphous ribbon, more $FeNi_3$ phase was observed for the partially amorphous ribbon after the secondary crystallization. This is due to the existence of the $FeNi_3$ phase in the as-spun partially amorphous ribbon which acted as nucleation center for the secondary crystallization to occur.

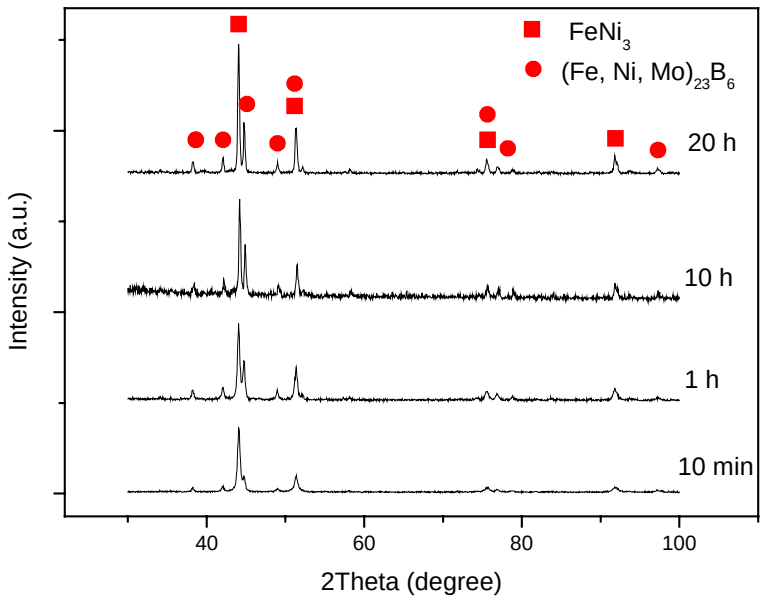

Fig.6.45 XRD results of the initially partially amorphous ribbon annealed at 600°C for different times.

Comparing the XRD results of the ribbons annealed for different durations at 500°C (Fig. 6.39) and 600°C (Fig. 6.45), it was found that there was an increase in the amount of $FeNi_3$ phase and decrease in the amount of $(Fe, Ni, Mo)_{23}B_6$ phase at 600°C. This observation confirmed the crystallization process of Ni-15%Fe-5%Mo-5%B alloy that the secondary crystallization was the precipitation of $FeNi_3$ phase from the $(Fe, Ni, Mo)_{23}B_6$ matrix.

(B) Microstructure observation

BF images of the partially amorphous ribbon (sample B) annealed at 600°C for 10 min and 10 h are shown in Fig. 6.46. Two types of grains were also observed for the ribbon annealed for 10 min, and this microstructure observation was similar to the ones observed in the first crystallization stage (Fig. 6.40). One type of grains existed at the grain boundary and inside the other type of grains. As the annealing time increased to 10 h, these grains grew to 100 nm, and the two types of grains became less obvious.

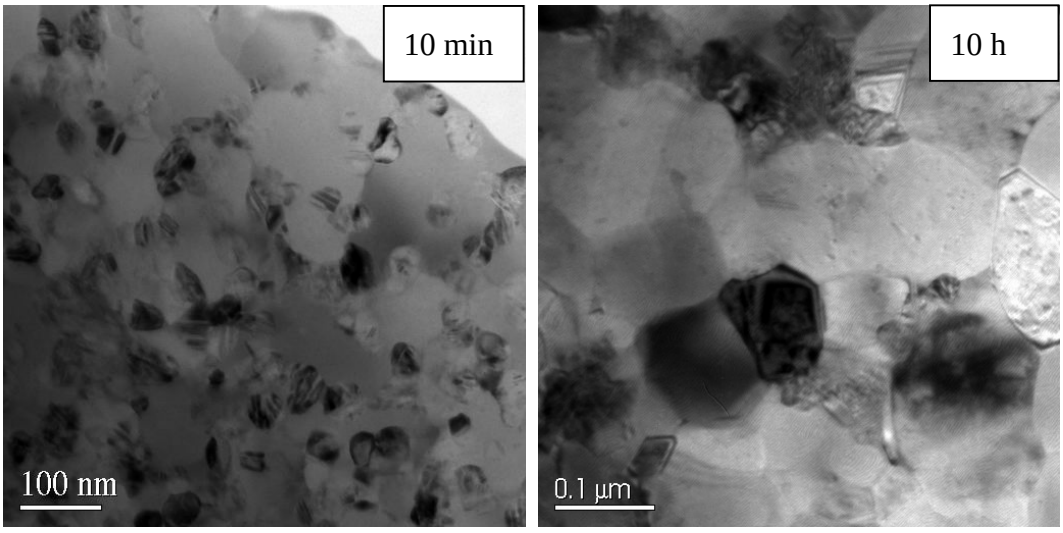

Fig.6.46 BF images of the initially partially amorphous ribbon annealed at 600°C for 10 m and 10 h.

BF image of the partially amorphous ribbon annealed at 600°C for 20 h is shown in Fig. 6.47. The microstructure of the ribbon annealed at 600°C for 10 min (Fig. 6.46) and 20 h (Fig. 6.47) showed a significant difference. The average grain sizes grew from less than 100 nm to 200 nm. It could be concluded that when the annealing time was increased to 600°C for the secondary crystallization, longer annealing time caused the growth of grains. At the secondary crystallization stage, $FeNi_3$ phase was precipitated, and no longer hindered the grain growth. Typical diffraction patterns taken from the $FeNi_3$ grains (labeled as R) are shown in Fig. 6.48.

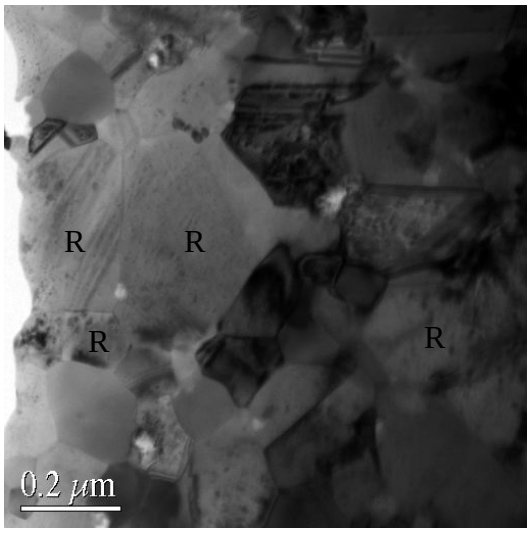

Fig.6.47 BF image of the initially partially amorphous ribbon annealed 600°C for 20 h.

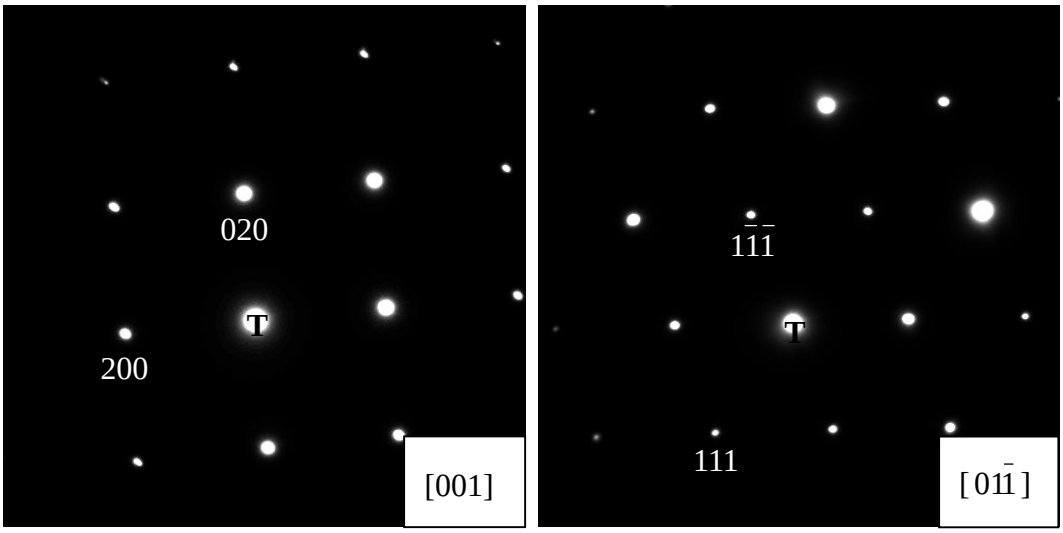

Fig.6.48 Typical diffraction pattern of the initially partially amorphous ribbon annealed at 600°C for 20 h.

Based on the microstructure analysis done on the partially amorphous ribbon, the crystallization process of the partially amorphous ribbon could be summarized as follows. Unlike the crystallization of a single amorphous phase for the completely amorphous ribbon (sample A), the partially amorphous ribbon (sample B) crystallized in the presence of $FeNi_3$ phase. As the amorphous phase and crystallized $(Fe, Ni, Mo)_{23}B_6$ phase had similar composition during the primary crystallization process, the mode of crystallization for the partially amorphous alloys was still polymorphous crystallization. The as-quenched state reduced its

free energy to a point. By this stage, the amorphous phase would have crystallized completely. The final product of the polymorphous crystallization contained both the $FeNi_3$ and $(Fe, Ni, Mo)_{23}B_6$ phases. As the annealing temperature increased to the secondary crystallization, more $FeNi_3$ phase crystallized at the cost of $(Fe, Ni, Mo)_{23}B_6$ phase. Thus, the crystallization reaction of the partially amorphous phase occurred two stages, and the secondary crystallization caused the precipitation of $FeNi_3$ from $(Fe, Ni, Mo)_{23}B_6$ phase and growth of $FeNi_3$ phase.

$$amorphous + FeNi_3 \xrightarrow{432^0 C} (Fe, Ni, Mo)_{23} B_6 + FeNi_3 \xrightarrow{600^0 C} (Fe, Ni, Mo)_{23} B_6 + FeNi_3$$

From the microstructure analysis, it was found that the microstructure of the partially amorphous ribbon (sample B) was finer than that of the completely amorphous ribbon (sample A) before and after annealing. Hence, nanostructured soft magnetic materials can only be obtained from the partially amorphous ribbon (sample B). The completely amorphous ribbon could not be used to produce nanostructured soft magnetic materials because no phase hinds the growth of $(Fe, Ni, Mo)_{23}B_6$ phase during the primary crystallization stage.

(C) Magnetic properties

Magnetic properties of the partially amorphous ribbon annealed during the secondary crystallization are listed in Table 6.8. Saturation magnetization of the partially amorphous ribbon annealed at 600°C for different durations is graphically presented in Fig. 6.49. Increase in saturation magnetization was observed as the annealing time increased. This was attributed to the increase in amount of the $FeNi_3$ phase during the secondary crystallization.

Coercivity of the partially amorphous ribbon annealed at 600°C for different time is shown in Fig. 6.50. Decrease in coercivity was observed as the annealing time increased. As the average grain size is nearly larger than 100 nm for the three annealed sample, this decrease was due to the grain growth in the secondary crystallization stage.

The magnetic properties of the partially amorphous ribbon after secondary crystallization were compared to the completely amorphous ribbon. It was observed that the value of saturation magnetization of the annealed partially amorphous ribbon was larger than that of the completely amorphous one. The initial composition of these two type samples was the same and they also underwent similar annealing process. The difference was attributed to the original status of the as-spun sample. It could be concluded that the presence of the $FeNi_3$ phase during the primary crystallization affected the magnetic properties even during the secondary crystallization.

The magnetic properties of the partially amorphous ribbons after annealing were also compared to the annealed partially amorphous powders. Saturation magnetization was almost the same for these two samples. However, higher coercivity was observed for the partially amorphous ribbon which could be caused by the pre-exist $(Fe, Ni, Mo)_{23}B_6$ phase in the as-spun ribbon. It can be concluded that the presence of the $FeNi_3$ phase before annealing was important not only for the refinement of the microstructure, but also for the optimization of the magnetic properties.

Better magnetic properties were also observed for α-$Fe/Nd_2Fe_{14}B$ samples annealed from the partially amorphous ribbons (Wu et al, 2000). It was observed that the magnetic properties obtained from the completely amorphous precursor were not as good as those obtained from partially crystallized ones.

Table 6.8 Saturation magnetization and coercivity of the initially partially amorphous ribbon annealed at 600°C for different time.

Annealing time (minutes)	Saturation magnetization (emu/g)	Coercivity (Oe)
10	25.4	191.2
60	29.3	173.5
600	46.3	122.7
1200	47.6	84.4

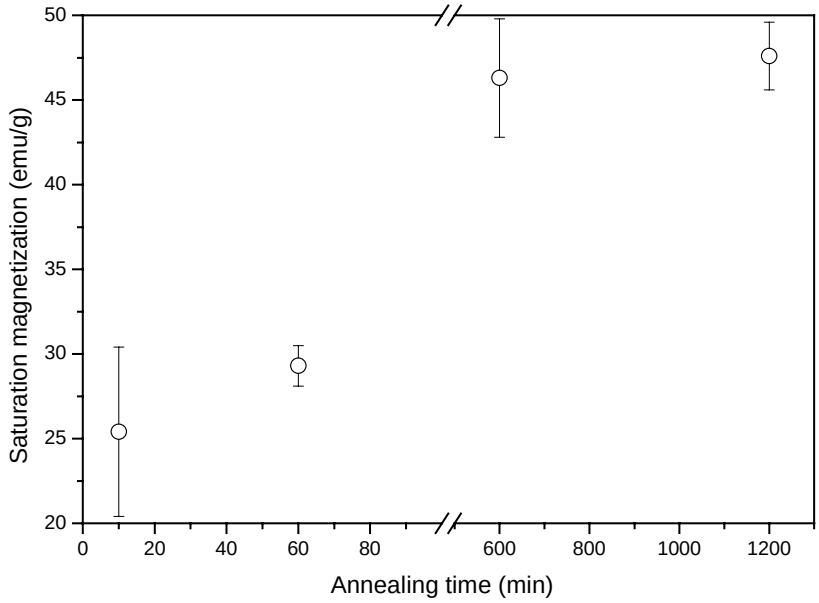

Fig.6.49 Saturation magnetization of the initially partially amorphous ribbon annealed at 600°C for different time.

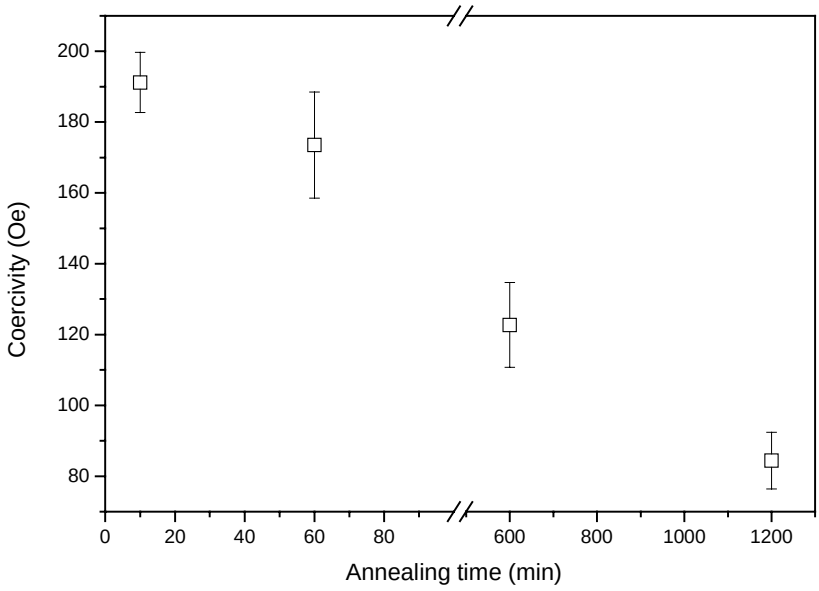

Fig.6.50 Coercivity of the initially partially amorphous ribbon annealed at 600°C for different time.

6.4 Conclusions

Completely amorphous and partially amorphous ribbons of Ni-Fe based alloys with the composition of Ni-15%Fe-5%Mo-5%B were obtained in this chapter. The microstructure, crystallization process and magnetic properties of these two types of ribbons were systematically studied.

These two types of ribbons experienced two crystallization processes: the primary crystallization with the temperature of 432°C and secondary crystallization with the temperature of 600°C at the heating rate of 10°C/min. The primary crystallization mode of the amorphous phase was polymorphous crystallization which indicated that the crystalline phase had the same composition as the amorphous phase after the primary crystallization. The phase precipitated from the amorphous matrix at the primary crystallization stage was $(Fe, Ni, Mo)_{23}B_6$. Ferromagnetic $FeNi_3$ phase formed during the secondary crystallization stage at the expense of the pre-existed $(Fe, Ni, Mo)_{23}B_6$ phase. The microstructure of the annealed partially amorphous ribbon was finer than that of the annealed completely amorphous ribbon due to the presence of the $FeNi_3$ phase in the as-spun ribbon. Magnetic properties of the annealed partially amorphous ribbon were also better. Nanostructured soft magnetic materials could only be obtained from the partially amorphous ribbon.

Chapter 7 Conclusions & Suggestions for Future Work

7.1 Summary and Results

Processing-properties relationship of nanostructured Ni-Fe-Mo soft magnetic materials has been undertaken in this study. Samples for examination were prepared by high energy ball milling (HEBM) and melt spinning (MS), and characterized using various analytical techniques such as x-ray powder diffraction (XRD), scanning electron microscopy (SEM), transmission electron microscopy (TEM) and differential scanning calorimetry (DSC). Magnetic properties were characterized by VSM for saturation magnetization $\boldsymbol{M_s}$ and coercivity $\boldsymbol{H_c}$.

The investigation of each processing technique has been considered individually with its own objectives in order to gain a better understanding of the effects of different processing on the microstructure and magnetic properties of Ni-based Permalloy. A summary of results is given as follows.

7.1.1 Mechanical alloyed Ni-Fe-Mo

The investigation of HEBM Ni-Fe-Mo powders with the composition of Ni-15%Fe-5%Mo was to study the magnetic properties of Ni-based nanostructured materials. This investigation served as the basis for the investigation of amorphous Ni-Fe-Mo-B system. Materials used in this experiment were elemental Mo powders and pre-alloyed $FeNi_3$ powders. The as milled powders were characterized using XRD, SEM, TEM and VSM.

(1) XRD result showed that Mo atoms substituted into the $FeNi_3$ phase during milling, and the substitution process was completed after 40 h of milling, and further milling only caused the slight decrease in grain size. During the milling process, no amorphous phase was observed.
(2) VSM results showed that saturation magnetization decreased as Mo atoms were substituted into the $FeNi_3$ phase. Coercivity was mainly affected by the milling process and the value was independent on the substitution of Mo atoms.

7.1.2 Mechanical alloyed and annealed Ni-Fe-Mo-B powder

In order to form the amorphous phase, B was added to Ni-Fe-Mo alloy system. The bulk composition considered was Ni-15%Fe-5%Mo-5%B. The as milled powders were characterized using DSC, XRD, SEM, TEM and VSM.

(1) DSC and TEM results showed that partially amorphous powders were obtained by mechanical alloying after 10 h of milling, and further milling up to 100 h did not produce completely amorphous powders. An exothermic peak of 530°C was observed at a heating rate of 10°C/min from DSC observation. The formation of partially amorphous powders was characteristic of solid-state amorphization process.
(2) VSM result showed that the magnetic properties of the milled powders were affected by the amorphization of the powders. The sharp decrease in saturation magnetization was mainly caused by the substitution process of Mo atoms, and low coercivity was related to the existence of the amorphous phase.

Based on the DSC results, the exothermic peaks observed were assumed to be the crystallization of the amorphous phase that was formed during the milling process. In order to study in detail the crystallization process of the amorphous phase, the powders milled for 40 h were subjected to a series of annealing experiments. Four annealing temperatures (480, 520, 600 and 700°C) were chosen, and the powders were annealed at these temperatures for 30 min in a vacuum furnace. XRD, TEM and VSM were used to characterize the annealed powders.

(1) After annealing, (Fe, Ni, Mo)$_{23}$B$_6$ phase was found to precipitate from the amorphous phase and co-existed with FeNi$_3$ phase from XRD observation. Based on this observation, the crystallization process of the partially amorphous powders could be summarized as follows:

$$amorphous + FeNi_3 \xrightarrow{530^{o}C} (Fe, Ni, Mo)_{23} B_6 + FeNi_3$$

(2) TEM result showed that the metastable (Fe, Ni, Mo)$_{23}$B$_6$ phase began to crystallize at 480°C, and the crystallization process was completed when the powders were held at 520°C for 30 min. Further annealing at 600°C and 700°C only caused the grain to grow.

(3) From VSM observation, it was found that magnetic properties of the annealed partially amorphous powders were affected by the crystallization process accordingly. The increase in saturation magnetization was mainly due to the crystallization of the amorphous phase. Coercivity after annealing was mainly affected by the crystallization process and the grain size.

7.1.3 Melt spun Ni-Fe-Mo-B ribbons

Melt spinning technique was also used in an attempt to obtain a completely amorphous ribbon for the same Ni-15%Fe-5%Mo-5%B bulk composition. Completely and partially amorphous ribbons were prepared by varying the rolling speed. The nucleation, thermal stability, grain growth and magnetic properties were investigated using DSC, XRD, TEM and VSM techniques.

(1) DSC results showed that these two type ribbons experienced two crystallization stages during the annealing process: primary crystallization and secondary crystallization.

(2) From XRD observation, it was found that the crystallization mode of the amorphous phase during the primary crystallization was polymorphous crystallization, which indicated that the crystallized phase had the same composition as the amorphous phase. The phase crystallized from the amorphous matrix during the primary crystallization was (Fe, Ni, Mo)$_{23}$B$_6$. Ferromagnetic FeNi$_3$ phase was crystallized during the secondary

crystallization stage at the expense of the pre-existing $(Fe, Ni, Mo)_{23}B_6$ phase.

(3) Microstructures of the annealed partially amorphous ribbon were found to be finer than those of the annealed completely amorphous.

(4) Magnetic properties of the annealed partially amorphous ribbon were better than the completely amorphous ribbon from VSM results. This observation was due to presence of the $FeNi_3$ in the partially amorphous ribbon.

Based on the observation, it can be said that nanostructured soft magnetic materials could only be obtained by annealing the partially amorphous ribbon, and not from the completely amorphous ribbon.

7.2 Conclusions

The comparison on the microstructure and magnetic properties of these three types of samples are summarized in Table 7.1 and Table 7.2, respectively. It is found that nanostructured magnetic materials can only be obtained from the partially amorphous powders prepared by HEBM and partially amorphous ribbons prepared by melt spinning for the compositions containing B. These two samples contain the pre-existed $FeNi_3$ phase, and this observation means that the pre-existed $FeNi_3$ phase exhibited the critical role for the formation of nanostructured materials for Ni based Permalloy. Grain size of the powders prepared by ball milling varied from 8 nm to 20 nm, while grain size of the samples prepared by melt spinning ranged from 30 nm to 80 nm. From the point of grain size, it is easier to obtain the nanostructured materials by ball milling. In addition, magnetic properties of the samples prepared by ball milling were also better than the ones prepared by melt spinning. Higher saturation magnetization and lower coercivity were obtained for the powder samples.

Table 7.1. Microstructure comparison of the three type's samples.

Sample	Microstructure	Crystallization stages
Milled Ni-Fe-Mo powders	Nanostructured powders with grain size of 8 nm	
Milled Ni-Fe-Mo-B powders	Partially crystalline powders with grain size of 10 nm	Crystallization temperature: 530°C, formation of (Fe, Ni, Mo)$_{23}$B$_6$ phase
Annealed Ni-Fe-Mo-B powders	Grains size of 20 nm at 480°C	
As-spun Ni-Fe-Mo-B ribbons	Partially crystalline ribbon with grain size of 30 nm and totally amorphous ribbon	Primary crystallization temp: 430°C and formation of (Fe, Ni, Mo)$_{23}$B$_6$ phase; secondary crystallization temp: 600°C and formation of FeNi$_3$ phase
Annealed sample A	Grain size varied from 100 nm to 200 nm after annealing	
Annealed sample B	Grain size varied from 30 nm to 80 nm after low temperature annealing	

Table 7.2. Magnetic properties comparison of the three type's samples.

Sample	Saturation magnetization	Coercivity
Milled Ni-Fe-Mo powders	53 emu/g after 40 h of milling	14 Oe after 40 h of milling
Milled Ni-Fe-Mo-B powders	40 emu/g after 40 h of milling	18 Oe after 40 h of milling
Annealed Ni-Fe-Mo-B powders	54 emu/g at 480°C for 30 min	13 Oe at 480°C for 30 min
As-spun sample A (totally amorphous)	2.4 emu/g	30 Oe
As-spun sample B (partially amorphous)	25 emu/g	15 Oe
Annealed sample A	11 emu/g at 600°C for 10 h	20 Oe at 600°C for 10 h
Annealed sample B	48 emu/g at 600°C for 20 h	84 Oe at 600°C for 20 h

Overall, from the comparison of these two types of samples, it can be concluded that ball milling process is more suitable to obtain nanostructured materials, and magnetic properties of the sample annealed from partially amorphous starting materials are better than the ones annealed from a completely amorphous starting material for Ni based Permalloy.

7.2 Future Work Plans

Nanostructured Ni-Fe-Mo alloy has been obtained from the partially amorphous powders prepared by high-energy ball milling and the annealed partially ribbon prepared by melt spinning. The formation of the $(Fe, Ni, Mo)_{23}B_6$ phase during the primary crystallization stage had no effect on the magnetic properties and the refinement of the microstructure. A few improvements can be made from the above research.

Firstly, information on the detailed microstructure and magnetic properties of the $(Fe, Ni, Mo)_{23}B_6$ phase is limited. The structure of $(Fe, Ni, Mo)_{23}B_6$ phase should be studied further in order to understand the formation kinetics of this phase. Secondly,

from our study, $(Fe, Ni, Mo)_{23}B_6$ and $FeNi_3$ phases co-existed for the final annealed Ni-Fe-Mo-B sample. As $(Fe, Ni, Mo)_{23}B_6$ is the metastable phase, it always exists in the primary crystallization stage. In order to inhibit the crystallization of this phase from the amorphous phase, quenching method can be tried to inhibit the formation of $(Fe, Ni, Mo)_{23}B_6$ phase at low annealing temperature.

According to the study of the magnetic properties for the milled, annealed and melt-spun Ni-15%Fe-5%Mo-5%B samples, non-optimized magnetic properties with high saturation magnetization and low coercivity were obtained. As Fe has better magnetic properties than Ni, more Fe can be added instead of Ni in future work. In addition, Mo was found to have nearly no effect on the optimization of magnetic properties from the current study and it will inhibit the formation of $FeNi_3$ phase during annealing, so this element could be removed from the sample composition.

Lastly, the control of $FeNi_3$ grain size during annealing needs to be studied carefully in order to maintain a nanocrystalline structure.

References

Ahmadi T.S., Wang Z.L., Green T.C., Henglein A. and El-Sayed M.A. (1996), Shape-controlled synthesis of colloidal platinum nanoparticles, *Science*, **272**, 1924.

Alben R., Becker J.J. and Chi M. (1978), Random anisotropy in amorphous ferromagnets, *J. Appl. Phys.* **49**, 1653.

Al-Khafaji M.A., Ahmad I., Rainforth W.M., Davies H.A. and Buckley R.A. (2001), Investigation of the phase constitution and structure of rapidly solidified magnetic $Nd_{18}Fe_{76}B_6$ ribbons by transmission electron microscopy, *Phil. Maga. A.* **81**, 11.

Arrott A.S. (1999), Production of magnetically soft materials by mechanical alloying. *Nanostruct. Mater.* **12**, 1135.

Arrott A.S. (2000), The past, the present and the future of soft magnetic materials, *J. Magn. Magn. Mater.* **215-216**, 6.

Barandiaran J.M., Telleria I., Garitaonandia J.S. and Davies H.A. (2003), Kinetic aspects of nano-crystallization in Finemet-like alloys, *J. Non-cryst. Solids.* **329**, 57.

Bate G. (1980), Ferromagnetic Materials, edited by Wohlfarth E.P., North-Holland, Amsterdam.

Bednarcik J., Kollar P., Roth S. and Eckert J. (2003), Co-based soft magnetic bulk amorphous ferromagnets prepared by powder consolidation, *Phys. Status. Solidi A.* **199**, 299.

Benjamin J.S. (1976), Mechanical alloying, *Sci. Amer.* **234**, 108.

Benjamin J.S. and Volin T.E. (1974), mechanism of mechanical alloying, *Meta. Trans.* **5**, 1929.

Bertotti G., Ferrara E., Fiorillo F. and Tiberto P. (1997), Magnetic properties of rapidly quenched soft magnetic materials, *Mater. Sci. Eng. A***. 226-228**, 603.

Billoni O.V., Bordone E.E., Urreta S.E., Fabietti L.M. and Bertorello H.R. (2000), Magnetic viscosity in a nanocrystalline two phase composite with enhanced remanence, *J. Magn. Magn. Mater.* **208**, 1.

Boll R. (1994), Soft magnetic metals and alloys, In: Bushow K.H.J. editor. Materials Science and technology: a comprehensive treatment, **3B**, 399.

Bordin G., Buattino G., Cecchetti A., Cecchetti M. and Poppi M. (1996), Influence of the structural instabilities on the anisotropy fields in Co-based amorphous alloys, *J. Magn. Magn. Mater.* **153**, 285.

Bozorth R.M. (1978), Ferromagnetism, Nostrand Company Inc, Princeton & New Jersey.

Bruning R., Samwer K., Kuhrt C. and Schultz L. (1992), The mixing of iron and cobalt during mechanical alloying, *J. Appl. Phys.* **72(7)**, 2978-2983.

Buffat P. and Borel J.P. (1976), Size effect on the melting temperature of gold particles, *Phys. Rev. A.* **13**, 2287.

Calka A. and Radlinski A. P. (1991), Universal high performance ball-milling device and its application for mechanical alloying, *Mater. Sci. Eng. A.* **134**, 1350.

Callister W.D. (2003), Materials science and engineering: an introduction,New York: Wiley.

Cardoso K.R., Garcia Escorial A., Lieblich M., Yavari A.R. and Botta F. (1999), Al-Fe-Nd powders prepared by gas atomisation, *Mater. Sci. Forum.* **312**, 253.

Chan S.L.I. and Chiang C.I. (1997), Hydroden permeability and diffusivity in amorphous Metglas 2826MB under AC excitation, *J. Alloy. Compd.* **253-254**, 370.

Chapman J.N., McFadyen I.R. and Bernades J.P.C. (1986), Investigation of Cr segregation within RF-sputtered CoCr films, *J. Magn. Magn. Mater.* **62**, 359.

Chen C.W. (1977), Magnetism and Metallurgy of Soft Magnetic Materials, North-holland publishing company, Amsterdam.

Chen T., Hampikian J.M. and Thadhani N.N. (1999), Synthesis and characterization of mechanically alloyed and shock-consolidated nanocrystalline NiAl intermetallic, *Acta. Mater.* **47**, 2567.

Chin G.Y. (1992), Magnetic Materials: an overview, in Cincise Encyclopedia of Magnetic and superconducting materials: edited by Evetts J., Pergamon press.

Chinnasamy C.N., Narayanasamy A., Chattopadhyay K. and Ponpandian N. (1999), Magnetic properties of mechanically alloyed nanocrystalline Ni_3Fe, *Nanostruct. Mater.* **12 (5-8)**, 951.

Chinnasamy C.N., Narayanasamy A., Ponpandian N., Chattopadhyay K. and Saravanakumar M. (2001), Order-disorder studies and magnetic properties of mechanically alloyed nanocrystalline Ni_3Fe alloy, *Mater. Sci. Engi.* **A304-306**, 408.

Chiriac H., Moga A.E., Urse M. and Hison C. (2001), Structural and magnetic investigation of mechanically alloyed $Fe_{80}Co_5(Nb_xZr_{1-x})_7B_8$ powders, *J. Non-cryst. Solids.* **287**, 50.

Chokshi A.H., Rosen A., Karch J. and Gleiter H. (1989), On the validity of the Hall-Petch relationship in nanocrystalline materials, *Scr. Metall.* **23**, 1679.

Coey J.M.D. (1996), Rare-earch iron permanent magnets, Oxford: Oxford Science Publications, Clarendon Press.

Coey J.M.D. (2001a), Magnetic Materials, *J. Alloy. Compd.* **326**, 2.

Coey J.M.D. (2001b), Magnetism in future, *J. Magn. Magn. Mater.* **226-230**, 2107.

Cullity B.D. (1972), Introduction to Magnetic Materials, Reading, Mass., Addison-Wesley Pub. Co.

Davis R.M. and Koch C.C. (1987), mechanical alloying of brittle components: silicon and germanium, *Scripta. Metall.* **21**, 305.
Davis R.M., McDermott B. and Koch C.C. (1988), Mechanical alloying of brittle materials, *Metall. Trans. A.* **19**, 2867.

DeCristofaro N. (1998), Amorphous metals in electric-power distribution applications, *MRS. Bull*, **May**, 50.

De Lima J.C., Dos Santos V.H.F., Grandi T.A., D'Ajello P.C.T. and Dmitriev A. (2000), Thermodynamic considerations about the formation of alloys by mechanical alloying, *Phys. Rev. B.* **62,** 8871.

Eckert J., Schultz L., Hellstern E. and Urban K. (1988), Glass-forming range in mechanically alloyed Ni-Zr and the influence of the milling intensity, *J. Appl. Phys.* **64**, 3224.

Eckert J., Holzer J.C., Krill III C.E. and Johnson W.L. (1993), Mechanically driven alloying and grain size changes in nanocrystalline Fe-Cu powders, *J. App. Phys.* **73**, 2794.

Edelstein A.S. (1998), Nanomaterials: synthesis, properties and applications, Ed. Edelstein A.S. and Cammarata R.C., J.W. Arrowsmith Ltd., Bristol.

Efthimiadis K.G., Achilleos C.A., Chadjivasiliou S.C. and Tsoukalas I.A. (1997), Crystallization of amorphous $Fe_{75-x}Cu_xSi_9B_{16}$, *J.Mag.Mag. Mater.* **171**, 141.

Elkalkouli R., Grosbras M. and Dinhut J.F. (1995), Mechanical and magnetic properties of nanocrystalline Fe-Co alloys produced by mechanical alloying, *Nanostructured. Mater.* **5(6)**, 733-743.

El-Eskandarany M.S. (2001), Mechanical alloying for fabrication of advanced engineering materials, Norwich, N.Y.: Noyes Publications.

Frase H.N. and Fultz B. (1998), Phonons in nanocrystalline Ni_3Fe, *Phys. Rev. B.* **57**, 898.

Frase H.N., Nagel L.J., Robertson J.L. and Fultz B. (1997), Vibrational density of states of nanocrystalline Ni_3Fe, *Phil. Mag. B.* **75**, 335.

Frase H.N., Fultz B., Spooner S. and Robertson J.L. (1999a), A small angle neutron scattering and Mossbauer spectrometry study of magnetic structures in nanocrystalline Ni_3Fe, *J. Appl. Phys.* **85**, 7097.

Frase H.N., Shull R.D., Hong L.B., Stephens T.A., Gao Z.Q. and Fultz B. (1999b), Soft magnetic properties of nanocrystalline Ni_3Fe and $Fe_{75}Al_{12.5}Ge_{12.5}$, *Nanostruct. Mat.* **11**, 987.

Fultz B., Kuwano H. and Quyang H. (1995), Average widths of grain boundaries in nanophase alloys synthesized by mechanical attrition, *J. Appl. Phys.***77**, 3458.

Frase H.N., Fultz B., Spooner S. and Robertson J.L. (2000), Structural relaxation within the grain boundaries of nanocrystalline Ni_3Fe, *Phil. Mag. B.* **80**, 1545.

Ganapathi S.K., Owen D.M. and Chokshi A.H. (1991), Kinetics of grain growth in nanocrystalline copper, *Scr. Metall. Mater.* **25**, 2699.

Gao Y., Zhang S. and Liu B. (2000), Crystallization of melt-spun $Nd_7Fe_{86}Nb_1B_1$ ribbons under different heating rates, *J. Magn. Magn. Mater.* **208**, 158.

Gayle, F.W. and Biancaniello, F.S. (1996), Stacking faults and crystallite size in mechanically alloyed Cu-Co, *Nanostruct. Mater.* **6**, 429.

Gilman P.S. and Benjamin J.S. (1983), mechanical alloying, *Annu. Rev. Mater. Sci.* **13**, 279.

Gleiter H. (1995), Nanostructured materials: state of the art and perspectives, *Nanostruct. Mat.* **6,** 3.

Gleiter H. (2000), Nanostructured materials: basic concepts and microstructure, *Acta. Mater.* **48** , 1.

Goldman A. (1999), Handbook of Modern Ferromagnetic Materials, Boston: Kluwer Academic Publishers.

Gong W., Hadjipanayis G.C. and Krause R.F. (1994), Mechanically alloyed nanocomposite magnets, *J. Appl. Phys.* **75**, 6649.

Grandi T.A., Dos Santos V.H.F. and De Lima J.C. (1999), Kinetics of formation of the γ-$Ni_{20}Zn_{80}$ alloy using nanocrystalline nickel, *Solid. State. Commun.* **112**, 359.

Greer A.L. (1998), Nanostructured Materials, Science and Technology, NATO ASI Series, Partnership Sub-Series 3: High Technology, edited by Chow G.M. and Noskova N.I., **50**, 143.

Gusev (1998), Effects of nanocrystalline state in solids, *Physics-Uspekhi*, **41**, 49.

Heck C. (1974), Magnetic Materials and their Applications, London, Butterworks.

Hellstern E. and Schultz L. (1987), Glass formation in mechanically alloyed transition metal-titanium alloys, *Mater. Sci. and Engi.* **93**, 213.

Herzer G. (1989), Grain structure and magnetism of nanocrystalline ferromagnets, *IEEE. Trans. Magn.* **25**, 3327.

Herzer G. (1990), Grain size dependence of coercivity and permeability in nanocrystalline ferromagnets, *IEEE. Trans. Magn.* **26**, 1397.

Herzer G. (1995), Soft magnetic nanocrystalline materials, *Scripta. Metall. Mater.* **33**, 1741.

Herzer G. (1997), Handbook of magnetic materials, Ed. Buschow K.H.J, **10,** Amsterdam: Elsevier Science.

Herzer G. and Hilzinger H.R. (1986), Surface crystallisation and magnetic properties in amorphous iron rich alloys, *J. Mag. Mag. Mater.* **62**, 143.

Herzer G. and Hilzinger H.R. (1992), Nanocrystalline soft magnetic materials, *J. Magn. Magn. Mater.* **112**, 258.

Herzer G. and Warlimont H. (1992), Nanocrystalline soft magnetic materials by partial crystallization of amorphous alloys, *Nanostruct. Mater.* **1**, 263.

Hono K. (2002), Nanoscale microstructural analysis of metallic materials by atom probe field ion microscopy, *Prog. Mater. Sci.* **47**, 621.

Host J.J., Block J.A., Parvin K., Dravid V.P., Alpers J.L. and Sezen T. (1998). Effect of annealing on the structure and magnetic properties of graphite encapsulated nickel and cobalt nanocrystals, *J. Appl. Phys.* **83**, 793.

Idzikowski B. and Szajek A. (2003), Magnetism of nanocrystalline and bulk $Fe_xNi_{23-x}B_6$ (x=0, 1, 22 and 23) alloys-experiment and theory, *Mater. Sci.* **21**, 73.

Idzikowski B., Szajek A., Greneche J.M. and Kovac J. (2004), Nanogranular $Fe_xNi_{23-x}B_6$ phase formation during devitrification of nickel-rich $Ni_{64}Fe_{16}Zr_7B_{12}Au_1$ amorphous alloy, *Appl. Phys. Lett.* **85**, 1392.

Inoue A. (2000), Stabilization of metallic supercooled liquid and bulked amorphous alloys, *Acta. Mater.* **48**, 279.

Inoue A. and Gook J.S. (1995), Fe-based ferromagnetic glassy alloys with wide supercooled liquid region, *Mater. Trans. JIM*, **36**, 1180.

Iwanabe H., Lu B., McHenry M.E. and Laughlin D.E. (1999), Thermal stability of the nanocrystalline Fe-Co-Hf-B-Cu alloy, *J. Appl. Phys.* **85B**, 4424.

Jakubovics J.P. (1987), Magnetism and magnetic materials, The Insitute of Metals, USA.

Jang J.S.C. and Koch C.C. (1990), Hall-Petch relationship in nanocrystalline iron produced by ball milling, *Scr. Metall. Mater.* **24**, 1599.

Jiang H.G., Perez R.J., Lau M.L. and Lavernia E.J. (1996), Formation kinetics of nanocrystalline Fe-4wt.%Al solid solution during ball milling, *J. Mater. Res.* **12**, 1429.

Jiang C.B., Venkatesan M., Gallagher K. and Coey J.M.D. (2001), Magnetic and structural properties of $SmCo_{7-x}Ti_x$ magnets, *J. Magn. Magn. Mater.* **236,** 49.

Jiles D. (1998), Introduction to Magnetism and Magnetic Materials, second edition, Chapman & Hall, London.

Johnson F., Hughes P., Gallagher R., Laughlin D.E., Willard M.A. and Harris V.G. (2001), Structure and thermomagnetic properties of new FeCo-based nanocrystalline ferromagnets, *IEEE. Trans. Magn.* **37**, 2261.

Kamzeeva E.E., Khatanova N.A. and Zhdanov G.S. (1984), Crystallization of alloy $Fe_{40}Ni_{38}Mo_4B_{18}$ from amorphous and liquid phases, *Sov. Phys. Crystallogr.* **29**, 338.

Kemner K.M., Harris V.G., Chakarian V., Idzerda Y.U., Elam W.T., Kao C.C., Feng Y.C., Laughlin D.E. and Woicik J.C. (1996), Role of Ta and Pt in segregation within Co-Cr-Ta and Co-Cr-Pt thin film magnetic recording media, *J. Appl. Phys.* **79**, 5345.

Kim Y.D., Chung J.Y., Kim J. & Jeon H. (2000), Formation of nanocrystalline Fe-Co powders produced by mechanical alloying, *Mater. Sci. Eng. A*, **291**, 17-21.

Kissinger H.E. (1957), Reaction kinetics in differential thermal analysis, *Anal. Chem.* **29**, 1702.

Klug H.P. and Alexander L.E. (1974), X-ray diffraction procedures for polycrystalline and amorphous materials, John Wiley & Sons, New York.

Knorr P., Nam J.G. and Lee J.S. (1999), Densification and microstructural development of nanocrystalline γ-Ni-Fe powders during sintering, *Nanostruct. Mater.* **12** , 479.

Koch C.C. and Whittenberger J.D. (1996), Mechanical milling/alloying of intermetallics, *Intermetallics* **4,** 339.

Koch C.C., Cavin O.B., McKamey C.G. and Scarbrough J.O. (1983), Preparation of amorohous $Ni_{60}Nb_{40}$ by mechanical alloying, *Appl. Phys. Lett.* **43**, 1017.

Korolev (1990), Features of the magnetic state of plastically deformed Ni-Cu alloys, *Phys. Metals. Metallog.* **70**, 94.

Kratschmer W., Lamb L.D., Fostiropoulos K. and Huffman D.R. (1990), Solid C_{60}. A new form of carbon, *Nature,* **347**, 354.

Kuhrt C. and Schultz L. (1992), Formation and magnetic properties of nanocrystalline mechanically alloyed Fe-Co, *J. Appl. Phys.* **71**, 1896.

Kuhrt C. and Schultz L. (1993), Phase formation and martensitic transformation in mechanically alloyed nanocrystalline Fe-Ni. *J. Appl. Phys.* **73(4)**, 1975.

Kuhrt C. and Schultz L. (1993), Formation and magnetic properties of nanocrystalline mechanically alloyed Fe-Co and Fe-Ni. *J. Appl. Phys.* **73(10),** 6588.

Kuhrt C. and Schultz L. (1993), Magnetic properties of nanocrystalline mechanically alloyed Fe-M, *IEEE Trans. Magn.* **29(6)**, 2667.

Kursumovic A. and Cantor B. (1996), Anelastic crossover and creep recovery spectra in $Fe_{40}Ni_{40}B_{20}$ metallic glass, *Script. Mater.* **34,** 1655.

Kwapulinski P., Chrobak A., Haneczok G., Stoklosa Z., Rasek J. and Lelatko J. (2003), Optimization of soft magnetic properties in nanosperm type alloys, *Mater. Sci. Eng. C.* **C23**, 71.

Lai M.O. (1998), Mechanical alloying, Kluwer Academic Publishers, Boston.

Lall C. (1992), Soft magnetism: Fundamentals for Powder Metallurgy and Metal Injection Molding, Princeton, N.J. Metal Powder Industries Federation.

Lee P.Y. and Koch C.C. (1987), Formation of amorphous Ni-Zr alloys by mechanical alloying of mixtures of the intermetallic compounds $Ni_{11}Zr_9$ and $NiZr_2$, *Appl. Phys. Lett.* **50**, 1578.

Lee P.Y. and Koch C.C. (1988), Formation of amorphous Ni-Zr alloy powder by mechanical alloying of intermetallic powder mixtures and mixtures of nickel or zirconium with intermetallics, *J. Mater. Sci.* **23**, 2837.

Lee P.Y., Yang J.L. and Lin H.M. (1998), Amorphization behavior in mechanically alloyed Ni-Ta powders, *J. Mater. Sci.* **33**, 235.

Lee S.J. and Kang S.Y. (2001), Processing of bulk nanostructured Ni-Fe materials, *Scripta. Mater.* **44**, 1591.

Lee S.J., Kim T.H., Yu J.H. and Chung S.W. (1997), In-situ alloying on synthesis of nanosized Ni-Fe powder, *Nanostruct. Mater.* **9**, 153.

Li L. and Masteller M.S. (1997), Effects of Mo content and baking temperature on permeability in Ni-Mo-Cu-Fe and Ni-Mo-Fe permalloy, *IEEE. Trans. Magnet.* **33**, 3769.

Li H.F. and Ramanujan R.V. (2004), Mechanical alloying of FeCo Nanocrystalline magnetic powders, *J. Electron. Mater.* **33**, 1289.

Li H.F. and Ramanujan R.V. (2005), Microstructural evolution and nanocrystalline formation kinetics in FeCo based alloys during mechanical alloying, *J. Metastable. Nanocryst. Mater.* **23**, 187.

Li J., Su Z., Wang T.M., Ge S.H., Hahn H. and Shirai Y. (1999), Microstructure of nanostructured $Fe_{40}Ni_{38}Mo_4B_{18}$ alloy, *J. Mater. Sci.* **34**, 111.

Liu Y.J., Chang I.T.H. and Lees M.R. (2001a), Thermodynamic and magnetic properties of multicomponent $(Fe, Ni)_{70}Zr_{10}B_{20}$ amorphous alloy powders made by mechanical alloying, *Mater. Sci. Eng. A.* **304-306**, 992.

Liu Y.J., Chang I.T.H. and Bowen P. (2001b), Amorphization and microstructural evolution in multicomponent $(FeCoNi)_{70}Zr_{10}B_{20}$ alloy system by mechanical alloying, *Mater. Sci. Eng. A.* **304-306**, 389.

Liu Y.J., Chang I.T.H. and Lees M.R. (2001c), Influences of oxide phases on the coercivity of mechanically alloyed multicomponent Fe-based amorphous alloys, *Scripta. Mater.* **44**, 2729.

Liu Y.J. and Chang I.T.H. (2002a), The correlation of microstructural development and thermal stability of mechanically alloyed multicomponent Fe-Co-Ni-Zr-B alloys, *Acta. Mater.* **50**, 2747.

Liu Y.J. and Chang I.T.H. (2002b), Compositional dependence of crystallization behavior of mechanically alloyed amorphous Fe-Ni-Zr-B alloys, *Mater. Sci. Eng. A.* **325**, 25.

Louzguine D.V. and Inoue A. (2000), Crystallization behavior of $Ti_{50}Ni_{25}Cu_{25}$ amorphous alloy, *J. Mater. Sci.* **35**, 4159.

Luborsky F.E. (1983), Amorphous Metallic Alloys, Ed. Luborsky F.E., Butterwords, London, Boston.

Maeda Y., Hirono S. and Asahi M. (1985), TEM observation of microstructure in sputtered Co-Cr film, *Japan. J. Appl. Phys.* **24**, L951.

Makino A., Suzuki K., Inoue A. and Masumoto T. (1991), Low core loss of a BCC $Fe_{86}Zr_7B_6Cu_1$ alloy with nanoscale grain size, *Mater. Trans.* JIM, **32**, 551.

Manivel Raja M., Chattopadhyay K., Majumdar B. and Narayanasamy A. (2000), Structure and soft magnetic properties of Finemet alloys, *J. Alloys. Comp.* **297**, 199.

Manna I., Nandi P., Bandyopadhyay B., Ghoshray K. and Ghoshray A. (2004), Microstructural and nuclear magnetic resonance studies of solid-state amorphization in Al-Ti-Si composites prepared by mechanical alloying, *Acta. Mater.* **52**, 4133.

Massalski T.B. (1986), Binary alloy phase diagrams (second edition), Metals Park, Ohio: American Society for Metals.

McCurrie R.A. (1994), Ferromagnetic Materials: Structure and Properties, Harcourt & Company, London.

McHenry M.E., Willard M.A. and Laughlin D.E. (1999a), Amorphous and nanocrystalline materials for applications as soft magnetis, *Progress in Materials Science*, **44**, 291.

McHenry M.E., Willard M.A., Iwanabe H., Sutton R.A., Turgut Z., Hsiao A. and Laughlin D.E. (1999), Nanocrystalline materials for high temperature soft magnetic application: a current prospectus, *Bulletin. Mater. Sci.* **22**, 495.

McHenry M.E. and Laughlin D.E. (2000), Nano-scale materials development for future magnetic applications, *Acta. Mater.* **48**, 223.

McHenry M.E., Johnson F., Okumura H., Ohkubo T., Ramanan V.R.V. and Laughlin D.E. (2003), The kinetics of nanocrystallization and microstructural observations in FINEMET, NANOPERM and HITPERM nanocomposite magnetic materials, *Script. Mater.* **48**, 881.

Miura. H, Isa S. and Omuro K. (1990), Preparation of Fe-Ni-Based Metal-Metalloid Amorphous Alloys by Mechanical Alloying and Mechanical Grinding Methods, *Japan. J. Appl. Phys.* **29**, L339.

Murty B.S. and Ranganathan S. (1998), Novel materials synthesis by mechanical alloying/milling, *International. Mater. Reviews.* **43,** 1.

Nakamura T., Koshiba H., Imafuku M., Inoue A. and Matsubara E. (2002), Determination of atomic sites of Nb dissolved in metastable $Fe_{23}B_6$ phase, *Mater. Trans.* **43**, 1918.

Nunes E., Larica C., Passamani E.C. and Fernandes A.A.R. (2002), Crystallization kinetics of the $Fe_{40}Ni_{38}Mo_4B_{18}$ amorphous alloy, *Phyical. B.* **320**, 278.

Ok H.N. and Morrish A.H. (1981), Surface crystallization and magnetic anisotropy in amorphous $Fe_{40}Ni_{38}Mo_4B_{18}$ ribbons, *J. Appl. Phys.* **52**, 1835.

Pan C.W., Hung M.P. and Chang Y.H. (1994), Magnetic properties of mechanically alloyed Fe_3Sn, *Mater. Sci. Eng. A.* **185**, 147.

Perepesko J.H. and Paik J.S. (1982), Rapid solidified amorphous and crystalline alloys, editor: Kear B.H., Giessen B.C. and Cohen M., New York: Elsevier.

Ponpandian N., Narayanasamy A., Chattopahyay K., Manivel Raja M., Ganesan K., Chinnasamy C.N. and Jeyadevan B. (2003), Low-temperature magnetic properties and the crystallization behavior of FINEMET alloy, *J. Appl. Phys.* **93**, 6182.

Pradell T., Sunol J.J., Clavaguera N. and Clavaguera-Mora M.T. (2000), Crystallization behavior of $Fe_{40}Ni_{40}Si_xP_{20-x}$ (x=6, 10, 14) amorphous alloys, *J. Non-cryst. Solids.* **276**, 113.

Qin X.Y., Kim J.G. and Lee J.S. (1999a), Synthesis and magnetic properties of nanostructured γ-Ni-Fe alloys, *Nanostruct. Mat.* **11**, 259.

Qin X.Y., Lee J.S. and Kim J.G. (1999b), Magnetic properties of nanostructured γ -Ni–46Fe alloy synthesized by a mechanochemical process, *J. Appl. Phys.* **86**, 2146.

Rho I.C., Yoon C.S., Kim C.K., Byun T.Y. and Hong K.S. (2003), Microstructure and crystallization kinetics of amorphous metallic alloy: $Fe_{54}Co_{26}Si_6B_{14}$, *J. Non-cryst. Solids.* **316**, 289.

Rupp J. and Birringer R. (1987), Enhanced specific-heat-capacity (C_p) measurements (150-300K) of nanometer-sized crystalline materials, *Phys. Review. B.* **36**, 7888.

Schwarz R.B. and Koch C.C. (1986), Formation of amorphous alloys by the mechanical alloying of crystalline powders of pure metals and powders of intermetallics, *App. Phys. Lett.* **49.** 146.

Scott H.J.J, Majetich S.A., Turget Z., McHenry M.E. and Boulos M. (1997), Carbon coated nanoparticle composites synthesized in an RF plasma torch, *Materials Research Society Symposium – Proceedings*, **457**, 219.

Scott, M.G. (1983), Amorphous Metallic Alloys, Editor: Luborsky F.E., Butterworths & Co (Publishers) Ltd.

Skorvanek I., Svec P., Marcin J., Kovac J., Krenicky T. and Deanko M. (2003), Nanocrystalline Cu-free HITPERM alloys with improved soft magnetic properties, *Phys. Status. Solidi. A.* **196**, 217.

Strnat K. (1988), Ferromagnetic Materials, edited by Wohlfarth E.P. and Buschow K.H.J., Amsterdam Publishers, Amsterdam.

Sui M.L., Qian L.H. and He K.Y. (2000), Nanocrystallization of Ni-Fe-Nb-Si-B amorphous alloys, *Mater. Sci. Eng. A.* **286**, 201.

Sun D.Z., Cheng L.Z., Zhang Y.M. and Ho K.Y. (1992), Calorimetry study of $Ni_{50}Ti_{50}$ ball milled powders, *J. Alloys. Comp.* **186**, 33.

Sunol J.J., Clavaguera N. and Clavaguera-Mora M.T. (2001), Comparison of Fe–Ni–P–Si alloys prepared by ball milling, *J. Non-Cryst. Solid.* **287**, 114.

Surinach S., Sunol J.J. and Baro M.D. (1994), Preparation of Fe-Ni based metal-metalloid amorphous powders by mechanical alloying, *Mater. Sci. Eng. A.* **181-182**, 1285.

Suryanarayana C. (2001), Mechanical alloying and milling, *Prog. Mater. Sci.* **46**,1.

Suzuki K. (1999), Nanocrystalline soft magnetic materials: a decade of alloy development, *Mater. Sci. Forum.* **312-314**, 521.

Suzuki K., Makino A., Tsai A.P., Inoue A. and Masumoto T. (1994), The role of boron in nanocrystalline Fe-Zr-B soft magnetic alloys, *Mater. Sci. Engi. A.* **179-180**, 501.

Suzuki K. and Cadogan J.M. (1998), Random magnetocrystalline anisotropy in two-phase nanocrystalline systems, *Phys. Rev. B.* **58**, 2730.

Suzuki K. and Cadogan J.M. (1999), The effect of the spontaneous magnetization in the grain boundary region on the magnetic softness of nanocrystalline materials, *J. Appl. Phys.* **85**, 4400.

Suzuki K., Herzer G. and Cadogan J.M. (1998), The effect of coherent uniaxial anisotropies on the grain-size dependence of coercivity in nanocrystalline soft magnetic alloys, *J. Mag. Mag. Mat.* **177-181**, 949.

Szabo S., Kis-Varga M., Beke D.L. and Juhasz R. (2000), Effect of residual strain, grain size and Fe impurities on magnetic properties of nanocrystalline Ni (Fe) alloys, *J. Magn. Magn. Mater.* **215-216**, 60.

Tabor D. (1951), The hardness of metals, London: Oxford University Press.

Tejedor M., Garcia J.A., Carrizo J., Elbaile L. and Santos J.D. (2002), Effect of residual stresses and surface roughness on coercivity force in amorphous alloys, *J. Appl. Phys.* **91**, 8435.

Tkatch V.I., Kimanovskii A.I., Denisenko S.N. and Rassolov S.G. (2002), The effect of the melt-spinning of processing parameters on the rate cooling, *Mater. Sci. Engi. A***. 323**, 91.

Umakoshi Y., Nakano T., Tsujimota T. and Fujitani W. (2000), Microstructure and plastic deformation of melt spun amorphous Fe-Zr-B alloy ribbons containing nanocrystallites, *Script. Mater.* **43**, 349.

Ungar U. and Borbely A. (1996), The effect of dislocation contrast on X-ray line broadening: A new approach to line profile analysis, *Appl. Phys. Lett.* **69**, 3173.

Valiev R.Z., Mulyukov R.R., Mulyukov Kh.Ya, Novikov V.I. and Trusov L.I. (1989), Curie temperature and saturation magnetization of nickel with a submicrograin structure, *Sov. Tech. Phys. Lett.* **15**, 33.

Varga L.K., Lovas A., Pogany L., Kiss L.F., Balogh J. and Kemeny T. (1997), The role of nucleating element additives in the crystallization and soft magnetic properties of Fe-Zr-B based amorphous alloys, *Mater. Sci. Eng. A.* **226-228**, 740.

Wakelin R.J. and Yates E.L. (1953), A study of the order-disorder transformation in Iron-Nickel alloys in the region $FeNi_3$, *Proc. Phys. Soc. B***. 66**, 221.

Wallace W.E. (1973), Rare Earth Inermetallics, Academic Press, New York.

Wallace W.E. and Nasasimhan K.S.V.L. (1980), The Science and Technology of Rare Earth mateials, Academic Press, New York.

Wang K.Y., Shen T.D., Wang J.T. and Quan M.X. (1991), Amorphization reaction during mechanical alloying: Influence of the milling atmospheres, *Scripta. Metall. Mater.* **25**, 2227.

Wang Z.C. and Davies H.A. (2003), effects of additions on the crystallization process, structure, and magnetic properties of (NdPr)-Fe-B amorphous ribbons, *J. Appl. Phys.* **93**, 8149.

Weertman J.R. and Averback R.S. (1996), Nanomaterials: Synthesis, Properties and Applications, Eds. Edelstein A.S. and Cammarata R.C., London, Institute of Phys. Publ., chapter 13.

Willard M.A. (1996), Structural and Magnetic Characterization of HITPERM Soft Magnetic Materials for High Temperature Applications, Ph.D. Thesis, Carnegie Mellon University, Pittsburgh, PA.

Willard M.A., Huang M.Q., Laughlin D.E., McHenry M.E., Cross J.O., Harris V.G. and Franchetti C. (1999), Magnetic properties of HITPERM (Fe, Co)$_{88}$Zr$_7$B$_4$Cu$_1$ magnets, *J. Appl. Phys.* **85,** 4421.

Wohlfarth E.P. (1980), in: Ferromagnetic Materials: a handbook on the properties of magnetically ordered substances, ed. E.P. Wohlfarth and K.H.J. Buschow, Amsterdam.

Wu Y.Q., Ping D.H., Hono K., Hamano M. and Inoue A. (2000), Microstructural characterization of an α-Fe/Nd$_2$Fe$_{14}$B nanocomposite magnet with a remaining amorphous phase, *J. Appl. Phys.* **87**, 8658.

Ye F. and Lu K. (1998), Pressure effect on polymorphous crystallization kinetics in amorphous selenium, *Acta. Mater.* **46**, 5965.

Yoshizawa Y., Oguma S. and Yamaguchi Y. (1988), New Fe-based soft magnetic alloys composed of ultrafine grain structure, *J. Appl. Phys.* **64**, 6044.

Zbroszczyk J., Fukunaga H., Olszewski J., Ciurzynska W.H. and Hasiak A. (1996), The role of Nb and Cu in the creation of nanostructure in Fe-based amorphous alloys, *J. Magn. Magn. Mater.* **160**, 277.

Zhang B.W. and Yi G. (1996), Investigation of magnetic properties for Fe-Ni-P-B nanosize amorphous alloy powders prepared by chemical reduction, *J. Phys: Condens. Matter.* **8**, 5451.

Zhang D.L. (2004), Processing of advanced materials using high-energy mechanical milling, *Prog. Mater. Sci.* **49**, 537.

Zhang J., Wu B., Wu X., Wang G. and Zhao J. (1996a), Crystallization behavior of a mechanically alloyed amorphous $Fe_{80}Zr_8B_{11}Cu_1$ alloy, *J. Appl. Phys.* **79**, 5473.

Zhang Y., Hono K., Inoue A. and Sakurai T. (1996b), Partitioning of Si in a $Fe_{87}Zr_7Si_4B_2$ nanocrystalline soft magnetic alloy, *Appl. Phys. Lett.* **69**, 2128.

Zhou F., Luck R., Lu K., Lavernia E.J. and Ruhle M. (2002), Amorphous-to-crystalline transformation induced by thermal annealing of a metastable $Al_{90}Fe_{10}$ composite, *Phil. Mag. A.* **82**, 1003.

Zhou F., Liao X.Z., Zhu Y.T., Dallek S. and Lavernia E.J. (2003), Microstructural evolution during recovery and recrystallization of a nanocrystalline Al-Mg alloy prepared by cryogenic ball milling, *Acta. Mater.* **51**, 2777.